Dario Hrupec

Extragalactic sources of rapidly variable high energy gamma radiation

Doctoral Thesis
submitted to the Department of Physics,
Faculty of Science, University of Zagreb,
for the academic degree of
Doctor of Natural Sciences (Physics)

Zagreb
2008.

This thesis was done at Ruđer Bošković Institute under the supervision of Professor Daniel Ferenc from the University of California at Davis.

Acknowledgments

I would like to thank my mentor Dr. Daniel Ferenc from the University of California at Davis for his great professional and personal support during my work on this thesis. I have received precious inspiration from him. Finally, he encouraged me to read a lot. It was an invaluable advice.

I am thankful to my co-mentor Dr. Silvio Pallua from the Faculty of Science at Zagreb for his support and for the thesis review. I am also thankful to Dr. Krešimir Pavlovski from the Faculty of Science at Zagreb for the thesis review. I am particularly thankful to him for his valuable support. In addition, his terminological arguments impressed me a lot.

Many thanks to Dr. Matko Milin from Faculty of Science at Zagreb for the time he spent on reading and commenting my thesis. I really appreciate his being my committee member.

I owe many thanks to Dr. Eckart Lorenz from the University of California at Davis and ETH-Zurich who made possible my observations with the *Čerenkov telescope 1* (CT1) at La Palma in 2003. His donation of two Čerenkov telescopes to Ruđer Bošković Institute established a base for the *Cosmic Ray Observatory At The Eastern Adriatic* (CROATEA) and also for my work in astroparticle physics in Croatia. Each time I meet him I feel inspired for months. I owe deep thanks to him also for the thesis review. Finally, thank him a lot for his time devoted to me as my committee member.

I am also thankful to Dr. Krunoslav Pisk from Ruđer Bošković Institute and Dr. Ivo Šlaus from Croatian Academy of Sciences and Arts for reading the thesis and valuable support during all the time I spent at Ruđer Bošković Institute.

Dr. Vuko Brigljević from Ruđer Bošković Institute was particularly kind to carefully read the whole thesis and give me a lot of suggestions to improve my English.

I am thankful to Dr. Vladis Vujnović for his interest to my studies. His textbooks in Croatian were invaluable to me for the writing of the extended abstract in Croatian, especially his book "*Rječnik astronomije i fizike svemirskog prostora*" (Školska knjiga, Zagreb, 2004.), the very first astronomical dictionary in Croatian.

Many colleagues are thanked for helping me during the work on the thesis:

- Dr. Daniel Kranich from Davis (and since recently Zurich) for essential discussions about CT1 data analysis;
- Dr. Abelardo Moralejo from Padua (and since recently Munich) for useful discussion about detector simulations;
- Alvin Laille from Davis and Dr. Dorota Sobczyńska from Lodz for discussions about Monte Carlo simulations;

- Dr. David Paneque from SLAC for fruitful discussions and support during our work on the paper about Mkn 501 variability;
- Mikko Pasanen, Dr. Aimo Sillanpää and Kari Nilsson from Tuorla Observatory for cooperation in the study of Mkn 421 γ-optical correlations. I have learned a lot from numerous useful discussion with them;
- Fabian Schmidt from Leeds (and since recently Chicago) for some early help with shower visualization;
- Heinz-Georg Börst from Kiel for technical discussion about CT1;
- Dr. Ivica Puljak, Dr. Željko Antunović and Dr. Nikola Godinović from Split for showing me great hospitality during my work at the Split University and for their constant enthusiasm for the CROATEA project;
- Dr. Vuko Brigljević and Dr. Saša Ceci from Zagreb for helping me with Linux and ROOT when I was an absolute beginner;
- Dr. Antun Marki from Zagreb for the very first discussion about clouds;
- Dara O'Hogain from Dublin for some early comments on my English;
- Dr. Tome Antičić from Zagreb for polishing up my English at the end; and
- Dr. Tihomir Surić from Zagreb for his outstanding support of my work at Ruđer Bošković Institute.

And finally, I owe deep thanks to my lovely wife Nataša for her consistent love, patience and support, without which this work would not have been done. I dedicated the thesis to her as well as to my marvelous son Martin and my charming daughter Lucija.

Preface

In 1997, ten years ago, I did my diploma thesis in the field of advanced photodetectors in order to improve the *Major Atmospheric Gamma-ray Imaging Čerenkov detector* (MAGIC) telescope camera. At that time, the MAGIC project was in an early proposal phase [98] and my thesis [271] (done under the supervision of Professor Daniel Ferenc) was the very first one. These new type of photodetectors, called *hybrid photodetectors* (HPD), are being presently implemented in the MAGIC II project, after many years of research and development. Today, MAGIC is the largest *Imaging Atmospheric Čerenkov Telescope* (IACT) in the world and MAGIC II will be the first one having an advanced camera instead of using ordinary *photomultipliers* (PMT).

During the time after my diploma thesis, it was not possible to continue in Croatia the work in this exceptionally interesting and prospective field of astroparticle physics. The situation significantly improved in 2002 when Professor Ferenc offered me to join his group in order to set up the *Cosmic Ray Observatory at the Eastern Adriatic* (CROATEA) based on two Čerenkov telescopes from the *High Energy Gamma Ray Astronomy* (HEGRA). The telescopes were donated to Ruđer Bokoviće Institute by Dr. Eckart Lorenz.

In 2002, I went to the *Roque de los Muchachos Observatory* (ORM) on La Palma to dismantle two telescopes for CROATEA. Next year, I participated in the latest HEGRA *multiwavelength* (MWL) campaigns on *Markarian 421* (Mkn 421) using *Čerenkov Telescope one* (CT1), a member of the former HEGRA experiment. Mkn 421, an active galaxy, is known to be one of the most intensive variable gamma-ray sources in the sky.

In this thesis, I present the analysis of the data of Mkn 421 that the CROATEA team (Ivica Puljak, Željko Antunović and I) collected during the ten-days long run in February/March 2003, as well as some data previously collected by the HEGRA Collaboration (February/May 2001).

The latter data set is particularly precious for me since it contains a period of very high gamma-ray activity taken under non-ideal atmospheric conditions. It has not been analyzed before since it was not clear how to properly correct observations for the influence of the *variable atmospheric transparency* (VAT). Therefore I could test my VAT correction method on these data.

Now, the right time for VAT is just coming. The recent advent of the *LIght Detection And Ranging* (LIDAR) technology in the field of ground-based gamma-ray astronomy enables one to probe local atmospheric transparency, especially clouds. Many IACT groups have started to take into account local atmospheric changes over observatories. For example, the MAGIC group is developing a low power lidar for atmospheric transmission study [425] and has plans to use the commercial software *MODerate resolution TRANsmittance code* (MODTRAN) in order to cope with VAT. Besides, in the days of my thesis writing, two satellites, *Cloud-Aerosol Lidar and Infrared Pathfinder Satellite Observation* (CALIPSO) and the CloudSat, have been launched in April 2006. These satellites use lidars and radars to provide global vertical profiles of clouds.

In this context, one of the aims of my thesis has been to study VAT, especially clouds, in order to show that **IACT observations are possible even during cloudy weather** and duty cycle of an IACT can be increased.

A general requirement in ground-based γ-ray astronomy is moonless night with good atmospheric transparency [354] [384]. However, from the HEGRA experience, it was sometimes possible to operate the HEGRA detector with high efficiency in the presence of high dense cloud layers [323].

This work is part of general effort to develop correction methods for non-optimal atmospheric transmission in ground-based γ-ray astronomy. At present, absolute energy measurements of γ-rays performed with the *atmospheric Čerenkov imaging technique* (ACIT) have an uncertainty of at least $\pm$ 50%, the dominant source of error being poor knowledge of the atmospheric characteristics [354]. More generally, there are two limiting factors for ground-based astronomy: climate changes and pollution from aircraft exhaust trails. Both of them increase global cloud cover. If recent trends stay constant, all ground-based telescopes could be worthless by 2050. In other words, VAT corrections seem to be even more important in the coming days.

We have done detailed *Monte Carlo* (MC) simulations to quantify VAT. Up to now, important decisions about accepting the observational data or discarding them have been based on very rough methods. For example, the Whipple group — now *Very Energetic Radiation Imaging Telescope Array System* (VERITAS) — has used an operator personal opinion about nightly weather conditions, graded from A to C−. The HEGRA group — now MAGIC and *High Energy Stereoscopic System* (HESS) — has used nightly atmospheric extinction values measured by optical telescopes.

The main disadvantage of the method based on the extinction values is that it gives average values for the whole night, while local atmospheric transmission can change rapidly due to clouds, almost from event to event. There is also an important difference between optical astronomy and ground-based gamma-ray astronomy: While photons in the optical astronomy practically come from infinity and go through the whole atmosphere, Čerenkov photons from *extensive air showers* (EAS) come, in average, from 10 km distance and could be produced mostly below clouds. Moreover, the typical clouds over La Palma can be transparent enough to allow one to do observations anyway. In general, a combination of lidar measurements and VAT simulations can improve the quality of observational data, and can also extend the observational time (increase the duty cycle). One of the aims of this thesis is to develop VAT simulations in the context of ground-based *very high energy* (VHE) gamma-ray astronomy.

VAT corrections enable continuous observations, even during bad weather. It can be crucial for the study of short flares in blazars, the *gamma-ray bursts* (GRB) study as well as for the multiwavelength correlation study in blazars.

Furthermore, we have proposed a new approach to correlation studies based on MC simulations of correlation coefficient distribution and the Fourier convolution of empirical *probability density functions* (PDF). Correlation studies are an important part of *multiwavelength* (MWL) campaigns which are pivotal for testing models of processes in astrophysical sources like blazars.

We applied our new method of correlation study to the Mkn 421 data collected in 2003, but also to several recent sets of MAGIC data of Mkn 421, Mkn 501, and newly discovered Mkn 180. Comparative results of these blazars confirm *Synchrotron Self-Compton* (SSC) as the dominant mechanism for high-energy γ-ray production. Additionally, the energy-dependent time delay in peak flare emission, recently found in Mkn 501 data, sheds new light on the physical mechanism of γ-ray emission in blazars, and sets new limits to quantum gravity.

Zagreb, May 2007.
Dario Hrupec

Table of Contents

University of Zagreb
Faculty of Science
Department of Physics

Doctoral Thesis

Extragalactic sources of rapidly variable high energy gamma radiation

Dario Hrupec
Ruđer Bošković Institute, Bijenička 54, Zagreb

Abstract

The atmosphere is an intrinsic part of any imaging atmospheric Čerenkov telescope and the telescope response is therefore sensitive to unpredictable changes in the atmosphere. A lot of observational data taken during non-ideal atmospheric transparency have not been analyzed because of a lack of an appropriate analysis method that would be able to provide corrections for the imperfect transparency.

On the other hand, extragalactic sources of high-energy cosmic gamma-rays (e.g. active galactic nuclei and gamma-ray bursts) are usually highly variable and the temporal characteristics of their light curves are key to the understanding of the physics of their sources. It is therefore very important to extend the observation time for variable sources as much as possible.

In order to significantly extend the effective observational time of variable gamma-ray sources, we have developed a new data analysis method, which first determines the actual variable atmospheric transparency from the gamma-ray measurements, and then corrects those measurements according to the estimated atmospheric effect. To learn how the clouds influence gamma-ray measurements, we have implemented the simulation of clouds into the Monte Carlo simulation chain. Simulations starts with program Corsika, which simulates the development of particle showers in the atmosphere, and traces the Čerenkov light emitted by charged particles to the telescope. This method may extend the effective observation time in ground-based gamma-ray astronomy in general. Here we report on the application of the method in the first analysis of a particularly important data set from 2001 that includes a period of very strong activity of the blazar Mkn 421. In the near future, modern lidars will be able to precisely measure the distribution of the cloud density along the line of sight of the telescope, and thus provide significantly more information for our correction method.

We also developed a new approach to correlation study based on MC simulations and the Fourier convolution. We applied the new method to analyze our CT1 data from 2003 of Mkn 421. We also reanalyzed correlation of some recent MAGIC data on blazars Mkn 421, Mkn 501 and newly discovered Mkn 180.

Thesis consists of:	*278 pages, 137 figures, 38 tables and 504 references*
Original in:	*English*
Thesis deposited in:	*Central Library for Physics, Bijenička 32, Zagreb*
Keywords:	*active galactic nuclei / blazars / correlations / cosmic gamma-rays / imaging atmospheric Čerenkov telescopes / Mkn 421 / Monte Carlo simulations / variable atmospheric transparency*
Mentor:	*Dr. Daniel Ferenc, Professor*
Co-mentor:	*Dr. Silvio Pallua, Professor*
Reviewers:	*Dr. Krešimir Pavlovski, Professor*
	Dr. Daniel Ferenc, Professor
	Dr. Matko Milin, Asst. Prof.
	Dr. Eckart Lorenz, Professor
	Dr. Silvio Pallua, Professor

Thesis accepted: December 4, 2007.

Sveučilište u Zagrebu
Prirodoslovno-matematički fakultet
Fizički odsjek

Doktorska disertacija

Izvangalaktički izvori brzo promjenljivog visokoenergijskog gama zračenja

Dario Hrupec
Institut "Ruđer Bošković", Bijenička 54, Zagreb

Sažetak

Atmosfera je sastavni dio svakog Čerenkovljevog teleskopa i odaziv teleskopa stoga ovisi o nepredvidljivim promjenama atmosfere. Mnoga opažanja, provedena pri nesavršenoj atmosferskoj transparentnosti, nisu dosad analizirana jer nije postojala prikladna metoda za korekciju podataka.

S druge strane, izvangalaktički izvori visokoenergijskih kozmičkih gama-zraka (npr. aktivne galaktičke jezgre i provale gama-zračenja) često su vrlo promjenljivi i njihove vremenske karakteristike krivulja sjaja ključ su razumijevanja fizike samih izvora. Stoga je važno opažanja produljiti što je moguće više.

Kako bismo značajno produljili vrijeme opažanja promjenljivih izvora gama-zračenja, razvili smo novu metodu analize podataka, kojom prvo određujemo promjenljivu atmosfersku transparentnost iz opažanja gama-zračenja, a potom mjerenja popravljamo prema procijenjenim atmosferskim učincima. Da bismo razumjeli kako oblaci djeluju na opažanja gama-zraka, uključili smo simulacije oblaka u lanac Monte Carlo simulacija. Simulacije počinju programom Corsika, koji simulira razvoj pljuska čestica u atmosferi, i do teleskopa prati Čerenkovljevu svjetlost koju emitiraju nabijene čestice. Ova metoda može povećati učinkovito vrijeme opažanja u gama-astronomiji općenito. Ovdje izvješćujemo o prvoj primjeni te metode na posebno važan skup podataka iz 2001. godine koji uključuje period vrlo jake aktivnosti blazara Mkn 421. U bliskoj će budućnosti moderni lidari moći precizno mjeriti raspodjele gustoće oblaka u smjeru opažanja teleskopa te tako pružiti značajno više informacija za naše korekcijske metode.

Razvili smo također novi pristup korelacijama temeljen na Monte Carlo simulacijama i Fourierovoj konvoluciji. Primijenili smo novu metodu na vlastita opažanja Mkn 421 teleskopom CT1 iz 2003. Također smo ponovili analizu korelacija nedavnih opažanja teleskopom MAGIC za blazare: Mkn 421, Mkn 501 i novootkriveni Mkn 180.

Rad sadrži:	*278 stranica, 137 slika, 38 tablica i 504 reference*
Jezik izvornika:	*engleski*
Rad je pohranjen u:	*Središnjoj knjižnici za fiziku, Bijenička 32, Zagreb*
Ključne riječi:	*aktivne galaktičke jezgre / blazari / Čerenkovljevi teleskopi / korelacije / kozmičke gama-zrake / Mkn 421 / Monte Carlo simulacije / promjenljiva atmosferska transparentnost*
Mentor:	*Dr. sc. Daniel Ferenc, red. prof.*
Komentor:	*Dr. sc. Silvio Pallua, red. prof.*
Ocjenjivači:	*Dr. sc. Krešimir Pavlovski, red. prof.*
	Dr. sc. Daniel Ferenc, red. prof.
	Dr. sc. Matko Milin, doc.
	Dr. sc. Eckart Lorenz, red. prof.
	Dr. sc. Silvio Pallua, red. prof.

Rad prihvaćen: 4. prosinca 2007.

Chapter 1

Introduction

The goal of an astronomer is to attempt to understand
the nature of the universe in all of its complexity,
simply for the sake of understanding.
Bradley W. Carroll & Dale A. Ostlie

During the last decade, there has been a huge explosion of knowledge of the heavens [155]. Elementary particle physics, astronomy & astrophysics, and cosmology have become woven together, and this symbiosis has led to great advances in our understanding of the universe at the largest and the smallest scales [384] (Figure 1.1). In the 1980's, high-energy physicists and very first observational $\gamma-$ray astronomers initiated a new research field [4]. This new interdisciplinary and rapidly expanding field, which combines the experimental techniques and theoretical methods from both astronomy and particle physics, has been named high-energy *Astroparticle Physics*[1].

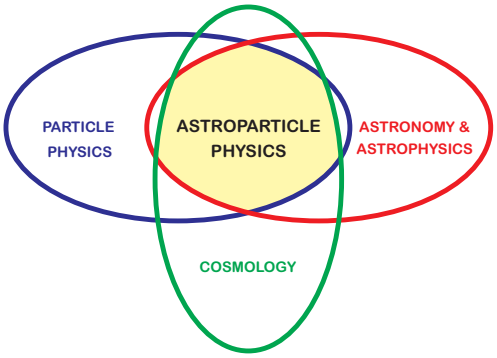

Figure 1.1: Astroparticle Physics is an interdisciplinary field at the interface of particle physics, nuclear physics, cosmology and astrophysics.

Astroparticle physics, which involves about two thousand European scientists today, addresses some of the most fundamental questions of contemporary physics: *What is the Universe made of? In particular: What is dark matter? What is the origin of cosmic rays? What is the view of the sky at extreme energies? In particular: What is the physics of cosmic objects?*

[1]Some authors, partially in the U.S.A., prefer the term *Particle Astrophysics*.

Like astronomy, astroparticle physics is an observational science. It includes [329]:
– γ-ray astronomy;
– neutrino astronomy;
– study of cosmic rays;
– dark matter searches;
– nuclear astrophysics; and
– gravitational wave detection.

Let me name just a few important discoveries in this field, made within the past decade:

- *The sources of long-lasting gamma-ray bursts (GRB) seem to be core-collapse of large supernovae (SN) into black holes (BH) in distant, very young galaxies* (April 1997) [382]; The origin of long GRBs was one of the greatest mysteries of astrophysics since their first detection in 1967.

- *Neutrinos have non-zero masses* (August 1998) [214]; It was the first experimental deviation from the standard model (SM).

- *The expansion of the universe is not slowing down but, rather, accelerating* (September 1998) [411];

- *Short GRBs are associated with the merger of two neutron stars (NS), or a NS and a black hole (BH), in binary systems* (October 2005) [212];

- *Recent data seem to confirm an old hypothesis, that the sources of galactic cosmic rays (GCR) are galactic supernova remnants (SNR)* (November 2005) [477]; They have also been called a mystery for a long time, since Hess's discovery of *cosmic rays* (CR) in 1912.

- *Direct evidence for the existence of dark matter (DM)* (August 2006) [167]; Weak lensing observations of the Bullet Cluster (1E 0657-56), two colliding clusters of galaxies, have provided the best evidence to date.

It is clear that this incredible decade of discoveries is only a prelude to further advances to come [155].

Since I started to work on my PhD thesis, two Nobel Prizes have been awarded in astrophysics. In 2002, Raymond Davis Jr. and Masatoshi Koshiba were awarded "*for pioneering contributions to astrophysics, in particular for the detection of cosmic neutrinos*" and Riccardo Giacconi "*for pioneering contributions to astrophysics, which have led to the discovery of cosmic X-ray sources*". Recently, the Nobel Prize for 2006 has been announced. John C. Mather and George F. Smoot have been awarded "*for their discovery of the blackbody form and anisotropy of the cosmic microwave background radiation*".

During the last ten years astroparticle physics has moved towards larger sensitivity and price, with costs of individual projects ordering of 100 M€ [84]. The European astroparticle community has a leading position in many of them. Hence, *Astroparticle Physics European Coordination* (ApPEC) has prepared[2] a roadmap for astroparticle physics in Europe which covers the next decade [84], whereby high priority is given to γ-ray astronomy.

[2]In the time of writing, second draft version (January 15, 2007) was available.

First steps toward high-energy astroparticle physics were made by discovery of high-energy "radiation from above" almost a century ago, in 1912.

1.1 Radiation from above

1.1.1 Cosmic rays

Cosmic rays (CR) are energetic particles of extraterrestrial origin. In traditional nomenclature CRs are stable charged particles – mainly protons ($\approx 90\%$) and α-particles ($\approx 9\%$). The rest are heavier nuclei with lifetimes of order 10^6 years or longer [219]. Electrons, γ rays, and high energy neutrinos make up a small fraction ($< 10^{-4}$) of the radiation from above and some authors used to include them in cosmic rays. But today, the term *cosmic rays* means charged particles only.

The kinetic energies of CRs extend over more than 14 orders of magnitude (from 10^6 to 10^{20} eV and above[3]), with the flux on the Earth's *top of the atmosphere* (TOA)

$$\frac{\mathrm{d}\Phi}{\mathrm{d}E} \propto E^{-\alpha} \tag{1.1}$$

where α is the differential spectral index of the cosmic ray flux which has values between 2.6 and 3.1 depending on the energy region (Figure 1.2). This power law spectrum confirms the non-thermal origin of CRs.

The spectral index α changes several times, e.g. around $3 \cdot 10^{15}$ eV (the "knee") and around $3 \cdot 10^{18}$ eV (the "ankle"), and these changes are linked to cosmic ray sources. The wide spectrum of particle energies indicates that there must be a wide variety of sources, but also requires a wide variety of detection techniques.

Cosmic rays are the most obvious manifestation of the non-thermal[4], relativistic universe [483]. They have continuously bombarded the Earth for billion of years.

The discovery of cosmic rays

High energy particles detected at the Earth's surface were initially believed to originate in radioactive isotopes in the ground [77]. This theory was disproved in 1912 by Austrian-American physicist Victor Hess (1883–1964). Using a simple electroscope during his famous balloon flights, Hess measured a stronger discharge at higher altitude, and concluded that the radiation came **from above** [413]. Hess further showed that the Sun could not be the primary source of CRs by taking balloon measurements during a 1912 solar eclipse. He received the Nobel Prize in physics in 1936 "*for his discovery of cosmic radiation*".

The term *cosmic rays* was coined in 1925 by American physicist Robert Andrews Millikan (1868-1953).

In 1938, Pierre Auger observed near-simultaneous ionization events at widely separated locations. He concluded that these events were created by incident high-energy particles which initiated a second-particles cascade. Today, such cascades are known as *extensive air showers* (EAS) or Auger showers.

[3]The most energetic event observed so far was $E_{\max} = 3.2 \cdot 10^{20}$ eV = 50 J.

[4]Radiation due to a cause other than the temperature of emitting body, e.g. synchrotron radiation. It has a different spectrum from that of the black-body radiation.

The spectrum of cosmic rays

Figure 1.2 shows a sketch of the energy spectrum of CRs. The spectrum follows a broken

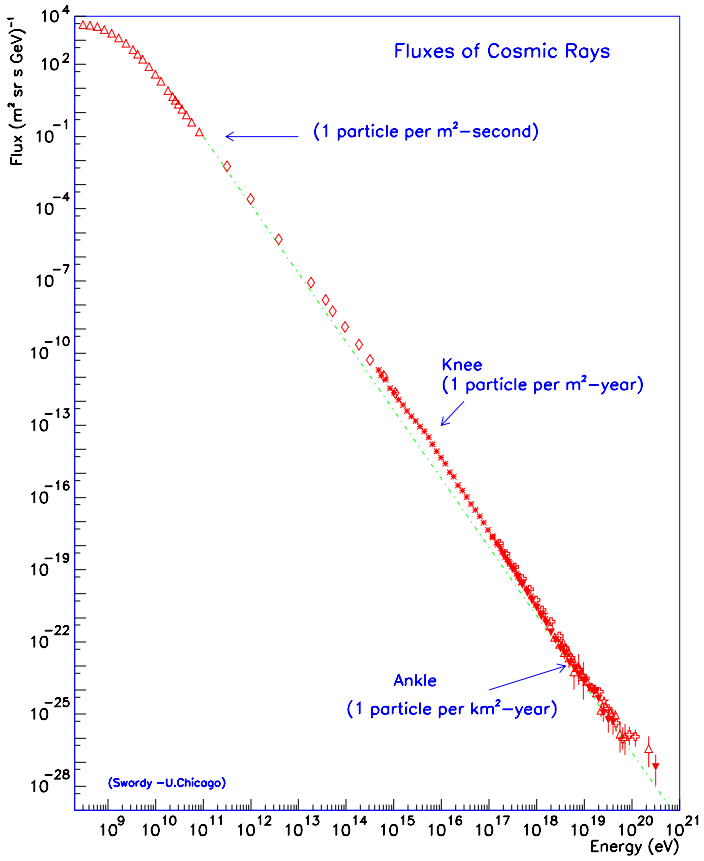

Figure 1.2: The energy spectrum of cosmic rays as a function of particle kinetic energy. Figure: *http://astroparticle.uchicago.edu/sciam1.eps* (Simon Swordy).

power law and contains two (or even three) bumps: the ankle and the knee. It was previously thought that the most likely explanation for the ankle is that the *extragalactic cosmic ray* (EGCR) flux begins to dominate over the flux of *galactic cosmic rays* (GCR). The situation now seems more complicated, due to the existence of the second knee near $5 \cdot 10^{17}$ eV [219]. Therefore, the GCR flux probably terminates there, and the flux above the second knee seems to be of cosmological origin. There should be a rapid change in α, around $E_{\mathrm{GZK}} = 5 \cdot 10^{19}$ eV, called *Greisen-Zatsepin-Kuzmin* (GZK) cut-off [219].

The flux and composition of *ultra high energy cosmic rays* (UHECR) are still very uncertain because of the low statistics of showers observed so far. Significant progress in this field is expected by the Pierre Auger Observatory. To study the flux at even higher energies (10^{21} eV) with sufficient statistics, new techniques will be required [199]. Possible solution could be the observation of the atmosphere from outer space e.g. *Extreme Universe Space Observatory* (EUSO) [151] or radio detection of extended air showers e.g. *ANtarctic Impulsive Transient Antenna* (ANITA).

Above E_{GZK}, space becomes opaque to CRs because of the interactions (photo-pion

production) with the *Cosmic Microwave Background* (CMB)

$$\begin{aligned} p + \gamma_{\mathrm{CMB}} &\longrightarrow \Delta^+ \longrightarrow p + \pi^0 \\ p + \gamma_{\mathrm{CMB}} &\longrightarrow \Delta^+ \longrightarrow n + \pi^+ \end{aligned} \tag{1.2}$$

Hence, UHECRs with $E > E_{\mathrm{GZK}}$ cannot come from sources uniformly distributed throughout the Universe. Instead, the Local super-cluster (15-20 Mpc) must make a strong contribution to any extragalactic source [256]. However, such acceleration sites are not known.

The origin of cosmic rays

It is widely believed that SNRs are the major source of galactic CRs [4] via the shock acceleration mechanism [23]. There are many observational evidences for this theory. For example, HEGRA's observations of TeV γ-rays from SNR *Cassiopeia A* gave such an indication [23]. One of the first strong evidences came from Chandra X-Ray observations of the forward shock acceleration in Tycho's SNR [477]. Recently, the HESS collaboration reported observations of VHE γ-rays from a complex of giant molecular clouds in the center of our Galaxy [55]. The observation of the correlation between target material and the TeV γ-ray emission is unique, and provides compelling evidence for the origin of the emission in the interaction of CRs. This is the first time that such **direct evidence for recently accelerated CRs** has been found [55].

The origin of cosmic rays at the highest energy is not known at all. Future data may reveal unexpected acceleration mechanisms, as well as new physics beyond the standard model [84]. The coming years may bring a breakthrough in CR physics.

Air shower experiments

Above 10^{14} eV, the showers of secondary particles created by CRs in the atmosphere are extensive enough to be detectable from the ground [84]. *Particle detector arrays* (PDA) can perform continuous observations (unlike IACTs) with duty cycles of almost 100%. They use water Čerenkov technique and can therefore also work during daytime. PDAs have very large *fields of view* (FoV) of more than 2 sr (again unlike IACTs), which provides simultaneous observations of large parts of the sky and also the sky survey. However, their sensitivity has been too low to reach the significance of 5σ needed for source detection. Different techniques have been developed to increase sensitivity. Some recent experiments (or experiments under construction) are:

KASCADE Grande is the extension of the original KASCADE array in Karlsruhe, Germany, to an area of 0.5 km^2. It detects CRs between 10^{13} eV and 10^{18} eV. KASCADE has contributed to the improvement of the understanding of the interaction models which are crucial for MC simulations of EAS (see Section 1.6.4).
Tibet III Air Shower Array consists of an array of plastic scintillators covering an area of currently more than 20.000 m^2 (50.000m^2 in the final configuration). The Array is placed in Tibet at the extreme height of 4300 m above sea level.
EAS-TOP will be a 1 km^2 array of ice Čerenkov detectors at the surface of IceCube, a neutrino telescope at the South Pole, to detect the electromagnetic shower component.
TUNKA experiment plans to extend the existing array of Čerenkov detectors in Siberia to cover an area of 1 km^2 and to extend the energy range up to 10^{18} eV. Precise energy

measurements by TUNKA are crucial to detect fine structures in the cosmic ray spectrum [84].

Fluorescence[5] **experiments** can study CRs of the highest energy – the *ultra high energy* (UHE) and *extremely high energy* (EHE) regions.

- A recent experiment, still under construction, is the **Auger** Observatory. It combines the air fluorescence technique (3 fluorescence stations, out of 4, have been built) and ground arrays covering an area of 3000 km^2 in Mendoza, Argentina. By now, 60% of ground detectors, out of 1600, have been finished.
- The *Extreme Universe Space Observatory* (EUSO) onboard the *International Space Station* (ISS) will be the first space mission devoted to the investigation of CRs (and neutrinos) of extreme energy ($E > 5 \cdot 10^{19}$ eV), using the Earth's atmosphere as a giant detector. EUSO will observe the fluorescence signal looking downward with 60^o full *field of view* (FoV). EUSO is planed to have more than 200000 photosensors [329].

1.1.2 γ-rays

Electromagnetic radiation spectra

The photon, a quantum of *electromagnetic* (EM) radiation, has been a traditional messenger in astronomy. Its straight propagation allows a study of its sources. Nearly all of our information about the Universe comes from studies of EM radiation, from radio to γ-rays (Table 1.1). γ-rays span over 15 orders of magnitudes in energy spectrum, almost

Region	Energy	Wavelength
γ-ray	**$E > 100$ keV** Precisely, $E > m_e c^2 = 511$ keV	**$\lambda < 1$ pm** Precisely, $\lambda < \lambda^e_{COMPTON} = 2.43$ pm
X-ray	100 eV $< E <$ 100 keV	1 pm $< \lambda <$ 10 nm
ultraviolet	10 eV $< E <$ 100 eV	10 nm $< \lambda <$ 100 nm
visible	1 eV$< E <$ 10 eV Precisely, 1.7 eV $< E <$ 3.2 eV	100 nm $< \lambda <$ 1 μm Precisely, 380 nm $< \lambda <$ 750 nm
infrared	1 meV $< E <$ 1 eV	1 μm $< \lambda <$ 1 mm
microwave	0.1 μeV $< E <$ 1 meV	1 mm $< \lambda <$ 10 cm
radio	$E <$ 0.1 μeV	$\lambda >$ 10 cm

Table 1.1: The energy and wavelength ranges for different bands in the EM spectrum.

as much as the rest of the EM spectrum. Therefore, a wide variety of detection techniques and instruments are necessary for the observation of the γ-ray sky. That naturally leads to an additional sub-division of the γ-ray spectrum (Table 1.2).

Among all different techniques developed so far for the detection of cosmic γ-rays, two have succeeded in providing the detection of many sources and their spectral measurements: space-borne experiments (satellite detectors) and ground-based experiments (Čerenkov telescopes).

[5]Fluorescence is a phenomenon in which a molecule absorbs a higher-energy photon (usually UV) and re-emits it as a lower-energy photon (usually visible). The energy difference ends up as molecular vibration (heat).

Region	Energy
LE/ME	100 keV $< E <$ 100 MeV
HE	100 MeV $< E <$ 100 GeV
VHE	**100 GeV** $< E <$ **100 TeV**
UHE	100 TeV $< E <$ 100 PeV
EHE	$E >$ 100 PeV

Table 1.2: Nomenclature for γ-rays in different energy ranges, according to [483] and [325]; *low energy* (LE), *medium energy* (ME), *high energy* (HE), *very high energy* (VHE), *ultra high energy* (UHE), *extremely high energy* (EHE). G means *giga* (10^9 or billion), T means *tera* (10^{12} or trillion), and P means *penta* (10^{15} or quadrillion).

Space-borne experiments

Satellite-borne detectors use a very efficient γ/hadron separation by using anti-coincidence counters that completely surround the active detection volume, but they also have very limited aperture (up to 1 m^2, but often just a few cm^2). Therefore, the corresponding γ-ray flux is low – the strongest sources produce about one γ-ray per minute only, and the space-borne γ-ray detectors can observe γ-rays of energies only up to 10 GeV.

Previous γ-ray satellites:

- The *Small Astronomy Satellite 2* (SAS-2) was the very first satellite devoted to γ-ray astronomy. It was launched in 1972. and stayed in orbit for six months only. Nevertheless, it gave the first detailed look at the γ-ray sky (in the energy range from 20 MeV to 1 GeV). Its detectors were spark chambers and scintillators.

- The *COsmic ray Satellite B* (COS-B) was active from 1975 to 1982 in the energy range 70 MeV – 5 GeV. COS-B made the first complete map of the γ-ray emission from the disc of our Galaxy, and the first detection from an extragalactic object, quasar 3C273.

- The *Compton Gamma Ray Observatory*[6] (CGRO) was a NASA satellite in orbit from 1991 to 2000. It consisted of four instruments:

  - *Energetic Gamma Ray Experiment Telescope* (EGRET)
  - *Compton Telescope* (COMPTEL)
  - *Burst and Transient Source Experiment (BATSE)*
  - *Oriented Scintillation Spectrometer Experiment (OSSE)*

  CGRO was observing the γ-sky up to 30 GeV and made a dramatic progress in the GeV range: e.g. the discovery of an isotropic distribution of the GRBs. EGRET discovered a large number of extragalactic sources, especially blazars as primary sources of HE γ-rays.

[6]It was named after the American physicist Arthur Holly Compton (1892–1962).

Recent γ-ray satellites:

- The *International Gamma-Ray Astrophysics Laboratory* (INTEGRAL) was launched in October 2002. It covers the energy range: 15 keV – 10 MeV with high spectral and spatial resolution. INTEGRAL simultaneously observes γ-rays, X-rays and visible light.

- The *Swift*, launched in November 2004, is a multiwavelength observatory devoted to GRBs, which carries 3 instruments: *Burst Alert Telescope* (BAT), *X-ray Telescope* (XRT) and *Ultraviolet/Optical Telescope* (UVOT)

Future γ-ray satellites:

- The *Astro-rivelatore Gamma a Immagini LEggero* (AGILE) is a small Italian γ-ray satellite sensitive in the energy range 30 MeV – 30 GeV. It was launched on April 23, 2007.

- The *Gamma-ray Large Area Space Telescope* (GLAST) is a promising advanced γ-ray observatory. GLAST will carry:

  - *GLAST Burst Monitor* (GBM)
  - *Large Area Telescope* (LAT): the main instrument on the GLAST observatory. It has superior performance compared to its predecessor EGRET: five times larger effective area, better angular and energy resolution, wider FoV, and much smaller dead time. This will provide more than a factor of 30 improvement in sensitivity.
  - *Anti-Coincidence Detector* (ACD): the outermost detector layer in the LAT, surrounding the tracker. The purpose of the ACD is to detect and veto incident cosmic rays (charged particles), which outnumber cosmic γ-rays by 3 to 4 orders of magnitude.

  GLAST, which is expecting to be launched soon, will probably increase the number of γ-ray sources to about 1000.

- The *Alpha Magnetic Spectrometer* (AMS) will be a magnetic spectrometer onboard *International Space Station* (ISS) [381] for identification of electrons and anti-nuclei in the energy range from 10^9 to 10^{12} eV/nucleon. AMS will contain 3D imaging *Electromagnetic CALorimeter* (ECAL).

Ground-based γ-ray experiments

In contrast to space astronomy which needs special, well-funded laboratories, ground-based experiments are usually conducted by smaller university groups.

- **Water Černkov detectors**
  The *Multiple Institution Los Alamos Gamma Ray Observatory* (MILAGRO) is a large water Čerenkov experiment located near Los Alamos in New Mexico at 2600 m asl. It uses the man-made pond 80 m × 60 m × 8 m. Milagrito, an intermediate size detector with 228 PMTs on the pond bottom, collected data from February 1997 to April 1998. The full MILAGRO detector with 723 PMTs was installed in 1998. Milagro is unique in its capability to continuously monitor the full overhead

sky at energies from 100 GeV to 100 TeV.

The *High Altitude Water Čerenkov* (HAWC) is a water Čerenkov detector proposed to be constructed at a high altitude site (Tibet at 4500 m or Atacama at 5200 m) by re-using 900 PMTs and electronics currently used by Milagro. HAWC will be an all-sky VHE instrument with the sensitivity 15 times that of Milagro.

- **Extensive Air Shower (EAS) Arrays**
  The *Astrophysics Research at Ground-based Observatory at Yang Ba Jing* (ARGO-YBJ) consists of array of *Resistive Plate Chamber* (RPC) detectors completely covering an area of more than 2000 m^2 (6000 m^2 in the final configuration). The Array is placed in Tibet (4300 asl). It covers the energy range from 100 GeV to 200 TeV and its sensitivity is three times better than Tibet III Air Shower Array. ARGO-YBJ can study a wide class of phenomena in astroparticle physics, but it is primarly devoted to γ-ray astronomy, e.g. GRB study.

- **Solar power stations as atmospheric Čerenkov telescopes**
  The "solar tower" detectors use huge mirror areas of ex solar power plants to sample the Čerenkov wavefront (thickness $\approx$ 1 m) from EAS. They usually have low threshold (about 50 GeV). The main problem of these experiments has been hadron rejection.

  The *Čerenkov Low Energy Sampling and Timing Experiment* (CELESTE) was an atmospheric Čerenkov telescope in the French Pyrénées (1650 m asl) detecting γ-rays from 20 GeV to 300 GeV. The experiment was active from 1998 to June 2004, when it was shut down (together with the CAT experiment). CELESTE was using 53 heliostats of a solar plant to collect Čerenkov light from air showers.

  The *Solar Tower Atmospheric Čerenkov Effect Experiment* (STACEE) is a wavefront sampling detector sensitive to γ-rays above 100 GeV which uses 64 heliostats and a 64 PMTs camera in New Mexico [439]. STACEE has been operational since fall 2002.

- **Wavefront sampling technique**
  The *Pachmarhi Array of Čerenkov Telescopes* (PACT) is an array consisting of 25 small telescopes located at Pachmarhi in India at 1075 m asl. Each telescope has seven mirrors with a reflector area of 4.5 m^2. PACT is based on the wavefront sampling technique (non-imaging). Hence, each telescope's "camera" consists of one PMT only.

  The *High Altitude GAmma-Ray observatory at Hanle* (HAGAR) is an array of 7 small telescopes planned to be constructed at Hanle in the Himalayas (northern India) at an altitude of 4200 m. This site is also planned for a huge imaging telescope MACE. HAGAR will not use the imaging technique but rather the wavefront sampling technique. Thanks to very high altitude, HAGAR will have energy threshold as low as 60 GeV for vertically incident showers. The first telescope has been tested

and moved to Hanle in June 2005 and the full array is expected to be operational by the end of 2007.

- **Combined techniques**
  The *All-sky Survey High Resolution Air shower detector* (ASHRA) is a quite unique observatory currently under construction at Mauna Loa on the Hawaii Island. It will consist of 12 light collection detectors covering entirely all sky with totally 80 mega pixels in photosensor arrays. ASHRA is primarily designed to explore transient objects such as GRBs detecting simultaneously optical light and VHE γ-rays.

• Imaging Atmospheric Čerenkov Telescopes (IACT)

The galactic and extragalactic[7] sources of *high energy* (HE) and *very high energy* (VHE) γ-rays have been successfully studied for the last 15 years, thanks to both *Compton Gamma Ray Observatory* (CGRO) and *Imaging Atmospheric Čerenkov Telescopes* (IACT).

The youngest astronomy branch, *ground-based gamma-ray astronomy*, was born with the development of the Whipple telescope. The breaking point was the introduction of the *atmospheric Čerenkov imaging technique* (ACIT) which led to the detection of the first VHE γ-ray source, the Crab Nebula, in 1989 [486].

Two key points of ACIT development were:
• Imaging technique
Imaging technique (IT) was introduced by Hillas in 1985 and implemented by the Whipple collaboration. The technique resulted in the very first TeV γ-ray source detection in 1989 [486]. The IT significantly improved signal-to-noise ratio (γ/hadron separation).
• Stereoscopic observations
Stereoscopic observations were introduced by the HEGRA collaboration. The HEGRA stereoscopic system started operations in December 1996 [183]. The system consisted of four IACTs. In 1997, the system was successfully used for the observations of the extraordinary outburst of Mkn 501.
Stereoscopic observation has many advantages over stand-alone IACT:
– improved sensitivity near the energy threshold;
– superior background rejection (γ/hadron separation);
– better angular resolution ($< 0.1^{\circ}$); and
– better energy resolution ($< 20\%$).

Detection principle of IACTs:
The detection method of all IACTs, the Whipple's successors, remains essentially unchanged today: mirrors are used to reflect Čerenkov light from EAS onto a camera (PMT detector package located in the focal plane), and fast electronics readout discriminate the brief (few nanoseconds) Čerenkov flashes from the background night-sky light [266].

Comparing to space-based γ-ray telescopes which have small apertures (with collection area up to 1 m^2), ground-based γ-ray telescopes have huge apertures and

[7]Galactic – located in our own galaxy, extragalactic – outside of the galaxy.

therefore superior sensitivity. Apertures of the third generation of IACT, given in Table 1.3 (10 - 17 m) refer to the optical reflectors only. The effective collection area is actually the area of the Čerenkov light pool (about $5 \cdot 10^4$ m^2). Therefore, a typical IACT has an effective aperture equal to the diameter of the Čerenkov light pool (Figure 4.8).

Previous IACTs:
The Whipple Observatory was built in 1968 and it has been in almost continuous nightly use since that time. It is the most important IACT in the history of γ-ray astronomy. The Whipple telescope discovered the first galactic source of VHE γ-rays, SNR the Crab Nebula, in 1989, and the first extragalactic source, AGN Mkn 421, in 1992.

The *High Energy Gamma Ray Astronomy* (HEGRA) consisted of six small IACTs: a stand-alone telescope CT1 (described in detail in Section 3.1.1) and a system of telescopes CT2-CT6. CT1 commenced working in 1992. CT2 was installed in 1993 and the full HEGRA system came into operation in 1996. The HEGRA system was the very first instrument operating in the stereoscopic observation mode. It was also a successful prototype for the future low-energy IACT arrays. The performance of the system was [297]:
– energy threshold of 500 GeV;
– angular resolution better than 0.1^o;
– shower impact point[8] less than 20 m;
– dynamic energy range of 500 GeV to 30 TeV; and
– energy resolution better than 20%.
HEGRA's results clearly demonstrated the power and the potential of the stereoscopic approach: the high level of suppression of the CR background and the superior angular resolution [183]. The HEGRA system was shut down in 2002, and the CT1 in 2003. In this thesis we analyzed the data observed with the CT1.

The *Cherenkov Array at Thémis* (CAT) was an imaging Čerenkov telescope located in the French Pyrénées at an altitude of 1650 m (at the same site where CELESTE was located). CAT was equipped with a high-resolution camera (600 PMTs with 4.8^o full field of view) and a reflector of 18 m^2. It was used to observe VHE γ-rays in the energy range from 250 GeV to 20 TeV. CAT had been in operation from 1996 until 2004 when the site at Thémis was closed.

The *Mark 6* was a ground-based γ-ray telescope of the University of Durham located in Narrabri, Australia. The telescope consisted of three large parabolic mirrors, each with an area of 42 m^2, and a camera of 109 PMTs. Mark 6 reached an energy threshold as low as 200 GeV. The telescope was commissioned in 1995 and it was collecting data until March 2000.

The Utah Seven *Telescope Array* (TA) was a telescope array in Utah at an altitude of 1600 m asl. Each telescope consisted of a 6 m^2 reflector and a high-resolution imaging camera of 256 PMTs. The threshold energy at zenith was 600 GeV. TA was in operation from 1997 to 2000.

[8]The point at which a shower core axis intersects a plane of a telescope level.

Recent IACTs:
European instruments (MAGIC and HESS) are now leading the field of ground-based γ-ray astronomy. Current generation of IACT include also American VERITAS and Japanese CANGAROO III. Table 1.3 shows their comparative characteristics.

	HESS	**MAGIC**	**VERITAS**	**CANGAROO III**
Location	Khomas Highlands (Namibia)	La Palma (Spain)	Montosa (Arizona)	Woomera (Australia)
Altitude (m)	1800	2200	1800	160
# of CTs	4	1 (+1)	4	4
Aperture (m)	13	17	12	10
The area (m^2)	107	236	110	57
# of mirrors	382	964	350	114
# of PMTs	960	576	499	427
FoV	5^o	3.6^o	3.5^o	4^o
Pixel size	0.16^o	0.10^o	0.15^o	0.17^o
$E_{threshold}$ (GeV)	100	30	50	600
Energy resolution	15%	15%	15%	35%
Angular resolution	$< 0.1^o$	$< 0.1^o$	0.17^o	0.3^o

Table 1.3: The big four - the leading IACTs that will dominate the field for the next 5 to 10 years. The reflector area, the number of mirrors and the number of pixels refer to a single telescope.

The *Major Atmospheric Gamma-ray Imaging Čerenkov detector* (MAGIC) is currently the largest IACT with an aperture of 17 m (an area of 236 m^2) capable to detect cosmic γ-rays at an energy threshold lower than any existing IACT (the target is < 30 GeV). It is sited at the Roque de los Muchachos Observatory on La Palma in the Canary Islands as the first element of the *European Čerenkov Observatory* (ECO) to study the deep universe with HE γ-rays [92]. MAGIC began taking data in 2004 and is a follow up to the HEGRA experiment [91]. In this thesis, we reanalyzed the data (from published papers) from several blazars observed by MAGIC.

The *High Energy Stereoscopic System* (HESS) is an array of four 13-meter telescopes in Namibia, composed of 382 round mirrors with an effective mirror surface area of 107 m^2. The mirrors are remotely adjustable by computer control. Each camera consists of a hexagonal array of 960 PMTs [60]. Initial data from the first telescope were recorded in June 2002 and the full array has been operational since December 2003.

The *Very Energetic Radiation Imaging Telescope Array System* (VERITAS) project uses four telescopes at a site in Arizona. Each telescope consists of a 12 m diameter reflector and a 499 element PMT imaging camera [266]. The reflector has 350 hexagonal mirror facets with a total mirror area of 110 m^2 [266]. The first of these telescopes was completed in February 2005 and full array has been operational since January 1, 2007.

The *Collaboration of Australia and Nippon for a GAmma Ray Observatory in the Outback* (CANGAROO III) consists of four IACTs located in the southern hemisphere[9] near Woomera, South Australia. Each telescope has a 10 m reflector with a total light collection area of 57.3 m^2 [200]. The first telescope, which was the CANGAROO-II telescope, was completed in May 2000. The full four-telescope array started operation in March 2004.

The current trend is to reduce the energy threshold. The fourth generation of IACTs has also reached unprecedented sensitivity that caused a big observational step (quantitative and qualitative) in the last year. Figure 1.3 shows the sensitivity for the leading γ-ray astronomy projects.

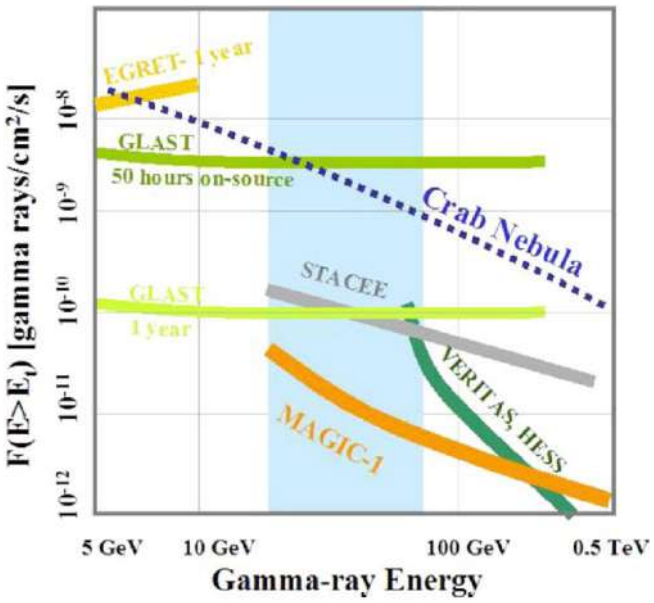

Figure 1.3: Sensitivity plot for the leading γ-ray astronomy projects. GLAST cannot reach the sensitivity of ground-based experiments in less than one year of on-source observation time and hence it cannot resolve short-time variations. Figure: [206] (Daniel Ferenc).

Future IACTs:

The MAGIC II will be a clone of MAGIC with high *quantum efficiency* (QE) *hybrid photodetector* (HPD) camera. The second telescope will enable the stereoscopic observations on La Palma.

The HESS II will be a huge IACT at the center of the current HESS array in Namibia. It will consist of a 30 m aperture reflector (600 m^2) and 2048 pixel camera. Operated in stand-alone mode, the large telescope will have the energy threshold as low as 40 GeV [84].

The *Major Atmospheric Čerenkov Experiment* (MACE) will be a huge IACT - very

[9] As well as HESS, whereas MAGIC and VERITAS are in the northern hemisphere.

similar to MAGIC - with 21 m aperture at Hanle, India at 4200 m asl [298].

The *European Čerenkov Observatory 1000* (ECO-1000) is a code-name of an huge IACT planned as a part of a further array of IACTs on La Palma (after MAGIC and MAGIC-II). It will be a device larger than MAGIC by a factor two with a mirror surface of 1000 m^2 and an energy threshold as low as 5 GeV [92]. It will be a *low threshold telescope* (LTT).

The Cosmic Ray Observatory At The Eastern Adriatic (CROATEA) is proposed to be a small IACT system based on two ex-HEGRA telescopes and sited near the Adriatic coast in Croatia. CROATEA will serve as a test telescope for new photodetector solutions as well as a long-term observatory devoted to known AGNs.

Nearly all modern detectors in astroparticle physics rely on photons [329]. Hence, photodetector development is crucial and better photodetectors will certainly result in better physics [329].

Recently, ideas on long-term observations[10] with small IACTs have become widely considered [328]. There are not enough large IACTs and they cannot spend much time to wait until an AGN becomes active (no chance to make deep observations e.g. 200-300 h/year). But, the smaller telescopes of last generation could be of help [328]. An important task of CROATEA will also be to participate in combined observation of γ-rays and neutrinos to test hadronic model of γ-ray production. The IceCube experiment combined with CROATEA could be a good example of a multimessenger study. Since astroparticle physics has a unique potential of attracting people's imagination by presenting discoveries related to exotic phenomena, smaller experiments as CROATEA can have great educational potential.

The **5@5** is proposed as a 5 GeV energy threshold array of IACTs at 5 km altitude (probably in the Atacama Desert in Northern Chile). It could serve as an ideal "Gamma-Ray Timing Explorer" for the study of transient non-thermal phenomena like GeV counterparts of GRBs and γ-rays from AGNs [20].

The *Gamma Air Watch* (GAW) will be a novel Čerenkov telescope located at the Calar Alto Observatory site in Spain at 2150 m asl. GAW is designed to be a "path finder" experiment. It should test the feasibility of a new generation of IACT that join high flux sensitivity and large FoV. The GAW array will have an energy threshold of 300 GeV. Its main features, different from present IACTs, will be:
(1) Optical system - Fresnel lenses as light collectors;
(2) Detector system - single photo-electron counting mode instead of usual charge integration mode [332].

The *High Altitude Telescope System* (HATS) will be a system of small IACTs at 4200 m asl with the energy threshold of 150 GeV, an inexpensive system, but com-

[10] In 1988, in the very first review of VHE γ-ray astronomy, Weeks noted: "If a source is truly variable on time scales of a day or less, than almost continuous monitoring is necessary."

petitive with current IACTs.

Many similar small systems have been proposed. Desirable parameters of such a small array are [292]:
– an effective energy threshold of 50–100 GeV;
– sensitivity to γ-ray flux as low as 10^{-11} cm^{-2}s^{-1};
– an energy dynamic range up to 50 TeV;
– an angular resolution of 0.l^{o};
– an energy resolution $< 20\%$ and
– a relatively large FoV ($> 4^{o}$).

To further explore the diversity of galactic and extragalactic γ-ray sources, the *Astroparticle Physics European Coordination* (ApPEC) has recommended with high priority construction of a *Čerenkov Telescope Array* (CTA) - a next-generation facility for ground-based VHE γ-ray astronomy [84]. CTAs with a detection area of 1 km^2 will also make possible study of γ-rays beyond 10 TeV.

Other applications of IACTs:

An IACT system can be used more generally, not only for γ-ray astronomy. It can also contribute to the study of CRs in the energy range 1 TeV – 100 TeV (that is a key energy region for the understanding of CR sources). For example, the HEGRA system was used to determine the flux and the spectrum of cosmic ray protons over a limited energy range around 1.5 TeV [9].

IACTs may even be used for *Optical Search for ExtraTerrestrial Inteligence* (OSETI) to search for short optical flashes as brief as nanosecond. Very first OSETI was by Schwartz and Townes in 1961, not long after the invention of the laser. The idea of searching for optical signals from extraterrestrial civilization has become increasingly popular over the last few years. In 2001, Eichler and Beskin proposed OSETI with IACTs [196]. The method relies on the detection of very short (a few ns) light pulses. IACTs are ideal instruments for this kind of observation. In 2005 at the 29^{th} ICRC in Pune, the Whipple collaboration presented an OSETI method based on IACT image shape analysis [264]. The first OSETI project to scan the entire sky has been recently established at the Oak Ridge Observatory [402].

Finally, modern IACTs satisfy many of the specifications for an intensity interferometer - devices used to determine the apparent angular diameter of a source (e.g. stellar diameter measurements or measurements of the parameters of binary systems). IACTs can be used for γ-ray observations only during moonless nights, but stray light from the Moon will only marginally reduce the sensitivity of an intensity interferometer.

1.1.3 X-rays

The observations of X-ray emission from celestial objects is X-ray astronomy. A first glimpse of the X-ray sky came in 1949, when X-rays from the Sun were discovered by rocket-borne experiments [407]. X-ray astronomy was the first "new astronomy" of the space age.

In 1962, the first extrasolar source of X-rays was found by the team of Riccardo Giacconi. Forty years later Giacconi won the Nobel Prize "*for pioneering contributions to astrophysics, which have led to the discovery of cosmic X-ray sources*".

Sources of cosmic X-rays

There is a plethora of cosmic X-ray sources: Solar system (The Sun's corona produces a lot of X-rays but other objects have been also seen in X-rays e.g. Jupiter and comets), stars, compact objects (white dwarfs, neutron stars, black holes), supernovae and supernova remnants, galaxies, galaxy clusters, and finally active galactic nuclei.

Cosmic X-rays are absorbed by the atmosphere. Therefore instruments to observe X-rays must be taken to very high altitude. In the past it could be done with balloons and sounding rockets. Nowadays, X-ray detectors are usually placed in satellites, but balloon-borne experiments are also present (balloons are much cheaper than satellites).

Balloon-borne experiments

The *High Energy X-ray Imaging Telescope* (HEXIT) is a new balloon-borne hard X-ray imaging telescope (the energy region from 20 to 800 keV), which combines a large area camera with a coded aperture mask. The first HEXIT flight, on 25 March 2005 lasted 6 hours.

Space-borne experiments

Previous:
The first X-ray satellite, Uhuru[11] which was launched in 1970 by NASA, made the first comprehensive survey of the X-ray sky.

In 1977 NASA launched the *High Energy Astrophysical Observatory* (HEAO) which had exceptional sensitivity in the energy range from 0.1 keV to 10 MeV. HEAO revolutionized X-ray astronomy, putting it on equal footing with other established fields of astronomy, optical and radio.

The *Röntgensatellit* (ROSAT) was a German X-ray satellite. It was launched in 1990 and operated until 1999. ROSAT made an X-ray all-sky survey catalog with more than 150.000 objects. It also discovery X-ray emission from comets and detected isolated neutron stars.

Recent:
The Chandra X-ray Observatory is NASA's satellite which is the most sophisticated X-ray observatory built to date. It was launched in July, 1999.

Chandra carries the X-ray telescope, whose mirrors focus X-rays from celestial objects (Figure 1.4). It has approximately fifty times better resolution than ROSAT, the observatory with the best imaging capability before Chandra. Chandra's improved sensitivity can make possible more detailed studies of black holes, supernovas, and dark matter.

Proportional Counter Array (PCA) and *All Sky Monitor* (ASM), both on board *Rossi X-ray Timing Explorer* (RXTE), are described in detail in Section 3.1.2.

The *X-ray Multi-Mirror* (XMM) Newton is an orbiting X-ray observatory launched in December 1999. It holds three X-ray telescopes of total collecting area of 4.300 cm^2

[11] It was also known as *Small Astronomy Satellite 1* (SAS-1).

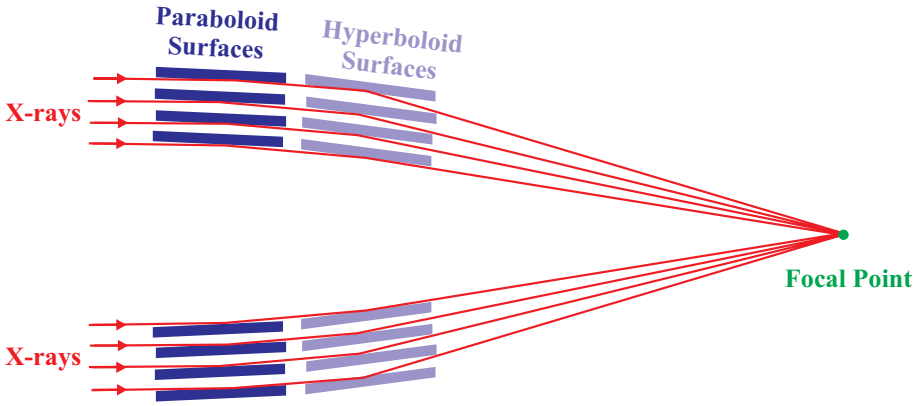

Figure 1.4: X-ray telescopes must be very different from optical telescopes. X-ray photons can penetrate into a mirror hence mirror should be shaped and aligned nearly parallel to incoming X-rays. Therefore, X-rays hit the mirrors at a grazing angle.

which are sensitive over the energy range 0.2 keV to 12 keV.

Future:
The *Energetic X-ray Imaging Survey Telescope* (EXIST) and *Coded Aperture Survey Telescope for Energetic Radiation* (CASTER) as *Black Hole Finder Probe* (BHFP) will be components of the NASA's *Beyond Einstein* program.

1.1.4 Neutrinos

The observation of HE astrophysical neutrinos will open a new window on the Universe. Among the all kind of HE astrophysical messenger, neutrinos are ideal probes (of dense regions, sources on cosmological scales, and acceleration processes) since they have no charge and interact only weakly. Neutrons are neutral (and hence straight traveling) but they are not stable – they cannot reach more than 10 kpc. Protons are charged so they do not travel on straight trajectories – they cannot be associate with astrophysical sources. Gamma-rays are neutral and stable, but there is GZK limit[12] for $\gamma-$rays (as well as for cosmic rays).

There is no GZK limit for neutrinos. However, they are the most challenging to detect of all astrophysical messengers (except gravitational waves).

The detection of neutrinos from SN1987A marked the beginning of a new phase of neutrino astrophysics.

VHE neutrino point sources have not been established yet[13], but neutrino astronomy is ready to be born. For example, detection of two HE neutrinos in coincidence with the flaring of the TeV blazar 1ES 1959+650 has been reported recently [245], but the statistical significance of the observation is low. Such simultaneous detection of γ-rays and neutrinos[14] would provide a conclusive proof for hadron acceleration [480].

[12]The *Greisen-Zatsepin-Kuzmin* (GZK) limit is a theoretical upper limit on the energy of cosmic rays from distant sources. Cosmic rays and $\gamma-$rays with highest energies would interact with microwave background photons to produce pions.

[13]An exception is a burst of neutrinos observed from supernova SN 1987A.

[14]Neutrino astronomy at energies of 1 TeV is complementary to VHE γ-ray astronomy [480].

The sources of astrophysical neutrinos

The only two confirmed astrophysical ν-sources are the Sun and SN 1987A. Supernovae are expected to be important sources of astrophysical neutrinos. They occur, in average, about once every 25 years in the Galaxy.

The sites where CRs are accelerated, SNRs and AGNs, are expected to produce neutrinos too. Other possible candidate sources can be microquasars (accreting binaries containing NS or BH) and GRBs.

Recent Experiments

There are four neutrino related **deep-water experiments** in the world: BAIKAL, AMANDA II, NESTOR and ANTARES.

The BAIKAL experiment is an underwater neutrino telescope located in the Siberian Lake Baikal at a depth of approximately 1 km. BAIKAL played a pioneering role in neutrino astronomy. In 1993, the first underwater telescope which took data for a whole year was installed in the Baikal lake. Since 1998 the Baikal collaboration takes data with the NT-200 telescope which consists of 192 optical sensors deployed on 8 strings.

The *Antartic Muon And Neutrino Detector Array II* (AMANDA II) is an operating neutrino telescope located at the South Pole. No extraterrestrial neutrino flux has been detected with AMANDA, but the increase in sensitivity with IceCube (currently under construction at the same location) is expected to be sufficient for its detection [236].

The *Astronomy with a Neutrino Telescope and Abyss environmental RESearch* (ANTARES) is a large area water Čerenkov detector in the deep Mediterranean Sea optimized for the detection of muons from HE astrophysical neutrinos.

The *Neutrino Extended Submarine Telescope with Oceanographic Research* (NESTOR) is a neutrino telescope at the deepest site (5200 m) in the Mediterranean Sea. NESTOR detects the Čerenkov radiation produced by muons resulting from interactions of upcoming TeV astrophysical neutrinos.

The *Super KAMIOKA Neutrino Detector Experiment* (Super-KAMIOKANDE)[15] is a water Čerenkov neutrino observatory in Japan. It consists of 50.000 tons of pure water surrounded by about 11.000 PMTs. Super-K observed:
– the first astrophysical neutrinos from SN 1987A in February 1987,
– solar neutrinos in 1988 (second of only two cosmic ν-sources ever), and
– the first evidence of neutrino oscillations in 1998, consistent with the theory that neutrinos have non-zero masses [214].

The *Large Volume Detector* (LVD) is located in Gran Sasso National Laboratory (Italy). It consists of a large amount of liquid scintillator (about 1000 tons) in which neutrinos may interact. LVD neutrino observatory is able to identify neutrino bursts from gravitational stellar collapses occurring in our galaxy or in the Magellanic Clouds. LVD keeps watch for SN events in our galaxy.

[15] Super-K for short.

The *ANtarctic Impulsive Transient Antenna* (ANITA) is a radio telescope to detect UHE cosmic neutrinos (with energies on the order of 10^{18} eV) from a long-duration balloon flying over the Antarctica. The radio pulses are emitted by neutrino interacting with the Antarctic ice. ANITA has launched on December 15, 2006.

Next generation of Experiments

IceCube is a neutrino telescope currently under construction in deep Antarctic ice at the South Pole (at the same site as AMANDA II). IceCube will have 80 strings at depths between of 1450 m and 2450 m, each with 60 optical modules. It is already taking data in the configuration of 9 strings only. Physics analysis is ongoing and first results are expected very soon [359]. The IceCube collaboration plans to deploy up to 14 strings per season and complete the telescope in the 2010/2011 season.

The *NEutrino Mediterranean Observatory* (NEMO) project aims at research and development of technologies for the construction of an underwater Čerenkov km^3 neutrino telescope in the Mediterranean Sea.

The KM3NeT is a future deep-sea research infrastructure hosting a neutrino telescope with a volume of at least one km^3 to be constructed in the Mediterranean Sea.

All neutrino experiment mentioned above use the common concept of Čerenkov light detection. HE neutrinos interact in the medium and produce relativistic charged leptons (muons or electrons) which cause Čerenkov light emission in a natural medium (water of ice).

1.1.5 Gravitational waves

Albert Einstein predicted the existence of gravitational waves in 1916 as part of the theory of general relativity. According to general relativity, gravity can be expressed as a spacetime curvature. A changing mass distribution can create ripples in spacetime which propagate away from the source at the speed of light. These freely propagating ripples are called gravitational waves.

Hulse and Taylor received the Nobel Prize in 1993 for the indirect detection of gravitational waves (in 1974) through the energy loss of the galactic binary pulsar PSR 1913+16. The direct observation of gravitational radiation is still a challenge for experimental physics, but after almost 40 years of experimental development, the technology now seems to be at hand [84]. It will open a new window for the observation of violent processes in the Universe.

Sources of gravitational waves

Gravitational waves that we can expect to observe must be emitted by massive objects submitted to large acceleration. Typical galactic examples are the **binary coalescences of compact objects** like neutron stars or black holes. During the merger of the two compact objects, gravitational waves are produced in abundance [114]. SN explosions should also produce enormous amounts of gravitational radiation in a short time.

Typical extragalactic sources are SMBH mergers.

Experiments on gravitational waves

The *Laser Interferometer Gravitational-wave Observatory* (LIGO) is a ground-based laser interferometer dedicated to the direct detection of gravitational waves of cosmic origin. It consists of two widely separated (about 3000 km) installations within the United States (Hanford and Livingstone). The two arms of each installation form an L shape, each 4 km long. The first observations started in 2002 but gravitational waves have not been observed yet. More ground-based gravitational wave detectors are currently under construction, e.g. VIRGO in Italy, GEO 600 in Germany, TAMA in Japan and AIGO in Australia.

The *Laser Interferometer Space Antenna* (LISA) will be the first space-based laser interferometer dedicated to the direct detection of gravitational waves in a low-frequency band that ground-based detectors can't achieve. LISA is planned to be launched in 2015. It will consist of three spacecrafts in the orbit of the Sun, $5 \cdot 10^6$ km apart, in an equilateral triangle.

1.2 Very high-energy γ-ray astronomy

Very high-energy γ-ray astronomy is the study of the sky in VHE γ-rays. It is an observational science and currently one of the most active and successful fields of astroparticle physics [329]. The two main fields of VHE γ-ray astronomy are [472]:

- **High energy astrophysics** – It is concerned with the most energetic and violent processes in the Universe and, in particular, their non-thermal aspects. The types of *very high energy* (VHE) and *high energy* (HE) γ-ray sources found or expected in the Galaxy are: pulsars, SNRs, X-ray binaries (or μ-quasars), diffuse galactic emission, molecular clouds etc. Extragalactic sources are AGNs, GRBs, radio galaxies, starburst galaxies, clusters of galaxies and galaxy mergers. Therefore, γ-ray astronomy opens the door of the extreme astrophysical environment [483];

- **Observational Cosmology** – A major aspect of cosmology is cosmic structure formation. One of its consequences is the extragalactic background light (EBL). Another major cosmological aspect of VHE γ-ray astronomy is an indirect *dark matter* (DM) search through the detection of annihilation radiation from the lightest *supersymmetric* SUSY particles, called neutralino (see Section 1.3.4).

Here is a short (pre)historical review of events which were precursors of VHE γ-ray astronomy [6]:

- In 1948, Blackett suggested that Čerenkov radiation from *cosmic rays* (CRs) constitutes a small fraction of *night sky background* (NSB);

- In 1953, Galbraith and Jelley confirmed the association of Čerenkov radiation with CR induced *extended air showers* (EAS);

- In 1958, Morrison provided the first arguments for searching for CRs in the seminal paper[16] "On Gamma-Ray Astronomy";

[16] P. Morrison, *Nuovo Cimento* **7** (1958) 858.

- In 1960, Cocconi gave the first prediction for γ-ray astronomy;
- In 1965, a Crimean group led by Čudakov was the first to seriously search for Čerenkov detection of EAS;
- In 1968, Fazio, Helmken, Rieke and Weekes completed the construction of the Whipple telescope;
- In 1972, SAS-II was launched and three years later COS-B was launched too. They opened up the field of γ-ray astronomy at low energy;
- In 1977, Turver and Weekes developed MC calculations of γ-ray and proton initiated EAS;
- In 1985, Hillas introduced shower image characterization, a base for *imaging technique* (IT);
- In 1989, the Whipple group detected the first VHE γ-ray source, the Crab Nebula, and ground-based γ-ray astronomy was born.

1.3 Cosmic VHE γ-ray sources

Cosmic VHE γ-ray sources (from few tens of GeV to few tens of TeV) are galactic and extragalactic. All extragalactic sources are point-like, but galactic ones can also be extended and diffuse. The very first VHE γ-ray source (Crab Nebula) was discovered by the Whipple Telescope in 1989 [486]. Today, more than 40 VHE γ-ray sources are known (Figure 1.5).

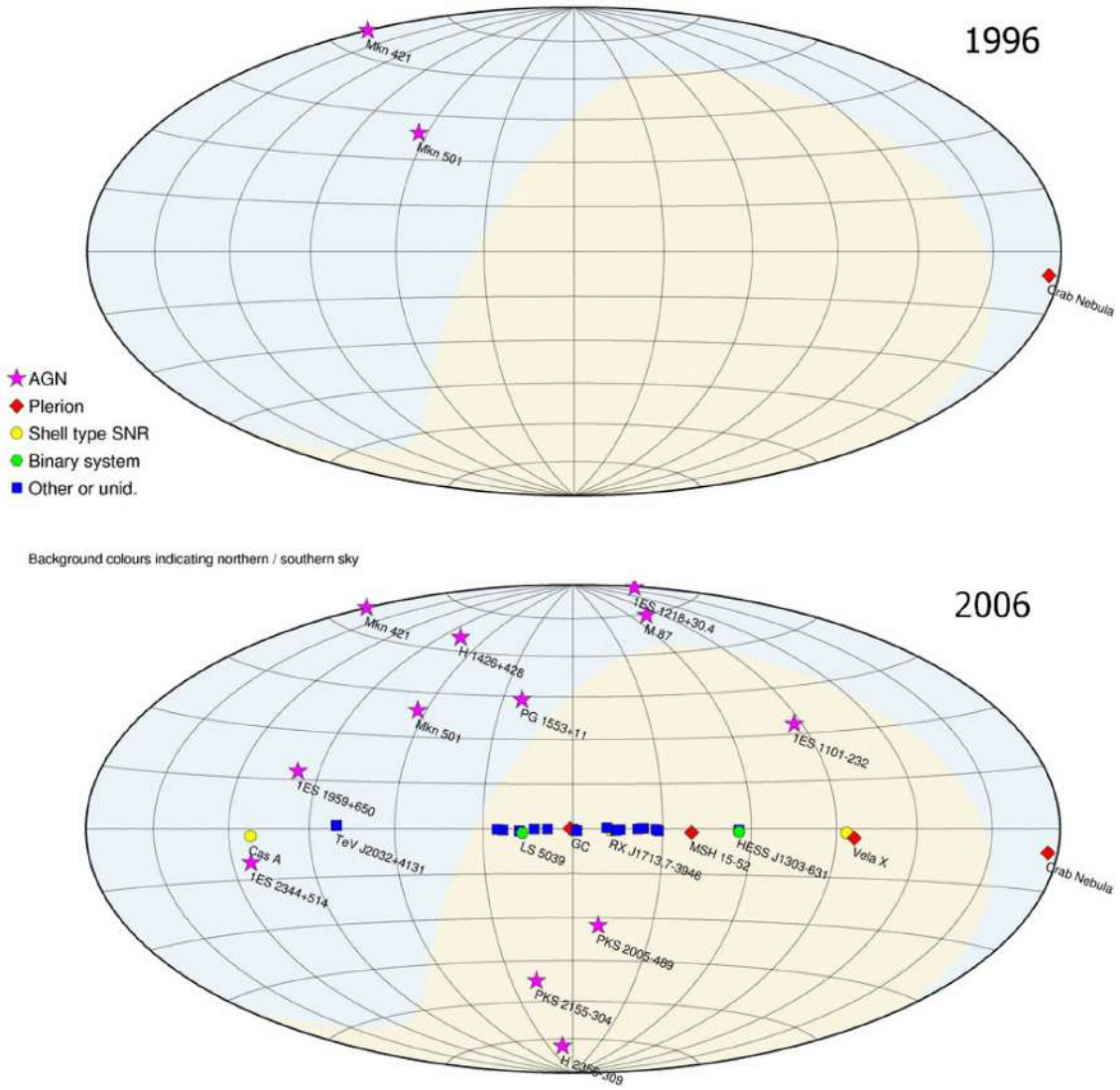

Figure 1.5: The TeV γ-ray sky as seen in 1996 and 2006. Recently, we learned about of a dozen of new sources under thorough investigation by MAGIC and HESS. Figure: [84].

1.3.1 Galactic γ-ray sources

The Crab Nebula

The Crab Nebula (also known as M1) is the first TeV γ-ray galactic source (and the first TeV γ-ray source ever[17]) discovered by the Whipple collaboration in 1989 [486].

It is a remnant of a star observed to explode by Chinese astronomers on July 4, 1054. It lies in the constellation of Taurus (RA 05h 34m 31.60s, DEC +22º 00' 56.40") at a distance of about 6500 light years (roughly 2 kpc). With an age of 950 years, the Crab Nebula is a prototypical center-filled SNR or *plerion*. Figure 1.6 is an image[18] (7.8 arcmin per side) of the nebula.

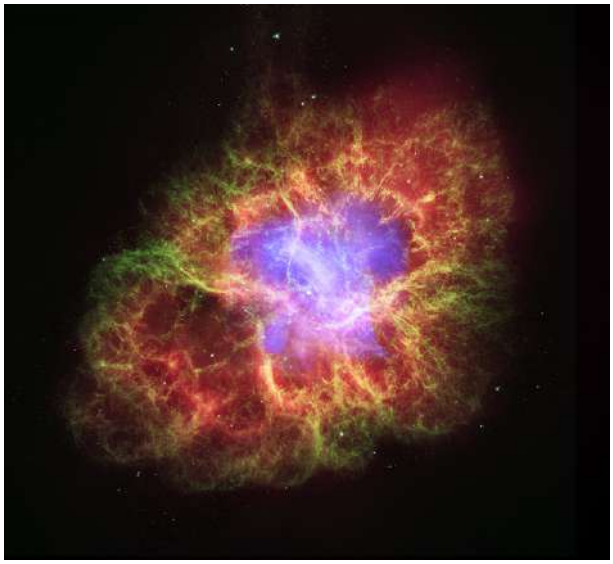

Figure 1.6: This composite image uses data from three of NASA's Great Observatories. The Chandra X-ray image is shown in light blue, the *Hubble Space Telescope* (HST) optical images are in green and dark blue, and the Spitzer Space Telescope's infrared image is in red. Its true dimensions are 6 × 4 ly.

The Crab pulsar lies at the heart of the nebula. The pulsar has a rotational period of 33.3 ms and is slowing down by 36.4 ns per day with a spin-down luminosity of $L = 5 \cdot 10^{38}$ erg s^{-1}. The total energy available from the pulsar to power a surrounding synchrotron nebula is of the order of 10^{49} erg. This is believed to be the power source for production of VHE γ-rays [60].

The Crab Nebula is an exceptionally well studied object across the entire accessible spectrum – from radio waves to γ-rays up to 100 TeV. Due the high flux relative to other known TeV sources, and expected flux stability, the source act as TeV standard candle for ground-based γ-ray astronomy. Hence, the sensitivity of any new IACT is best tested against this benchmark [266]. Consequently, each IACT spends a part of its observing time studying the nebula.

For example, the source was observed by HEGRA during almost all working period (1997–2002). Results of the first two observational campaigns, from September 1997 to

[17]By the end of 2006, nearly 40 sources have been identified.

[18]CREDIT: **X-ray**: NASA/CXC/ASU/J.Hester et al.; **Optical**: NASA/ESA/ASU/J.Hester&A.Loll; **Infrared**: NASA/JPL-Caltech/Univ.Minn./R.Gehrz.

March 1998 and from August 1998 to April 1999, were presented in [19]. The Crab data were fitted in the energy range from 1 to 20 TeV by a simple power law with a slope index of $(-2.59 \pm 0.03 \pm 0.05)$.
The Crab nebula was observed with HESS between October 2003 and January 2005. The energy spectrum (between 440 GeV and 40 TeV) was found to follow a power law with an exponential cutoff, with photon index $\Gamma = 2.39 \pm 0.03$ and cutoff energy $E_{\mathrm{cut}} = 14.3 \pm 2.1$ TeV. The observed integral flux above 1 TeV was found to be $(2.26 \pm 0.08) \cdot 10^{-11}$ cm^{-2}s^{-1} [60].

Galactic Plane and Galactic Center

The galactic Plane is the imaginary circle on the sky marked out by the highest concentration of stars in the Galaxy [234]. *Galactic Center* (GC) is the center of our own galaxy which lies in the direction of the constellation Sagittarius, as seen from Earth. It is almost totally obscured by gas and dust. Hence, optical astronomy fails completely in the direction of the Galactic Plane, especially in the direction of the Galactic Center.

On the other hand, γ-ray astronomy is expecting to be very promising for explanation of the Galactic Center. In 1997 and 1998, HEGRA surveyed one quarter of the galactic plane. The motivation for this survey was to search for γ-ray point sources and moderately extended sources in the TeV energy range (mostly pulsars and SNRs). No evidence for emission of TeV γ-radiation was detected [27].

In 2004, HESS conducted the first sensitive survey of the inner part of the Milky Way. This survey revealed a population of eight previously unknown VHE γ-ray sources. Three of them are potentially associated with SNRs, two with EGRET sources, and at least two sources have no identified counterpart in radio or X-rays, which suggests the exciting possibility of a new class of 'dark' nucleonic particle accelerators [35]. The HESS collaboration also reported a discovery of an unidentified extended TeV γ-ray source close to the Galactic Plane named HESS J1303-631 [47].

Supernova remnants

A *supernova* (SN) is a powerful stellar explosion which can be as bright as the whole host galaxy, for a short time. A *supernova remnant* (SNR) is a diffuse nebula consisting of the remains of the outer layer of a star that has been blown into space by a SN explosion. Massive star ends its life in such a catastrophic explosion.

There are two types of SN explosions:

- SN I – releases typically 10^{51} erg[19] and has no core remnant left;
- SN II – releases typically 10^{53} erg and a neutron star or a pulsar is left in the core.

SN Ia[20] is an especially important type of SN explosion with reproducible intrinsic luminosity. For that reason, SN Ia events are used as standard candles for the cosmology study. One of the greatest results of this study is the conclusion that the Universe expansion is accelerating [411]. A recent project, the *SuperNova Legacy Survey* (SNLS), is expected to give better constraints on cosmological parameters. The SNLS will study about 1000 SN Ia in the next five years with redshifts in the range from 0.1 to 1.3 [416].

[19] Erg is a non-SI energy unit used in astrophysics. 1 erg = 10^{-7} J.

[20] The most commonly accepted theory of this type of supernova is that they are the result of a white dwarf accreting matter from a nearby companion star, typically a red giant.

There are also two types of SNRs with no hard distinction: plerions and shell-type SNR. Plerion is a rare form of SNR, in which radiation is being emitted from the central region as well as from the exploding shell [407]. They are young SNRs containing a pulsar and often are **VHE** γ-ray sources. The best-known examples of plerions are the Crab nebula and the Vela. Shell-type SNRs are **HE** γ-ray sources [483]. Examples are SN1006, Cassiopeia A[21] and RXJ1713 [471].
SN explosions are characterized by:

- production of heavy elements;
- formation of the next generation of stars;
- *cosmic ray* (CR) acceleration.

In the context of γ-ray astronomy, the third point is the most interesting one. SNRs are most likely the main sources of *galactic cosmic rays* (GCR). They can accelerate charged particles (mainly electrons and protons) up to 100 TeV ($\sim$ knee of CR spectrum). The first confirmation of SNRs as particle accelerators came from the simultaneous observations of X-rays and γ-rays. For example, the supernova remnant Cassiopeia A was observed by the HEGRA IACT system from 1997 to 1999. The detection of TeV γ-rays proved that Cas A is a site of CR acceleration. It was further support to the theory of SNRs being responsible for CR acceleration [23]. *Ultra high energy cosmic rays* (UHECR) seem to have extragalactic origin.

An acceleration mechanism of CRs in SNRs is shock wave[22]. A model based on shock wave gives power law spectrum

$$\frac{\mathrm{d}N}{\mathrm{d}E} \propto E^{-2}. \tag{1.3}$$

Correction for the effect of propagation in the Galaxy gives finally

$$\frac{\mathrm{d}N}{\mathrm{d}E} \propto E^{-2.7} \tag{1.4}$$

as shown in Figure 1.2.

Pulsars

A pulsar is a rapidly spinning *neutron star* (NS). A neutron star is a compact object (Table 2.1) predicted by Baade & Zwicky in 1934. Typical parameters of a NS are: $M = 1.4\ M_\odot$, $R = 10$ km, and $B = 10^{12}$ gauss [483]. More than 650 active pulsars have been catalogued in the Galaxy, since the first one was discovered in 1967. There should be even more "dead" pulsars (quiet NS) around.

Pulsars were the first astrophysical sources discovered in HE γ-rays. Most of them were created in SN explosions by the collapse of the core of a super-giant star. Some of them originate from white dwarfs in binary systems that collapsed into NS because of the mass accretion from a companion star [407].

Pulsars and SNRs are sources of *synchrotron radiation*[23] – the emission of a continuous spectrum extending over a wide range of wavelength (from radio to γ-rays). Synchrotron

[21] Cas A is also the strongest source in the radio sky.
[22] Shock wave is a supersonic disturbance of the pressure level.
[23] It is called so because it was first observed in a synchrotron accelerator (1948). Theoretical predictions were even older (1912).

radiation, also known as magneto-bremsstrahlung, has a very different spectrum shape from the black-body spectrum. It is emitted by relativistic charged particle moving in a strong magnetic field.

Some pulsars have unusually strong magnetic fields, the strongest ever measured, more than 10^8 T. They are called magnetars [299].

Microquasars

Microquasars (hereafter μ-quasars) are galactic sources with two **relativistic jets**, discovered in 1994. They are binary systems where one object is compact (BH or NS) and the other is a mass-donating companion star, a source of accretion material e.g. a red giant. The accretion disk forms by accretion and a "hot-spot" forms where the stream of material hits the outer edge of the disk. This process is a strong source of X-rays, hence μ-quasars are also known as *X-ray binaries* (XRB).

Accordingly, a μ-quasar is a small version of an AGN, but it is a galactic phenomena. Like some AGNs, they are expected to be sources of TeV γ-rays which should be created inside the jets by the *inverse Compton* (IC) process. By studying μ-quasars, we can learn a lot about quasars or AGNs in general.

Some known μ-quasars are: GRS 1915+105 (jets with $\beta = 0.98$ [483]), Cygnus X-3, and SS433 (the best studied of them and one with complex behavior). When SS433 was observed for the first time (25 years ago), it was the strangest object in the sky [164]. It is a galactic object (just 17000 ly away from us) but it looks like an AGN (Figure 1.7). The mechanical power of the jets of SS433 is comparable with the total production rate of CRs in the Galaxy [4].

The HEGRA collaboration observed the famous galactic object SS433 for more than 100 hours but no evidence of steady or variable emission was found [48]. It seems that the beam of SS433 missed[24] us. Recently, the MAGIC collaboration discovered μ-quasar LS I +61 303 which shows periodic VHE γ-ray emission with a 26 day period that corresponds to the orbital motion of a binary system [64].

1.3.2 Extrgalactic γ-ray sources

Gamma-Ray Bursts (GRB)

Gamma-ray bursts[25] (GRB) are the most luminous events known in the Universe since the Big Bang. They are flashes of γ-rays coming from random directions in deep space. GRBs were discovered in 1967 by the US Vela nuclear test detection satellite and their origin has been a mystery for the next 30 years. The *Burst and Transient Source Explorer* (BATSE) aboard *Compton Gamma Ray Observatory* (CGRO) showed that GRBs are isotropic, ruling out nearly all Galactic origins.

The so-called "afterglow" of a GRB was predicted to exist by most models. Afterglow is the fading emission at longer wavelengths (X-ray, UV, optical, IR, and radio) following the burst itself. Despite intensive searches, no such emission had been found until 1997 when the BeppoSAX satellite detected a GRB followed by fading X-ray emission. Additional follow-up from ground-based telescopes identified a fading optical counterpart as

[24] The jet should be pointed toward an observer for γ-rays to be detectable.

[25] A burst is a period of sudden intense emission having a rapid rise and decay [407].

well. Then the sources of long-lasting GRBs were identified as the implosions of cores of very large supernova into black holes at cosmological distances [382].

Recently, most short GRBs were found to be created in mergers of neutron star or black hole binaries outside of the Galaxy [212] [422] [386]. Some short GRBs may origin from galactic magnetar flares.

GRBs are currently detected by orbiting satellites about once a day. They are generally divided in two[26] classes: [276]
1. LONG GRBs (lasting typically 20 s). They are redshifted, have afterglow and have been detected up to 18 GeV.
2. SHORT GRBs (lasting typically 0.2 s). They are also extragalactic, but come from a lower-redshift population. They are less luminous than long GRBs and have no afterglow.

Therefore, GRB are cosmological phenomena. They and their afterglows have been predicted to be visible out to the redshifts of even 20 [242]. The most distant GRB ever observed was 050904 in September 2005. From photometric measurements, its redshift was found to be 6.39 ± 0.12 [242]. Hence, the corresponding explosion happened 12.8 billion years ago. In that time the Universe was just about 900 million years old. Such GRBs serve as a powerful probe of the conditions of the early Universe.

Recently, NASA's *Wilkinson Microwave Anisotropy Probe* (WMAP) satellite have shown that stars emerged just 400 million years after the Big Bang [162]. Hence, the star whose explosion caused GRB 050904 could not be more than 500 million years old. That means it was very massive, more than 10 solar masses (maybe up to 60 solar masses). It seems that in very early stage of the Universe the concentration of very massive stars was much larger than today.

GRBs are predominantly HE (not VHE) phenomena. Although, γ-rays from GRB could be more energetic than a few tens GeV. Such GRBs should be observable by low-energy threshold IACT. For example, MAGIC is predicted to detect about one GRB per year at a 5σ level [68]. In 2005, MAGIC observed the first GRB – GRB050713a, but no evidence for a γ-ray signal was found [68].

Starburst galaxies

Starburst galaxies are irregular galaxies containing a messy distribution of dust, in which a large outburst of star formation is going on [234]. They are a class of galaxies between normal ones (e.g. the Milky Way or Andromeda) and active ones (e.g. blazars such as Mkn 421).

Most of starburst galaxies are interacting or colliding with other galaxies. The stars themselves do not collide with one another, but clouds of gas and dust do collide sending shock waves and triggering star formation.

Starburst galaxies (e.g. NGC 253) and all star-forming regions in general seem to be sources of VHE γ-rays.

Active Galactic Nuclei

Active galactic nucleus (AGN) is a general term used to described the existence of extremely energetic phenomena in the central region of some galaxies. AGNs are extremely compact objects with luminosity 10.000 times greater than the host galaxy. Such considerable energy is obviously generated by processes other than those operating in normal

[26]Some very recently observed GRBs do not fit into the "two classes" scenario. They probably belong to a new, third class and that imply a new production mechanism too.

stars. The most extreme examples are called quasars [114]. AGNs are prime targets for γ-ray studies [483].

Currently, the weakest form of unification, the hypothesis that all AGNs are powered by *supermassive black holes* (SMBH), is completely accepted [489]. Masses[27] of SMBHs range from 10^7 to $10^{9.5}$ $M_\odot$.

Figure 1.7 shows the key elements of an AGN: SMBH, an accretion disk, an obscuring torus, and two jets with radio lobes. The accretion disk is a structure that forms around a compact object (white dwarf, NS or BH) when matter flows towards it. The obscuring torus is a thick torus of dust. Lobes are extended regions of diffuse radio emission, often dumbbell shaped. SMBH and the jets are described in detail in Section 2.2.

According to the model, the classification (Figure 1.8) results from viewing an AGN

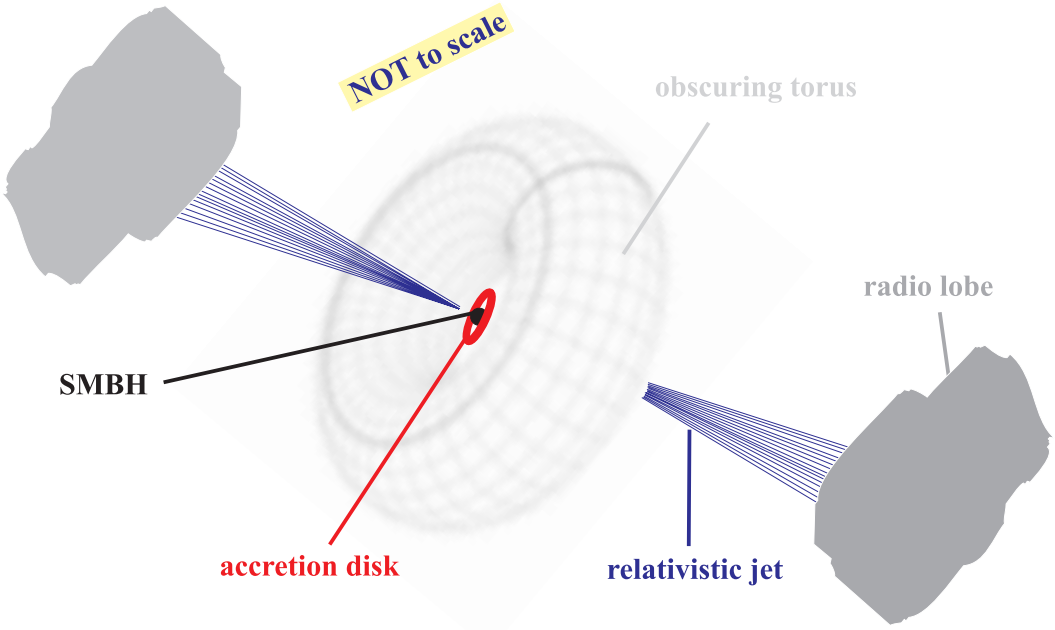

Figure 1.7: The key elements of an AGN in a widely accepted generalized model: supermassive black hole, accretion disk, relativistic jets, radio lobes, and obscuring torus. Typical size of the accretion disk is 10^{-3} pc, the torus is about 1 pc, and the jets 10^3 pc.

from different angles with respect to the jet or to the torus. Hence, the wide variety of AGNs types is a result of geometry rather than physics [483]: All radio-loud AGN can be unified through an orientation based scheme where jet direction plays a key role, and all radio-quiet AGN can be unified through an orientation based scheme where an obscuring torus plays a key role [489].

[27]Mass of an astrophysical object is usually expressed in unit of $M_\odot$ where $M_\odot = 1.989 \cdot 10^{30}$ kg is the mass of the Sun.

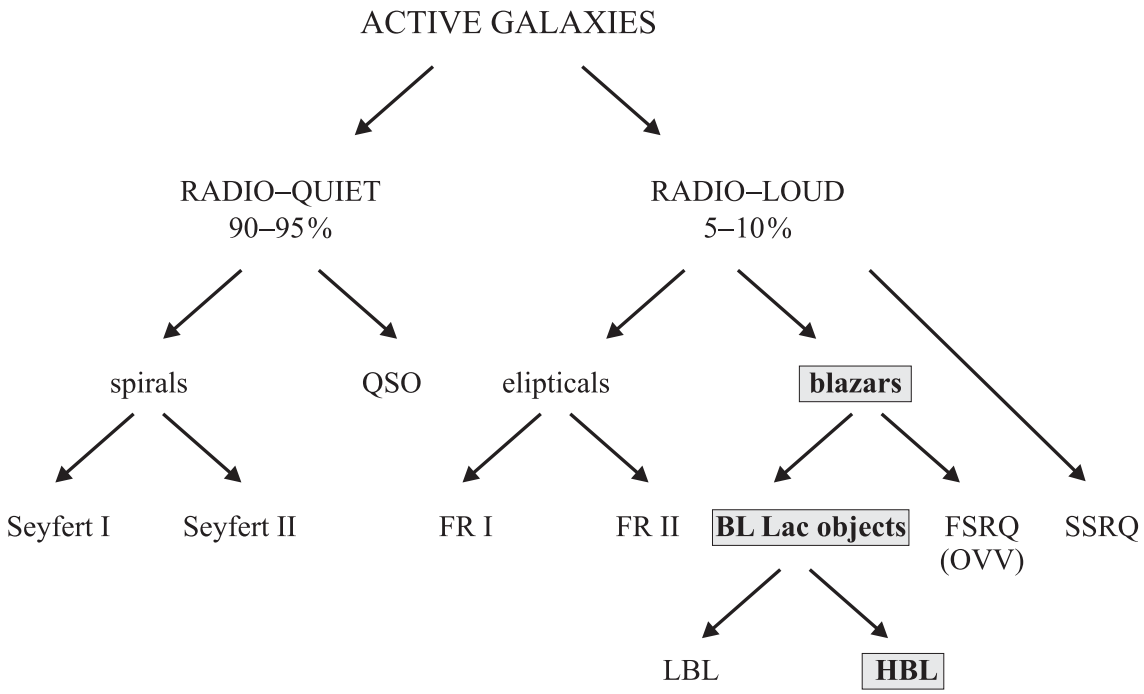

Figure 1.8: The classification of AGNs. FR1 and FR2 are Fanaroff-Riley radio galaxies, OVV are Optically Violently Variable, and QSO stands for Quasi-Stellar Object. FSRQ/SSRQ means Flat/Step Spectrum Radio Quasar, and HBL/LBL stands for High/Low-frequency peaked BL Lac objects. Almost all VHE γ-ray sources are HBL.

1.3.3 Unidentified sources of γ-rays

3rd *Energetic Gamma Ray Experiment Telescope* (EGRET) Catalogue consists of 271 sources. There are 101 identified sources (5 pulsars, 1 solar flare, 66 high-confidence blazar identifications, 27 possible blazar identifications, 1 likely radio galaxy, and 1 normal galaxy) and even **170 unidentified sources**. The nature of these objects is completely unknown.

HEGRA's deep observation of the Cygnus region at TeV energy revealed a signal inside the core of the OB association Cygnus OB2 [29]. An OB association is a dense concentration of young, massive stars of O and B type in the spiral arms of galaxies and it provides an environment to multi-TeV particle acceleration. The HEGRA collaboration later confirmed this new source as steady in flux. There was no obvious counterpart at radio, optical nor X-ray energies, leaving **TeV J2032+4130 unidentified** [49].

1.3.4 Exotic sources of γ-rays

An exciting possibility is that the highest energy CRs are not generated "bottom-up" by an acceleration process, but rather "**top-down**" through non-acceleration mechanism by decays of some exotic, very heavy particles beyond *Standard model* (SM). Such particles must be relics of the Big Bang e.g. *topological defects* (TD) or *cold dark matter* (CDM).

Topological defects

Topological defects (TD) are extremely HE phenomena theoretically predicted to form at phase transitions in the very early Universe. The strong gravitational effect of TD might have assisted in the formation of galaxies and of large-scale structure in the Universe. The well-known TDs are:

- *magnetic monopoles* (point-like defects formed when a spherical symmetry was broken);
- *cosmic strings* (1D lines formed when an axial symmetry was broken) e.g. a cosmic string would be 10^{-31} m thick and have a mass of about $10^7 M_\odot$ per ly [407]. If anything like cosmic string exist and could be captured, it would be capable of holding wormholes open [457];
- *domain walls* (2D membranes formed when a discrete symmetry was broken); and
- *cosmic textures* (formed when larger, more complicated symmetry groups were broken).

There is no evidence yet for the existence of TDs.

Dark matter

The existence of *dark matter* (DM) is by now well established [192]. The earliest evidence for DM came from the measurement of galactic rotational curves which implied the existence of dark halo[28]. Most of DM is expected to be *cold dark matter* (CDM).

[28] Alternative could be *modified Newtonian dynamics*.

The CDM model has become the leading theoretical picture for the formation of structure in the Universe [447]. Simulations of the formation, evolution and clustering of galaxies and quasars also include the growth of DM structure. The known elementary particles account for only about 4% of the total energy density in the universe. The rest are *dark energy*[29] (DE) and *dark matter* (DM). Their nature and origin are so far unknown. It is one of the most important problems in physics and cosmology today. Figure 1.9 illustrates amounts of DE and DM in the Universe.

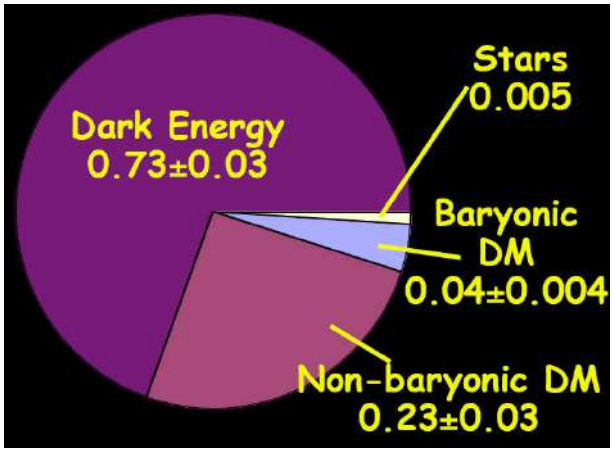

Figure 1.9: There seems to be at least 10 times more DM in the Universe then luminous matter [114]. Figure: [380].

Candidates for non-barionic DM include axions and *weakly interacting massive particles* (WIMP) whereas barionic DM candidates are called *massive compact halo object* (MACHO)[30] All of them are, in principle, detectable with present or near-future technology.

MACHOs are massive dark objects, such as brown dwarfs, in the outermost region of a galaxy that may explain the observed anomalous rotation of most galaxies. BHs have also been proposed as MACHO candidates, especially PBHs.

Axions were first postulated to solve the strong CP[31] problem of *quantum chromodynamics* (QCD) – why QCD does not seem to break the CP-symmetry. Axions also occur naturally in superstring theories [233]. They can be detected by looking for axion $\longrightarrow$ photon conversion in a strong magnetic field.

WIMPs are particles with mass roughly between 10 GeV and a few 10 TeV [192]. WIMP direct detection involves detecting the energy deposited in a detector due to elastic scattering [232]. The detection event rate depends on two astrophysical inputs:
– the local dark matter distribution, and
– the Earth's velocity with respect to the Galactic rest frame.
The best WIMP candidate is the lightest *supersymmetry* (SUSY) particle – neutralino [384]. Discovery of such a particle could be a long-awaited window beyond the Standard model. WIMPs can annihilate and their products (neutrinos, γ-rays, positrons, anti-

[29] Dark energy is a substance of negative pressure needed for an accelerated cosmology.
[30] A name was chosen to contrast with WIMP (in Croatian *muškarčina* vs *mlitavac*).
[31] CP is the product of two symmetries: C for charge conjugation and P for parity.

protons, anti-nuclei) can be detected. Hence WIMP can be seen indirectly. Concerning γ-rays, the GLAST satellite [474] or IACTs (like MAGIC and HESS) should be able to test SUSY models [192].

At the beginning of 2006 Gerry Gilmore and his team from Cambridge University mapped the positions and velocities of thousands of stars in 10 mini-galaxies around the Milky Way [166]. They found that all of them had a core of DM of a uniform size (about 1000 ly across) and temperature (about 10.000 K). Each dwarf galaxy seemed to contain the same amount of DM (about 30 million solar masses). It represents the minimum amount of DM needed for a stable clump to hang together. The temperature was the first physical characteristic of DM ever determined.

Recent weak lensing observations seem to provide the ultimate evidence for the existence of DM. The observations of the merging galaxy cluster 1E0657-558 [167] (and also for galaxy cluster 1E0657-56 [137]) have provided the strongest evidence yet. These results are independent of assumptions regarding the nature of the gravitational force law.

Primordial black holes

A *primordial black hole* (PBH) is a spontaneously radiating microscopic *black hole* (BH) of radii 10^{-15} m (the size of an atomic nucleus) with masses of about 10^{12} kg (the weight of an asteroid). Such BH would have a temperature of 10^{11} K, high enough for it to radiate X-rays and γ-rays as evaporate[32]. As a PBH radiates, it shrinks, until it finally disappears in a **flash of γ-rays**. However, γ-rays from evaporating PBHs do not have the right properties to account for GRBs [114].

PBHs have been predicted as relicts of the Big Bang formed before the era of nucleosynthesis. PBHs are, hence, possible "fossils" of the ultra-early Universe [114].

PBHs could provide a unique probe of at least four areas of physics [154]:
– the early Universe (useful constraints can be placed on inflationary scenarios),
– gravitational collapse (PBHs could show how gravity links to other forces),
– HE physics (information may come from observing CRs from evaporating PBHs), and
– quantum gravity (the formation and evaporation of small BHs could be observable in CR events and accelerator experiments if the quantum gravity scale is around a TeV).

PBHs would be a missing link between the cosmos and the micro-world [114].

There is an observational window using ground-based IACTs to measure γ-ray burst emission from PBH decay. This technique is based on the detection of multiphoton-initiated EAS [306]. Since March of 2003, the *Short GAmma Ray Front Air Cherenkov Experiment* (SGARFACE) was operating at the Whipple Observatory in order to observe microsecond GRBs.

1.4 Blazars

A blazar is an *active galactic nucleus* (AGN) dominated by a highly variable component of non-thermal radiation produced in relativistic **jets**[33] close to the line of sight (Figure 1.7). The term *blazar* was coined in 1978 by astronomer Ed Spiegel to denote the combination of **BL** Lac and qu**asar**.

[32]Hawking's idea on BH evaporation, proposed in 1974, is now generally accepted.

[33]The jet is a narrow beam of plasma and radiation moving at relativistic velocity. It may extend for many hundred of kiloparsecs.

Blazars include BL Lacertae (BL Lac) objects and *flat spectrum radio quasars* (FSRQ) (Figure 1.8). FSRQ is highly variable quasar, sometimes also called *optically violently variable* (OVV) quasar. It has **broad emission lines** in the spectrum. FSRQs make just a small subset of all quasars.

BL Lac object is an extragalactic highly variable AGN. BL Lac objects include *low-frequency peaked BL Lac* (LBL) and *high-frequency peaked BL Lac* (HBL)[34]. They are apparently star-like objects with near-featureless spectrum (with **no emission lines** in the optical part of the spectrum) also known as Lacerid [407]. The prototype was originally classified as a peculiar variable star in the constellation of Lacerta (The Lizard). The synchrotron emission of LBLs is stronger in the radio–IR band while HBLs have stronger synchrotron emission in the UV–X-ray band.

HBLs are TeV γ-ray emitters characterized by continued and violent non-thermal emission produced in the jets. Their γ-ray spectra extend up to 20 TeV.

So far, there are 19 known extragalactic TeV γ-ray sources (Table 1.4). Almost all these sources are blazars, belong to the class of HBL. An exception is, for example, M87 which is class of *Fanaroff-Riley I* (FRI). TeV photons from M87 are thought to originate in the *inverse Compton* (IC) process, as for blazars, but the jet is quite far from the line of sight. Accordingly, M87 is a "mis-aligned" blazar [178].

#	**Object name**	**Redshift**	**Discovery reference**
1.	M 87	0.0044	Aharonian et al. A&A **421** (2004) 529
2.	Mkn 421	0.031	Punch et al. Nature **358** (1992) 477
3.	Mkn 501	0.034	Quinn et al. ApJL **456** (1996) L83
4.	1ES 2344+514	0.044	Catanese et al. ApJ **501** (1998) 616
5.	Mkn 180	0.045	Albert et al. ApJL **648** (2006) L105
6.	1ES 1959+650	0.047	Nishiyama, Proc. 26$^{\text{th}}$ ICRC **3** (1999) 370
7.	PKS 0548-322	0.069	Superina et al. 30$^{\text{th}}$ ICRC (2007)
8.	BL Lacertae	0.069	Albert et al. ApJL **666** (2007) L17
9.	PKS 2005-489	0.071	Aharonian et al. A&A **436** (2005) L17
10.	PG 1553+113	0.09	Aharonian et al. A&A **448** (2006) L19 Albert et al., ApJL 654 (2007) L119
11.	PKS 2155-304	0.116	Chadwick et al. ApJ **513** (1999) 161
12.	1H 1426+428	0.129	Horan et al. ApJ **571** (2002) 753
13.	1ES 0229+200	0.14	Aharonian et al. A&A accepted
14.	H 2356-309	0.165	Aharonian et al. Nature **440** (2006) 1018
15.	1ES 1218+304	0.182	Albert et al. ApJL **642** (2006) L119
16.	1ES 0347-121	0.185	Aharonian et al. A&A **473** (2007) L25
17.	1ES 1101-232	0.186	Aharonian et al. Nature **440** (2006) 1018
18.	1ES 1011+496	0.212	Albert et al. ApJL **667** (2007) L21
19.	3C 279	0.536	Teshima et al. 30$^{\text{th}}$ ICRC (2007)

Table 1.4: A list of GeV/TeV extragalacic γ-ray sources known to be AGNs, detected by IACTs (status from October 2007). The list is sorted by redshift and updated according Robert Wagner's on-line catalog (see Figure 1.10).

[34]Before the LBL/HBL division (based on the "different viewing angle" hypothesis), there was an old (now obsolete) division: *radio selected BL Lacs* (RBL) and *X-ray selected BL Lacs* (XBL).

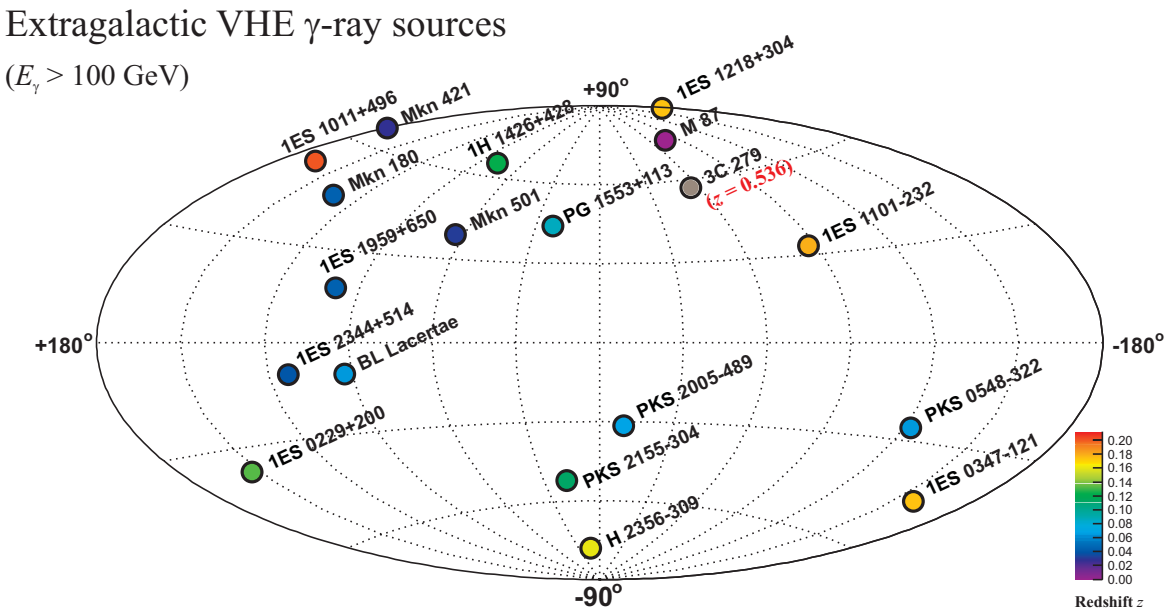

Figure 1.10: A sky map of extragalactic sources of VHE $\gamma-$rays. This figure is a modified version of Robert Wagner's sky map which is available on-line: *http://www.mppmu.mpg.de/∼rwagner/sources/*.

1.5 Extensive Air Showers

1.5.1 The basic processes

An *extensive air shower* (EAS) is caused by a single CR or γ-ray with energy high enough for its cascade (secondary charged particles and photons) to be detectable at the ground. Primary VHE cosmic particles, which hit the Earth's atmosphere, interact with air molecules in the upper layer of the atmosphere at typical altitude between 10 and 15 km [373]. In such collisions, many new particles are usually created. These secondary particles propagate down through the atmosphere.

1.5.2 Hadron showers

If the primary cosmic ray particle is a hadron (proton or nucleus) a hadronic interaction occurs and secondary particles are created. They are mostly pions (about 90 %) but also kaons, anti-protons, and nuclear fragments. Secondary particles can induce new nuclear interactions and hence a cascade occurs.

Charged pions decays into muons (and also create atmospheric neutrinos) and neutral pions decay into two photons which induce electromagnetic sub-showers. Figures 1.11 and 1.12 show development of cosmic ray induced EAS.

1.5.3 Electromagnetic showers

Primary cosmic high-energy γ-ray initiates a shower which starts with electron-positron **pair production** (in the field of a nucleus):

$$\gamma \longrightarrow e^+ \, e^- \tag{1.5}$$

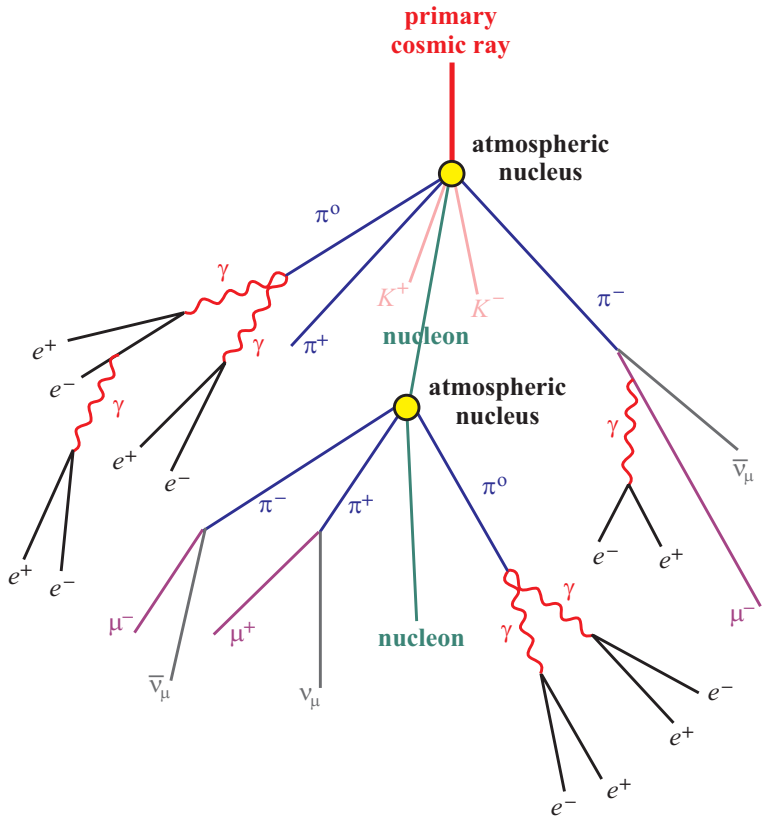

Figure 1.11: A sketch of the development of cosmic ray air shower.

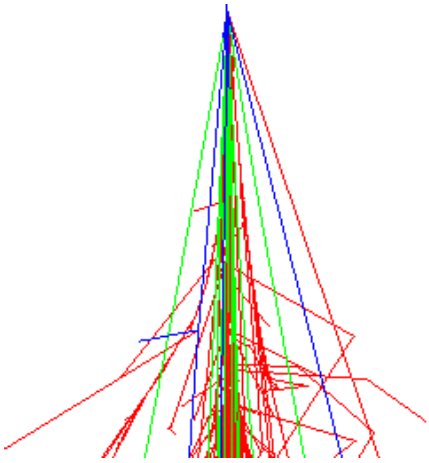

Figure 1.12: Monte Carlo simulation of the beginning of an EAS initiated by 300 GeV proton. This figure is a magnified part of Figure 4.12. Red tracks are electrons, positrons and secondary γ-rays, green ones are muons, and blue ones specify hadrons. First interaction with nuclei occurs at 25 km *above sea level* (asl).

or **pion photoproduction**

$$\gamma + \text{nucleus} \longrightarrow \text{hadrons} \ \ (\text{mostly } \pi) \tag{1.6}$$

The cross section for photoproduction in the energy range of a typical IACT (100 GeV – 10 TeV) is 1–2 mb, which is about 300 times smaller than the cross section for pair production [300].

High-energy (HE) electrons and positrons ($E > 10$ GeV) from the pair production process mainly loose their energy in matter by bremsstrahlung (in the field of a nucleus) and thus generate secondary photons. Subsequent electron-positron pairs are created from HE photons ($E > 10$ MeV). Bremsstrahlung (stopping radiation) is a radiation mechanism in which a charged particle is decelerated and loses energy in the form of EM radiation. Pair production is the production of an electron-positron pair from a γ-ray of energy greater than 1.022 MeV near an atomic nucleus.

The characteristic amount of matter traversed for these interactions is called the *radiation length* (RL). It is the mean distance over which an ultra-relativistic electron loses all but $\frac{1}{e}$ of its energy due to bremsstrahlung. It is also $\frac{7}{9}$ of the mean free path of a HE photon. RL is usualy measured in g/cm^2.

The RL in the atmosphere is 37.1 g/cm^2. The total thickness of the atmosphere is 1030 g/cm^2 which correspond to 28 RL (the atmosphere has as strong blocking power as 1 m of lead). The first interaction occurs typically after 1 RL which correspond to the altitude of about 20 km.

1.6 The atmosphere as a giant calorimeter

1.6.1 General remarks

For the observation of high-energy particles one needs the calorimetric detection principle [329]. The atmosphere is a natural calorimeter for cosmic high-energy particles (mostly protons but also γ-rays). Hence, while for most astronomers the Earth's atmosphere is a troublesome filter, for ground-based γ-ray astronomers it is an essential ingredient that makes observations possible [483].

1.6.2 Atmospheric extinction

The term **extinction** refers to the decrease in the intensity[35] of light from a celestial body in passing through Earth's atmosphere. This occurs due to attenuation (absorption and scattering) in the atmosphere. Atmospheric extinction is proportional to the airmass and atmospheric pressure. Therefore, extinction increases with the *zenith angle* (ZA).

Most of the extinction is due to scattering and the most critical loss is Mie scattering (or scattering on aerosols and clouds). It can be highly variable, even on a time scale of hours or less [323].

The term is used in meteorological optics and astronomy in the context of starlight loss in the atmosphere. Figure 1.13 shows the extinction curve $\mathcal{A}_{\rm total}$ for the sky over Observatorio del Roque de los Muchachos (ORM) at La Palma [290]. The extinction is expressed in *magnitude per airmass*, a unit used in optical astronomy. The calculated extinction curve $\mathcal{A}_\lambda$ includes dominant Rayleigh scattering, but also absorption in the ozone layer. The contribution from aerosol scattering was deduced by comparing the observed mean extinction coefficient from the *Carlsberg Meridian Telescope* (CMT) and the theoretical extinction coefficient in the **V** band $\mathcal{A}_{\rm V}$

$$\mathcal{A}_{\rm aerosol} = \mathcal{A}_{\rm CMT} - \mathcal{A}_{\rm V} \tag{1.7}$$

[35] *Extinction ratio* is $10\log(\textit{intensity ratio})$ which is measured in decibel (dB).

The total extinction, shown in Figure 1.13, is then given by

$$\mathcal{A}_{\text{total}} = \mathcal{A}_{\lambda} + \mathcal{A}_{\text{aerosol}} \tag{1.8}$$

Airmass is the optical path length of starlight through Earth's atmosphere. For example,

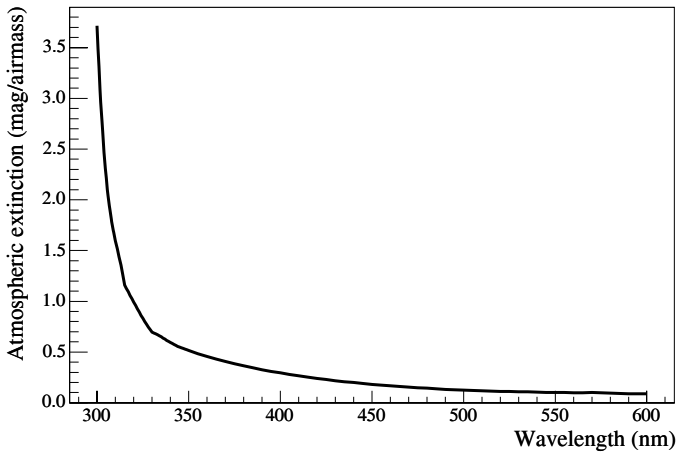

Figure 1.13: Atmospheric extinction at ORM on La Palma [290].

airmass = 1 at the zenith ($ZA = 0^{\text{o}}$) and *airmass* ≈ 2 at an altitude of 60^{o} ($ZA = 60^{\text{o}}$) [407].

The *magnitude* is a measure of the brightness of a star. An absolute magnitude M is an intrinsic brightness, the property of a star. An apparent magnitude m is the brightness as seen from Earth; it depends on M but also on the distance. A difference $\Delta m = 1$ mag corresponds to a difference in brightness of a factor[36] 2.512. The bolometric magnitude includes all wavelengths, and **V** magnitude includes only wavelengths passing a **V** filter[37].

At La Palma, a period with significantly higher level of extinction occurs every summer due to the presence of the Saharan dust in the atmosphere. This effect is clearly visible in Figure 1.14 which shows the development of Western Sahara dust from February 24 to February 27, 2000. These pictures were obtained using *Total Ozone Mapping Spectrometer* (TOMS). Saharan sand particles, called *calima*, have the same size as typical cloud water droplets: 5 to 10 μm.

Certain optical telescopes at La Palma regularly take dedicated measurements of some objects of standard brightness in order to monitor the **variable atmospheric transmission** (VAT). The HEGRA Observatory has relied on the VAT measurements taken by the Carlsberg Meridian Telescope.

The Carlsberg Meridian Telescope

The *Carlsberg Meridian*[38] *Telescope* (CMT) is an optical telescope at the *Observatorio del Roque de los Muchachos* (ORM) on La Palma. The telescope has a refractor with an

[36] This factor was chosen in order to get the brightness factor of 100 for $\Delta m = 5$ mag.

[37] A **V** filter accepts the range with central wavelength of 545 nm (middle of the visible spectrum), and bandwidth of 88 nm.

[38] The meridian astronomy is a branch of astronomy concerned with accurate measurements of positions in the sky (RA and DEC).

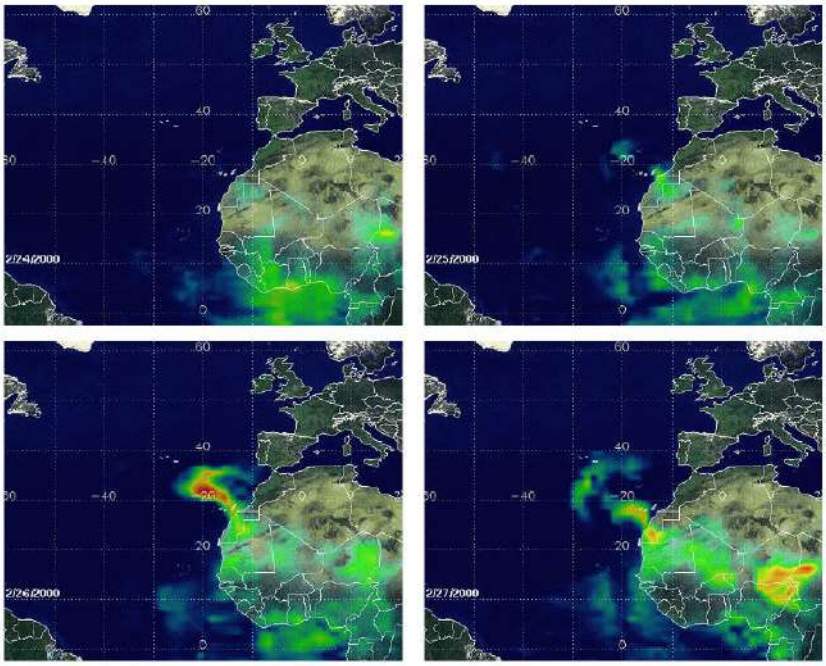

Figure 1.14: Saharan dust extends over the Atlantic Ocean and Canary Islands (La Palma is approximately at latitude +29 and longitude -18). The green to red false colors in the dust image represent increasing amounts of aerosol. Figure: *http://toms.gsfc.nasa.gov/aerosols/africa/canary.html*

objective of 17.8 cm diameter and focal length of 266 cm. The observing procedure is entirely automatic. In 1984, it was one of the first fully automatic telescopes in the world. Since June 1998, the telescope was equipped with a *charge-coupled device* (CCD) camera.

The CMT provides nightly values of atmospheric extinction in the Sloan **r'** band (effective wavelength of 625 nm) for La Palma from observations of about 50 stars per night. The mean extinction value for each night is given in a file accessible on-line[39].

A typical value of the extinction in the **r'** band for a *good quality dust-free night* is **0.09 mag**.

The main disadvantage of the CMT extinction coefficient measurement is the fact that it presents an average over the entire night. For IACTs, it would be ideal to have the extinction value for each particular observed event.

1.6.3 Atmospheric remote sounding

A study of the atmosphere requires suitable observations e.g. remote sounding. Atmospheric remote sounding is the probing of the atmosphere *at a distance*[40] using EM radiation emitted, scattered or transmitted by the atmosphere.

Ground-based remote sounding

The ground-based devices for the atmospheric remote sounding are radars and lidars.

[39] *http://www.ast.cam.ac.uk/∼dwe/SRF/camc_extinction.html*

[40] Complementary techniques for observing the atmosphere *in the vicinity of apparatus* are "in situ" measurements: balloon-borne radiosonde, aircraft and rocket measurements [80].

In the context of atmospheric remote sounding, *radio detection and ranging* (radar) measures the backscattering pulses of radio waves from water droplets and ice crystals in the troposphere. Radar is important for weather forecasting. It does not "see" cloud droplets, but it detects the large precipitation particles [110].

Light detection and ranging (lidar) consists of a laser pulser and a small telescope with an appropriate light sensor for backscattered photon detection. It uses the same principle as radar. A vertically directed laser transmits short light pulses of radiation into the atmosphere. The backscattered photons return to the lidar with a time delay proportional to the distance of the scattering event.

Typical lidar wavelengths are a few hundred nm (e.g. 532 nm) while radars use typically wavelengths of a few cm.

The three main types of lidars are: range lidars, DIAL lidars and Doppler lidars. Range lidar is the simplest one. It is used to measure the distance from the lidar to a target. *DIfferential Absorption Lidar* (DIAL) lidar is used to measure the concentrations of e.g. O_3 or H_2O in the atmosphere. It uses two different wavelengths which are selected so that one is absorbed by the molecule of interest and the other is not. Doppler lidar is used to measure the velocity of a target.

Lidar can give the total number density for atmospheric molecules $n(h)$ and therefore the atmospheric density $\rho(h) = \langle m_{\text{MOLECULE}} \rangle \, n(h)$. It is difficult, but possible, to use lidar measurements to quantify aerosol concentration [80]. Such an instrument is able to detect distant thin clouds and haze layers that still have a significant transparency [425]. *The combination of lidar and radar can give a reliable cloud boundary estimate. For water clouds, radar is best at measuring the cloud top, and lidar at measuring the base* [467].

Lidar is an active system, it detects light but it also **emits** lights. Hence, it could cause saturation of the *data acquisition* (DAQ) systems [1]. Furthermore, it could also damage a very sensitive IACT camera.

Space-based remote sounding

CloudSat is an experimental satellite that uses radar to study clouds and precipitation from space. CloudSat flies in orbital formation as part of the A-Train constellation of satellites (Aqua, CloudSat, CALIPSO, PARASOL, Aura, and OCO) dedicated to the observation of clouds, aerosols, and the water cycle.

Cloud-Aerosol Lidar and Infrared Pathfinder Satellite Observation (**CALIPSO**) is a satellite mission devoted to the study of clouds and aerosols. Their radiative impact now represents the main uncertainty on the prediction of climate evolution. The CALIPSO satellite has a payload composed of one backscattering lidar, a visible camera, and an infrared imager.

Launch of CloudSat and CALIPSO successfully occurred on 28 April 2006.

1.6.4 Simulations

CORSIKA

COsmic Ray SImulations for KAscade (CORSIKA) is a *Monte Carlo* (MC) code for detailed simulation of *extended air showers* (EAS) initiated by HE CRs [253] [254]. Protons, light nuclei, photons, and other particles may be treated as primaries up to the highest energies of 10^{20} eV. Secondary particles are tracked through the atmosphere until decay or reaction with air nuclei. CORSIKA includes options for Čerenkov radiation and

neutrinos.

Most of IACTs today use CORSIKA (e.g. MAGIC, HESS, VERITAS, and CANGAROO III) as well as some particle detector arrays and neutrino telescopes.

A detailed description of our usage of CORSIKA, for the VAT simulations, is presented in this thesis in Section 4.3.

ALTAI

The numerical code ALTAI was developed particularly for the simulations of Čerenkov light emission from EAS of energy below 50 TeV [296]. ALTAI is an acronym for *Atmospheric Light Telescope Array Image*. It is also a Russian mountain. The ALTAI code was used by the HEGRA collaboration at the beginning but was later replaced by CORSIKA. ALTAI was not used in the thesis, but CORSIKA only.

MODTRAN

MODerate resolution TRANsmittance code (MODTRAN) is commercial software developed by The Air Force Research Laboratory. It is the state-of-the-art atmospheric radiation-transport model. Current version MODTRAN 4 has been available[41] since January 2000 and follows the prior releases of LOWTRAN 7 (now fully obsolete).

MODTRAN is capable of predicting atmospheric transmittance for wavelengths greater than 200 nm (from radio to UV) at moderate spectral resolution of 2 cm^{-1} (20 cm^{-1} in UV region). The current release, MODTRAN 4 version 3.1, includes for example:
• 6 climatological descriptions: tropical, middle-latitude summer and winter, subarctic summer and winter, and U.S. standard atmosphere.
• 6 atmospheric trace gases: H_2O, CO_2, O_3, N_2O, CO, and CH_4.
• Aerosol profiles: rural, urban, desert, navy, and fogs.
• **Clouds**: cumulus, altostratus, stratus, stratocumulus, nimbostratus, and cirrus.

A few IACT groups were studying some atmospheric effects on Čerenkov light from EAS using *LOW resolution TRANsmittance code* (LOWTRAN), precursor of MODTRAN [79] [90].

The main disadvantage of MODTRAN is that it uses only predefined aerosol models. The right solution for IACTs would be to measure current, local aerosol distribution by lidar and to use such lidar measurements to correct observation data.

I have not used MODTRAN in my VAT study (I have used my own simulations), but the MAGIC collaboration has some plans to use it. The VERITAS collaboration uses MODTRAN 4 to estimate atmospheric extinction values from measurements of the atmospheric properties at the site [266].

[41] *http://www.vs.afrl.af.mil/ProductLines/IR-Clutter/modtran4.aspx*

Chapter 2

The Markarian 421 Active Galactic Nucleus

2.1 Introduction

Markarian 421 (Mkn[1] 421) is a giant elliptical[2] galaxy that contains an *active galactic nucleus* (AGN) which is a blazar of HBL type (see Figure 1.8 for the classification), located in the constellation Ursa Major[3]. These types of galaxies are named after the Armenian astronomer Benjamin Eghishe Markarian (1913–1985) who first detected them in the 1960s [407]. In 1968 Markarian published a catalogue of these galaxies whose spectra showed unusually strong near-ultraviolet continua [155].

Figure 2.1 shows where Mkn 421 is in the sky. The position of a celestial object can be

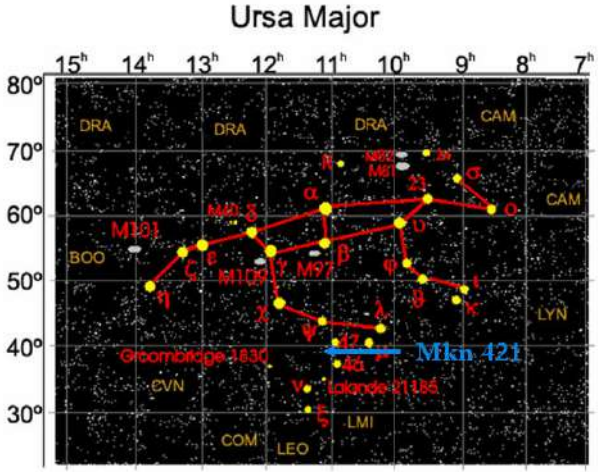

Figure 2.1: The position of Mkn 421 in the sky: $\alpha = 11.04$ h, $\delta = +38.2^{\circ}$.

specified using a fixed set of celestial coordinates: the *right ascension* (RA or α) and the *declination* (DEC or δ). RA on the celestial sphere is similar to longitude (or meridian) on the Earth. The zero point of RA is the point of intersection of the celestial equator and the ecliptic plane – it is the vernal equinox. The unit of RA is hour such that 24

[1] American books and papers (e.g. [483], [155], [401] ...) use abbreviation **Mrk** instead of Mkn.

[2] An old galaxy which looks like an elliptical patch of light in the sky, probably formed from collision and mergers between spiral galaxies [234].

[3] Ursa Major is also known as the Great Bear or Big Dipper.

hours correspond to a full circle of 360°. DEC on the celestial sphere is similar to latitude on Earth. The zero point of DEC is the celestial equator. The celestial north pole (the mean direction of the rotation axes of the Earth) has $\delta = +90^{\circ}$ and the celestial south pole has $\delta = -90^{\circ}$.

Mkn 421 is one of the closest blazars to the Earth (and the nearest TeV blazar as shown in Table 1.4), making it one of the brightest quasars in the night sky. Due to its brightness (around 13.3 magnitude[4]) it can be viewed even by six-inch amateur telescopes. Mkn 421 has a cosmological redshift[5] $z = 0.031$. At redshifts smaller than 0.1, z is related to the velocity of the object by the simple redshift–velocity expression [407]

$$z = \frac{v}{c} \tag{2.1}$$

Therefore, the recession velocity of Mkn 421 is 9000 km/s. According to the redshift–distance relation in the non-relativistic form ($z \ll 1$) [114]

$$z = \frac{H_{\rm o}\, d}{c} \tag{2.2}$$

and using Hubble expansion rate $H_{\rm o} = 71$ km/s/Mpc, Mkn 421 is about **130 Mpc** (or 420 million light years) away from the Earth[6]. It is about 200 times farther away than the Andromeda galaxy (M31), the nearest to our own galaxy. Photons we observe today from Mkn 421 started their journey 420 million years ago[7].

Figure 2.2 shows[8] a finding chart for Mkn 421. Chandra X-ray Image of Mkn 421 is shown[9] in Figure 2.3.

2.2 Physics of Mkn 421

2.2.1 Prelude

The luminosity (total energy loss rate)

$$L = \frac{{\rm d}E}{{\rm d}t} \tag{2.3}$$

is an intrinsic property of an astrophysical source. The luminosity of a normal galaxy like the Milky Way is about 10^{43} erg/s or $10^9\ L_{\odot}$ [10]. But, luminosities for active galaxies (especially for some quasars) range from 10^{45} to even more than 10^{48} erg/s (with $5 \cdot 10^{46}$ being a typical value[11]) [155]. Therefore, quasars are up to 100.000 times more energetic than a normal galaxy or even 10^9 times more than that of the Crab. What is the source of such enormous amount of energy? Can it be explained in terms of known physics?

[4]Light output is highly variable; therefore magnitude varies from around 12.5 to nearly 13.5.
[5]An increase in the λ of EM radiation received compared with the λ emitted: $z = \Delta\lambda/\lambda$.
[6]*Parsec* (pc) is 3.262 *light years* (ly), approximately $3 \cdot 10^{18}$ cm.
[7]200 million years **before** first dinosaurs appeared.
[8]Source: *http://www.lsw.uni-heidelberg.de/projects/extragalactic/charts/1101+384.html*
[9]Source: *http://chandra.harvard.edu/photo/2005/mkn421/mkn421_xray.jpg*
[10]For comparison, the luminosity of the Sun is $L_{\odot} = 3.826 \cdot 10^{33}$ erg/s, where 1 erg = 0.1 μJ.
[11]It is equivalent to more than 500 galaxies of the Milky Way size!

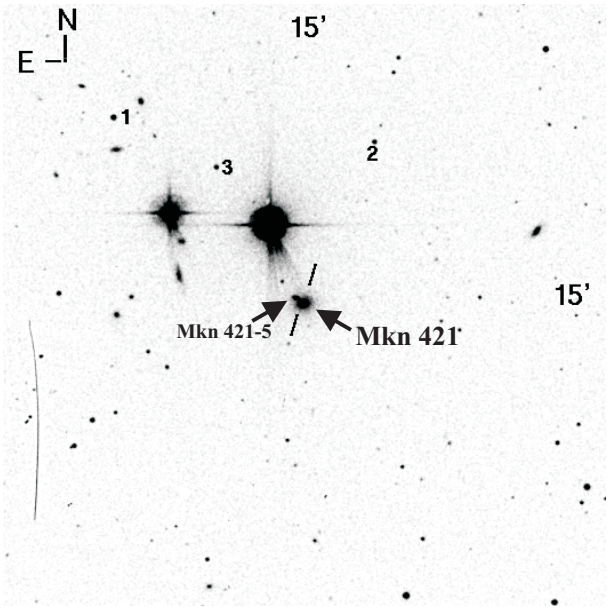

Figure 2.2: An optical image (15'×15') of Mkn 421. An unusual satellite galaxy Mkn 421-5 is also visible very next to Mkn 421.

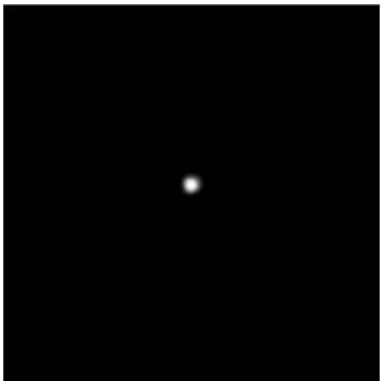

Figure 2.3: This Chandra X-ray image of Mkn 421 was taken on July 1, 2003. Scale: 0.5 arcmin per side. *Credit: NASA/SAO/CXC/F.Nicastro et al.*

2.2.2 Accretion onto supermassive black hole

Most astrophysicists today believe that the questions above can be understood in terms of the interaction between BH and surrounding matter [114]. Hence, it is widely accepted that AGNs are powered[12] by accretion onto *supermassive black holes* (SMBH) [126], just like stars are powered by nuclear fusion.

Accretion is a process by which the mass of a body increases by the accumulation of matter in the form of either gas or small solid bodies which collide with and adhere to the body [407]. Hence, the source of energy is the release of gravitational energy by matter falling towards a BH. It is the most efficient way of generating energy.

There is strong evidence that a SMBH inhabits the centers of a great many, perhaps most, spiral and large elliptical galaxies [155]. The existence of a SMBH at the center of our own galaxy has now been confirmed beyond reasonable doubt [114].

The presence of SMBHs in the center of normal galaxies is hidden from us because

[12]The first one who suggested this was Soviet astrophysicist Yakov Borisovich Zel'dovich (1914–1987).

such SMBHs simply ran out of fuel - gas falling toward SMBH. In other words, our Galaxy (and many other) was possibly active in the past but its central engine is now "turned off" (or in "hibernation"). Yet, SMBHs could reawake and turn violent once again [114].

But, how does an AGN become active? New data from the Chandra X-ray Observatory may provide clues to how a quasar (or any AGN) "turns on". The merger of two galaxies drives gas toward the central regions where it triggers a burst of star formation and provides fuel for the growth of a central BH. The inflow of gas into the BH releases a tremendous amount of energy, and a quasar is born.

Generally, it requires some sort of interaction, either between a massive gas cloud and a galaxy or between two *colliding galaxies*[13], to send enough material into the central region to power the quasar or blazar. Mkn 421 has a companion galaxy (unusual satellite galaxy **Mkn 421-5**) which probably fuels material (mostly gas) toward the center of Mkn 421 and therefore feeds its SMBH.

Accretion onto SMBH is the most powerful energy source known: 10% or more of the mass of the in-falling material can be converted into energy[14]. For example, a non-rotating BH surrounded by one-solar-mass accretion disk is the energy reservoir of 6% $m_{\rm disk}c^2$. For maximally rotating BH mass to energy conversion efficiency even increases to 42%!

Therefore, BHs are the most fuel-efficient engines in the Universe. Most of the energy released by matter falling toward a SMBH is in the form of relativistic jets.

2.2.3 Black-hole astrophysics

A *black hole* (BH) is a compact astrophysical object (Table 2.1) which has a gravitational field strong enough to curve spacetime completely round upon itself so that nothing can escape, not even light [234].

Object	Mass limit	support the gravitational attraction
White dwarf	$1.44M_\odot$ (Chandrasekhar)	the pressure of degenerate electrons
Neutron star	$1.6 - 2M_\odot$ (Oppenheimer-Volkoff)	the pressure of degenerate nucleons
Black hole	no limit	no way ("fatal attraction" [114])

Table 2.1: Compact astrophysical objects which are the end-point of stellar evolution. The mass limit is the largest possible mass an object can have, without being overwhelmed by its own gravity. Emission from these objects is highly variable [483]: isolated flares, periodic oscillations, and *quasi-periodic oscillations* (QPO).

The modern description of the Universe at large scales is almost entirely based on Einstein's theory of *general relativity* (GR). The most fascinating object predicted by GR is a BH. When we really understand BHs, we will understand the origin of the Universe itself [114].

One way in which BHs are believed to form is when massive stars collapse at the end of their lives. A BH appears when a star of mass M collapses down within a radius R_S

$$R_S = \frac{2GM}{c^2} \tag{2.4}$$

[13]When two galaxies collide, massive black holes at their centers form *binary black hole system* (BBHS). Galactic mergers help to grow SMBH.

[14]Nuclear burning releases at most 0.7% of mass-energy.

where c is the speed of light and $G = 6.672 \cdot 10^{-11}$ N m^{2}kg^{-2} is the gravitational constant. R_S is called the **Schwarzschild radius**. The surface having this critical radius, on which the escape velocity is equal to c, is referred to as the **event horizon**. It is an imaginary surface and need not to coincide with any physical surface.

There are several theoretically possible forms of BH [407].

- A non-rotating BH without electrical charge is known as a **Schwarzschild** BH;
- A non-rotating BH with electrical charge is termed a **Reissner-Nordström** BH;
- A rotating BH with electrical charge is called a **Kerr-Newman** BH.
- BHs are likely to be rotating and uncharged, a form known as a **Kerr** BH.

According to theory, BHs are as standardized as elementary particles. All BHs of a given mass, spin and charge are exactly alike [114].

There are about 20 confirmed BH candidates in the mass range 5–20 $M_\odot$ (X-ray binaries[15]) and about 30 SMBH candidates in the mass range 10^6–$10^{9.5}$ $M_\odot$ (in galactic nuclei) [126]. Being so massive, SMBH are described completely by classical GR.

There are some indications that *intermediate-mass black holes* (IMBH) also exist. SMBHs and IMBHs were never predicted to exist by any theorist [457].

The BH paradigm may be proved or ruled out by comparing BH candidates with credible alternatives. For example, for a stellar-mass BH, the standard astrophysical alternative are *neutron stars* (NS) [126]. The first important criteria that may be used to distinguish a BH from a NS are their masses. If a compact astrophysical object has a mass larger than about $3M_\odot$, then the object is very likely a BH.

Several BH candidates have been located in our galaxy. The first one and the most famous one is Cygnus X-1 (Cyg X-1 for short). It is an X-ray binary, about 8000 ly away, where the optical companion star is a typical supergiant star with mass of at least $8.5M_\odot$, and its compact object has a mass range of $6.8 - 13.3M_\odot$.

Some BH binaries show *quasiperiodic oscillations* (QPOs) in X-rays. QPOs were found in X-ray binaries in the mid-1980s. In February 1996, ultra fast variations were found in X-ray light curves observed by RXTE. These QPOs had frequencies of about 1000 Hz and hence were named "kHz QPO". It was the most important scientific result to date of RXTE. The QPO with the highest frequency probably corresponds to the *innermost stable circular orbit* (ISCO) predicted by GR. SMBH binaries are supposed to have QPO too but on the larger time scale. E.g. very recent analysis of the optical and radio light curves of the blazar AO 0235+164 has revealed a characteristic time scale of variability of ≈8 years [397].

2.2.4 Jets

A SMBH creates a gravity field of enormous strength. But it does not just draw material into itself from far away. However, if any material, e.g. an interstellar gas cloud, passes close enough to a SMBH the material starts to orbit and an accretion disk is formed.

Due to the way orbits work; the inner layers of the disk rotate more rapidly than the outer layers. Consequently, the friction of particles moving at different speeds causes the material to spiral. As the gas spirals and crashes, rather than falling into the SMBH,

[15] A binary system in which accretion of material onto compact object release energy in the form of X-rays.

much of it gets ejected. Because of the thick disk the gas can only be easily ejected at right angles to the disk, where there is nothing blocking its way out.

As a result, **two relativistic jets** (narrow beams of material and radiation) emerge from the accretion disk and go in opposite directions as shown in the Figure 1.7. In the case of blazars (e.g. Mkn 421) one of the jets is pointed at the Earth. The Lorentz factor for particles in the blazar jet is

$$\gamma = \frac{1}{\sqrt{1-\beta^2}} \approx 10^7 - 10^8 \tag{2.5}$$

These jets are the most remarkable manifestations of supermassive black holes in AGNs.

2.2.5 The energy spectrum of γ-rays

The spectrum of γ-rays from an AGN is clearly different from the thermal (or black-body) spectrum of a star [155]. In blazars, the thermal component is entirely missing. Blazars, like Mkn 421, show only strongly polarized power-law continua

$$F_\nu \propto \nu^{-\alpha} \tag{2.6}$$

where F_ν is the flux as a function of the frequency ν and α is the spectral index. A pure power-law spectrum with constant α is a signature of synchrotron radiation [155].

A broad-band *spectral energy distribution* (SED) of a blazar stretches through 20 orders of magnitude over the complete EM spectrum – from radio waves to VHE γ-rays. Therefore, *multiwavelength* (MWL) campaigns are necessary to test AGN models.
Figure 2.4 shows an example of theoretical shape of the SED for Mkn 421 from Krawczynski's SSC code[16] [240] and Figure 2.5 shows[17] an example of real data from radio waves to VHE γ-rays.

The *Whole Earth Blazar Telescope* (WEBT) is a network of optical and radio observers that provides continuous monitoring of blazars[18]. The optical and radio blazar light curves obtained by the WEBT are usually studied in conjunction with observations at shorter wavelengths by X-ray satellites, γ-ray satellites (MeV to GeV), and IACTs (γ-rays of GeV to TeV).

[16]The code can be downloaded on *http://jelley.wustl.edu/multiwave/*
[17]Source: *http://www.astr.ua.edu/keel/agn/mkn421.html*
[18]Source: *http://www.to.astro.it/blazars/webt/homepage.html*

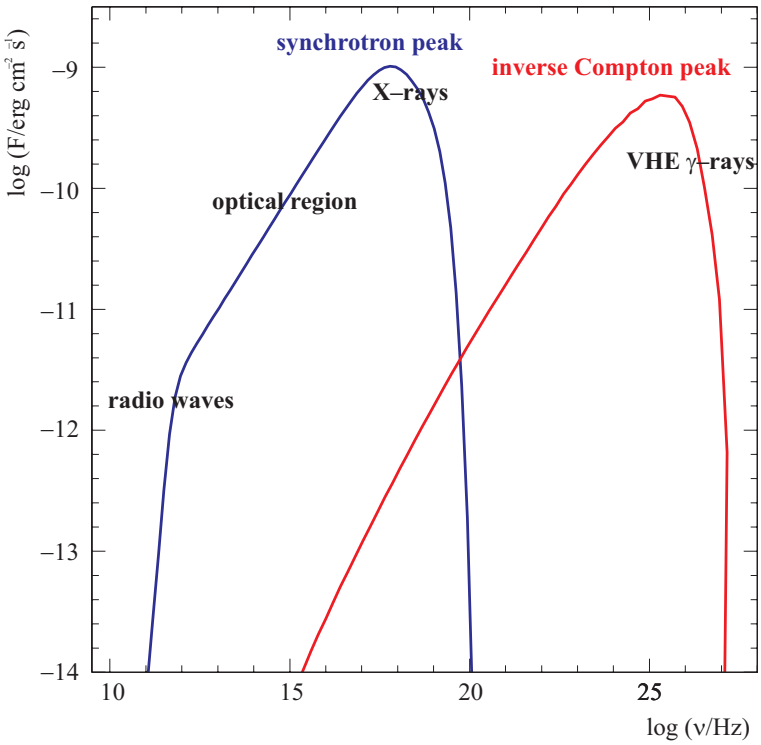

Figure 2.4: *Spectral energy distribution* (SED) of Mkn 421 consists of two parts: first one comes from synchrotron radiation and the second one from inverse Compton process.

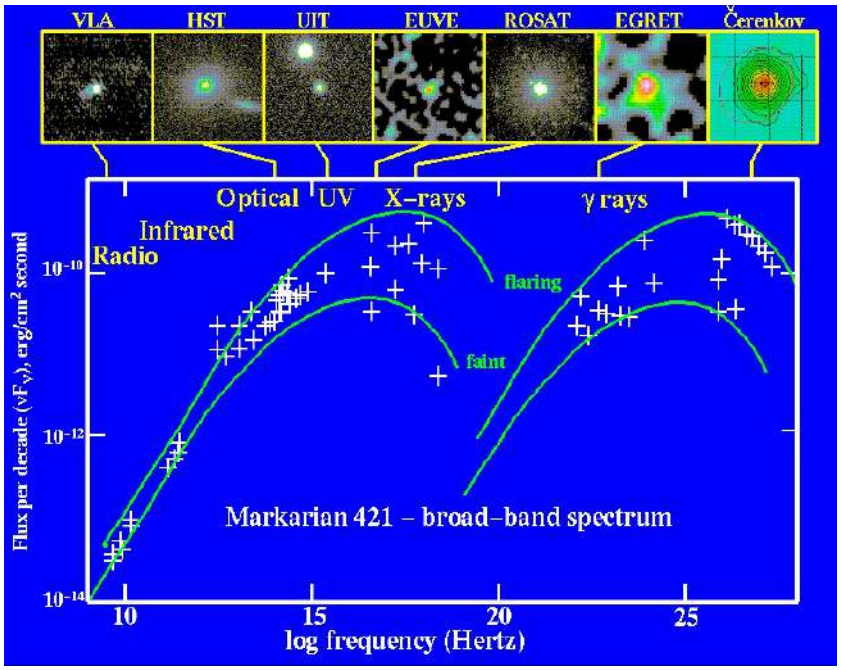

Figure 2.5: Mkn 421 across the *electromagnetic* (EM) spectrum. The radio map is from the *Very Large Array* (VLA) and the optical image was obtained with the *Hubble Space Telescope* (HST). The ultraviolet images are from both *Ultraviolet Imaging Telescope* (UIT) and *Extreme Ultraviolet Explorer* (EUVE). The X-ray image was obtained with the *Röntgen satellite* (ROSAT) and γ-ray images came from the *Compton Gamma-Ray Observatory* (CGRO) and a ground-based Čerenkov telescope.

2.2.6 TeV γ-ray emission models

Any interpretation of an astronomical observation requires identification of the relevant radiation mechanism [4].

In practice, the γ-ray spectrum may be the result of different processes [483]. The acceleration (of charged particles) scenario can be divided in two classes: hadronic and leptonic.

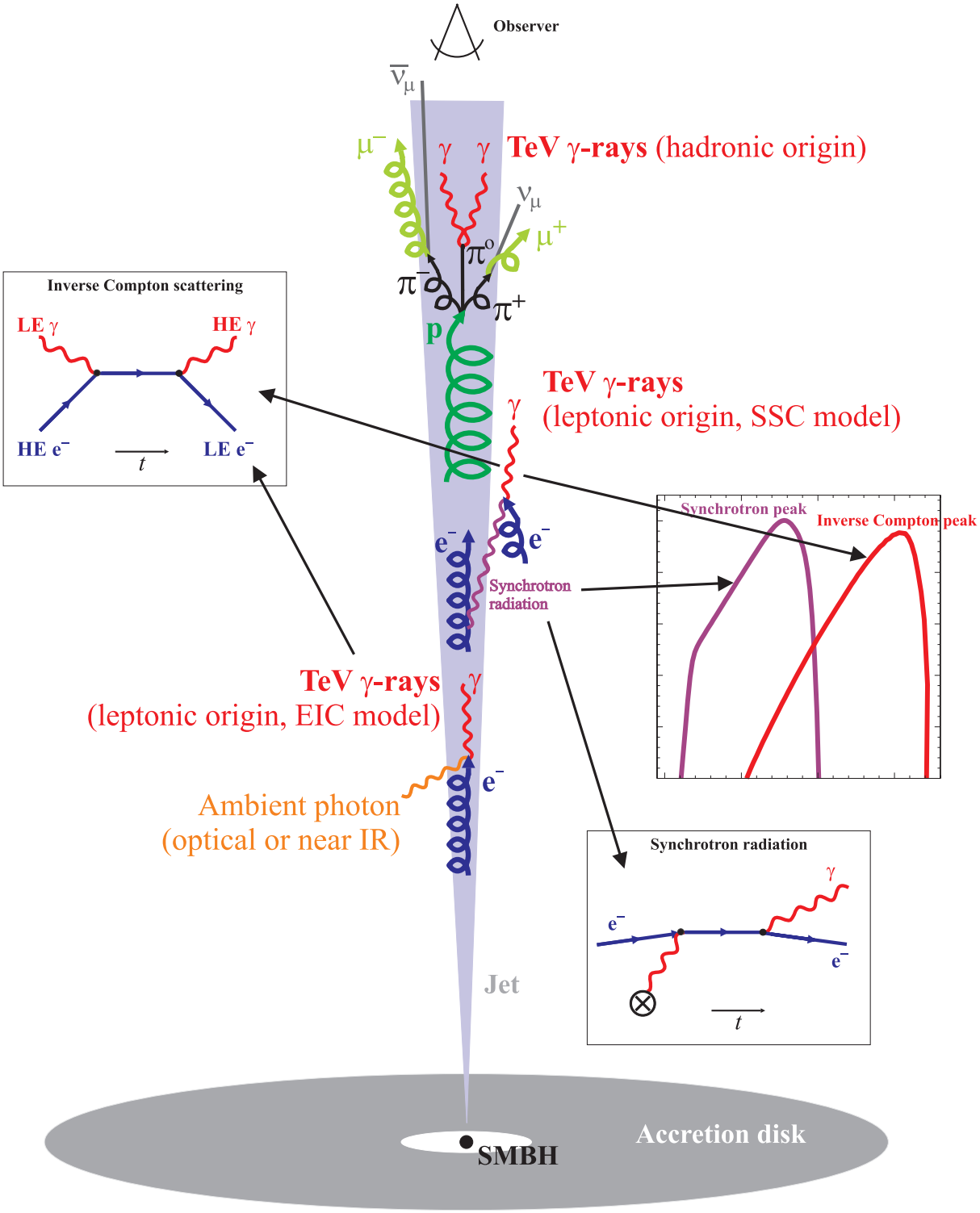

Figure 2.6: Sketch of γ-ray production mechanism in a TeV blazar.

Hadronic model of VHE γ-ray emission

Several hadronic models exist for the accelerated proton interaction.

The hadronic (or proton) model of VHE γ-ray emission in blazar jets requires acceleration of protons up to the energy of 10^{20} eV. Otherwise, protons cannot produce γ-rays in the jets with enough efficiency [4].

The **photo-pion model** involves the interaction with the photon field

$$\mathrm{p_{HE}} + \gamma_{\mathrm{LE}} \longrightarrow \mathrm{p_{LE}} + \gamma_{\mathrm{HE}} \tag{2.7}$$

The **proton synchrotron model** implies the interaction with magnetic field where VHE γ-rays are part of synhrotron radiation (or magneto-bremsstrahlung).

In the **mass-loaded model** protons undergo nuclear reactions with ambient matter, and create a lot of pions

$$\mathrm{p} + \mathrm{p} \longrightarrow \mathrm{N} + \mathrm{N} + n_1(\pi^+ + \pi^-) + n_2(\pi^\mathrm{o}) \tag{2.8}$$

Neutral pions decay into γ-rays

$$\pi^\mathrm{o} \longrightarrow \gamma\gamma \tag{2.9}$$

Charged pions decay into muons and muon **neutrinos** (or antineutrinos for π^-)

$$\pi^+ \longrightarrow \mu^+ + \nu_\mu \tag{2.10}$$

$$\pi^- \longrightarrow \mu^- + \overline{\nu}_\mu \tag{2.11}$$

Hence, neutrino detection from charged pions decays in AGN jets could be the unambiguous proof of the hadronic model of VHE γ-ray emission. As we already mentioned in Section 1.1.2, an important task of the CROATEA Observatory will be the participation in simultaneous observations of γ-rays and neutrinos to test hadronic model of γ-ray production. The IceCube experiment combined with CROATEA could be a good example of such multimessenger (ν & γ) study.

Hadronic models are strongly motivated by the desire to explain both: the production of VHE γ-rays in AGN and the origin of *ultra high-energy cosmic rays* (UHECR) [483].

They have no problem explaining the highest γ-ray energies, but they do have a problem in explaining short time variations (as short as 1 hour or less). Hence, the observations of short-term variations generally favor leptonic models.

Leptonic model of VHE γ-ray emission

Leptonic (or electron) model implies accelerating electrons, and subsequent conversion of their energy into γ-rays. It assumes that both the X-ray and TeV γ-ray emission components originate in relativistic jets due to synchrotron and *Inverse Compton* (IC) radiation of accelerated electrons [4].

In the IC process relativistic electrons produce *high energy* (HE) photons through Compton scattering of *low energy* (LE) photons[19] (Figure 2.7):

$$\mathrm{e^-_{HE}} + \gamma_{\mathrm{LE}} \longrightarrow \mathrm{e^-_{LE}} + \gamma_{\mathrm{HE}} \tag{2.12}$$

Electrons can transfer most of their energy to photons.

[19] In blazars, LE photons are typicaly of eV energy (optical or near IR) and HE photons are typically of TeV energy.

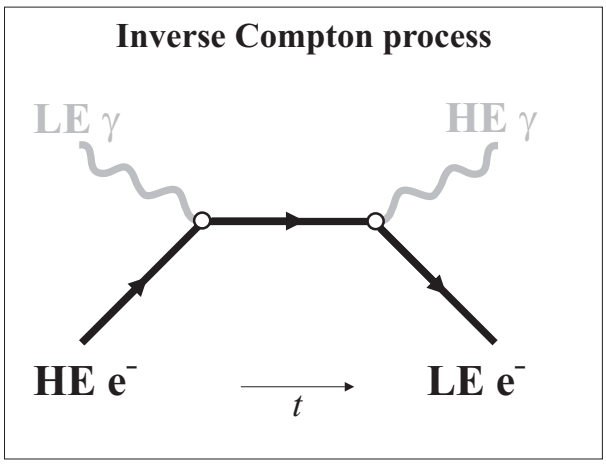

Figure 2.7: Feynman diagram of Inverse Compton scattering, one of the most important processes in high-energy astroparticle physics.

The *External Inverse Compton* (EIC) model assumes an external *low energy* (LE) photon seed, e.g. *microwave background radiation* (MBR), while *Synchrotron Self-Compton* (SSC) model supposes that the LE photon seed comes from synchrotron emission of the same population of HE electrons (accelerated through shock mechanism and rotating in the magnetic field at nearly the speed of light). External photons are usually denser than the synchrotron soft photons [483].

SSC is the preferred concept for TeV blazars today [4]. One important feature of this model is a strong **correlation** between X-ray and γ-ray emission. Hence, matching the observed X-ray and γ-ray light curves should provide a test of the SSC model.

2.2.7 Extragalactic background light and observational γ-ray cosmology

If SCC works, then one can calculate the intrinsic spectrum of a TeV blazar. Furthermore, having the intrinsic spectrum, we are able to estimate the intergalactic absorption effect and get information about *cosmic infrared background* (CIB) radiation [4]. CIB is a part of the *extragalactic background light* (EBL) which carries crucial cosmological information about the formation and evolution of galaxies (Figure 2.8).

γ-rays from distant blazars are being absorbed by EBL. EBL consists of the combined flux of all extragalactic sources at all wavelengths: *cosmic microwave background*[20] (CMB), CIB, radio, optical and UV background and even *extragalactic gamma-ray background* (EGB).

A γ-ray interacts with background photon and produces an electron/positron pair

$$\gamma\gamma \longrightarrow e^- e^+ \tag{2.13}$$

It is one of the most relevant elementary processes in high-energy astrophysics. $\gamma\gamma$ pair production characterizes the optical depth τ which connects the initial (source) spectrum J_o and the observed (absorbed) spectrum J

$$J(E) = J_\mathrm{o} \exp\{-\tau(E)\} \tag{2.14}$$

[20]For the discovery of blackbody form and anisotropy of CMB using *Cosmic Microwave Background Explorer* (COBE), Nobel prize for 2006 has been recently awarded to J.C. Mather and G.F. Smoot.

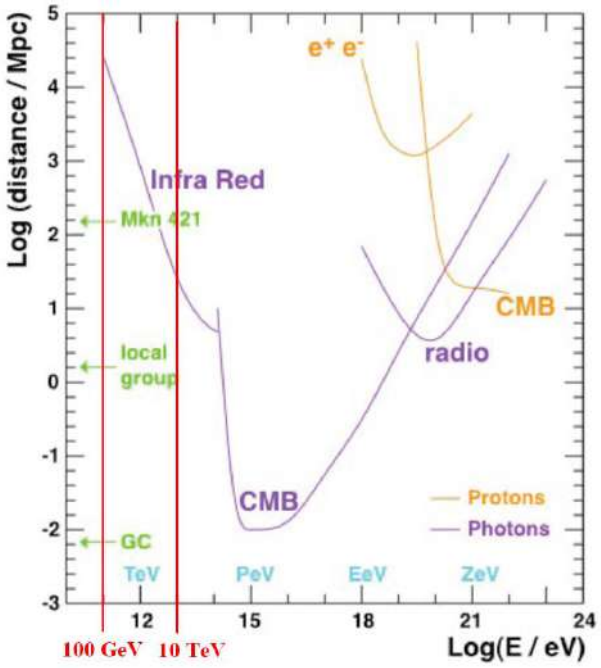

Figure 2.8: In the energy region where a typical IACT is sensitive (vertical red lines), the most important component of EBL is the *cosmic infrared background* (CIB). Source: [380].

The initial spectrum is usually known from models and the observed one from observations. Hence, equation (2.14) gives us information about *diffuse extragalactic background radiation* (DEBRA), but also about *inter galactic magnetic field* (IGMF).

As a consequence of γ-ray attenuation, the *gamma-ray horizon* (GRH) exists: if an extragalactic source is far enough, its VHE γ-rays are totally attenuated.

VHE γ-rays can penetrate cosmological distances up to redshift $z = 1$ only, but HE γ-rays have extremely good penetrating power – up to $z = 100$. The attenuation of the VHE γ-rays by electron-positron pair production with CIB is the reason for the cutoff in the energy spectrum of TeV blazars. Hence, the intrinsic differential energy spectrum of a blazar has a power law form

$$\frac{\mathrm{d}\Phi}{\mathrm{d}E} \sim E^{-\alpha} \tag{2.15}$$

where α is the spectral index. The observed attenuated spectrum has a power law form with a cutoff

$$\frac{\mathrm{d}\Phi}{\mathrm{d}E} \sim E^{-\alpha} \exp(-\frac{E}{E_{\mathrm{cut}}}) \tag{2.16}$$

where E_{cut} is the cutoff energy.

EBL is dominated by thermal emission produced by stars and dust[21] and it is sometimes refers as *diffuse extragalactic background radiation* (DEBRA). Since it is correlated with extragalactic high-energy sources, the main significance of EBL for astronomers is that it contains information regarding the evolution of galaxies, and formation of the large-scale structure in the Universe. The question of how much light the first stars produced is fundamental to models of the Universe's development [333]. Hence, the observational γ-ray cosmology is a new and exciting research area of γ-ray astronomy.

[21] Cosmic dust absorbs UV starlight and re-emits IR.

A direct measurement of EBL is very difficult, since the light originating from the Solar System and from the Galaxy should be corrected for, which implies large uncertainties. A better approach is to study the absorption features imprinted on the γ-ray spectra of distant extragalactic objects by interaction of TeV photons with the EBL photons. The HESS collaboration has recently observed two distant TeV blazars: 1ES 101-232 ($z = 0.186$) and H 2356-309 ($z = 0.165$) [53]. Their results indicate that the intergalactic space is more transparent to γ-rays than it was previously thought [333].

2.3 Previous TeV observations of Mkn 421

Mkn 421 was discovered as the first extragalactic VHE γ-ray source in 1992, by the Whipple telescope [396]. The HEGRA's Čerenkov telescope CT1 started operation in August of the same year. After initial Crab observations, CT1 was devoted to the observation of Mkn 421 since 1994 [385]. The HEGRA Telescope System (CT2–CT6) was also used to monitor Mkn 421 on a regular basis since its commissioning in the fall of 1996 [11]. All later Čerenkov telescopes (MAGIC, HESS, VERITAS, CANGAROO III) have devoted significant amount of their observation time to Mkn 421.

2.3.1 Rapid variability

Rapid time variability in γ-rays is a generic feature of AGNs [114]. BL Lac objects are characterized by their extreme variability on time scales ranging from minutes to years [483]. Their luminosity may change up to $\pm 30\%$ in just 24 hours, and by a factor 100 over a longer time period [155].

The first clear detection of flaring activity in the VHE emission of an AGN came in 1994. In these observations of Mkn 421 by the Whipple telescope, the flux was found to increase 10 times (from 0.15 crab to 1.5 crab[22]) [216]. In 2001, Mkn 421 underwent an extraordinary period of activity during which it was brighter than the Crab nebula continuously over a three-month period [483].

The variability in Mkn 421 is present at all wavelengths, from radio waves to γ-rays. The observed variability in γ-rays has been very rapid – on time scales as short as 15 minutes or even 4 minutes as recently published in [74]. Rapid variability implies that the emission region is much smaller than the galaxy as a whole. E.g. variations in the luminosity as short as 1 hour show that the radiation is coming from a region about 1 light hour across (roughly the distance from Saturn to the Sun).

2.3.2 Correlated variability

One of the earliest MWL campaigns was organized in 1995 to measure the MWL properties of Mkn 421. This campaign revealed, for the first time, the correlation between VHE γ-rays and X-rays [483].

The first clear evidence that the X-ray and TeV γ-ray intensities for Mkn 421 are well correlated on time-scales of hours was published in 1999 [339]. The data were collected as part of a world-wide multiwavelength campaign by the Whipple Collaboration in the TeV γ-ray region and by the BeppoSAX Satellite X-ray detector in April 1998. It is interesting

[22] $1\ \text{crab} = 1.75 \cdot 10^{-11}\ \text{cm}^{-2}\text{s}^{-1}$

that this very first paper about correlated variability does not show any numerical calculation of correlation coefficients, just light curves accompanied by the comment "The strong correlation between the TeV and X-ray flares on short time-scales (is) demonstrated by these data" [339].

The aim of this publication is to study optical/X-ray/γ-ray correlations for all currently available data, including the very latest measurements by the MAGIC Observatory and RXTE. We have mostly studied the nearest blazars Mkn 421 and Mkn 501, but also the recently discovered (in γ-rays) Mkn 180. As presented in Section 6.2, with our new method for correlation studies we found that the X-ray/γ-ray correlations are, in some cases, virtually as strong as one could expect for the case of perfect correlation. Our results support the expectation that X-ray and γ-ray emission are tightly connected. In term, that is a strong indication that a SSC model might indeed be at work in BL Lac objects. Up to now, the optical data have not shown correlation with TeV γ-rays [483]. Recently, we have found, for the very first time γ/optical and X/optical correlation in CT1/KVA data from 2003.

Chapter 3

The observations of Mkn 421

3.1 Detector description

3.1.1 Čerenkov telescope (CT1)

Figure 3.1: Picture of CT1 taken in 1999 by Gerhard Rauterberg from Kiel. Source: *http://www.hegra.uni-kiel.de/hegra/La_Palma_images/March99/outside*

Čerenkov Telescope 1 (CT1) was a stand-alone *Imaging Atmospheric Čerenkov Telescope* (IACT) located at the *Observatorio del Roque de los Muchachos* (ORM) on the island of La Palma in the Canaries, Spain (28°45'30" North, 17°52'48" West). ORM, at an altitude of 2200 m, is one of the best observing sites in the world. CT1 was a part of the *High Energy Gamma Ray Astronomy* (HEGRA) and the experimental precursor of MAGIC.

The HEGRA collaboration also ran the stereoscopic system CT2-CT6. The technical performance of the system is described in one of the latest HEGRA's papers [394]. After

six years of operation, the system was shut down in September 2002, since the manpower was needed for the new MAGIC and HESS experiments.

CT1 started operation in August 1992. It had an equatorial mounting[1] and a tracking accuracy better than 0.1°. More details can be found in [13]. The telescope was dismantled in 2003.

The CT1 reflector

Optical collectors for ground-based γ-ray astronomy do not need to be as good as for the optical astronomy. Therefore, IACTs reflectors consist of tessellated (or segmented) mirrors. The cost of such reflectors is much lower than for a one-piece mirror of the same aperture. They are shaped according to two basic designs:

1. The spherically shaped Davis-Cotton reflector, which minimizes spherical aberrations. E.g. the HEGRA CT1 telescope, which is used to collect a part of the data for this analysis, is of that type. It has: *radius of curvature* = 4.9 m, *focal length* = 4.9 m, *area* = 10 m^2, and *diameter* = 3.6 m.

2. The parabolically shaped reflector, consisting of spherically shaped mirror elements of a variable radius of curvature, which depends on the distance of the mirror element from the center of the reflector. E.g. the MAGIC telescope is the largest telescope of that kind. A parabolic reflector ensures isochronous arrival of photons from a short light pulse to the camera.

Figure 3.2 shows the geometry of CT1 reflector made of 33 aluminum hexagonal mirror tiles. The reflector shape was of Davis-Cotton type.

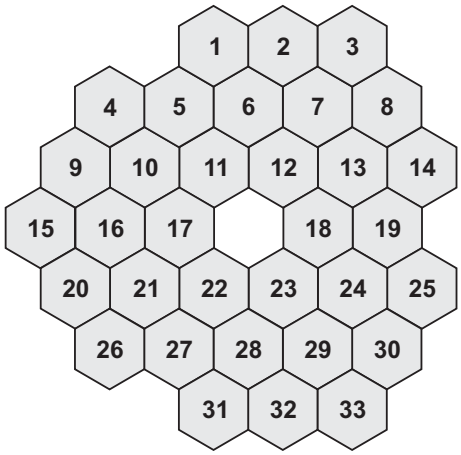

Figure 3.2: Segmented mirror area of CT1 was made of 33 hexagonal mirrors.

At the beginning of CT1 operation, the reflector was made of 18 aluminized glass mirrors, with SiO_2 coating [471]. The reflector size was 5 m^2 only. In 1998, the mirror area was increased to 10 m^2.

The reflector facets were aligned manually using a laser system installed at a point facing the centre of the reflector. The alignment resulted in a *point spread function* (PSF)

[1]One telescope axis is parallel to Earth rotation axis. The advantage of it lies in using constant speed movement around only one axis, unlike alt-azimuth mounting which requires variable speed motion around both axes. Also, for the equatorial mounting the telescope's FoV does not rotate.

of about 0.2° *full-width at half-maximum* (FWHM).

The reflectivity of CT1 mirrors was about 80% [471].

The CT1 camera

CT1, the very first Čerenkov telescope of the HEGRA experiment, working since 1992, had a camera of 37 pixels only. Each pixel represents a channel consisting of a PMT and read-out electronics. It gives ADC counts as output.

In December 1993, a second telescope with a new 61 pixel camera was built. The higher pixel number improved the angular resolution and the gamma/hadron separation. The positive experience with that camera led the HEGRA collaboration to replace the 37 pixel camera of CT1 with a new camera with 127 pixels, in 1994 [399] (Figure 3.3).

Figure 3.3: The front plate of the CT1 camera. In front of PMTs are the Winston cones – designed to minimize the dead-space between the photocathodes of the PMTs. Picture by Nikola Godinović from Split.

Classical *photomultipliers* PMTs with bialkali photocathodes were used as photodetectors (each PMT was one pixel). PMTs can measure light in the wavelength range 300–600 nm. Below 300 nm Čerenkov light is strongly absorbed by ozone. Above 700 nm the intensity of the *light of the night sky* (LONS) increases rapidly [354].

Coaxial cables were used for data transmission. The camera was in operation from 1995 to 2003. In 2004, the CT1 camera came to Croatia as a donation of Professor Eckart Lorenz from Max-Plank Institute, Munich. We are going to use this camera as the CROATEA first camera until we develop a new one.

Figure 3.4 shows the geometry of the front plate of the CT1 camera. The diameter of the cluster of *PhotoMultiplier Tubes* (PMT) is 273 mm. 127 PMTs are packed in hexagonal rings. The distance from PMT center to center is 21 mm, but the sensitive area of one PMT is only 16 mm in diameter. Winston cones were used in order to decrease the dead area between PMTs (EMI 9083B) which had been specially designed for Čerenlov telescopes [399].

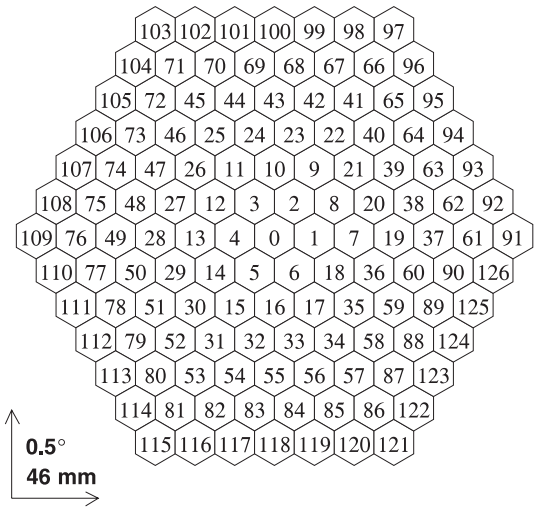

Figure 3.4: Geometry of the CT1 camera as defined in the *MAGIC Analysis and Reconstruction Software* (MARS). The diameter of the camera is 273 mm which corresponds to a FoV of 3.12°.

Quantum efficiency[2] (QE) was about 25%.

The camera was placed in the focus of the reflector (precisely, a little bit in front of the focus because the source was not at infinity). The camera *field of view* (FoV) - the full angular extent of the camera - can be easily calculated. From a point on the reflector surface each PMT is seen under the angle φ

$$\varphi = \frac{180^{\circ} \cdot d}{f\pi} \tag{3.1}$$

where $d = 21$ mm (a PMT diameter) and $f = 490$ cm (the reflector focus). The angular size of one pixel is 0.24°. There are 13 PMTs in the camera diameter, therefore the FoV for the whole camera is $13 \cdot 0.24^{\circ} = 3.12^{\circ}$.

For observation of point gamma-ray sources the FoV of the camera should not be significantly smaller than 4° [7]. To study extended sources (e.g. the Crab nebula, not just the pulsar in the middle) or sources whose positions are only known within 1°, a camera with 5° FoV is required [7].

A pixel size $\approx 0.25^{\circ}$ provides high accuracy in determination of the Hillas parameters *Width* and *Length* (see Section 5.1.2) but for the best determination of the image orientation, the pixel size should be 0.15° [7].

The CT1 Trigger

In the earliest usage, **trigger** refers to a mechanical mechanism, the pulling or pushing of which sets a device into action. Today in a wider sense, a trigger is also used to activate some event recording. Trigger need not be a necessary condition for the event, it can be a sufficient condition only. A trigger system uses simple criteria to rapidly decide which events to keep when only a few can be recorded.

In 1998, when the CT1 mirror area was increased, a two *next-neighbor* (NN) trigger was also implemented. Previous trigger condition required just the coincidence of two

[2]QE is the ratio of number of photons detected to the number that strike the detector [407]. E.g. QE of the human eye is 1-5% whereas a *charge-coupled device* (CCD) has QE of 60-80%.

pixels (or PMTs). The NN trigger required any **2 out of 127** triggering pixels to be neighbors **within 13 ns and above 50 mV**[3] to accept an event. Both improvements resulted in the energy threshold reduction down to 700 GeV [146]. Hence, the energy region covered by the CT1 was from 700 GeV up to about 20 TeV.

The *trigger rate* (TR) on *cosmic rays* (CR) close to the zenith, and after the filter cut, was about 3.5 Hz [31]. The hadron rate is at least 100 times larger than the γ-ray rate. For example, the highest flares reach up to 120 γ-rays per hour what corresponds to 0.033 Hz.

The hadron rate is an excellent indicator[4] of *variable atmospheric transparency* (VAT). During stable weather condition, TR (corrected for zenith angle) is constant to the fluctuations (an example in Table 5.2). As transparency decreases, TR decreases too (an example in shown in Figure 5.18).

3.1.2 X-ray satellite (RXTE)

Figure 3.5: Artist's view of RXTE: *http://heasarc.gsfc.nasa.gov/Images/xte/xte.gif*

The *Rossi X-ray Timing Explorer*[5] (RXTE) is a NASA X-ray satellite aimed to explore **the variability of X-ray sources**. The satellite was launched on December 30, 1995. It was designed for a lifetime of two years with a goal of five, but it is still performing well now in 2006.

RXTE has unprecedented time resolution (from μs to months) in combination with moderate spectral resolution (from 2 to 250 keV).

There are three instruments on board the satellite:

- *Proportional Counter Array* (PCA) is an array of five proportional gas counters which covers the lower part of the energy range: 2–60 keV. It is the largest array ever flown with a total collecting area of 6500 cm^2. PCA has an energy resolution of 18% (at 6 keV) and a time resolution of 1 μs.

[3] 50 mV was equivalent to approximately 13 *photoelectrons* (PE).

[4] TR, of course, depends on hardware setting, especially *high voltage* (HV) setting, but here we suppose fixed hardware settings.

[5] The satellite is named after Italian-born American astronomer Bruno B. Rossi (1905–1993).

- *All Sky Monitor* (ASM) consists of three wide-angle *scanning shadow cameras* (SSC) equipped with proportional counters of total collecting area of 90 cm^2. It scans about 80% of the sky in every orbit, [6] respectively every 90 minutes. ASM covers the energy range of 2–12 keV and its sensitivity is 30 mCrab, where the Crab nebula flux is about 75 ASM counts per second.

- *High Energy X-ray Timing Experiment* (HEXTE) consists of two clusters of four NaI/CsI scintillation counters and covers the upper energy range: 15–250 keV. Each cluster has a collecting area of 800 cm^2 and an energy resolution of 15% (at 60 keV).

In this thesis, I have used only data from the ASM. More details concerning the ASM data analysis is given in Section 5.4.4.

3.1.3 Optical telescope (KVA)

Figure 3.6 shows the *Kungliga Vetenskaps Akademien*[7] (KVA), an optical, robotic telescope located at *Observatorio del Roque de los Muchachos* (ORM) on the island of La Palma in the Canaries at an altitude of 2200 m. Since the autumn of 2003, the telescope allows fully remote observing from Tuorla observatory of the University of Turku, Finland. The KVA is a Cassegrain telescope with 60 cm aperture and equatorial mounting. The

Figure 3.6: KVA-60 optical Cassegrain telescope located at ORM on La Palma. Source: *http://www.astro.utu.fi/telescopes/60lapalma.htm*

telescope is devoted to long-term photometric monitoring of blazars truly simultaneously in the optical and γ-ray regions (in close collaboration with the MAGIC project).

The KVA has been equipped with a Santa Barbara Instrument ST-1001E CCD camera and a standard Johnson-Cousins R filter.

[6] A circular orbit at an altitude of 580 km, corresponds to an orbital period of 96 minutes.

[7] Royal Swedish Academy

3.2 Observations of the blazar Mkn 421

3.2.1 Multiwavelength campaigns

The best hope for understanding of emission mechanism in blazars comes from the combination of observational data over the whole electromagnetic spectrum [483]. Simultaneous observations where several telescopes observe in different wavelength bands are called *multiwavelength* (MWL) campaigns.

MWL campaigns were performed on Mkn 421 for many years. One of the earliest was organized in 1995 to measure MWL properties of Mkn 421 [483]. In January 2001, after receiving information from HEGRA that Mkn 421 was in high-flaring state at TeV energies, the *Whole Earth Blazar Telescope* (WEBT) campaign started on February 19, 2001. The WEBT[8] is a network of optical and radio observers devoted to continuous monitoring of blazars.

The most remarkable result from MWL campaigns has been that there is good evidence for a correlation between the X-ray flux and the TeV γ-ray flux. No highly significant evidence has yet been found that the radio, IR, optical or UV fluxes are correlated with the X-ray and/or the TeV γ-ray emission [303].

3.2.2 High flaring state: from February to May 2001

These data were published by the HEGRA collaboration [31] except of a small subset which has been analyzed, corrected for *variable atmospheric transmission* (VAT) and presented here.

3.2.3 Quiet state: from February to March 2003

Simultaneous CT1 TeV γ-ray, RXTE X-ray, and KVA optical observations of Mkn 421 were performed during the period from February 25 to March 6, 2003. The source was found in a quiet state. However, even when a source is in a low state, the detection of VHE γ-rays provide valuable data that can be combined with simultaneous observations at other wavelengths to estimate the physical processes involved in TeV γ-ray emission. The data of the MWL campaign on Mkn 421 in February and March 2003, in which I have participated, is analyzed and presented here for the first time and is expected to be published soon.

[8] *http://www.to.astro.it/blazars/webt/*

Chapter 4

Extended particle showers in the atmosphere

4.1 The atmosphere

The atmosphere is an intrinsic part of any *imaging atmospheric Čerenkov telescope* (IACT) and the telescope response is therefore sensitive to unpredictable changes in the atmosphere [310]. Since IACTs cannot be calibrated using a test beam, the flux and energy calibration relies entirely on *Monte Carlo* (MC) simulations. MC simulations usually consist of two parts:

- simulations of *extended air showers* (EAS) in the atmosphere (this part is equal for all IACTs and also for neutrino and cosmic ray experiments);
- simulation of the detector, specific for each experiment.

In this thesis, we have introduced *variable atmospheric transparency* (VAT) simulations – a special part of MC simulations which deals with bad weather conditions. In order to develop VAT simulations, we had to study physics of the atmosphere and especially clouds.

4.1.1 General remarks on the properties of the atmosphere

The atmosphere is a thin[1] gaseous envelope surrounding the planet Earth. It consists of nitrogen (N_2, ∼78%), oxygen (O_2, ∼21%), argon (Ar, $< 1\%$), and some minor species or trace gases: carbon dioxide (CO_2, ∼0.03%), water vapor (H_2O, 0–4%), and ozone (O_3, 0–0.0012%). Therefore, the atmosphere is a mixture of gases and behaves as an ideal gas. N_2, O_2, Ar, and CO_2 are well-mixed; H_2O has a maximum in the troposphere, and O_3 in the stratosphere. Although N_2 and O_2 predominate by volume, the minor constituents O_3 and H_2O play crucial roles.

The atmosphere is conventionally subdivided into layers (atmospheric shells), in the vertical direction, according to the variation of temperature with altitude. Figure 4.1 shows the common subdivision.

The lowest part is the **troposphere**. It contains 75% of the air mass and extends up to 20 km asl, but may vary from 10 km at the pole to 20 km at the equator. Most weather

[1] More than 99% of the air mass is below 40 km which is less than 1% of the Earth's radius.

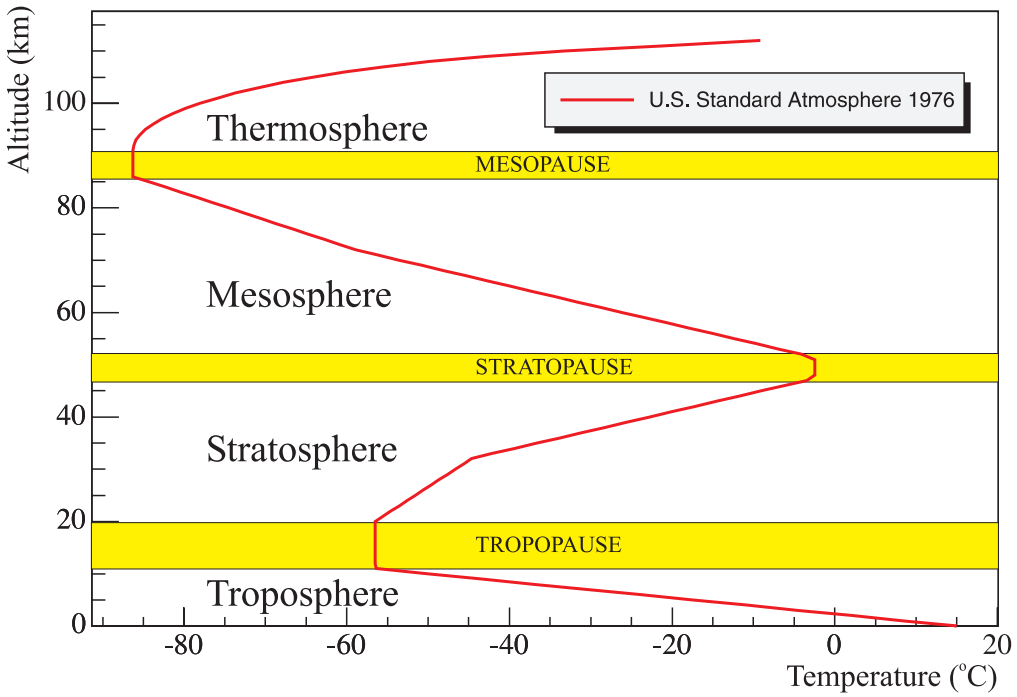

Figure 4.1: Typical vertical structure of atmospheric temperature. Data from U.S. Standard Atmosphere 1976 (NASA).

phenomena occur in the troposphere and also life forms. It contains hydrometeors (clouds and precipitation). The temperature decrease linearly with altitude ($\mathrm{d}T/\mathrm{d}h = -6.5$ K/km) up to the tropopause ($\mathrm{d}T/\mathrm{d}h \approx 0$).

The next layer is the **stratosphere**. It contains 24% of the air mass and extends from 20 to 50 km asl. It also contains an ozone[2] layer (bulk of O_3 molecules from 15–30 km with maximum at 20–25 km). The temperature rises with increasing altitude. The troposphere and the stratosphere contain almost all the air-mass. Therefore the end of the stratosphere can be regarded as the beginning of *space*. The concentration of water vapor in the stratosphere is low and clouds are rare.

The layer extending from 50 to 90 km is called the **mesosphere**. The temperature there decreases with altitude again. It is the coldest part of the atmosphere. It contains a few molecules and shooting stars burn up in this layer.

The next layer is the **thermosphere** containing fewer molecules and characterized by large temperature fluctuations. It extends from 90 to approximately 600 km.

Finally, the **exosphere**, above 600 km, contains occasional molecules gradually escaping into space. Satellites are usually placed here. *Top of atmosphere* (TOA) is, in practice, at 1000 km.

The majority of EAS, created by CRs, start and extend in the troposphere. Some of them may start in the stratosphere but the bulk of Čerenkov light is generated in the troposphere anyway.

All clouds also lie in the troposphere. One can find reports about mysterious high-

[2]Ozone concentration versus altitude is shown later (see Figure 4.19).

altitude clouds e.g. *mother-of-pearl* clouds (20 to 30 km asl) and *noctilucent* clouds (more than 80 km asl). They exist, but they have no impact at all on the atmospheric transparency in the context of ground-based gamma-ray astronomy.

4.1.2 An atmospheric model

The atmosphere is too large and too complex to be fully described. Instead, we can only use an approximate model. Hence, to interpret atmospheric observations we need to develop physical and mathematical models of the atmosphere [80]. A widely used example[3] of an atmospheric model is the **U.S. Standard Atmosphere 1976**. A standard atmosphere is a hypothetical vertical distribution of atmospheric temperature, pressure, and density which roughly represents year-round, middle-altitude conditions. The U.S. Standard atmosphere 1976 is an idealized representation of mean annual conditions of the Earth's atmosphere at a latitude of 45°N. It uses *standard temperature and pressure* (STP) for sea-level values:
$T = 288.15$ K (15°C), $p = 101\,325$ Pa, and $\rho = 1.225$ kg/m^3. Figures 4.1, 4.2 and 4.3 show the vertical distribution of temperature, pressure, and density for the Standard atmosphere. The model takes into account the subdivision of the atmosphere into distinct levels (Figure 4.1).

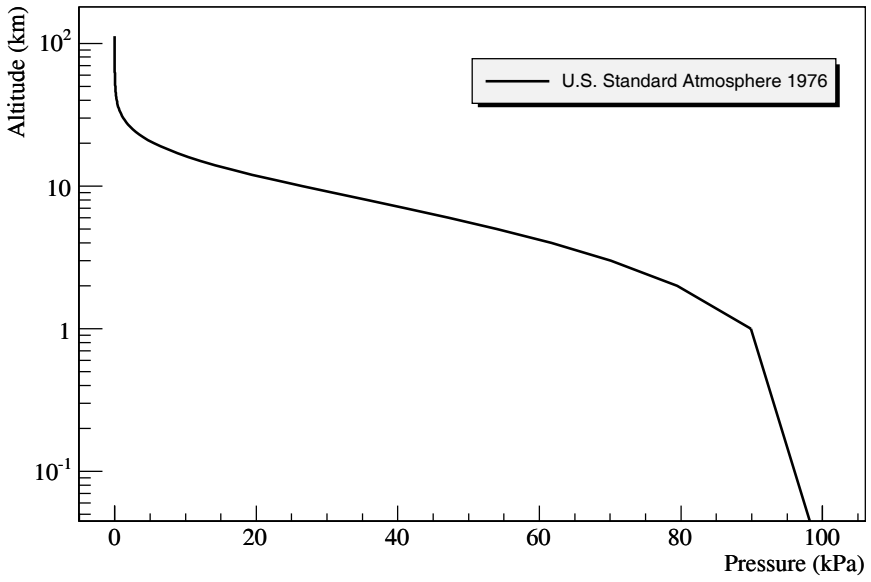

Figure 4.2: Atmospheric pressure decreases exponentially with height. Data from U.S. Standard Atmosphere 1976 (NASA).

We have used this atmospheric model in CORSIKA for EAS simulations as well as in the Reflector program for Rayleigh scattering. However, it would be better to use local atmospheric density profiles[4] because it depends on geographic position and it is generally time-variable [116]. The daily profiles determined locally at the site are recommended [490]. The Auger collaboration compared available atmospheric models to

[3]Source: *http://modelweb.gsfc.nasa.gov/atmos/us_standard.html*

[4]It could be measured using balloon-borne radiosondes. E.g. the Auger experiment uses such sondes to measure altitude profiles of $T(h)$ and $\rho(h)$ [285].

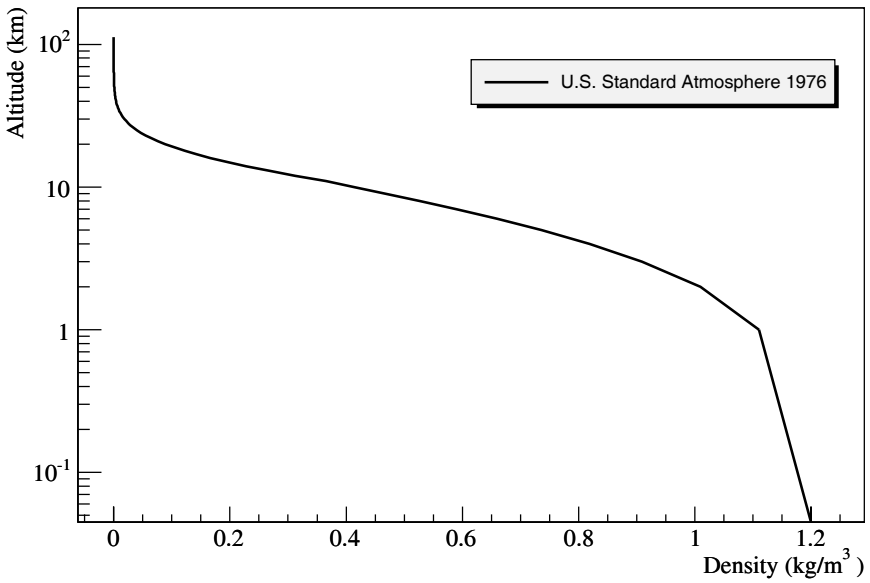

Figure 4.3: Density of the atmosphere decreases exponentially with height. Data from U.S. Standard Atmosphere 1976.

realistic atmospheric conditions, and found a difference of 5-10% near ground, concerning the fluorescence light emission [287].

4.2 Clouds

4.2.1 Water

Roughly speaking, *clouds are water*.[5] They are visible clusters of small liquid water droplets or ice crystals hanging in the air. They form when water vapor in the air condenses into liquid water droplets or sublimates into ice crystals. Each tiny droplet or crystal is light enough to float in the air.

From all the water on Earth, the atmosphere contains just 0.001%. The largest fraction of water is in the oceans (97%) and the polar ice caps (2.1%). Despite the small amount of water in the atmosphere, the transport of water is the main feature of Earth's climate. Therefore, clouds are one of the most significant elements of the atmospheric system yet they remain one of the less understood components [316]. Satellites *CloudSat* and *Cloud-Aerosol Lidar and Infrared Pathfinder Satellite Observation* (CALIPSO) should change this very soon (see Section 1.6.3).

Clouds form from water vapor evaporated from the sea or from moist soil and plants. Water vapor cools as it rises and condensation appears. If the temperature is lower than 40 °C, sublimation occurs – water vapor goes directly into ice crystals. E.g. cirrus clouds are formed of ice crystals.

[5]People sometimes say clouds are water vapor. That is not true. Water vapor is as transparent as dry air, it is invisible. The difference is crucial in the context of VAT.

4.2.2 Cloud condensation nuclei

In perfectly clean air, approximately 130 H_2O molecules should collide at the same time to produce the smallest water droplet. The probability for such an event is practically zero. But clouds do form anyway. The reason for that is dirty air. There are many small particles in the air called *aerosols*. Some of them are hygroscopic (e.g. small sea salt crystals) and act as *cloud condensation nuclei* (CCN). CCN are baits for strolling water molecules. They are **building blocks of clouds** [110].

There are three major sources of CCN:
(1) salt particles from oceans (size from 0.01 μm to 10 μm);
(2) sulphates from coil burning (size a few 0.1 μm);
(3) soil particles from ground carried by wind (size less than 10 μm).
In fact, the atmosphere is full of particles ranging in diameter from 0.01 μm to 10 μm, but only a small fraction of them take part in the cloud formation process [110].

4.2.3 Cloud microphysical characteristics

Cloud droplet size

The size of cloud water droplets can vary from 2 μm (in high thin clouds) up to even 200 μm (in vertically developed rainy cloud). The average diameter is from 5 to 20 μm. In comparison, rain droplets range from 0.5 mm to 7 mm. Droplets smaller than 0.5 mm are not called rain, but **mist**[6].

The cloud-droplet size-distribution is a **modified gamma distribution** [316]

$$n(r) = N\frac{6^6}{5!}\frac{1}{r_\mathrm{m}}\left(\frac{r}{r_\mathrm{m}}\right)^6 \exp\left(-6\, r/r_\mathrm{m}\right) \tag{4.1}$$

where N is the cloud droplet concentration, and r_m is the mean radius. A graph of the distribution (4.1) is shown in Figure 4.4 for $N = 450$ cm^{-3}.

Marine clouds (clouds over oceans) tend to have bigger droplets than continental clouds. This fact is in close connection with the cloud droplet concentration as one can see in the next subsection.

Cloud droplet concentration

The *cloud droplet concentration* or cloud water-droplet density N can be calculated from the cloud droplet size distribution $n(r)$

$$N = \int n(r)\mathrm{d}r. \tag{4.2}$$

Cloud droplet concentrations vary from 10 cm^{-3} to 1000 cm^{-3} with the average droplet concentration of a few 100 cm^{-3}. **The typical droplet concentration in clouds is 200 cm^{-3}** [110]. For the size distribution shown in Figure 4.4 the integral (4.2) gives the value $N = 450$ cm^{-3} for an altostratus cloud.

Generally, for stratus clouds (layer-type clouds) the mean radius range from 4 to 10 μm, and the cloud droplet concentration from 200 cm^{-3} to 600 cm^{-3} [110].

[6]Smaller droplets often mean higher concentration and that means worse optical transparency or "not easy to see". It is interesting to note the similar meaning of word "**myst**ery"

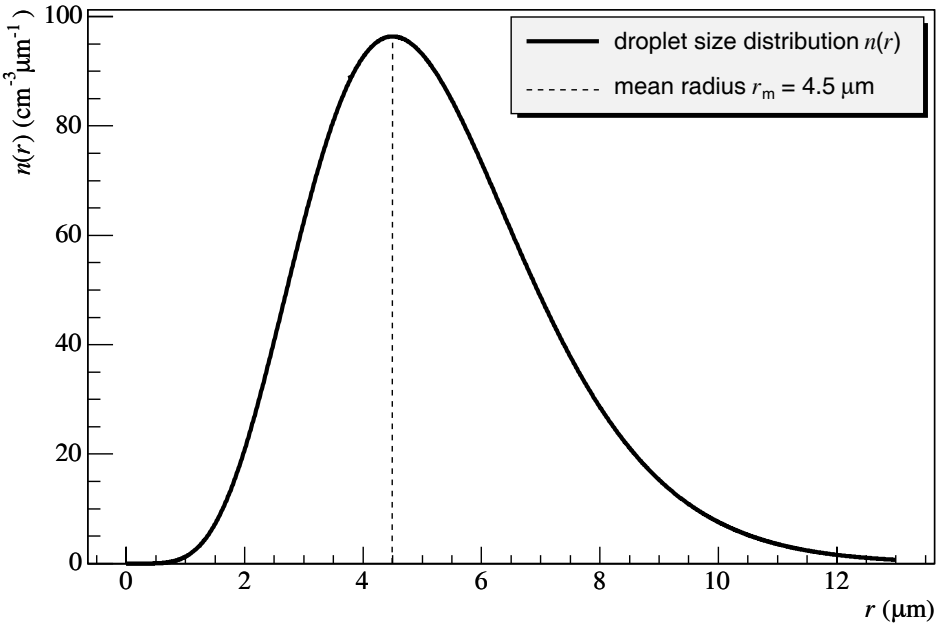

Figure 4.4: Altostratus water-droplet size-distribution for $N = 450$ cm^{-3}.

The liquid water content (LWC) can also be calculated from the size distribution $n(r)$

$$\mathrm{LWC} = \frac{4\pi}{3}\rho \int r^3 n(r)\mathrm{d}r. \tag{4.3}$$

LWC of typical clouds vary from 0.05 to 3 g/m^3 with the average value from 0.1 to 0.3 g/m^3. E.g. for typical altostratus clouds, as shown in Figure 4.4, LWC is 0.4 g/m^3.

The density of the atmosphere is not significantly different inside and outside a cloud. Anyway, clouds are very heavy. The altostratus mentioned above can extend to more than 100 billion cubic meters, therefore it can weigh more than 40 000 tons.

Marine clouds usually have smaller droplet concentrations than continental clouds. The consequence of that is better transparency of marine clouds.

4.2.4 Cloud classifications

Clouds are named by how high in the sky they form and by their appearance. Usually the first part of the name has to do with the height, and the second part refers to the appearance. If the clouds form at the highest altitude, they get the prefix *cirro*. Cirrus clouds are hair-like and icy. Middle clouds get the prefix *alto*, and low clouds do not have a prefix. There are two typical cloud appearance types: *cumulus* and *stratus*. Cumulus are individual clouds and look like cauliflower. They usually signal fair weather. A stratus cloud build an uniform layer which covers most of the sky. When they are very thick e.g. nimbostratus[7], they become dark and produce precipitation. There are also vertically developed clouds: cumulus (Cu) and cumulonimbus (Cb). This classification scheme based on Latin names was introduced by Luke Howard in 1803. Table 4.1 and Figure 4.5 show the common cloud classification. Very low clouds, in contact with the ground, are called *fog*. Dirty fog is *smog* (**sm**oke+f**og**).

[7] *Nimbus* is latin word for cloud, but it also means a rain-storm.

level	type	abbreviation	height (km)	thickness (m)	appearance
low	Stratocumulus	Sc	0 - 2	100 - 200	puffy on top
low	Stratus	St	0 - 2	a few 100	uniform, flat
low	Nimbostratus	Ns	0 - 4	a few 1000	uniform, dark
mid	Altocumulus	Ac	2 - 6	about 1000	puffy, scattered
mid	Altostratus	As	2 - 6	300 - 900	uniform
high	Cirrus	Cwe	6 - 18	about 100	thin, wispy
high	Cirrostratus	Cs	6 - 18	a few 100	appear in sheets
high	Cirrocumulus	Cc	6 - 18	about 100	small and puffy

Table 4.1: Common cloud classification and cloud characteristics.

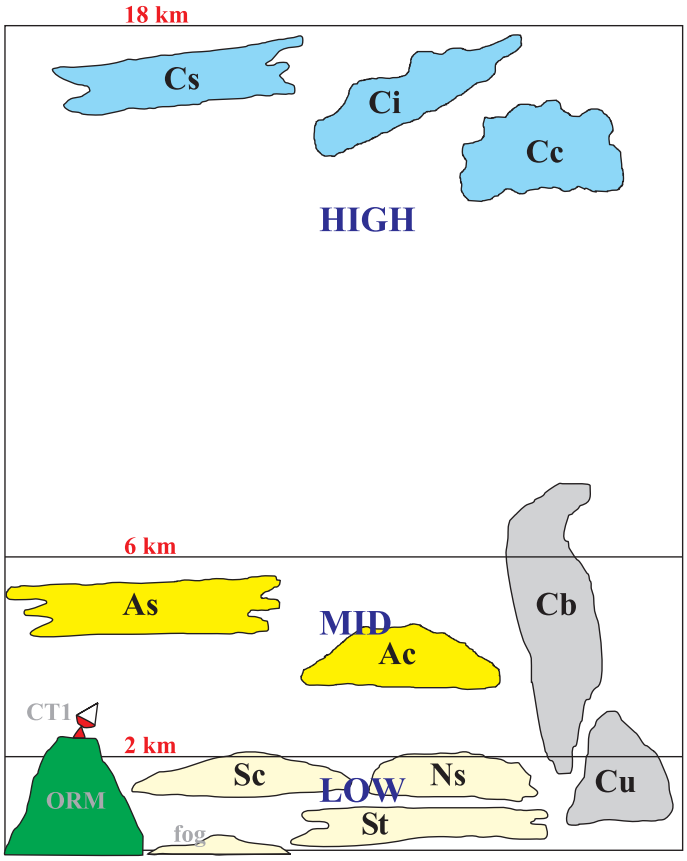

Figure 4.5: Types of clouds. See Table 4.1 and Section 4.2.4 for cloud full names and characteristics. See also real photo from the top of La Palma island (Figure 4.6).

4.2.5 Cloud coverage

Clouds are global in nature and regularly cover approximately 50% of the Earth's surface [316]. Average coverage over the oceans is slightly greater than over land. The occurrence of clouds shows dramatic geographical variations.

4.2.6 Clouds over La Palma

The *Observatorio del Roque de los Muchachos* (ORM) on La Palma, Canary Islands is a privileged site for astronomical observation. It benefits from exceptionally good sky

Figure 4.6: Low stratus and stratocumulus clouds surround the top of La Palma. The ORM is placed on the edge of the *caldera* (the Spanish word for volcanic hole). Few wispy high cirrus clouds are also visible. Photo: D. Hrupec (March 2003).

conditions [354] and low-altitude clouds generally remain well below the mountain peaks (Figure 4.6). An additional advantage of this fact is the blocking of artificial light sources from populated areas. The average *light of the night sky* (LONS) intensity on La Palma is $(1.7 \pm 0.4) \cdot 10^{12}$ photon $\mathrm{m}^{-2}\mathrm{s}^{-1}\mathrm{sr}^{-1}$ over the wavelength range 300–600 nm [354].

Given the fact that the main emission region of a typical EAS is about 7 km asl and that high altitude clouds are thin and scattered, we decided not to include them in our MC simulations.

Therefore, only mid altitude clouds are left. Altocumulus can be thick, but they are scattered. Therefore, an EAS can go through them or it can miss them. In the first case the picture of an EAS in the camera will be so weak and distorted and such an event will be probably cut in the data analysis. In our opinion, only altostratus clouds are worth to be simulated. For the ORM (2200 m above sea level) very low altostratus (2000 to 3000 m) can be treated as fog and there is no data taking during foggy time. In such a manner we took the height of the base from 3000 to 7000 m. For the La Palma site we mostly used the following values: mean water droplet size 4.5 μm and water droplet concentration of 450 cm^{-3}.

It is worth noting that mid altitude clouds are mostly *water* (no ice) clouds although the temperature is far below 0 °C (see Figure 4.1). However, the pressure is also low (see Figure 4.2) and ice crystals start to form typically at −12 °C and they dominate below −41 °C.

4.3 CORSIKA

COsmic Ray SImulations for KAscade (CORSIKA) is a *Monte Carlo* (MC) program for detailed simulation of the evolution of *extensive air showers* (EAS) initiated by high-energy *cosmic ray* (CR) particles [254]. Primary CR particles may be protons, light nuclei up to iron, γ-rays, and many other particles. All particles in CORSIKA are tracked

through the atmosphere until they decay or interact with the air nuclei.

CORSIKA takes into account all present knowledge of strong and electromagnetic particle interactions.

The hadronic interactions at HE may be described by six models [251]:
VENUS is mainly designed to treat nucleon-nucleon, nucleon-nucleus, and nucleus-nucleus scattering at ultrarelativistic energies. VENUS is based on single or multiple Pomeron[8] exchange. As jets, which become important at extremely HE, are not contained within the model, an upper limit of 20 PeV is recommended.
QGSJET describes hadronic interactions in terms of supercritical Pomeron exchange. QGSJET includes minijets to describe the hard interactions which are important at the highest energies.
DPMJET is based on the two component Dual Parton Model and contains multiple minijets. Interaction are described by multi-Pomeron exchange.
SIBYLL is a minijet model essentially designed for MC simulations of EAS.
HDPM is an alternative model of the interactions between hadrons and nuclei at HE. HDPM is a phenomenological model based on results from $p\overline{p}$-collider experiments.
neXus is obsolete and not supported any more. Today it is replaced by EPOS.

The hadronic interactions at LE can be described by three models [251]:
GHEISHA is the recommended model for LE hadronic interactions. The GHEISHA routines are designed for laboratory energies up to a few hundred GeV.
FLUKA is a fully integrated particle physics MC simulation package for calculations of particle transport and interactions with matter. FLUKA[9] has many applications in HE experimental physics and engineering, shielding, detector and telescope design, CR studies, dosimetry, medical physics and biology.
UrQMD is a microscopic model used to simulate ultra relativistic heavy ion collisions. UrQMD[10] has been used as a component of various hybrid transport approaches, e.g. with CORSIKA for EAS simulations.

For the EM interactions two approaches may be used [253]:
EGS4 is a MC code for doing simulations of the transport of electrons and photons in arbitrary geometries. EGS4[11] was originally developed for HE physics applications and has been extended later to apply for LE applications.
NKG is an approach in which the analytical *Nishimura Kamata Greisen* (NKG) formulas are used.

We have used VENUS, GHEISHA and EGS4 models in the CORSIKA compilation called *MAGIC Monte Carlo software* (Mmcs). Mmcs was prepared and described by Dorota Sobczyńska [441].

[8] The Pomeron is a force-carrying pseudo-particle postulated in 1961 to explain energy behavior of hadronic collisions at HE.
[9] *http://www.fluka.org/*
[10] *http://www.th.physik.uni-frankfurt.de/∼urqmd/*
[11] *http://www.irs.inms.nrc.ca/EGS4/get_egs4.html*

4.4 Čerenkov light in the atmosphere

4.4.1 Čerenkov light production

Introduction

Čerenkov light is the radiation emitted by a dielectric medium[12] when a **charged** particle moves through it at superluminal velocity. The characteristic "blue glow" of pool-type nuclear reactors is Čerenkov light.

It is named after the Russian physicist Pavel A. Čerenkov (1904-1990) who noted the phenomenon and carried out a series of experiments from 1934 to 1938. In 1937, two Russian theorist Ilija M. Frank and Igor J. Tamm explained correctly the origin of Čerenkov radiation. Frank, Tamm and Čerenkov shared the 1958 Nobel Prize "*for the discovery and the interpretation of the Čerenkov effect*".

Characteristics of Čerenkov radiation

When the charged particle passes through the medium the atoms are distorted and they behave like elementary dipoles – a net polarization is induced. The polarization field which surrounds the charged particle is symmetrical at low velocity. There will be no resultant field at large distances and therefore no radiation. On the other hand, if the particle is moving fast, the polarization is no longer completely symmetrical [282]. If *the velocity of the particle is higher than the phase velocity of light in the medium*[13] then the resultant dipole field will be non-zero even at large distances. As a result of coherence, radiation (over a band of frequencies) will be emitted – molecules of the medium are caused to radiate.

It can be understood from the Huygens construction shown in Figure 4.7

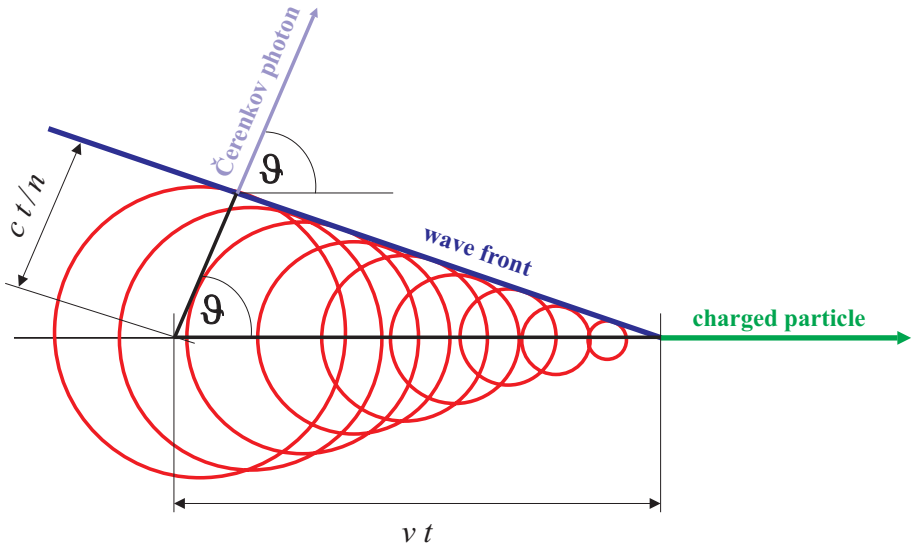

Figure 4.7: Čerenkov light production can be illustrated by using Huygens principle. The Čerenkov angle ϑ is greatly exaggerated. In the atmosphere $\vartheta \approx 1°$.

Figure 4.7 has been drawn in one plane only, but there is naturally complete symmetry around the shower axis. Hence, the Čerenkov cone forms along the particle track. The

[12]The medium is what produces the radiation, not the particle [483].

[13]This is called the Čerenkov condition.

effect is analogous to the sonic boom or a shock wave in acoustics, when an object travels through the air at supersonic speed.

The Čerenkov condition is

$$v_{\text{particle}} > v_{\text{light}} \Rightarrow v > \frac{c}{n} \Rightarrow \beta > \frac{1}{n} \tag{4.4}$$

where n is the refractive index of the medium. Hence, the threshold energy for a charged particle of rest mass m (to emit Čerenkov light) is

$$E_{\text{th}} = \gamma mc^2 = \frac{mc^2}{\sqrt{1-\beta^2}} = \frac{mc^2}{\sqrt{1-\frac{1}{n^2}}} \tag{4.5}$$

Table 4.2 shows the values of the threshold energy for some typical charged particles in the atmosphere. We calculated the threshold energy for sea level as well as for the *Roque de los Muchachos Observatory* (ORM) on La Palma (2200 m asl).

	E_{th} (sea level)	E_{th} (ORM)
proton	38 GeV	47 GeV
charged pion	5.7 GeV	7.0 GeV
muon	4.3 GeV	5.3 GeV
electron	21 MeV	26 MeV

Table 4.2: Threshold energy for typical charged particles in an extended air shower. For sea level we used $n = 1.0003$, and for the ORM site (2200 m asl) we used $n = 1.0002$.

When the condition (4.4) is fulfilled, Čerenkov light appears and propagates with a fixed angle ϑ with respect to the particle direction.

From the geometry in Figure 4.7 it follows

$$\cos\vartheta = \frac{\frac{c}{n}t}{vt} = \frac{1}{n\beta} \tag{4.6}$$

Equation (4.6) is known as **Čerenkov relation**. It shows several important facts [282]:
– There is a threshold velocity $v_{\text{min}} = \frac{c}{n}$ below which no radiation takes place (the Čerenkov condition);
– For ultrarelativistic particle ($\beta \approx 1$), a maximum angle of emission is $\vartheta_{\text{max}} = \cos^{-1}(\frac{1}{n})$;
– The radiation occurs mainly in the visible and near UV region for which $n > 1$. E.g. emission in X-region (where $n < 1$) is impossible.

The spectrum of Čerenkov radiation is continuous and the total amount of energy emitted per unit path (in CGS units) is [282][14]

$$\frac{\mathrm{d}E}{\mathrm{d}l} = \frac{e^2}{c^2}\int(1 - \frac{1}{\beta^2 n(\omega)^2})\omega \mathrm{d}\omega \tag{4.7}$$

where n is an index of refraction of the medium which is frequency dependent. Equation (4.7) is known as the **Frank-Tamm formula**. The total amount of energy that goes into Čerenkov light is very small, a fraction of about 10^{-4}.

[14] Jelley's classical book is still the best reference.

It is usually more useful to express the radiation intensity in terms of the number of photons. Within a spectral region of 300 nm $< \lambda <$ 700 nm, where typical PMTs (with bialkali photocatodes) are sensitive[15], dispersion it the air is so small[16] that $n(\omega) \approx$ const. It leads to an approximation of the number of Čerenkov photons per unit path emitted by an electron within a spectral region $\lambda_1 < \lambda < \lambda_2$

$$\frac{\mathrm{d}N}{\mathrm{d}l} = 2\pi\alpha\left(\frac{1}{\lambda_1} - \frac{1}{\lambda_2}\right)\sin^2\vartheta \tag{4.8}$$

where $\alpha = \frac{e^2}{\hbar c} = \frac{1}{137}$ is the fine structure constant and n is the average refractive index of the medium.

Within the spectral region mentioned above (300 nm $< \lambda <$ 700 nm) the number of Čerenkov photons, emitted by one electron near the ground, is about 45 per meter (or, more generally, about 10^4 per radiation length [483]).

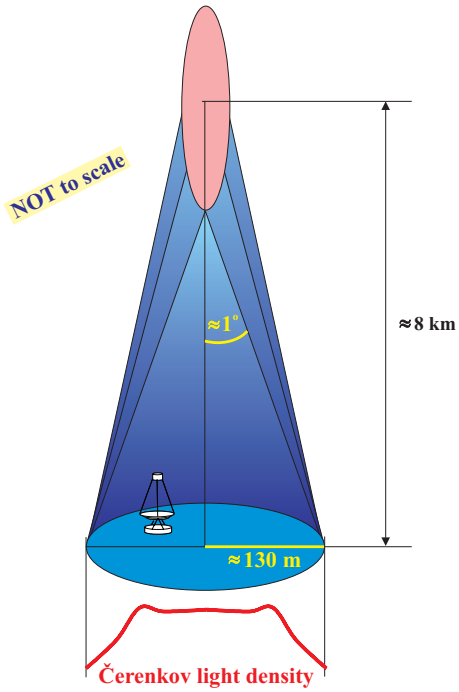

Figure 4.8: Čerenkov light pool of a typical EAS covers about 10^5 m^2. It is an effective detection area of an IACT. When the IACT is anywhere inside the lightpool, it can detect an EAS. The observed Čerenkov light comes from nearly the entire region of the EAS.

Applications of Čerenkov radiation

Applications in high energy physics experiments began since 1951 when J.V. Jelley detected single fast charged particles with high efficiency using distilled water and a PMT [282]. Today, a very common use of Čerenkov radiation are *ring imaging Čerenkov* (RICH)[17] detectors, which are used for *particle identification* (PID).

[15] At 290-300 nm is ozone cutoff. At 600-700 nm is the sensitivity limit of PMTs.

[16] E.g. at standard conditions in the air n(400 nm) = 1.000299 and n(700 nm) = 1.000292.

[17] RICH was proposed and developed by Tom Ypsilantis (1928-2000). It was a great pleasure for me to work with him at CERN in 1997.

In 1953, Jelley and Galbraith observed first Čerenkov light pulses from the night sky and then in 1965, the Crimean group led by Čudakov was the first one to seriously search for Čerenkov detection of EAS. A more detailed historical review of applications of Čerenkov light in VHE γ-ray astronomy is given in Section 1.2.

Due to the small refractive index of air ($n \approx 1.0003$ at sea level and $n \approx 1.0002$ at 2200 m asl) the Čerenkov angle is small – about 1° (reaching 1.3° at sea level). Hence, Čerenkov light is strongly collimated and the corresponding light pool at the ground is typically 130 m in radius (Figure 4.8).

For a 1 TeV primary γ-ray, there are about 100 Čerenkov photons per square meter at the ground, but that is enough for IACT to observe an event (a flash of Čerenkov light corresponding to a primary CR or γ-ray).

4.4.2 Čerenkov light attenuation

The attenuation of Čerenkov light in the atmosphere occurs both due to *absorption* and *scattering*.

In the wavelength region of our interest (290 to 600 nm), the absorption of light by ozone is the dominant absorption process. In the UV region there are strong absorption bands (Hartley, 200–300 nm), and the weak bands (Huggins, 300–360 nm). There are also weak bands (Chappius) in visible and near IR [316].

Many strong absorption lines of H_2O, and a few of O_2 and CO_2 also exist, but all of them are in the IR region (e.g. 3.5–4.2 μm and 8–12 μm), out of our interest. Therefore, most of the wavelength range of our interest is *absorption free*.

Scattering is the process by which small particles suspended in the atmosphere diffuse a part of incident radiation. No energy transformation results, only a change in the spatial distribution of radiation. Two scattering processes are important for Čerenkov light in the atmosphere: the Rayleigh scattering by molecules in the atmosphere and the *Mie scattering* by aerosols[18], haze[19] and clouds.

Both processes will be treated in detail later in Section 4.7.1. The types and properties of the particles that cause the scattering of light in the atmosphere are listed in Table 4.3. In clouds, scattering plays the dominant role.

particle	**radius**	**number density** (cm^{-3})
air molecule	≈ 1 Å	$2.7 \cdot 10^{19}$
aerosol	≈ 1 μm	5–100
cloud water droplet	≈ 10 μm	50–500
cloud ice crystal	≈ 100 μm	≈ 0.1
raindrop	≈ 1 mm	$\approx 5 \cdot 10^{-4}$

Table 4.3: Particles responsible for atmospheric scattering of *electromagnetic* (EM) waves [316] [456]. Fog is ground-based cloud, but its density can be much higher than 500 cm^{-3}. An extremely thick fog can reach even 100 000 cm^{-3}.

[18] Small particles, either solid or liquid, suspended in the atmosphere which cause atmospheric extinction.

[19] Haze consists of fine dust or salt particles dispersed through the atmosphere.

4.4.3 Čerenkov light detection

A simple but fast[20] light detector (mirror + PMT + FADC) is enough for the detection of Čerenkov light pulses from EAS.

Figure 4.9 shows the evolution of Čerenkov spectra of 1 TeV γ-ray initiated EAS. The violet curve is the original spectrum of Čerenkov photons from the MAGIC MC

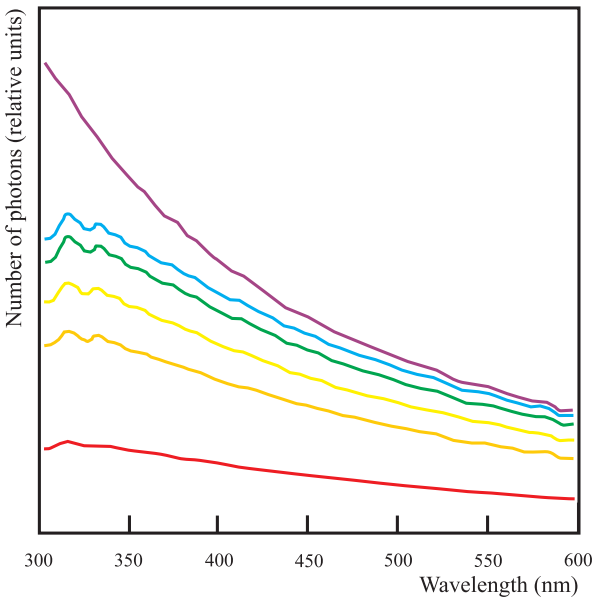

Figure 4.9: The results of the MAGIC Monte Carlo simulation of the evolution of the spectral shape from the original Čerenkov spectrum (violet), to the light actually detected in the camera (red). Source of data: [98].

simulations [98]. The blue curve shows the spectrum after transmission through the atmosphere. The spectrum is distorted due to Rayleigh scattering which is strongly wavelength dependent as

$$I(x) = I_{\mathrm{o}} \exp(-\beta x) \tag{4.9}$$

$$\beta = \frac{32\pi^3(n-1)^2}{3N} \cdot \frac{1}{\lambda^4} \tag{4.10}$$

where β is the attenuation coefficient, N is the air molecule density ($2.7{\cdot}10^{19}$ at sea level), and n is the refractive index of air (1.00029 at sea level).

The green curve shows the intensity changes due to the photon loss in the gaps between the mirrors. The yellow and the orange curves show changes in the intensity due to mirror reflectivity and light guide efficiency, both assumed to be 90%. Finally, the red curve includes the QE of photodetectors.

[20] Čerenkov light flash lasts a few nanoseconds only.

4.5 Monte Carlo simulations of extended air showers

4.5.1 The Isabella cluster

MC simulations of EAS require a large amount of CPU time. Therefore computing center resources are favorable [252]. We have used the Isabella cluster[21] at the Computing Center called SRCE in Croatia.

Isabella was founded in 2002 in order to allow Croatian experts to participate in the European DataGrid Project which was initiated by CERN. Today, Isabella is a shared resource of all Croatian scientists.

The cluster consists of 95 computers with 264 processors. It has 448 GB of RAM and more than 8 TB of local disk space.

4.5.2 Visualization of showers

Figures 4.10, 4.11, 4.12, and 4.13 are images of *extensive air showers* (EAS) created in the atmosphere by a primary cosmic $\gamma-$ray or proton. We generated these images using the CORSIKA program [253] (version 6.6 released on April 20, 2007) with *PLOTSH* option and Fortran code *plottracks3c* (both developed at the University of Leeds). All figures contain 3D particle tracks, as traced by CORSIKA, projected onto planes. There are x-z and x-y projections where x and y are coordinates on the ground and z is vertical. The ranges are $\pm$ 5 km around the shower core and 0 to 25.1 km in the vertical.

We chose the primary $\gamma-$ray energy to be 100 GeV and the primary proton energy 300 GeV (hadron initiated EAS have to have about three times greater primary energy to produce an equal amount of Čerenkov light). First interaction height was fixed at 25 km.

Particle type is encoded in track color: red (EM components: electrons, positrons and secondary γ-rays), green (muons), and blue (hadrons). Color scale is logarithmic, color value = log(1 + number of tracks), where white color, in the center of an image, corresponds to high track density. Colors are mixed – an intersection of a red track and a green track gives a yellow pixel.

Only tracks of particles with kinetic energy above the **cut** are plotted. We chose two energy cut values:

• 0.1 MeV for EM components and 0.1 GeV for muons and hadrons (Figures 4.10 and 4.12), as on web page *http://www.ast.leeds.ac.uk/∼fs/showerimages.html*;

• 26 MeV for EM components, 5.3 GeV for muons and 47 GeV for hadrons (Figures 4.11 and 4.13), as threshold energy[22] for the emission of Čerenkov light (Table 4.2).

[21] *http://isabella.srce.hr/*

[22] The threshold energy increase with altitude. Here we used a single value for 2200 m above sea level.

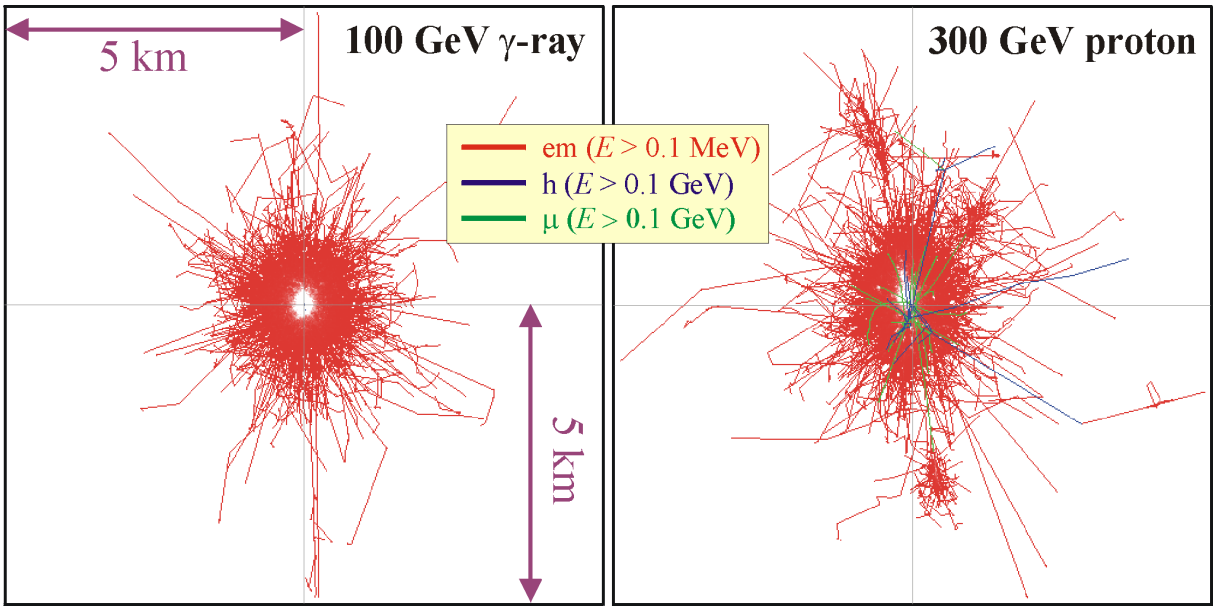

Figure 4.10: Horizontal (x–y) projection of an EAS initiated by a 100 GeV γ-ray (left) and a 300 GeV proton (right). The incident angle of the primary particle is 0° and the first interaction occurs at 25 km asl. The energy cut is 0.1 MeV for EM components and 0.1 GeV for muons and hadrons.

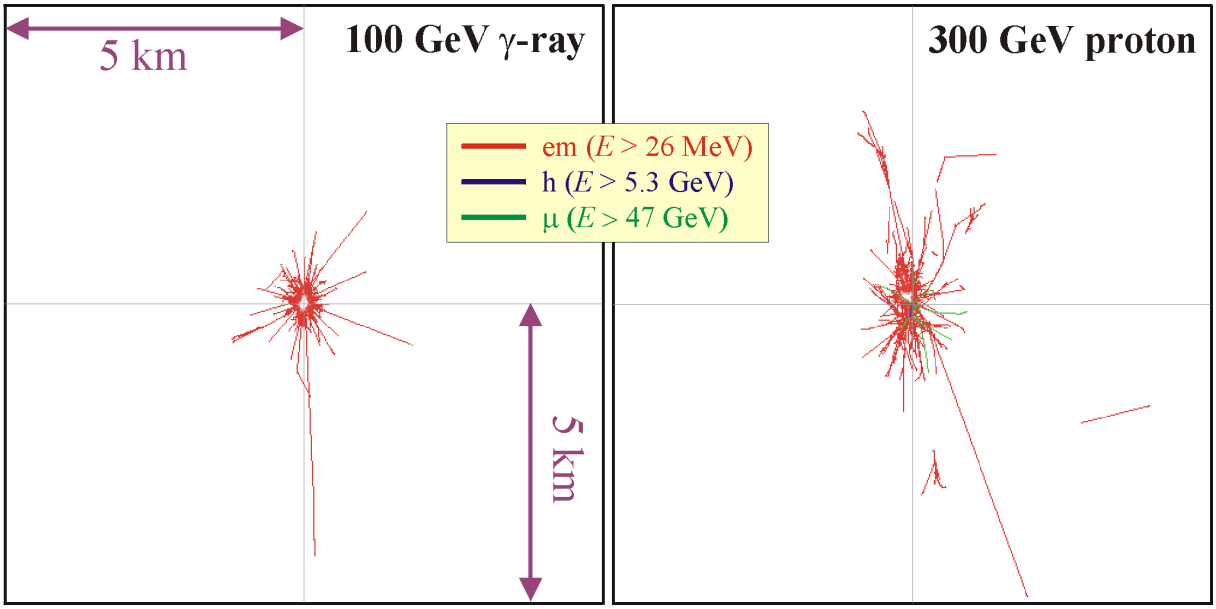

Figure 4.11: The same two showers as in Figure 4.10, but here we chose a more restrictive energy cut: 26 MeV for EM components, 5.3 GeV for muons, and 47 GeV for hadrons.

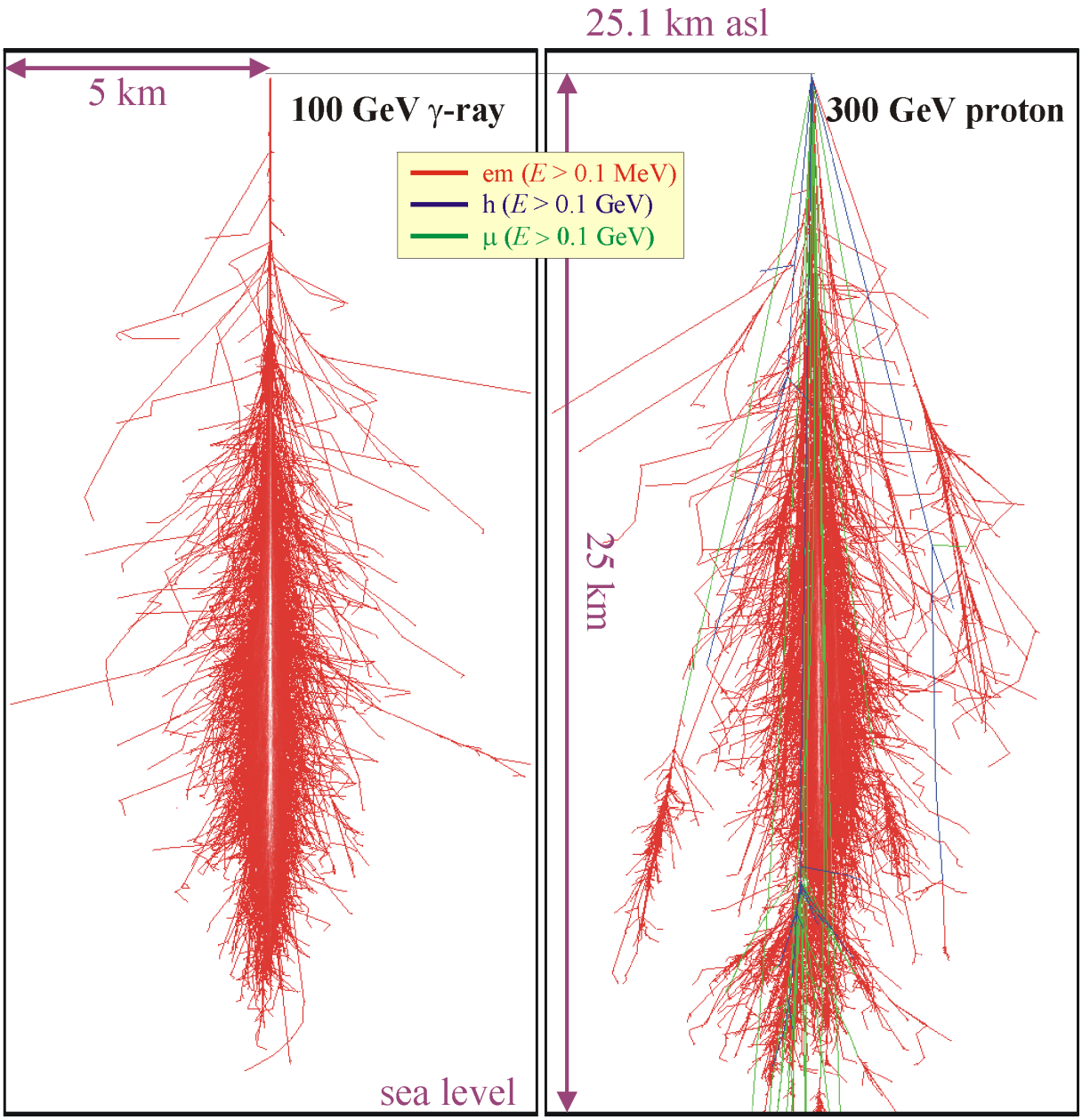

Figure 4.12: Vertical (x–z) projection of an EAS initiated by a 100 GeV γ-ray (left) and a 300 TeV proton (right). The incident angle of the primary particle is 0° and the first interaction occurs at 25 km asl. The energy cut is 0.1 MeV for EM components and 0.1 GeV for muons and hadrons.

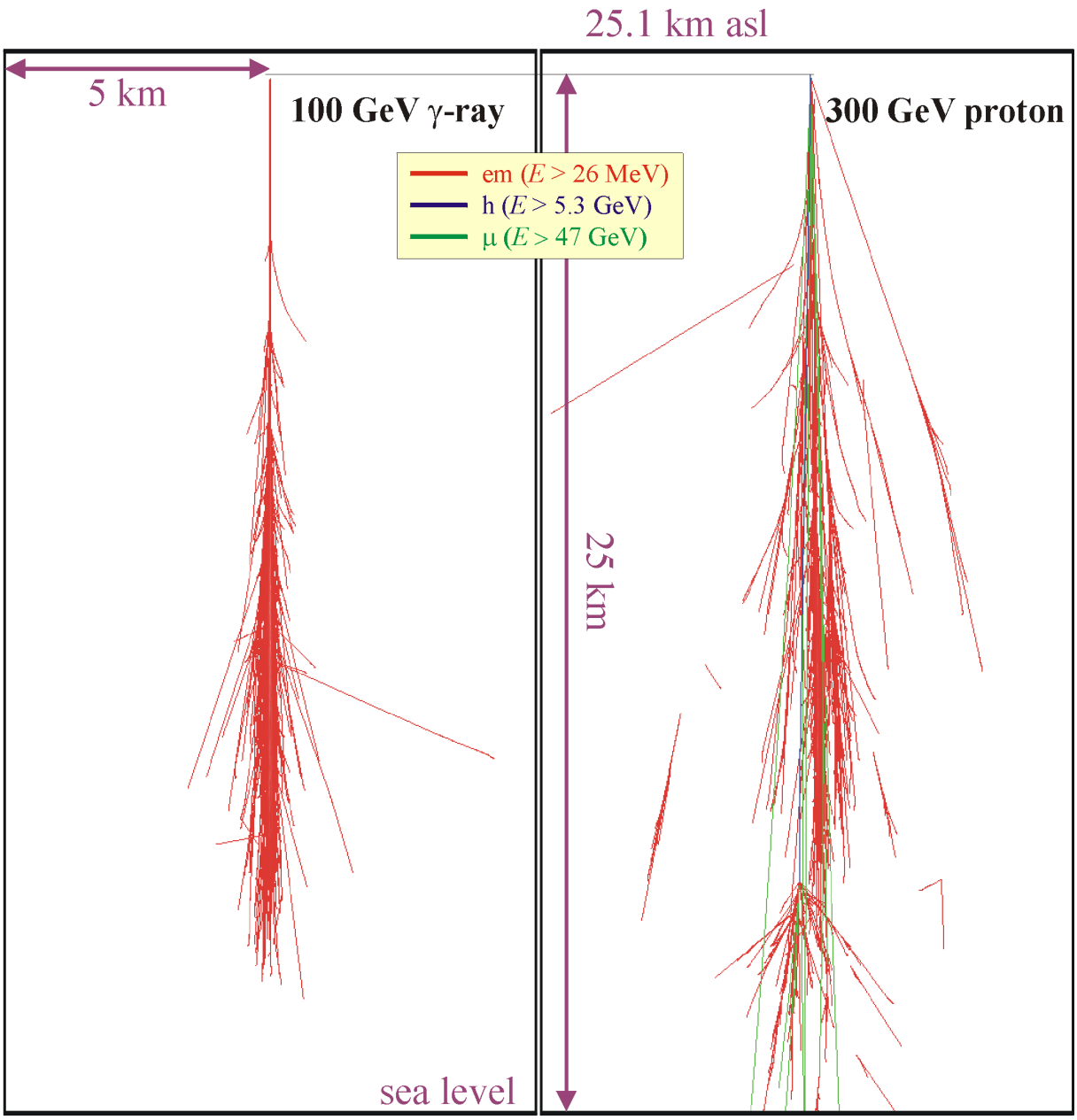

Figure 4.13: The same two showers as in Figure 4.12, but here we chose a more restrictive energy cut: 26 MeV for EM components, 5.3 GeV for muons, and 47 GeV for hadrons.

4.6 The detector simulation

In order to accurately calculate source fluxes and energy spectra, it is necessary to develop a detailed model of the telescope performance, to which simulated EAS are presented such that the telescope detection efficiencies can be calculated [266].

Hence, MC simulations of IACT experiments in the field of ground-based γ-ray astronomy consist of two main parts: EAS simulations and the detector (reflector and camera) simulation as shown in Figure 4.14.

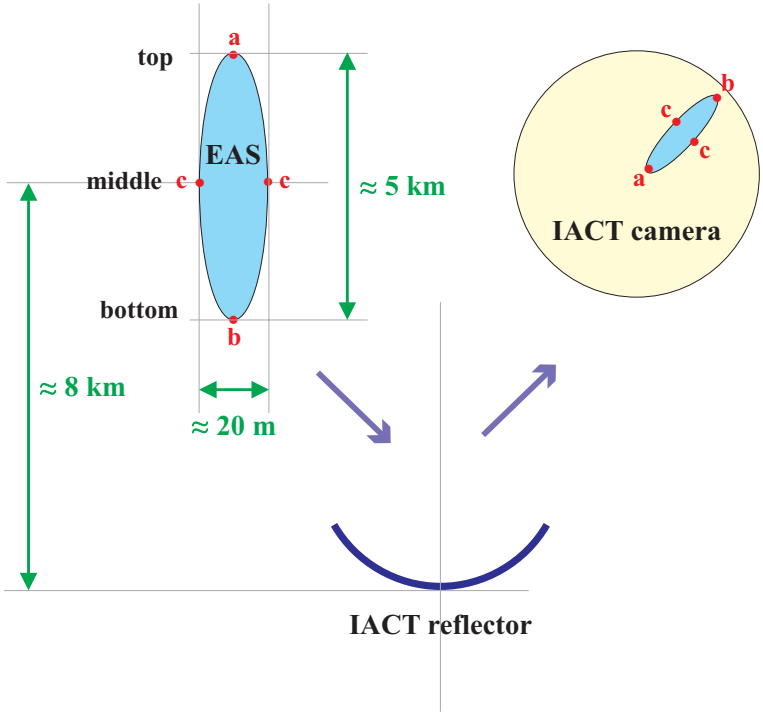

Figure 4.14: The geometry of the Čerenkov light image in an IACT camera from a γ-ray induced EAS.

First part is the same for all IACTs (even for the all experiments in related fields e.g. particle air shower arrays, fluorescence experiments, solar power stations, and extragalactic neutrino experiments). Most of astroparticle physics experiments have used CORSIKA to simulate EAS.

Second part, the detector simulation, describes specific detector characteristics. Therefore, it is developed by each experimental group itself. We have used slightly modified MAGIC's programs: the Reflector and the Camera.

4.6.1 The reflector simulation

The Reflector program (version 0.6) was released in December 2002 [360]. The program was originally written by Jose Carlos González and then improved by Harald Kornmayer. The recent version is significantly modified by Abelardo Moralejo. He was very kind to help us explain how to use and modify the program. The Reflector reads CORSIKA output and writes its own output which is input for the Camera program. The Reflector's output is a file with the information about all Čerenkov photons from EAS which reach the telescope focal plane. The MAGIC telescope geometry (3D location of each mirror

and its focal length) is defined in the file **magic.def**. We defined CT1 reflector geometry, **CT1.def**, in the manner of the MAGIC. The main steps of the simulation are [360]:

- Atmospheric attenuation (including Rayleigh scattering, Mie scattering and ozone absorption);
- Checking if the Čerenkov photon hits the dish;
- Mirror absorption;
- Determination if the mirror was hit;
- Mirror reflection;
- Checking if the photon is inside the camera border;
- Calculation of the photon arrival time into the camera.

4.6.2 The camera simulation

The camera simulation is the last step in the simulation chain. We have used the *Camera simulation program 0.7* which has been written by Oscar Blanch and Abelardo Moralejo and released in September 2004. The program was originally written by Jose Carlos González and then improved by many authors [131]. It is able to process files created with the *Reflector simulation program*. The output of the program is in the same format as real telescope data.

The camera program simulates the camera of a Čerenkov telescope (e.g. MAGIC or CT1) and corresponding electronics. That means the geometry of the front of the camera including all photomulipliers (Figure 3.4) and the behavior of the trigger and flash analog to digital converter (FADC) or equivalent system. The behavior of the *night sky background* (NSB) can also be included in the simulation.

For the visualization of the output of the Camera program We have used MARS and STAR. *MAGIC Analysis and Reconstruction Software* (MARS) is a software package developed for use with the MAGIC telescope. It is based on C++ and ROOT. *STandard Analysis and Reconstruction* (STAR) is a program to calculate image parameters. STAR is part of MARS.

Figures 4.15 and 4.16 show examples of typical images in the CT1 camera which we generated using our MC data as well as the MARS software.

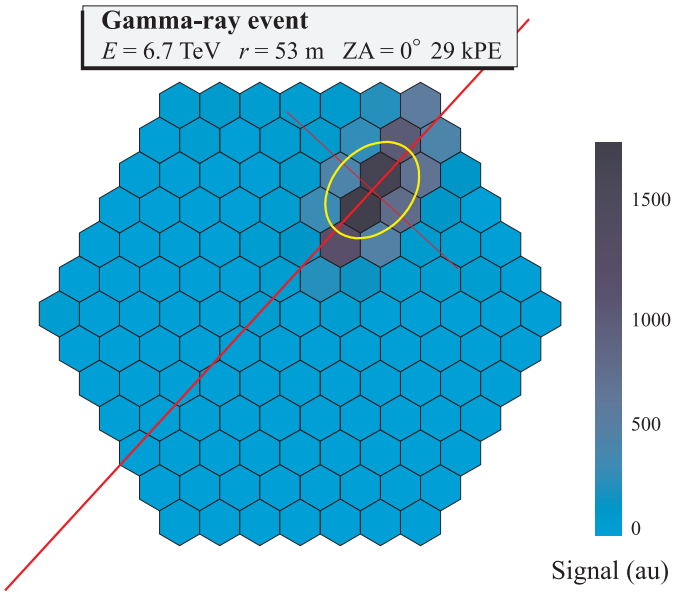

Figure 4.15: An example of an EAS image in the CT1 camera induced by a **gamma-ray**. The event is MC generated and the figure is produced using MARS.

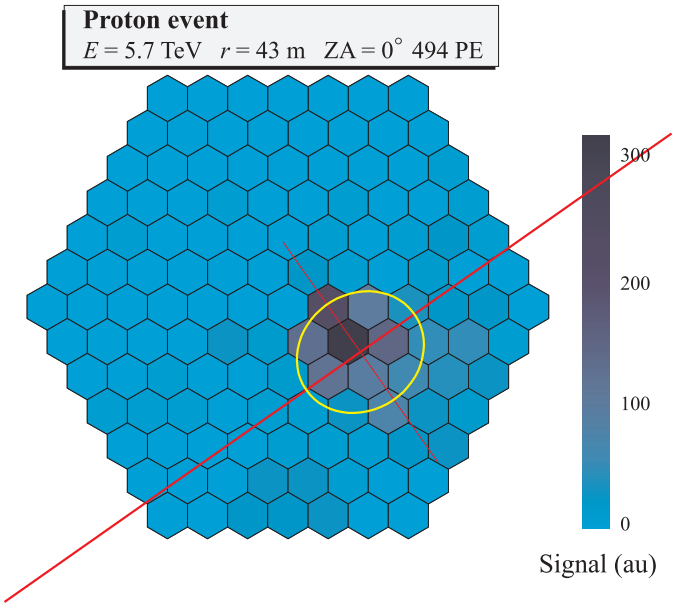

Figure 4.16: An example of an EAS image in the CT1 camera induced by a **proton**. The event is MC generated and the figure is produced using MARS.

4.7 Variable atmospheric transparency for Čerenkov light

4.7.1 Attenuation of Čerenkov light in the atmosphere

Geometry of the problem

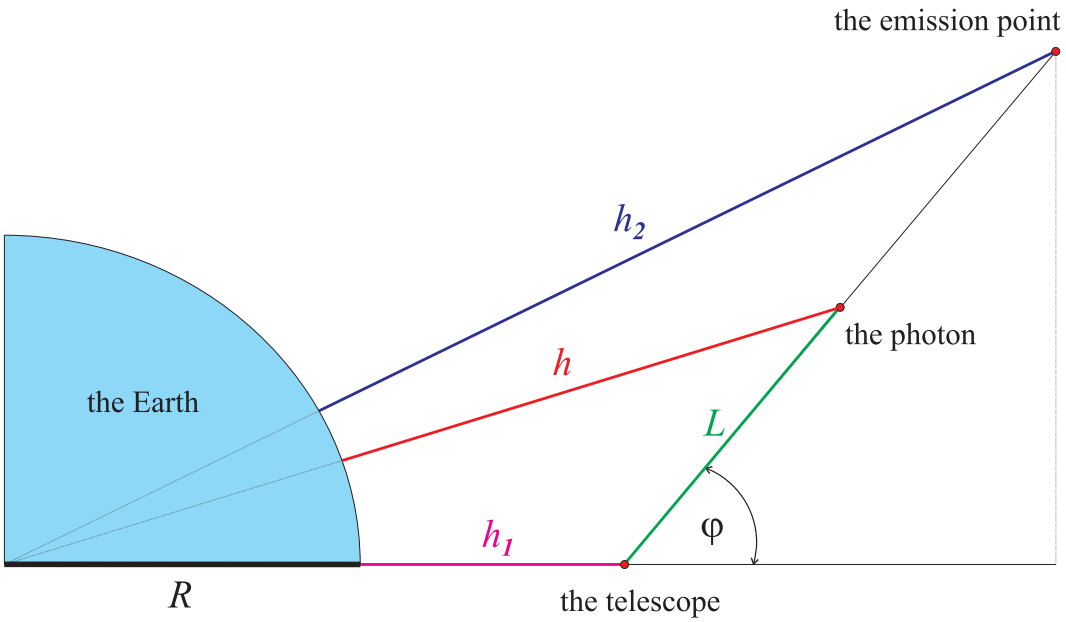

Figure 4.17: Geometry of a Čerenkov photon trajectory and relevant heights above sea level.

At a given time, h is the height of a Čerenkov photon above sea level (asl), and L is the distance between the photon and the telescope. φ is the zenith angle (ZA) of the photon trajectory *measured at the telescope site*, and h_1 is the height of the observation level[23]. h_2 is the true vertical height of the emission point, and R is the radius of the Earth. From Figure 4.17 it follows

$$(R+h)^2 = (R+h_1)^2 + L^2 - 2(R+h_1)L\cos(180-\varphi). \tag{4.11}$$

The mean radius of the Earth $R = 6370$ km, and the typical height of the emission point h is about 10 km. Therefore,

$$\frac{h}{R} \ll 1, \tag{4.12}$$

and finally we have

$$L = -2(R+h_1)\cos\varphi + \sqrt{(R+h_1)^2\cos^2\varphi + 2R(h-h_1)}, \tag{4.13}$$

and

$$\frac{dL}{dh} = \frac{R}{\sqrt{(R+h_1)^2\cos^2\varphi + 2R(h-h_1)}}. \tag{4.14}$$

[23] $h_1 = 2200$ m for CT1 at ORM.

Rayleigh scattering of light

Rayleigh scattering is the scattering of light by particles *smaller* than its wavelength. In the atmosphere such particles are air molecules with a typical size of 0.2 nm. The wavelengths of Čerenkov light, detectable by the *photomultipliers* (PMT) of the CT1 camera, range from 290 nm to 600 nm. Therefore

$$\frac{d_{\text{AIR MOLECULE}}}{\lambda_{\text{ČERENKOV}}} \simeq 10^{-3} \tag{4.15}$$

The **transmission factor** for Rayleigh scattering T_{R} is

$$T_{\mathrm{R}} = \exp(-\tau_{\mathrm{R}}), \tag{4.16}$$

where τ_{R} is the **optical depth** (in general, $\tau_{\mathrm{R}} = \beta_{\mathrm{R}} \cdot x$ where β_{R} is the attenuation coefficient)

$$\tau_{\mathrm{R}} = \frac{I(\varphi, h_1, h_2)}{x_{\mathrm{R}}} \left(\frac{400 \text{ nm}}{\lambda}\right)^4. \tag{4.17}$$

Therefore, Rayleigh scattering depends strongly on wavelength. This explains the blue sky, and the fact that objects near the horizon appear redder[24] at sunset.
The mean free path of Rayleigh scattering at $\lambda = 400$ nm is $x_{\mathrm{R}} = 2970$ g/cm^2.

The **optical path** $I(\varphi, h_1, h_2)$ (in g/cm^2) is a product of the atmospheric density and physical path. E.g. for horizontal path at sea level, the density is constant and the optical path is simply

$$I = \rho_{\mathrm{o}} x. \tag{4.18}$$

The attenuation coefficient β_{R} in such a case can be derived as

$$\beta_{\mathrm{R}} = \frac{32\pi^3 (n-1)^2}{3N} \cdot \frac{1}{\lambda^4} \tag{4.19}$$

where N is the air molecule density ($2.7{\cdot}10^{19}$ cm^{-3} at sea level), and n is the refractive index of air (1.00029 at sea level). Lord Rayleigh derived this inverse-fourth-power-law in order to show that the blue sky could be explained as scattering by small particles[25].

More generally, for an inclined path

$$\mathrm{d}I(\varphi, h_1, h_2) = \rho(h)\mathrm{d}L = \rho(h)\frac{\mathrm{d}L}{\mathrm{d}h}\mathrm{d}h. \tag{4.20}$$

From equation (4.14)

$$\mathrm{d}I(\varphi, h_1, h_2) = \rho(h)\frac{R}{\sqrt{(R+h_1)^2 \cos^2\varphi + 2R(h-h_1)}}\mathrm{d}h. \tag{4.21}$$

A simple atmospheric model is accurate enough for our purpose [360]:

$$\rho = \rho_{\mathrm{o}} \exp(-h/H) \tag{4.22}$$

[24]The phenomenon of selective absorption is also called *reddening*. In astronomy, extinction usually refers to reddening and dimming of light as it passes through gas and dust.

[25]Rayleigh's original paper (Phil. Mag. **41** (1871) 107-120) was published before Maxwell's theory and before it was clear that small particles were air molecules. Rayleigh later re-derived the same result from EM theory.

where $H = 7.4$ km, and $\rho_o = 1.1919$ kg/m^3. Finally, we obtain

$$T_R = \exp\left[-\left(\frac{400\text{ nm}}{\lambda}\right)^4 \frac{\rho_o}{x_R}\int_{h_1}^{h_2} \frac{R\exp\left(-h/H\right)}{\sqrt{(R+h_1)^2\cos^2\varphi + 2R(h-h_1)}}\mathrm{d}h\right]. \tag{4.23}$$

The emission height asl h_2, and ZA φ are parameters obtained from CORSIKA simulations for each Čerenkov photon. We have used $h_1 = 2200$ m for the CT1 observation level, and $R = 6371.315$ km for the radius of the Earth (the same value as used in the CORSIKA). For numerical calculation of (4.23), we have used the Reflector program [360].

Mie scattering of light

Mie scattering[26] is the scattering of light by spherical, dielectric particles of any size. In the atmosphere particles are small dust particles suspended in air (**aerosols**) or small water droplets (**cloud**). These particles are *comparable or larger* than the wavelength of Čerenkov light. The typical size of water droplets in cloud is 10 μm. Therefore

$$\frac{d_{\text{WATER DROPLET}}}{\lambda_{\text{ČERENKOV}}} \simeq 10. \tag{4.24}$$

Both scattering and absorption of EM waves by spherical water droplets can be exactly computed by the Mie theory[27], which is a complete formal theory describing the interaction of a plane EM wave with a dielectric sphere [316]. The Mie theory is important in meteorological optics e.g. for haze and **clouds** [456].

Mie scattering is almost independent on wavelength in the visible range. We will treat it in detail later, in Section 4.7.2.

Ozone absorption of light

The **transmission factor** for ozone absorption T_o is

$$T_o = \exp(-\tau_o), \tag{4.25}$$

where τ_o is the **optical depth**

$$\mathrm{d}\tau_o = \beta_o(h,\lambda)\mathrm{d}L = \beta_o(h,\lambda)\frac{\mathrm{d}L}{\mathrm{d}h}\mathrm{d}h. \tag{4.26}$$

We have used Elterman's model in the Reflector program [360] for ozone absorption. The **absorption coefficient** β_o can be expressed as a product of the Vigroux ozone absorption coefficient $A_v(\lambda)$ (in cm^{-1}) and the ozone concentration $D(h)$ (dimensionless)

$$\beta_o(h,\lambda) = A_v(\lambda)D(h). \tag{4.27}$$

Finally,

$$T_o = \exp\left[-A_v(\lambda)\int_{h_1}^{h_2} D(h)\frac{R}{\sqrt{(R+h_1)^2\cos^2\varphi + 2R(h-h_1)}}\mathrm{d}h\right] \tag{4.28}$$

where h_2 is the emission height asl, and φ is ZA. These parameters are obtained from CORSIKA for each Čerenkov photon. $h_1 = 2200$ m is the CT1 observation level, and $R = 6371.315$ km is the value we have used for the radius of the Earth.

Tables 4.4 and 4.5 show Vigroux ozone absorption coefficients and ozone concentrations that we have used for the numerical integration of (4.28).

[26] It is named after the German physicist Gustav Mie (1868–1957).

[27] Original Mie's paper in German: Ann. Physik **25** (1908) 377–445.

λ (nm)	280	300	320	340	360	380	400	450	500	550	600	650
A_{v} (cm^{-1})	106	10.1	0.898	0.064	0.0018	0	0	0.0035	0.035	0.092	0.132	0.062

Table 4.4: Vigroux ozone absorption factors as used in the Reflector program.

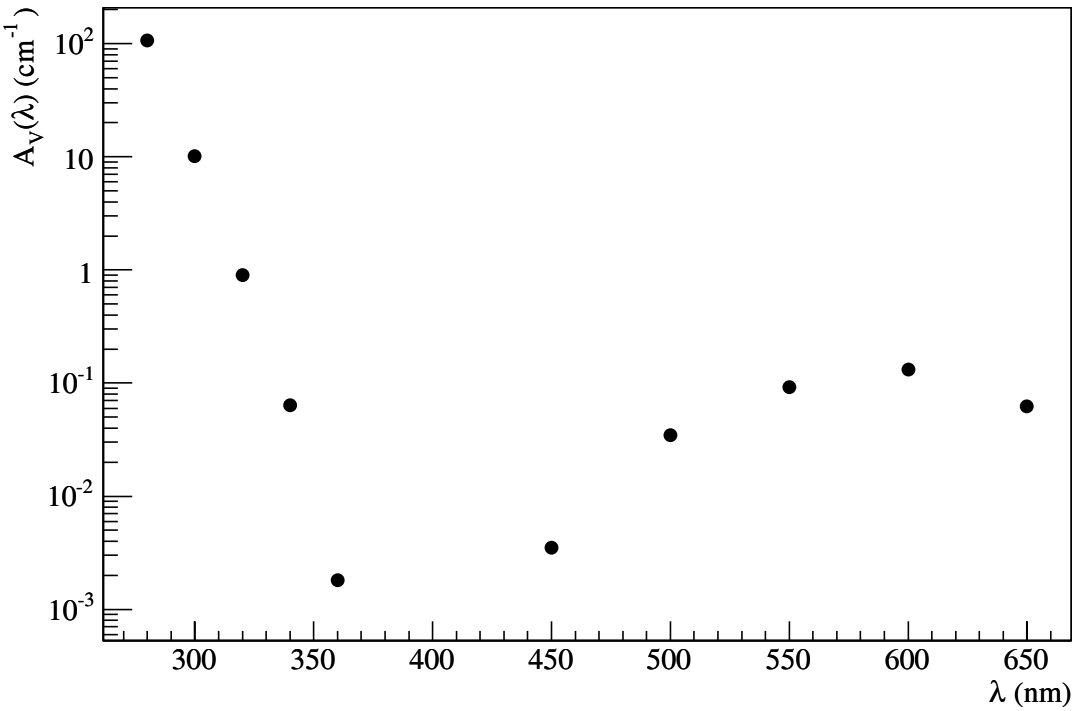

Figure 4.18: Vigroux ozone absorption factor $A_{\mathrm{V}}(\lambda)$ from Table 4.4.

h (km)	0	1	2	3	4	5	6	7	8	9	10
$D(h) \cdot 10^8$	3.557	3.264	2.934	2.500	2.264	2.208	2.160	2.226	2.283	2.811	3.500
h (km)	...	11	12	13	14	15	16	17	18	19	20
$D(h) \cdot 10^8$	...	4.603	6.208	8.453	9.528	9.906	10.28	11.13	12.17	14.25	16.42
h (km)	...	21	22	23	24	25	26	27	28	29	30
$D(h) \cdot 10^8$	...	18.39	19.72	19.81	19.34	18.02	16.32	14.06	12.26	10.66	9.028
h (km)	...	31	32	33	34	35	36	37	38	39	40
$D(h) \cdot 10^8$	...	7.933	6.830	5.821	4.830	4.311	3.613	3.019	2.528	2.170	1.858
h (km)	...	41	42	43	44	45	46	47	48	49	50
$D(h) \cdot 10^8$	...	1.518	1.189	0.930	0.744	0.576	0.446	0.352	0.279	0.223	0.186

Table 4.5: Ozone concentration $D(h)$ as used in the Reflector program [360].

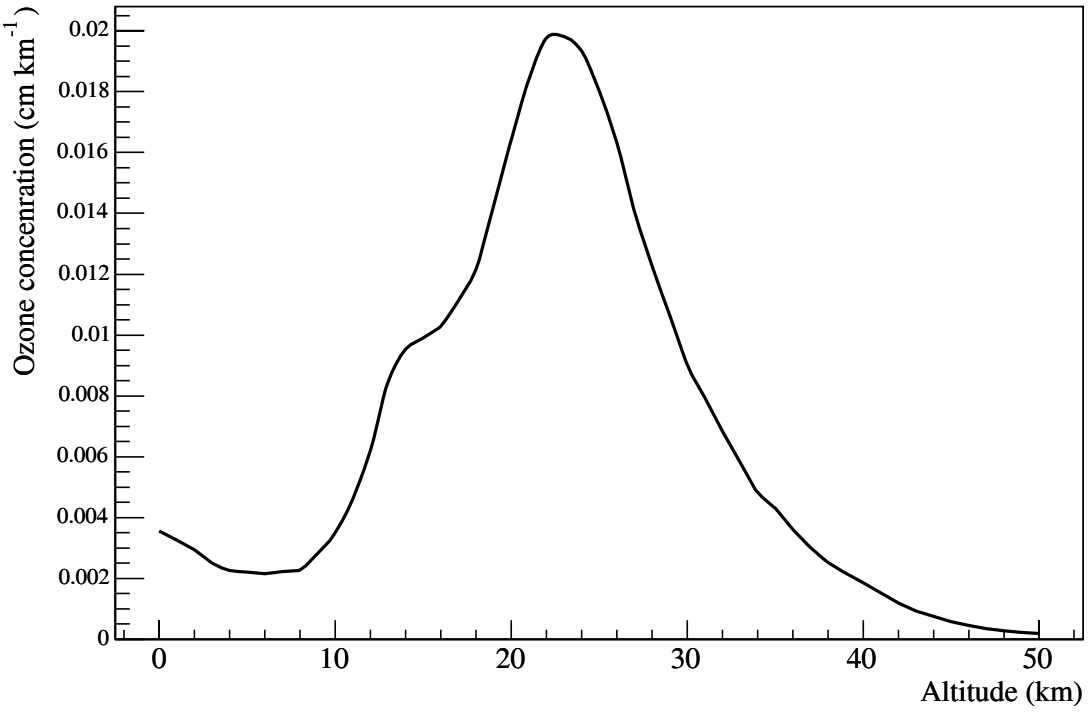

Figure 4.19: Ozone concentration $D(h)$ from Table 4.5.

4.7.2 VAT simulations

The **transmission factor** for the Mie scattering T_{M} is

$$T_{\mathrm{M}} = \exp(-\tau_{\mathrm{M}}), \tag{4.29}$$

where τ_{M} is the aerosol **optical depth** of the path from *the emission point* to *the observation point* (or *the telescope* as denoted in Figure 4.17). One can write the transmission factor as ratio of intensity of transmitted light I and intensity of incident light I_{o}

$$T = I/I_{\mathrm{o}}. \tag{4.30}$$

On the other hand, the optical depth can be expressed as a product[28] of the physical path x and the **attenuation coefficient** or extinction coefficient β

$$\tau = \beta x. \tag{4.31}$$

Therefore, the equation (4.29) can be rewritten in the form known as Bouguer's law or Beer's law or Lambert's law

$$I = I_{\mathrm{o}} \exp(-\beta x). \tag{4.32}$$

The law is experimentally established by Bouguer, applied later by Beer and re-discovered by Lambert. It describes the rate of decrease of the flux of a plane-parallel beam of monochromatic radiation as it penetrates a medium which both scatters and absorbs.

Equation (4.31) is true if β is independent of the path e.g. for horizontal path at sea level. More generally, e.g. for a vertical path

$$\mathrm{d}\tau = \beta \mathrm{d}x. \tag{4.33}$$

The attenuation coefficient β is the product of the number density N and the total cross section σ

$$\beta = N\sigma. \tag{4.34}$$

For Mie scattering in the atmosphere, the aerosol number density depends only on the altitude h, and the cross section depends only on the wavelength λ. Therefore, (4.34) for any level is

$$\beta(h, \lambda) = N(h)\sigma(\lambda), \tag{4.35}$$

and (4.34) for sea level

$$\beta(0, \lambda) = N(0)\sigma(\lambda). \tag{4.36}$$

From (4.35) and (4.36) we can obtain

$$\beta(h, \lambda) = \beta(0, \lambda)\frac{N(h)}{N(0)}. \tag{4.37}$$

This formula is very important for practical purposes. The attenuation coefficient can be easily measured at sea level for the horizontal path. We have used the measured values $\beta(0, \lambda)$ for 12 wavelength [198] as shown in Table 4.6 and Figure 4.20. The attenuation coefficient does not depend much on wavelength (in the range of our interest, 300-600 nm, it varies by less than a factor two).

[28] Assuming $\mathrm{d}\beta/\mathrm{d}x = 0$, otherwise $\tau = \int \beta(x)\mathrm{d}x$.

λ (nm)	280	300	320	340	360	380	400	450	500	550	600	650
$\beta(0,\lambda)$ (km^{-1})	0.27	0.26	0.25	0.24	0.24	0.23	0.2	0.18	0.167	0.158	0.15	0.142

Table 4.6: Spectral aerosol attenuation coefficients at sea level. Source of data: [198].

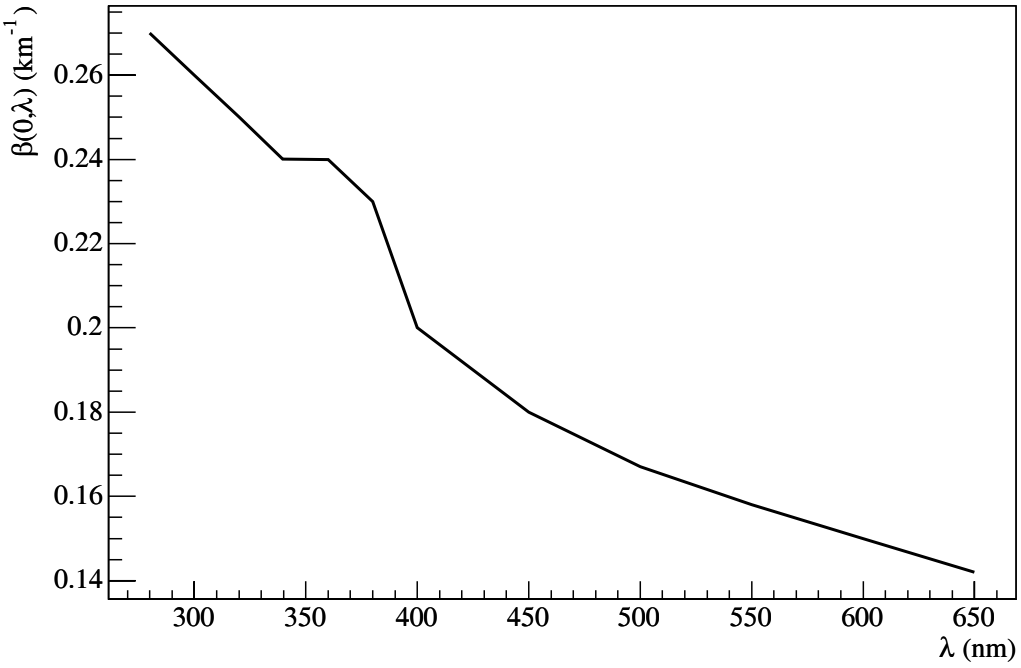

Figure 4.20: Spectral aerosol attenuation coefficients from Table 4.6.

For the **aerosol number density**, we have used a model proposed by Elterman [198]. The aerosol number density decreases exponentially with altitude, from sea level up to 10 km:

$$N = N_{\mathrm{o}} \exp(-h/H) \tag{4.38}$$

where $N_{\mathrm{o}} = 200$ cm^{-3} and $h = 1.2$ km. The overall density distribution is not a simple exponential, therefore we have to calculate the optical depth τ_{M} using numerical integration.

For an inclined path we have to substitute $\mathrm{d}x$, in equation (4.33), with $\mathrm{d}L$

$$\mathrm{d}\tau_{\mathrm{M}} = \beta(h,\lambda)\mathrm{d}L. \tag{4.39}$$

$$\mathrm{d}\tau_{\mathrm{M}} = \beta(h,\lambda)\frac{\mathrm{d}L}{\mathrm{d}h} \cdot \mathrm{d}h. \tag{4.40}$$

From (4.14) and (4.37), we obtain

$$\mathrm{d}\tau_{\mathrm{M}} = \beta(0,\lambda)\frac{N(h)}{N(0)}\frac{\mathrm{d}L}{\mathrm{d}h} \cdot \mathrm{d}h, \tag{4.41}$$

$$\mathrm{d}\tau_{\mathrm{M}} = \beta(0,\lambda)\frac{N(h)}{N(0)}\frac{R}{\sqrt{(R+h_1)^2\cos^2\varphi + 2R(h-h_1)}}\mathrm{d}h. \tag{4.42}$$

Finally, the optical depth $\tau_{\rm M}$ for Mie scattering is

$$\tau_{\rm M} = \frac{\beta(0,\lambda)}{N(0)} \int_{h_1}^{h_2} N(h) \frac{R}{\sqrt{(R+h_1)^2 \cos^2\varphi + 2R(h-h_1)}} {\rm d}h, \tag{4.43}$$

and the transmission factor for Mie scattering $T_{\rm M}$ is

$$T_{\rm M} = \exp\left(-\frac{\beta(0,\lambda)}{N(0)} \int_{h_1}^{h_2} N(h) \frac{R}{\sqrt{(R+h_1)^2 \cos^2\varphi + 2R(h-h_1)}} {\rm d}h \right). \tag{4.44}$$

The emission height h_2, and ZA φ are parameters obtained from CORSIKA for each Čerenkov photon. $h_1 = 2200$ m is the CT1 observation level, and $R = 6371.315$ km is the value we have used for the radius of the Earth (the same value as used in CORSIKA).

We have used the linear interpolation of data from the Tables 4.6 and 4.7 to obtain values $N(h)$ for any height, and $\beta(0,\lambda)$ for any wavelength.

h (km)	0	1	2	3	4	5	6	7	8	9	10
$N_{\rm p}$ (cm^{-3})	200	87	38	16	7.2	3.1	1.1	0.4	0.14	0.05	0.026
h (km)	...	11	12	13	14	15	16	17	18	19	20
$N_{\rm p}$ (cm^{-3})	...	0.023	0.021	0.023	0.025	0.041	0.067	0.073	0.08	0.09	0.086
h (km)	...	21	22	23	24	25	26	27	28	29	30
$N_{\rm p}$ (cm^{-3})	...	0.082	0.08	0.076	0.052	0.036	0.025	0.024	0.022	0.02	0.019

Table 4.7: The aerosol number density. Source of data: [198].

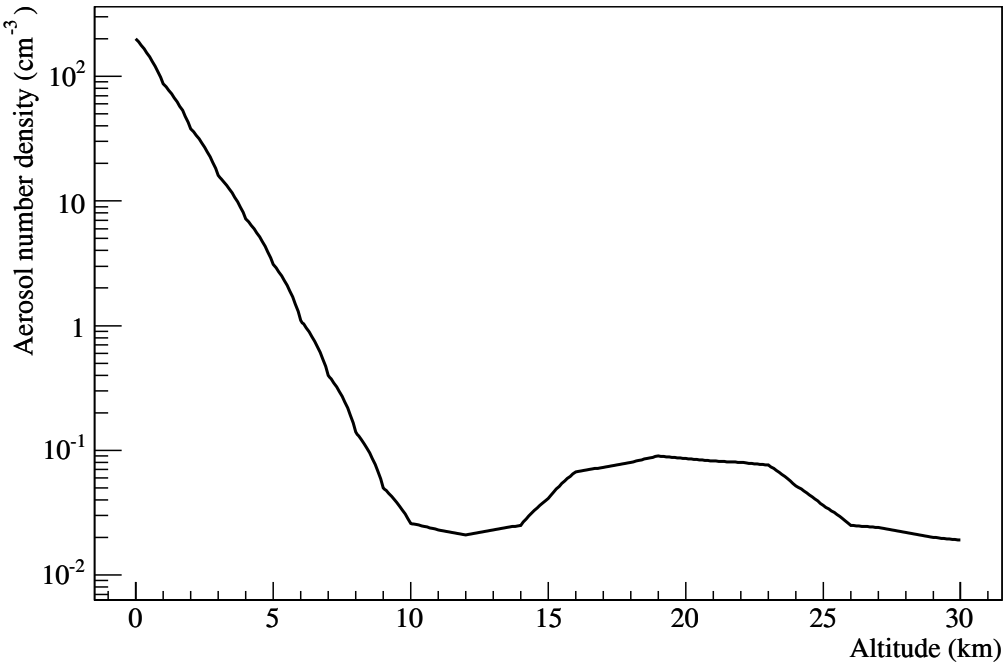

Figure 4.21: The aerosol number density from Table 4.7.

For the numerical integration of (4.44), we have used an algorithm developed by Abelardo Moralejo in the Reflector program for the MAGIC telescope [360].

The overall atmospheric transmission coefficient is

$$T_{\text{total}} = T_{\text{R}} \cdot T_{\text{M}} \cdot T_{\text{o}} \tag{4.45}$$

and it describes the probability for a Čerenkov photon (which may come to the mirror area) **not** to be scattered in the atmosphere.

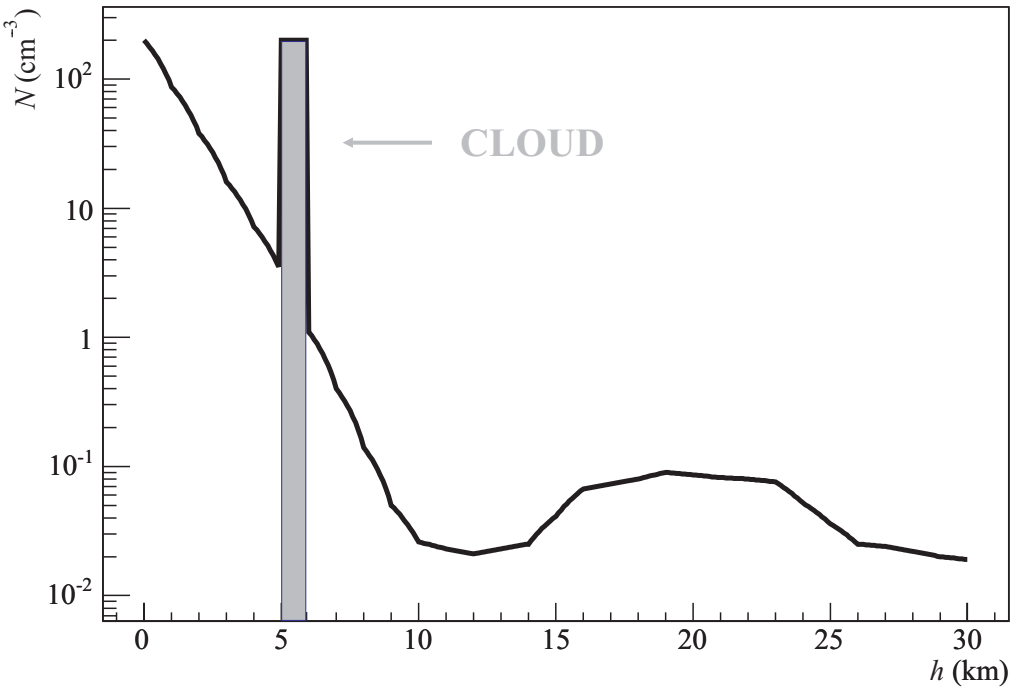

Figure 4.22: Aerosol number density (as in Figure 4.21) modified by the presence of a cloud with the base height of 5 km, with the thickness 1000 m, and the number density of 200 cm^{-3}.

In Figure 4.22, *the peak height* is the cloud density, *the peak width* is the cloud thickness, and *the peak position* is the cloud height base.
The key point of all our VAT simulations is the equal treatment of aerosols and water droplets. This approximation is good enough for our purpose.

Figure 4.23 shows the Mie transmission factor T_{M} as a function of the emission point of a Čerenkov photon (the emission point distance to the telescope) with the wavelength of the Čerenkov photon as parameter. We have used the aerosol number density from the Table 4.7 for the numerical calculation of the curves shown in this figure. Figure 4.24 shows the Mie transmission factor T_{M} modified by cloud. We calculated the transmission factors for a single Čerenkov photon of 450 nm which is emitted at some distance to the telescope. An altostratus cloud, 1000 m thick and containing 200 water droplets per cm^3, is placed at height h. Therefore, $h = 3$ km means 800 m above the telescope level.

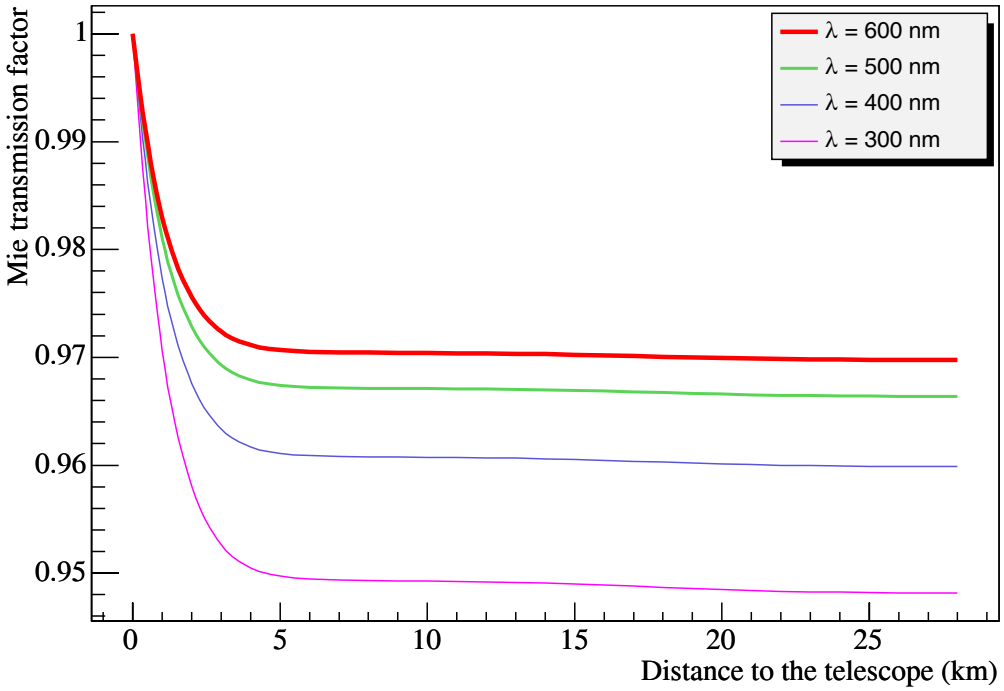

Figure 4.23: The Mie transmission factor T_{M} for a single Čerenkov photon as a function of the emission point distance to the telescope.

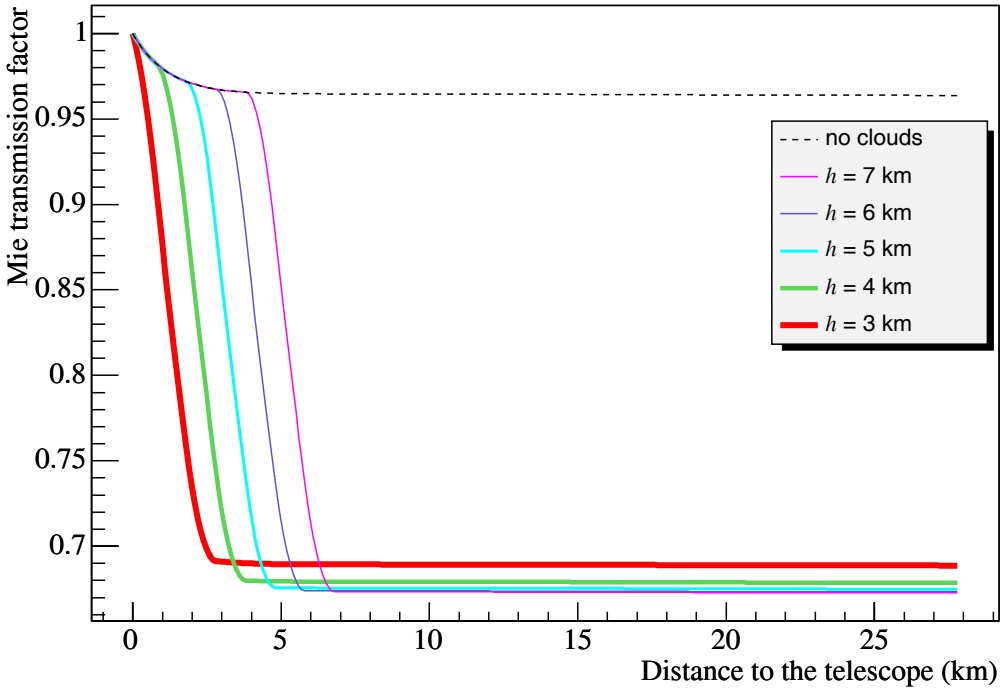

Figure 4.24: The same as in Figure 4.23 but in the presence of an altostratus cloud with the base height h. The Čerenkov photon wavelength is 450 nm, and the cloud droplet density is 200 cm^{-3}.

Chapter 5

Data analysis

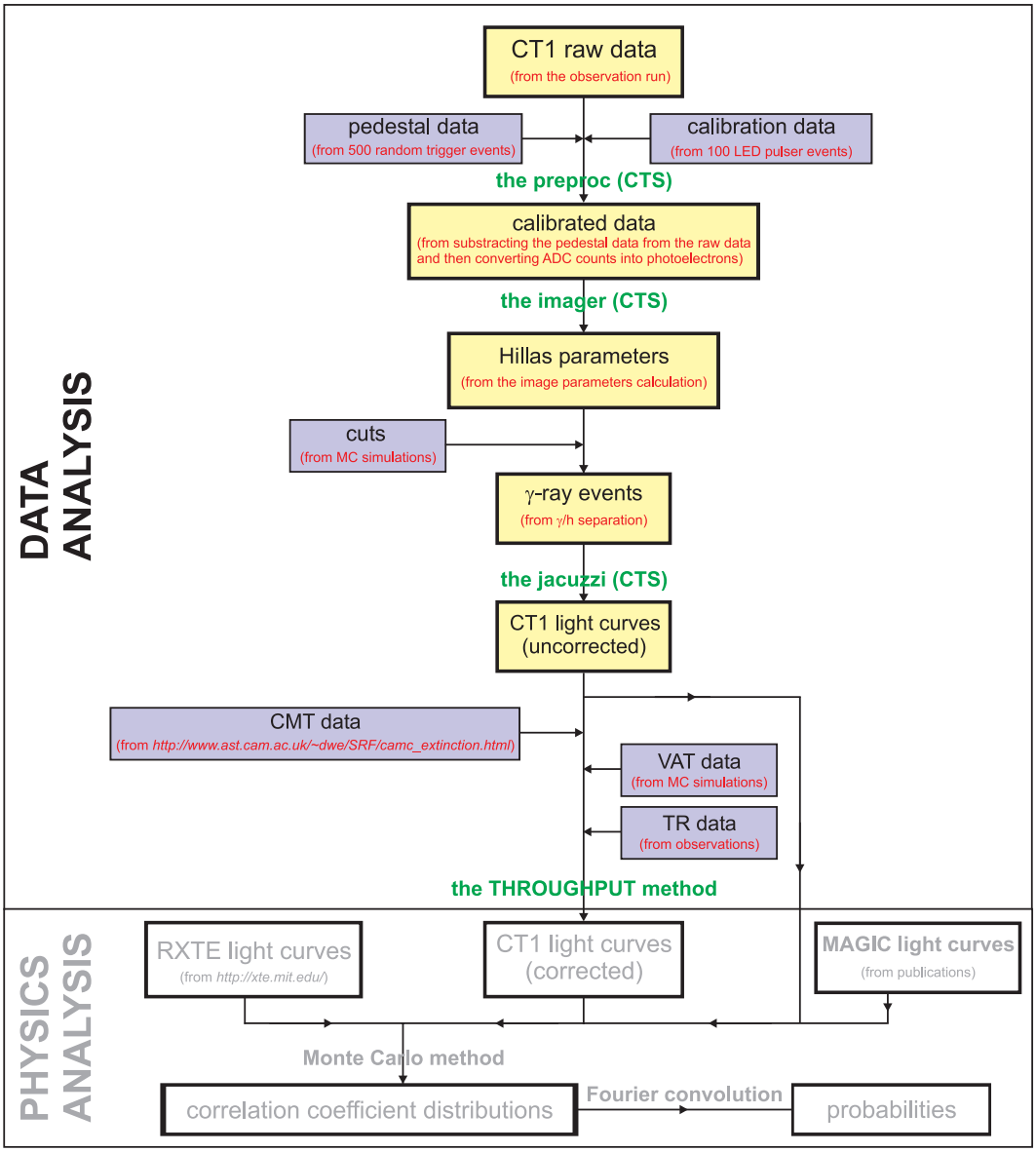

Figure 5.1: The analysis flowchart: first part of the analysis (underlying analysis or hereafter **data analysis**) includes all steps from the raw data (in a form as collected by ground-based telescopes and satellite detectors) to the corrected light curves.

5A Analysis methods

5.1 Analysis of shower images

Less than 0.1% of all CRs entering the Earth's atmosphere are γ-rays. Most of them are hadronic particles, mainly protons, which are the background for IACTs. Therefore, γ/hadron separation is one of the main challenges of ground-based γ-ray astronomy.

Efficient γ/hadron separation was firstly introduced by A.M. Hillas in 1985[1]. It is based on the *Imaging Technique* (IT): EAS images in the telescope camera are parameterized and cuts (usually optimized in MC simulations) enable one to separate γ-rays from hadrons very effectively in the energy range from 500 GeV to 10 TeV.

Since then other γ/hadron separation techniques have been developed but the imaging technique is still one of the most efficient and robust.

5.1.1 From raw data to calibrated data

A typical CT1 run consisted of

- pedestal run (lasting about 30 seconds),
- calibration run (lasting about 30 seconds),
- observation run (lasting 20 minutes).

Each sequence of pedestal, calibration and data run was assigned a run-number [289].
The **raw data** S_i are data from the observation run. They are not yet organized into a form in which they can easily be used or understood.
The **pedestal data** P_i are data without signal present in the detector. They serve to determine the zero level of each channel and the width of the fluctuations. Sources of pedestal data are electronic noise and *night sky background* (NSB). Pedestals have been measured by taking data with random trigger (500 triggers for CT1) with the telescope oriented toward the source. For the i^{th} channel, the mean value P_i has been calculated

$$P_i = \frac{1}{500}\sum_{j=1}^{500} P_{ij}. \tag{5.1}$$

The **calibration data** L_i are data from LED pulses of equal amplitude (e.g. 100 pulses per calibration run for CT1). The mean laser gain L_i (in units of ADC count) is

$$L_i = \frac{1}{100}\sum_{j=1}^{100}(L_{ij} - P_i), \tag{5.2}$$

where L_{ij} is the signal of i^{th} PMT ($i = 1, 2, 3...127$) for the j^{th} laser event.

The relative laser gain l_i is

$$l_i = \frac{L_i}{\frac{1}{127}\sum_{j=1}^{127} L_j}. \tag{5.3}$$

[1]The method was originally presented on 19$^{\text{th}}$ ICRC at La Jolla.

Finally, the **calibrated data** s_i are data ready for further analysis – calculation of the image parameters. They are obtained by subtracting the pedestal data from the raw data and then converting ADC counts into photoelectrons (PE)

$$s_i = \frac{1}{l_i}(S_i - P_i)\chi \tag{5.4}$$

where χ is the *conversion factors* (CF) used to convert ADC counts into the number of PE for each pixel.

This first stage of the CT1 analysis is called pre-processing. It can be done by using the *preproc* program, a part of the *Čerenkov telescope software* (CTS). Before the image parameter calculation, data has to be filtered in order to:

- **reject** noise (*night sky background* (NSB) component) triggered events by applying a two *next-neighbor* (NN) software trigger;
- **correct** positioning of the telescope. The pointing of the CT1 is controlled by the tracking system which provides the equatorial coordinates with a precision of 0.1° [471].

5.1.2 From the calibrated data to the image parameters

The image parameters or **Hillas parameters** are a set of parameters which describe an image of extended air shower in the CT camera. Let x_i and y_i be pixel coordinates of the i^{th} PMT (Figure 5.2 and Table 5.1) and s_i is the calibrated signal (the charge collected in unit of PEs) in the i^{th} PMT.

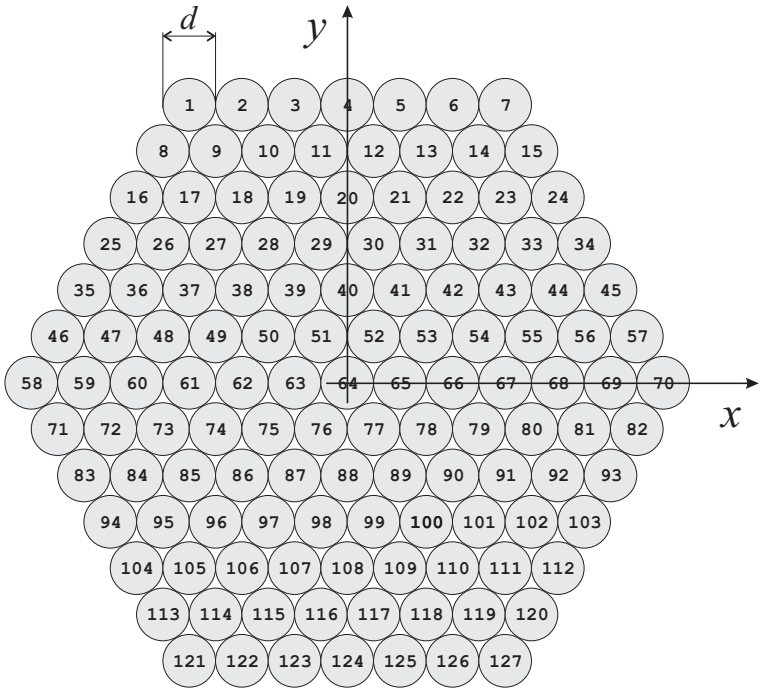

Figure 5.2: The camera coordinate system in degrees. Pixel angular resolution is $d = 0.24^{\text{o}}$ therefore the camera *field of view* (FoV) is 3.12°.

i	1	2	3	4	5	6	7	$\cdots$	121	122	123	124	125	126	127
x_i	$-3d$	$-2d$	$-d$	0	d	$2d$	$3d$	$\cdots$	$-3d$	$-2d$	$-d$	0	d	$2d$	$3d$
y_i	$6d$	$6d$	$6d$	$6d$	$6d$	$6d$	$6d$	$\cdots$	$-6d$	$-6d$	$-6d$	$-6d$	$-6d$	$-6d$	$-6d$

Table 5.1: Pixel coordinates of the PMTs in the camera shown in the Figure 5.2.

Second moment statistics

The first moments are average values:

$$\langle x \rangle = \frac{\sum_i s_i x_i}{\sum_i s_i} \qquad \langle y \rangle = \frac{\sum_i s_i y_i}{\sum_i s_i} \tag{5.5}$$

The second moments are:

$$\langle x^2 \rangle = \frac{\sum_i s_i x_i^2}{\sum_i s_i} \qquad \langle y^2 \rangle = \frac{\sum_i s_i y_i^2}{\sum_i s_i} \tag{5.6}$$

The second central moment is the variance:

$$V_x = \sigma_x^2 = \frac{\sum_i s_i (x_i - \langle x \rangle)^2}{\sum_i s_i} = \frac{\sum_i s_i x_i^2}{\sum_i s_i} - 2\langle x \rangle \frac{\sum_i s_i x_i}{\sum_i s_i} + \langle x \rangle^2 \frac{\sum_i s_i}{\sum_i s_i} \tag{5.7}$$

$$\sigma_x^2 = \langle x^2 \rangle - \langle x \rangle^2 \tag{5.8}$$

$$\sigma_y^2 = \langle y^2 \rangle - \langle y \rangle^2 \tag{5.9}$$

Covariance:

$$\mathrm{COV}_{xy} = \sigma_{xy} = \frac{\sum_i s_i (x_i - \langle x \rangle)(y_i - \langle y \rangle)}{\sum_i s_i} \tag{5.10}$$

$$\sigma_{xy} = \frac{\sum_i s_i x_i y_i}{\sum_i s_i} - \langle y \rangle \frac{\sum_i s_i x_i}{\sum_i s_i} - \langle x \rangle \frac{\sum_i s_i y_i}{\sum_i s_i} + \langle x \rangle \langle y \rangle \frac{\sum_i s_i}{\sum_i s_i} \tag{5.11}$$

$$\sigma_{xy} = \langle xy \rangle - \langle x \rangle \langle y \rangle \tag{5.12}$$

The Maximum Likelihood Method

In order to derive main Hillas parameters, we used the maximum likelihood method[2]. The image of a γ-ray event in the camera has the shape of an ellipse (Figure 4.15). Let $y = ax + b$ be the line that passes through the major axis of the ellipse (Figure 5.3).

$$h_i = (y_i - y(x_i)) \cos\varphi \tag{5.13}$$

$$a = \tan\varphi \tag{5.14}$$

$$h_i = \frac{1}{\sqrt{1+a^2}} (y_i - a x_i - b) \tag{5.15}$$

$$\begin{aligned} \sum_i s_i h_i^2 &= \frac{1}{1+a^2} \left(\sum_i s_i y_i^2 + a^2 \sum_i s_i x_i^2 + b^2 \sum_i s_i \right. \\ &- \left. 2a \sum_i s_i x_i y_i - 2b \sum_i s_i y_i + 2ab \sum_i s_i x_i \right) \end{aligned} \tag{5.16}$$

[2]It is the most important general method of estimation so far known [280]

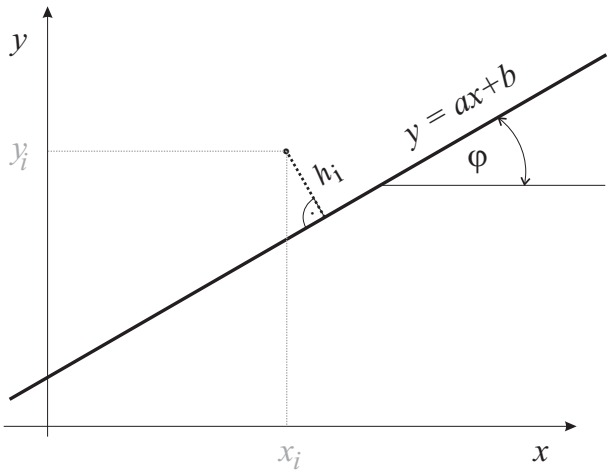

Figure 5.3: The definition of h_i from equation (5.13).

$$\langle h^2\rangle = \frac{1}{1+a^2}\left(\langle y^2\rangle + a^2\langle x^2\rangle + b^2 - 2a\langle xy\rangle - 2b\langle y\rangle + 2ab\langle x\rangle\right) \tag{5.17}$$

$$\begin{aligned}\partial_a\langle h^2\rangle &= \frac{-2a}{(1+a^2)^2}\left(\langle y^2\rangle + a^2\langle x^2\rangle + b^2 - 2a\langle xy\rangle - 2b\langle y\rangle + 2ab\langle x\rangle\right)\\ &+ \frac{1}{(1+a^2)}\left(2a\langle x^2\rangle - 2\langle xy\rangle + 2b\langle x\rangle\right) \equiv 0\end{aligned} \tag{5.18}$$

$$(1+a^2)(a\sigma_x^2 - \sigma_{xy}) = a(\sigma_y^2 + a^2\sigma_x^2 - 2a\sigma_{xy}) \tag{5.19}$$

$$a^2\sigma_{xy} + a(\sigma_x^2 - \sigma_y^2) - \sigma_{xy} = 0 \tag{5.20}$$

$$\boxed{a = \frac{\sigma_y^2 - \sigma_x^2 + \sqrt{(\sigma_y^2 - \sigma_x^2)^2 + 4\sigma_{xy}^2}}{2\sigma_{xy}}} \tag{5.21}$$

$$\partial_b\langle h^2\rangle = \frac{1}{1+a^2}\left(2b - 2\langle y\rangle + 2a\langle x\rangle\right) \equiv 0 \tag{5.22}$$

$$\boxed{b = \langle y\rangle - a\langle x\rangle} \tag{5.23}$$

Transformation of coordinates

$$\bar{x}\cos\varphi = x + \bar{y}\sin\varphi \qquad y = \bar{x}\sin\varphi + \bar{y}\cos\varphi \tag{5.24}$$

$$\bar{x} = x\cos\varphi + y\sin\varphi \tag{5.25}$$

$$\bar{y} = -x\sin\varphi + y\cos\varphi \tag{5.26}$$

Rotation (Figure 5.4) and translation of the coordinate system:

$$\bar{x} = \langle x\rangle + x\cos\varphi + y\sin\varphi \tag{5.27}$$

$$\bar{y} = \langle y\rangle - x\sin\varphi + y\cos\varphi \tag{5.28}$$

And finally, the average value of the new coordinates are:

$$\langle\bar{x}\rangle = \langle x\rangle\cos\varphi + \langle y\rangle\sin\varphi \tag{5.29}$$

$$\langle\bar{y}\rangle = -\langle x\rangle\sin\varphi + \langle y\rangle\cos\varphi \tag{5.30}$$

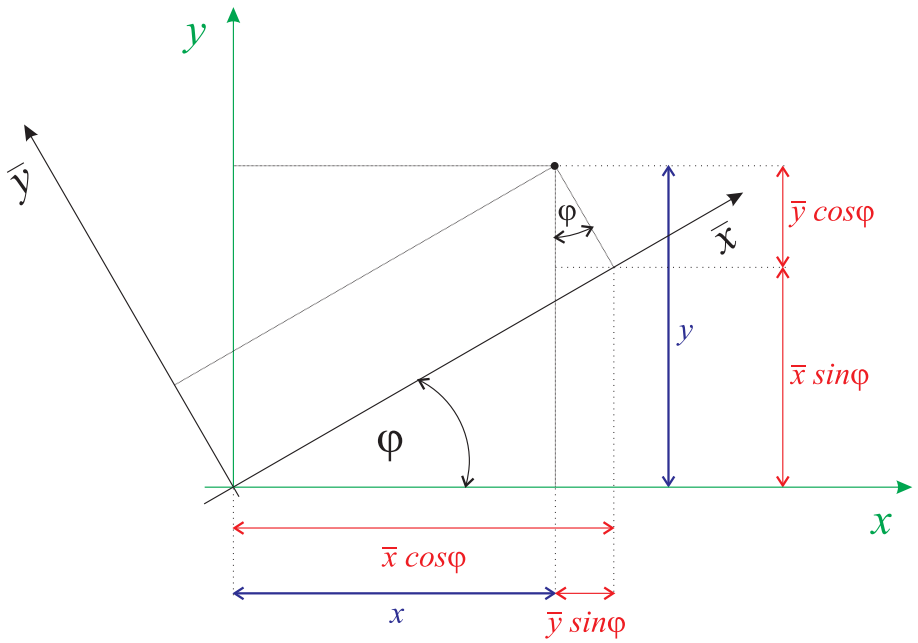

Figure 5.4: Rotation of the coordinate system for the angle φ.

Width and Length

The Hillas parameters Width and Length are standard deviations in the coordinate system rotated by φ (Figure 5.4).

By the definition

$$\text{WIDTH} \stackrel{\text{def}}{=} \sigma_{\bar{y}} \tag{5.31}$$

From (5.8)

$$\sigma_{\bar{y}}^2 = \langle \bar{y}^2 \rangle - \langle \bar{y} \rangle^2 \tag{5.32}$$

From (5.26) and (5.30)

$$\sigma_{\bar{y}}^2 = \sigma_x^2 \sin^2 \varphi + \sigma_y^2 \cos^2 \varphi - 2\sigma_{xy} \sin \varphi \cos \varphi \tag{5.33}$$

From (5.14)

$$\sigma_{\bar{y}}^2 = \frac{1}{1+a^2} \left(\sigma_y^2 + a^2 \sigma_x^2 - 2a\sigma_{xy} \right) \tag{5.34}$$

So, finally we have

$$\boxed{\text{WIDTH} = \sqrt{\frac{\sigma_y^2 + a^2\sigma_x^2 - 2a\sigma_{xy}}{1+a^2}}} \tag{5.35}$$

WIDTH is the semiminor axis (one half the minor axis) of the shower image as shown in Figure 5.5. WIDTH is a measure of lateral development of an EAS.
By the definition

$$\text{LENGTH} \stackrel{\text{def}}{=} \sigma_{\bar{x}} \tag{5.36}$$

From (5.9)

$$\sigma_{\bar{x}}^2 = \langle \bar{x}^2 \rangle - \langle \bar{x} \rangle^2 \tag{5.37}$$

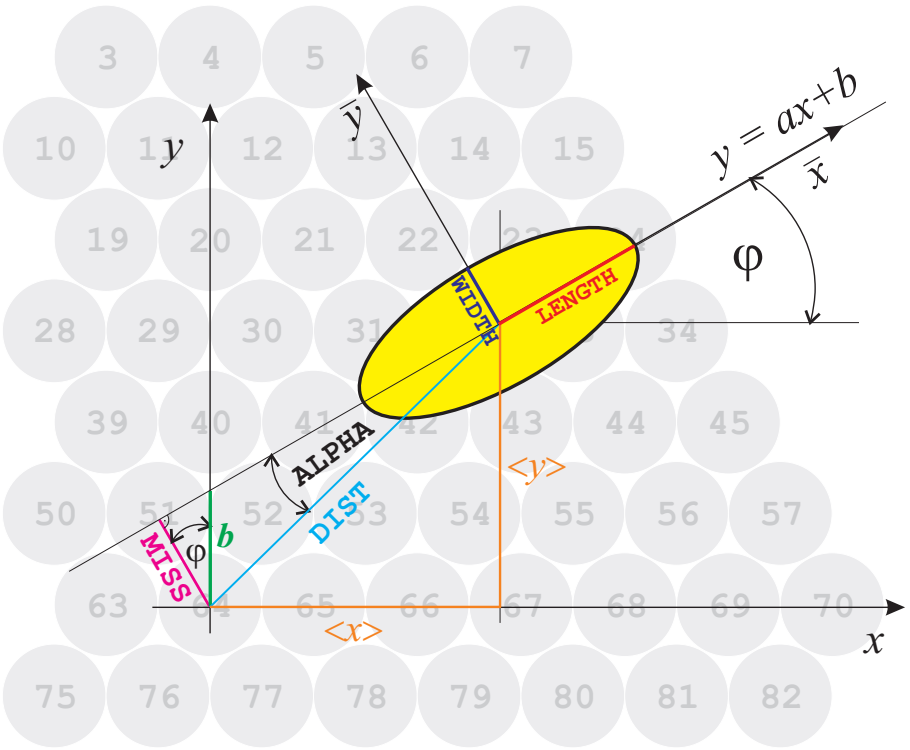

Figure 5.5: The definition of the Hillas parameters. Figure shows the Hillas ellipse in a part of the CT1 camera.

From (5.25) and (5.29)

$$\sigma_{\bar{x}}^2 = \sigma_x^2 \cos^2\varphi + \sigma_y^2 \sin^2\varphi + 2\sigma_{xy} \sin\varphi \cos\varphi \tag{5.38}$$

From (5.14)

$$\sigma_{\bar{x}}^2 = \frac{1}{1+a^2}\left(\sigma_x^2 + a^2\sigma_y^2 + 2a\sigma_{xy}\right) \tag{5.39}$$

So, finally we have

$$\boxed{\text{LENGTH} = \sqrt{\frac{\sigma_x^2 + a^2\sigma_y^2 + 2a\sigma_{xy}}{1+a^2}}} \tag{5.40}$$

LENGTH is the semimajor axis (one half the major axis) of the shower image as shown in Figure 5.5. LENGTH is a measure of longitudinal development of an EAS.

Other Hillas parameters

A few more parameters are useful in the classical image parameter analysis. From Figure 5.5

$$\boxed{\text{DIST} = \sqrt{\langle x\rangle^2 + \langle y\rangle^2}} \tag{5.41}$$

where DIST is the distance from the camera center to the center of gravity of the image in degrees and it depends on the energy E, the impact parameter r and the zenith angle ϑ. DIST is a measure of the impact parameter of an EAS.

$$\cos\varphi = \frac{\text{MISS}}{b} \tag{5.42}$$

From equation (5.14)

$$\boxed{\text{MISS} = \frac{b}{\sqrt{1+a^2}}} \tag{5.43}$$

From Figure 5.5

$$\boxed{\text{ALPHA} = \sin^{-1}\frac{\text{MISS}}{\text{DIST}}} \tag{5.44}$$

ALPHA is the most important cut parameter for **point sources**[3]. It is defined as the angle from the longitudinal axis of the image to the connection line between the center of the camera and the image center of gravity [427].
If the telescope points towards the point source, the image axis of γ-ray induced showers points toward the center. Therefore the ALPHA parameter distribution has the maximum near zero value. On the other hand, hadronic showers arrive from all directions and therefore the ALPHA distribution is uniform in all angles.

Two more useful parameters are

$$\text{SIZE} = \sum_i s_i \tag{5.45}$$

$$\text{CONC} = \frac{s^{\max} + s^{2\text{nd max}}}{\text{SIZE}} \tag{5.46}$$

where s_i is defined by equation (5.4). SIZE is the total number of PEs in the shower image. It is the main estimator for the energy. If too few PEs are collected from an EAS then the shower image is not well defined.
CONC is the ratio of the sum of PEs contained in the two brightest pixels to the total sum of PEs. It provides information about the shower core. CONC is bigger for γ-ray images than for images of hadronic showers.

γ/hadron separation

The background rejection or γ/hadron separation is the most important problem in ground-based γ-ray astronomy. The majority of Čerenkov light flashes observed by IACT comes from hadrons. E.g. for the Crab Nebula, the number of proton induced showers is approximately a few hundredth times the number of γ-ray induced ones.

We have used the simplest method for γ/hadron separation which consists of a **static cut** on the image parameter values [427]. The cuts on the Hillas parameters were obtained

[3] A source with an angular size less than the resolution of the instrument used to observe it, and hence unresolved.

from MC simulations done by Dorota Sobczyńska. We have used the following values:

$$0.05^{\circ} \leq \text{WIDTH} \leq 0.11^{\circ} \tag{5.47}$$
$$0.1^{\circ} \leq \text{LENGTH} \leq 0.42^{\circ} \tag{5.48}$$
$$0^{\circ} \leq \text{ALPHA} \leq 12^{\circ} \tag{5.49}$$
$$0.31^{\circ} \leq \text{CONC} \leq 0.7^{\circ} \tag{5.50}$$
$$0.5^{\circ} \leq \text{DIST} \leq 1.0^{\circ} \tag{5.51}$$

Advanced γ/hadron separation techniques

Low-energy-threshold IACTs ($E_{\text{threshold}} < 100$ GeV) of third generation (see Table 1.3) need better γ/hadron separation techniques than the standard Hillas method. Images of EAS below 100 GeV are circles rather than ellipses. Hence, the most important Hillas parameter ALPHA, defined in equation (5.44), is not useful anymore. For **extended sources**[4] the ALPHA parameter also cannot be used. Accordingly, some new γ/hadron separation techniques have been developed. For example, MAGIC uses the *Random Forest* (RF) method; HESS developed a new method based on shower parameters in 3D, not on image parameters. The HESS method does not rely on simulations [311].

5.1.3 From image parameters to light curves

The flux calculations

The flux Φ is an energy outflow, a measure of energy passing through a given area of surface per unit time

$$\Phi = \mathrm{d}L/\mathrm{d}A \tag{5.52}$$

where L is the luminosity, defined in equation (2.3), and A is area. In fact, Φ from equation above is the **energy flux** which is usually expressed in erg/cm^2/s. In this thesis we do not use energy flux but the **photon flux** which has unit cm^{-2}s^{-1}. A typical integral flux in the TeV range is of the order 10^{-11} cm^{-2}s^{-1}

An alternative unit for the γ-ray photon flux is the **crab**. The crab unit is the average flux of the Crab Nebula (which is a steady source and a kind of standard candle for VHE γ-ray astronomy):

$$1 \text{ crab} = 1.75 \cdot 10^{-11} \text{ cm}^{-2}\text{s}^{-1}. \tag{5.53}$$

A common plot, flux vs time, is called a **light curve**. In a light curve, time is usually expressed in terms of MJD. The *Modified Julian Day* (MJD) is an abbreviated version of the *Julian Day* (JD) – dating method which has been in use by astronomers for centuries. The system was begun in 1582 by French scholar Joseph Justus Scaliger (1540–1609) who named it to honor his father Julius[5].

JD is the number of days since **noon** of January 1, 4713 BC. The starting date is chosen sufficiently far in the past to predate all known recorded astronomical observations [407]. The MJD is defined as

$$\text{MJD} = \text{JD} - 2400000.5 \tag{5.54}$$

[4] A source of angular size greater than the resolution of the instrument used to observe it, and hence resolved.

[5] Hence, JD has no direct connection with Roman emperor Julius Caesar or the Julian calendar [234].

The offset of 0.5 means that MJD started at **midnight** of November 17, 1858.

The differential flux of γ-rays is defined as

$$\frac{\mathrm{d}F}{\mathrm{d}E} = \frac{\mathrm{d}N}{\mathrm{d}E\,\mathrm{d}A\,\mathrm{d}t} \tag{5.55}$$

where F is the flux, E is the energy of a γ-ray, A is the area, N is the number of γ-rays, and t is the time.
Using CTS, the differential flux of γ-rays has been calculated as

$$\frac{\mathrm{d}F}{\mathrm{d}E} = \frac{\mathrm{d}N_{\mathrm{excess}}}{\mathrm{d}E}\frac{1}{\sum_l T^l_{\mathrm{obs}}\; A_{\mathrm{eff}}(E,\vartheta_l)} \tag{5.56}$$

where N_{excess} are the **excess events**: the number of measured events remaining after subtraction of background events[6], T^l_{obs} is the observation time at zenith angle bin ϑ_l, and $A_{\mathrm{eff}}(E,\vartheta_l)$ is the effective area [427].
The effective area is obtained from MC studies

$$A_{\mathrm{eff}}(E_k,\vartheta_l) = \pi \sum_i \frac{N_{selected}(E_k,\vartheta_l,r_i)}{N_{simulated}(E_k,\vartheta_l,r_i)}(r^2_{up}(i) - r^2_{low}(i)) \tag{5.57}$$

where $r_{up}(i)$ and $r_{low}(i)$ are the upper and lower edge of the impact parameter bin. $N_{simulated}(E_k,\vartheta_l,r_i)$ is the number of events (in the energy/zenith angle/impact parameter-bin) which were MC simulated, and $N_{selected}(E_k,\vartheta_l,r_i)$ is the number of events which passed the selection cut [427].
The error on the flux was calculated using CTS via Gaussian error propagation from errors on N_{excess} and A_{eff}.

The significance

Figure 5.6 shows a typical observation in γ-ray astronomy. A Čerenkov telescope points

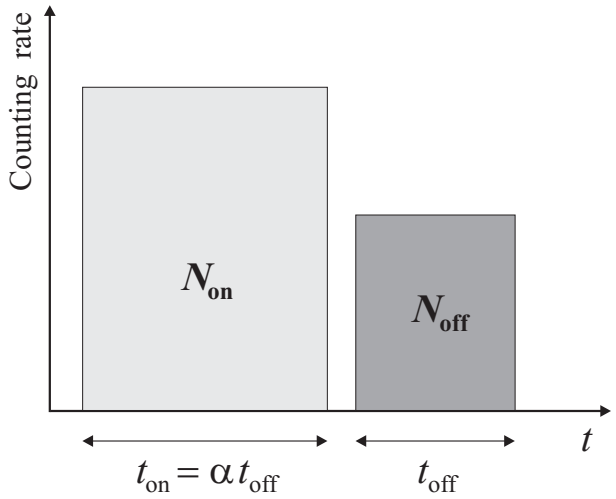

Figure 5.6: A typical observation in γ-ray astronomy. Source: Li & Ma paper [312].

in the direction of a γ-ray source for a certain time t_{on} and counts N_{on} photons. Then it

[6]The measured events are the events which passed the selection cuts.

observes background for a time interval t_{off} and counts N_{off} photons [312]. α is the ratio of the on-source and off-source time

$$\alpha = \frac{t_{\text{on}}}{t_{\text{off}}}. \tag{5.58}$$

Then we can estimate the number of background photons

$$N_{\text{B}} = \alpha N_{\text{off}}. \tag{5.59}$$

Therefore, the observed signal (the excess counts above background) is

$$N_{\text{S}} = N_{\text{on}} - N_{\text{B}} = N_{\text{on}} - \alpha N_{\text{off}}. \tag{5.60}$$

The **significance** is defined as a ratio of the observed signal to its standard deviation

$$S = \frac{N_{\text{S}}}{\sigma_{N_{\text{S}}}}. \tag{5.61}$$

Some experimenters use the standard deviation of the number of background photons $\sigma_{N_{\text{B}}}$ as a measure of $\sigma_{N_{\text{S}}}$ supposing that N_{B} simply follow a Poisson distribution

$$S = \frac{N_{\text{S}}}{\sqrt{N_{\text{B}}}} = \frac{N_{\text{on}} - \alpha N_{\text{off}}}{\sqrt{\alpha N_{\text{off}}}}. \tag{5.62}$$

In the general case of $\alpha \neq 1$ this is not true and the significance is overestimated [312].

From equation (5.60), by using the error propagation and expressions $\sigma(N_{\text{on}}) = \sqrt{N_{\text{on}}}$ and $\sigma(\alpha N_{\text{off}}) = \alpha\sqrt{N_{\text{off}}}$, it follows

$$\sigma_{N_{\text{S}}} = \sqrt{N_{\text{on}} + \alpha^2 N_{\text{off}}} \tag{5.63}$$

Li and Ma derived the standard deviation of the observed signal from the Poisson-Gaussian distribution of counts [312]

$$\sigma_{N_{\text{S}}} = \sqrt{\alpha(N_{\text{on}} + N_{\text{off}})} \tag{5.64}$$

and therefore the significance is

$$S = \frac{N_{\text{on}} - \alpha N_{\text{off}}}{\sqrt{\alpha(N_{\text{on}} + N_{\text{off}})}}. \tag{5.65}$$

For the case $\alpha \sim 1$ ($0.5 \leq \alpha \leq 1.5$), equation (5.65) can be used, but for more general case $0.1 \leq \alpha \leq 10$ Li and Ma derived a formula (5.66) by applying the method of statistical hypotheses test

$$S = \sqrt{2}\left\{ N_{\text{on}} \ln\left[\frac{1+\alpha}{\alpha}\left(\frac{N_{\text{on}}}{N_{\text{on}} + N_{\text{off}}}\right)\right] + N_{\text{off}} \ln\left[(1+\alpha)\left(\frac{N_{\text{off}}}{N_{\text{on}} + N_{\text{off}}}\right)\right]\right\}^{1/2} \tag{5.66}$$

5.2 Software used for the analysis of shower images

5.2.1 Čerenkov telescope software

Čerenkov telescope software (CTS) consists of the CT1 software (written in C programming language) and MARS (written in C++). *MAGIC Analysis and Reconstruction Software* (MARS) is a software package developed for use with the MAGIC telescope. We have adopted it to visualize events in the CT1 camera. The CT1 software is a set of programs developed for *Čerenkov Telescope 1* (CT1) data analysis. The source code was written by many authors from the HEGRA Collaboration. This program package uses the raw data and produces the light curves and the energy spectra. We have used the following parts of the CT1 software:

- **preproc** – reads the CT1 raw data, binary files which contain:
  - *pixel signals* S_i in units of ADC counts of i^{th} pixel,
  - *times*,
  - *shaft encoders* (SE) which represent positions in the sky.
- **imager** – takes the output from the *preproc* and produces the final event ntuples.
- **xeos** – a graphical user interface (GUI) for the raw data analysis. We have used it to run the *preproc* and the *imager*.
- **jacuzzi** – derives and plots the light curves (flux vs time) from given on-data and off-data.

The *preproc* was written by Dirk Petry and later improved by Martin Kestel. The *imager*, the *xeos*, and the *jacuzzi* were written by Thomas Schweizer and Daniel Kranich.

5.3 Correction for imperfect atmospheric transparency

When reporting on IACT observations, many authors highlight the importance of *variable atmospheric transparency* (VAT). For example:
– "One has to worry about varying atmospheric conditions, which might introduce time-dependent variations in the light yield" [24].
– "Most critical are short-term variations in atmospheric transmission" [24].
– "Bad weather conditions and the rising moon prevented continuous observation" [8].
– "The main source of systematic errors may be a not-so-detailed knowledge of the atmospheric transmission" [471].
– "The atmospheric properties are extremely important for reliable analysis" [289].

The response of an IACT is sensitive to *variable atmospheric conditions* (VAT). Hence, the atmospheric conditions are continuously monitored and the data corresponding to bad weather have been being throw away. The criterion for accepting/rejecting the data has been usually based on:

- the extinction values from an optical telescope which shows the atmospheric transparency;
- the *trigger rate* (TR) on CRs from IACT.

The CT1 data selection (relating to weather condition) used to happen in several steps [300]:

- the operator run-books were searched for notes on bad weather and corresponding data were removed;
- the atmospheric extinction measurements from the *Carlsberg Meridian Telescope* (CMT) were used, and r' **was required to be below 0.25** [7];
- the mean TR, corrected for the *zenith angle* (ZA), was required to be close to the nominal rate, e.g. not more than 8σ below the nominal rate.

In this analysis, we found that the most useful indicator of atmospheric conditions, from those mentioned above, is the mean TR on CRs. It can be also used for the $\gamma-$ray flux correction.

In 2001, LeBohec and Holder from the VERITAS Collaboration developed a simple but useful tool – *the throughput method* – for correcting the light curves [310]. The method is particularly important for the rapid variability study of VHE γ-ray sources e.g. blazars. We modified the original throughput method in order to adapt it for the CT1 data.

5.3.1 The throughput method

Each recorded Čerenkov event can be characterized by its luminosity Q [310]. For data obtained with the CT1, we have used the SIZE parameter defined by equation (5.45) as the luminosity of a CR event (the sum of photoelectrons in all pixels that gave a contribution to the image in the camera). Since the CR rate is constant (up to fluctuations), the differences in the distribution of SIZE (obtained at the same zenith angle) reflect only variations in light collection efficiency due to *variable atmospheric transparency* (VAT). We assumed here that the hardware setup of the experiment remind unchanged, especially the high voltage of PMTs in the CT1 camera.

On the other hand, if atmospheric transparency is constant, the distribution of SIZE reflects a ZA dependence. As ZA increase, the atmospheric depth roughly increases with $\frac{1}{\cos\vartheta}$. Therefore, TR on CRs roughly decreases with $\cos\vartheta$ as shown in Figure 5.7.

We constructed the histogram of SIZE obtained from observation during a specific night which had good[8] weather conditions (Figure 5.9). Then we used it as a reference for the calibration of other nights. The reference observation is taken at ZA $\vartheta_{\rm ref}$. For each of the other nights we have constructed the histogram of the $F_{\rm meas}\times$ SIZE. Then we adjusted the **throughput factor** $F_{\rm meas}$ until the distribution best fits the reference ones as in [310].

LeBohec and Holder suggested applying the correction directly to the measured $\gamma-$ray flux [310]

$$\Phi_{\rm corr}(\vartheta) = \frac{\Phi(\vartheta)}{(F_{\rm meas}/F_{\rm exp})^{\alpha}} \tag{5.67}$$

where α is power law spectral index. For Mkn 421, we have used $\alpha = 2.41$ from [31].

To apply the throughput corrections, the expected throughput factor $F_{\rm exp}(\vartheta)$ have to be calculated. Instead of using an approximate analytical model (as in the paper [310]),

[7] r' means narrow passband filter with effective wavelength of 625 nm. Typical value of r' for good quality dust-free night at La Palma is 0.09 magnitudes.

[8] Due to both **trigger rate** and **extinction value** criteria.

we fitted the reference data in order to get ZA dependence of the throughput factor F (Figure 5.8).

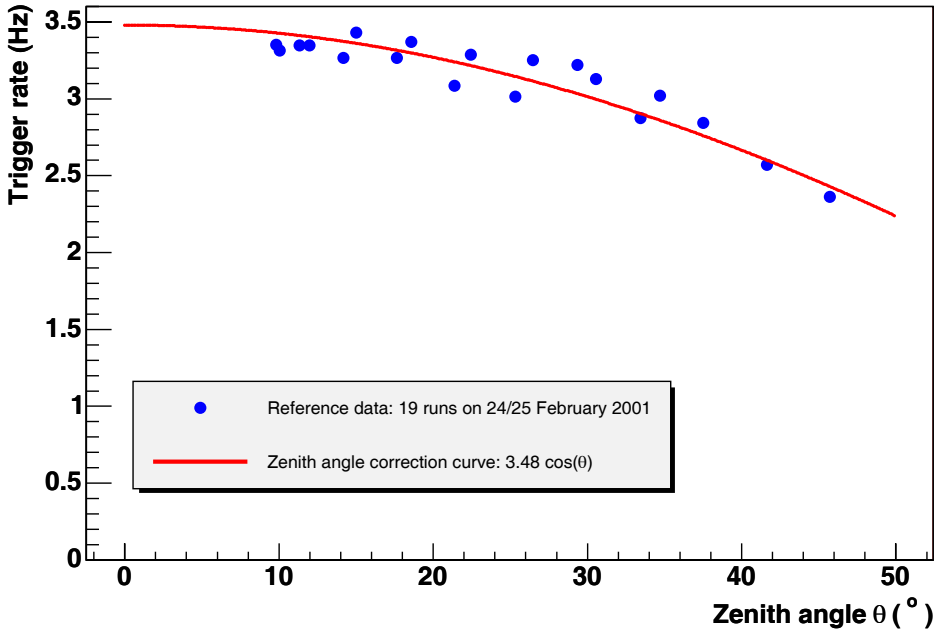

Figure 5.7: *Trigger rate* (TR) vs *zenith angle* (ZA) for a selected run with perfect atmospheric transparency (according to the extinction value). The fitted curve is $A \cos \vartheta$ which corresponds to TR of 3.48 Hz at zenith ($\vartheta = 0^o$). Fluctuations of TR, after ZA corrections, are **up to 6%**.

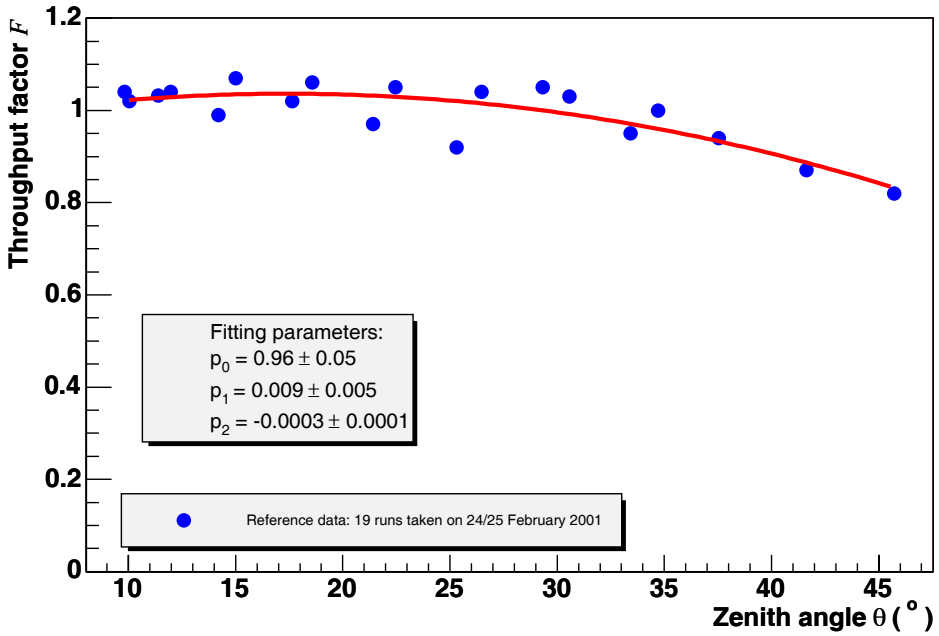

Figure 5.8: *Throughput factor* (TF) vs *zenith angle* (ZA) for the same run as in Figure 5.7. The fitted curve is $p_0 + p_1\vartheta + p_2\vartheta^2$. All observations in our data set (2001 – CT1 – Mkn 421) were taken in ZA range $< 9^o, 45^o >$.

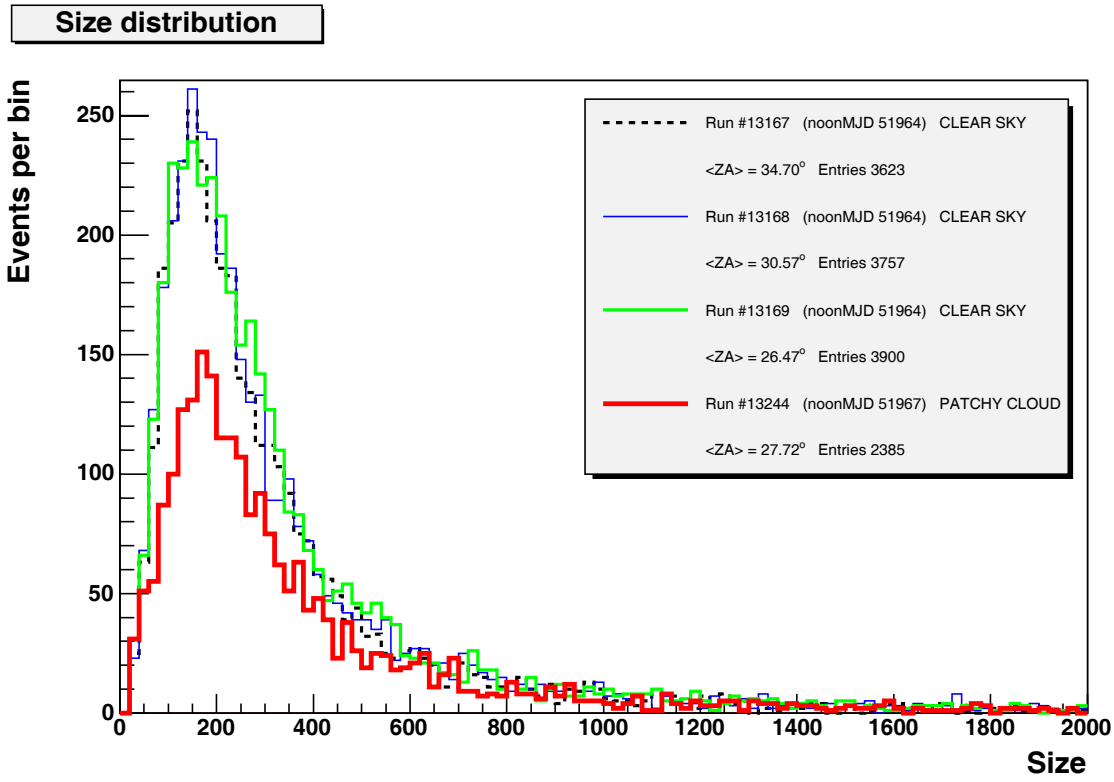

Figure 5.9: Example of the distributions of the SIZE Čerenkov light image parameter defined by equation (5.45). The small differences seen in the first three runs are due to statistical fluctuations. The large difference in the forth run is due to cloudy sky. Run # 13167 has been used as the reference one for further analysis.

5B Results and discussion

5.4 Multiwavelength campaign on Mkn 421 (2003): the low state

Multiwavelength (MWL) studies of the variable emission from AGNs are extremely important to our understanding of the nature of the particles and acceleration mechanism in jets [310].

Here we report on MWL campaign on Mkn 421 from February/March 2003. Table 5.2 shows the observation times and conditions.

Evening date	**run#**	**obs. time/min**	$< \Delta TR_{rel} >$	**Extinction in r'**	**Comment**
February 25	20114 – 20122	180	+4.6 %	0.094	rain at first
February 26	20129 – 20146	360	+3.7 %	0.096	—
February 27	20157 – 20173	340	−7.9 %	0.097	—
February 28	20181 – 20201	420	+1.7 %	0.092	—
March 1	20207 – 20224	360	+4.9 %	0.122	—
March 2	20235 – 20250	320	+0.2 %	0.095	—
March 3	20262 – 20278	340	−1.8 %	0.095	—
March 4	20290 – 20306	340	−3.3 %	0.119	clouds at end
March 5	20309 – 20324	320	−2.1%	0.082	clouds at start
		TOTAL: **49.7 h**			

Table 5.2: The CT1 data set of Mkn 421 from **February/March 2003** (9 nights). The trigger rate was constant, up to fluctuations. Extinction values and comments on weather conditions are from *Carlsberg Meridian Telescope* (CMT).

5.4.1 The CT1 γ-ray light curve

We analyze the complete data set of Mkn 421 from MWL campaign in February/March 2003. These observations (**49.7** hours in total) were done under good atmospheric conditions and have not been published yet.

The obtained light curves shows flux variability although the activity level of the source was low. Contrary, observations of blazar 1ES1959+650 in September and October 2004 by MAGIC showed that the source was in "low state" and no significant variation of γ-ray flux was found [72].

The mean trigger rate at zenith was 3.43 Hz.

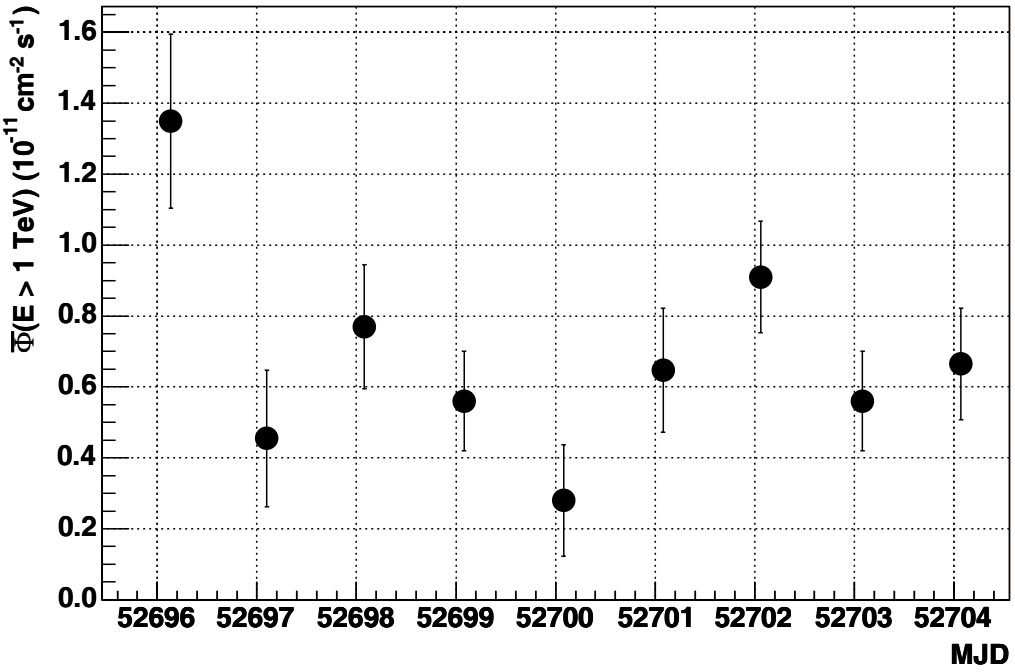

Figure 5.10: CT1 γ-ray flux above 1 TeV from multiwavelength campaign on Mkn 421 in February and March 2003.

MJD	$\overline{\Phi}(E > 1\text{TeV})$ ($10^{-11}\text{cm}^{-2}\text{s}^{-1}$)
52696.13	1.35 ± 0.25
52697.10	0.46 ± 0.19
52698.08	0.77 ± 0.18
52699.08	0.56 ± 0.14
52700.08	0.28 ± 0.16
52701.08	0.65 ± 0.18
52702.06	0.91 ± 0.16
52703.08	0.56 ± 0.14
52704.07	0.67 ± 0.16

Table 5.3: Data from Figure 5.10.

5.4.2 The CT1 differential energy spectrum

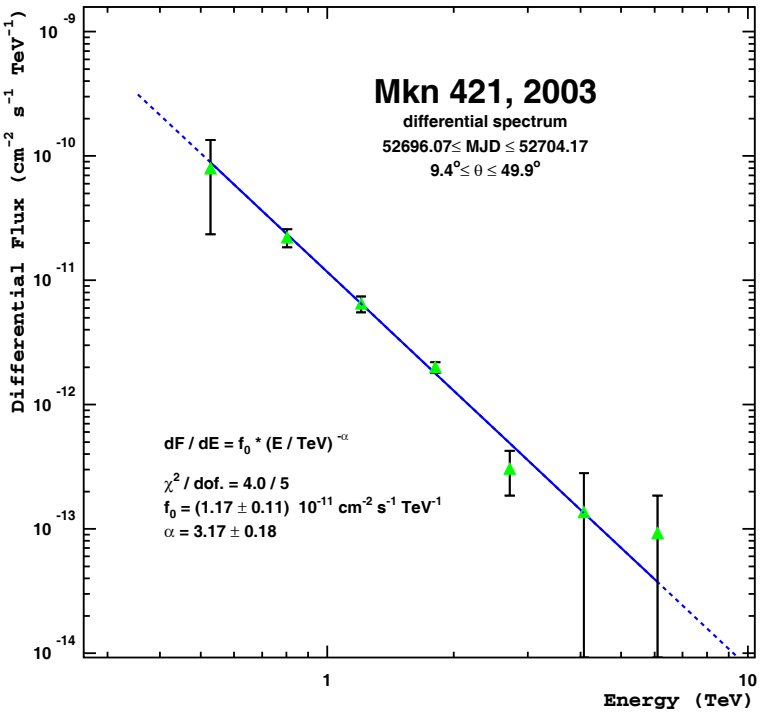

Figure 5.11: Differential energy spectrum (**power law only**) for multiwavelength campaign on Mkn 421 in February and March 2003. Figure: Daniel Kranich.

5.4.3 The CT1 alpha plot

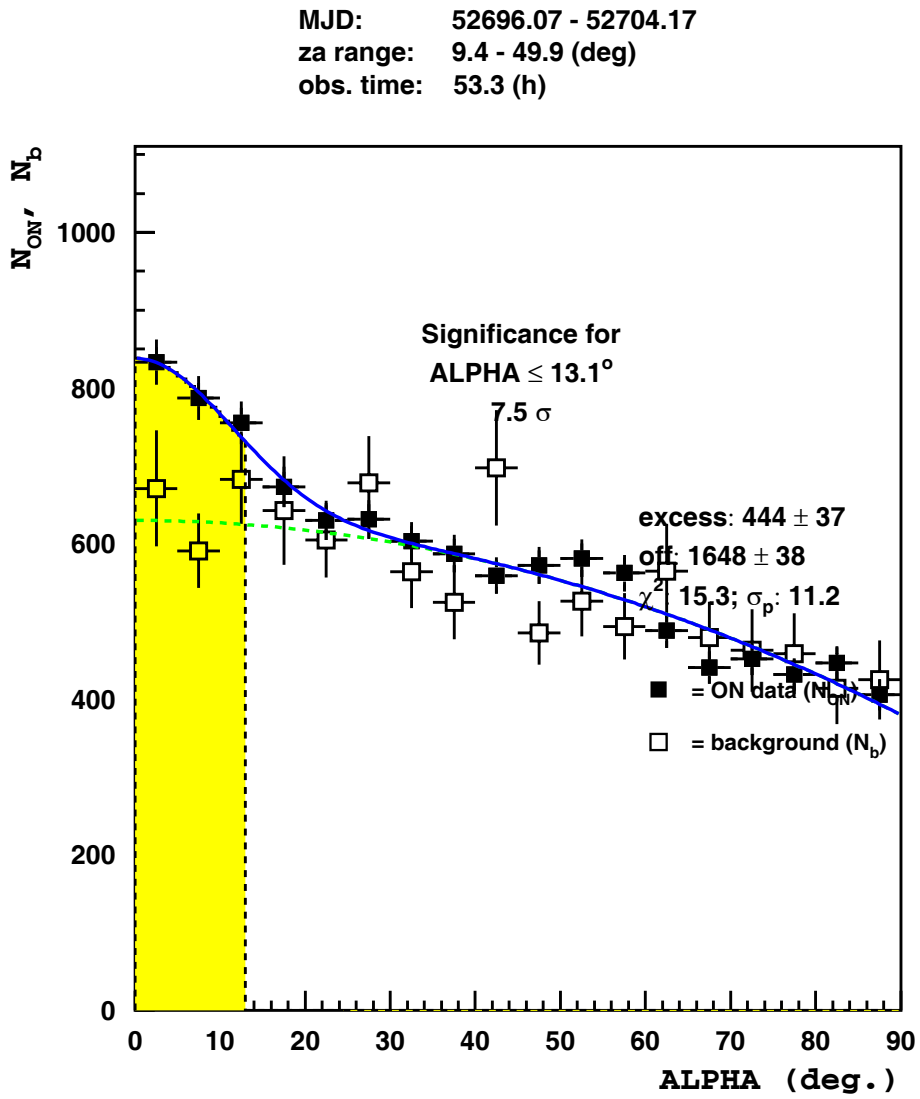

Figure 5.12: Alpha plot for multiwavelength campaign in February and March 2003 (from MJD 52696.07 to MJD 52704.17). The significance for the overall period is 7.5 σ.

5.4.4 The ASM/RXTE X-ray light curve

The observational data from the *All Sky Monitor* (ASM) aboard *Rossi X-ray Timing Explorer* (RXTE) are available on the web[9]. These ASCII-formatted data are "quick-look results provided by the ASM/RXTE team".
Each raw data point represents the fitted source flux from one 90 seconds dwell[10]. Data were taken using three *Scanning Shadow Camera*[11] (SSC) and were quoted as nominal 2–10 keV rates in ASM *counts per second* (cts/s), where the Crab nebula flux is about 75 cts/s.
Data files, available on the RXTE web, are:

[9] *http://xte.mit.edu/ASM_lc.html*
[10] Dwell is a unit period during an X-ray source is being observed by RXTE.
[11] The full SSC *field of view* (FoV) is 110 degrees (θ) by 12 degrees (φ).

- The "Dwell by Dwell" ASCII files (they contain 13 columns: MJD of the observation, fitted ASM unit count rate r_i, estimated error σ_i, etc.)
- The "One-Day Averages" ASCII files (they contain 5 columns: MJD of the observation, averaged ASM unit count rate **one-day averages** (midday $\pm$ 12 h), RMS estimated error, etc.)

Instead of using one-day averages (available at *http://xte.mit.edu/*), we have recalculated RXTE/ASM X-ray rates to get **"nightly averages"** (middle of a nightly CT1/KVA observation $\pm$ 12 h). If r_i is the AMS unit count rate which have the estimated error σ_i then the weighted average is

$$\overline{r} = \frac{1}{\sum_i \frac{1}{\sigma_i^2}} \sum_i \frac{r_i}{\sigma_i^2} \tag{5.68}$$

and the minimal variance is

$$\sigma_r = \frac{1}{\sqrt{\sum_i \frac{1}{\sigma_i^2}}} \tag{5.69}$$

<MJD>	One-Day Averaged ASM Unit (cts/s)
52696.56	0.893 $\pm$ 0.164
52697.57	0.547 $\pm$ 0.134
52698.58	0.481 $\pm$ 0.144
52699.58	0.317 $\pm$ 0.142
52700.61	0.476 $\pm$ 0.137
52701.49	0.569 $\pm$ 0.139
52702.37	1.177 $\pm$ 0.150
52703.50	0.761 $\pm$ 0.129
52704.37	0.661 $\pm$ 0.160

Table 5.4: One-Day averaged RXTE/ASM light curve of Mkn 421 from February/March 2003.

<MJD>	Nightly Averaged ASM Unit (cts/s)
52696.181	1.120 $\pm$ 0.445
52696.949	0.790 $\pm$ 0.139
52697.906	0.566 $\pm$ 0.136
52698.939	0.238 $\pm$ 0.143
52699.971	0.409 $\pm$ 0.146
52700.945	0.463 $\pm$ 0.127
52702.074	1.150 $\pm$ 0.128
52703.140	0.667 $\pm$ 0.151
52704.060	0.734 $\pm$ 0.124

Table 5.5: Nightly averaged (to get overlapping data points) RXTE/ASM light curve of Mkn 421 from February/March 2003.

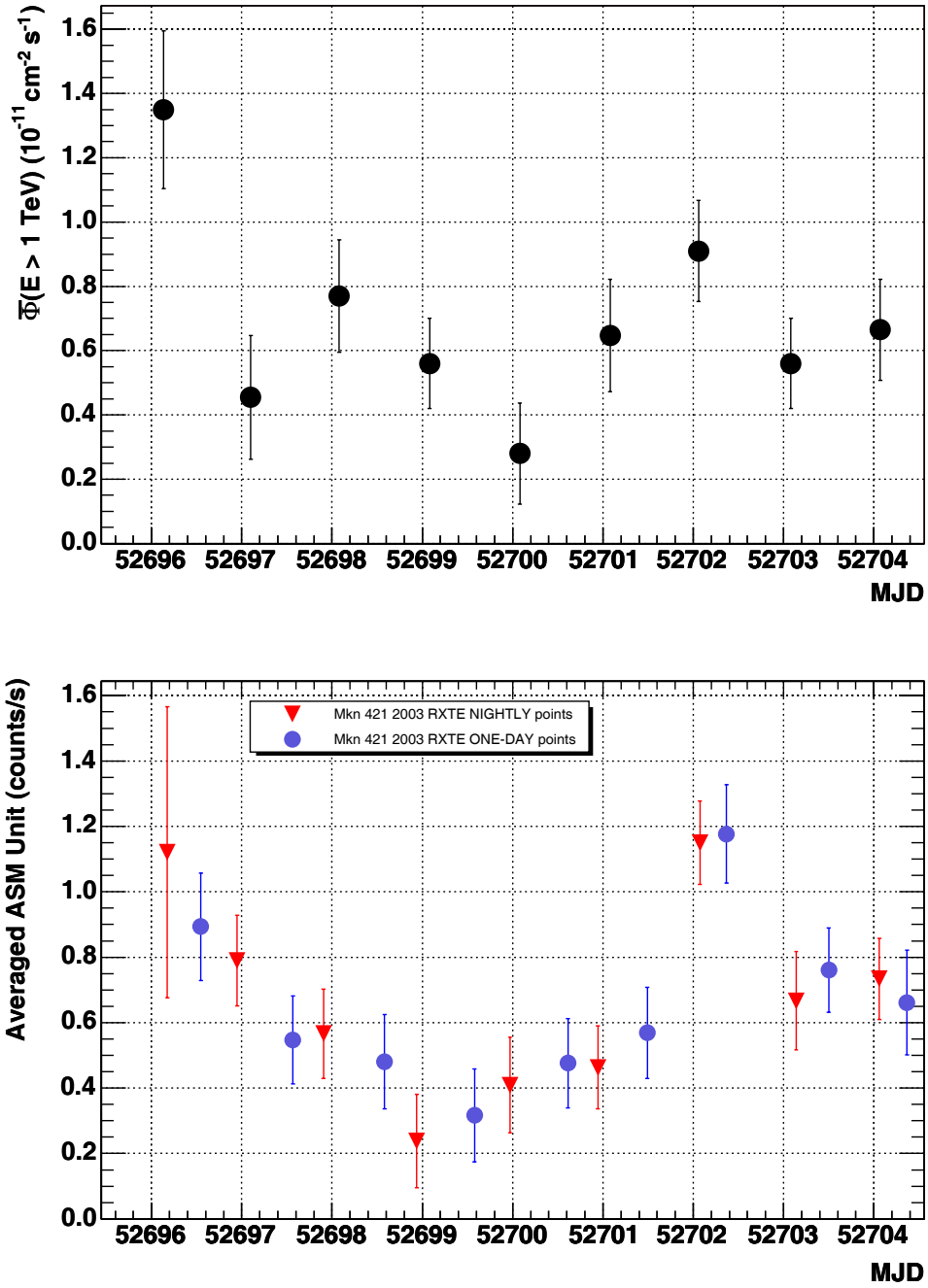

Figure 5.13: CT1 γ-ray flux above 1 TeV from Table 5.3 (upper panel) and **RXTE/ASM X-ray flux** (lower panel) from Table 5.5.

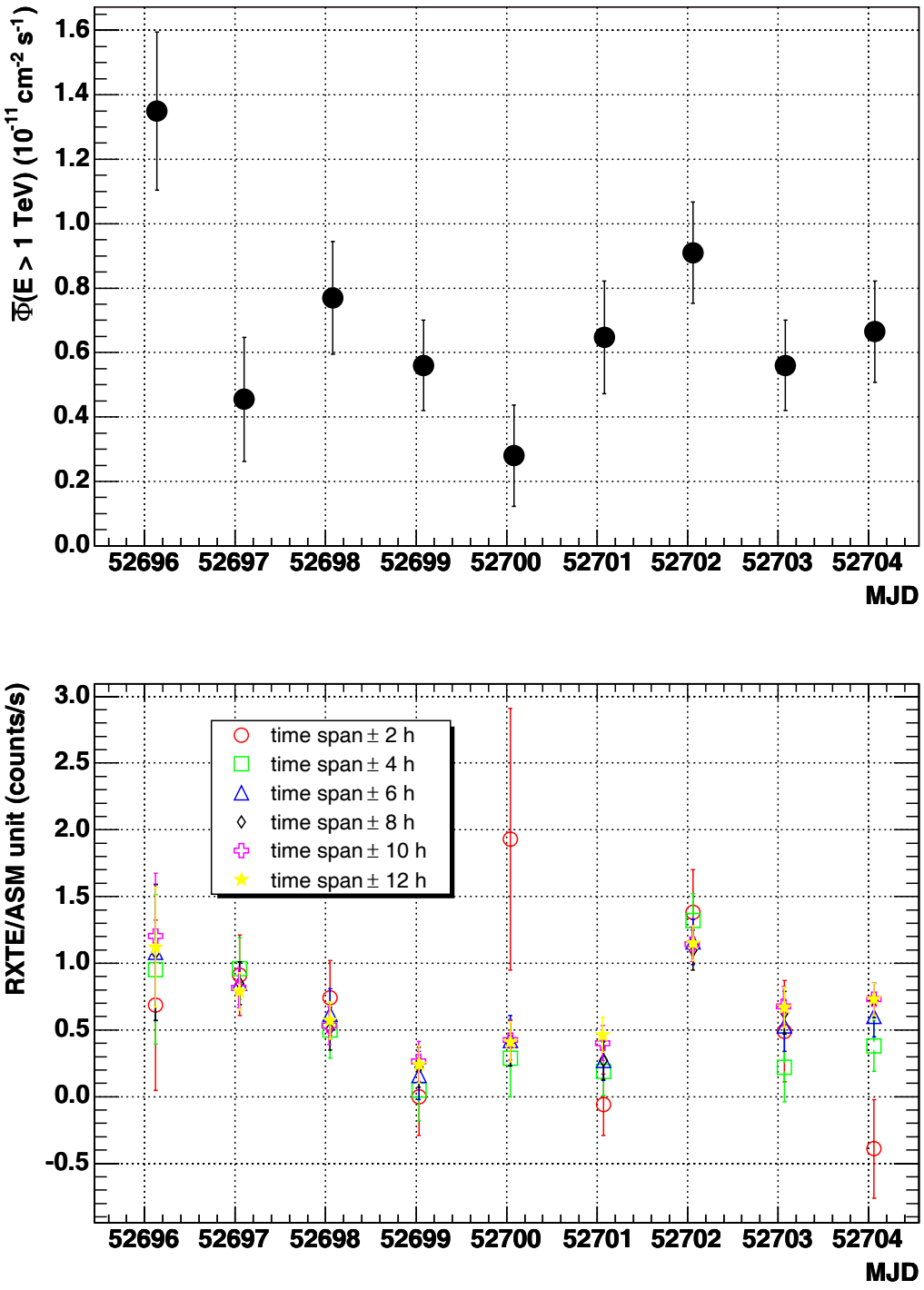

Figure 5.14: Upper panel is Figure 5.10 (CT1 light curve from MWL campaign in 2003). Lower panel shows RXTE/ASM data reanalyzed in 6 different ways (see text).

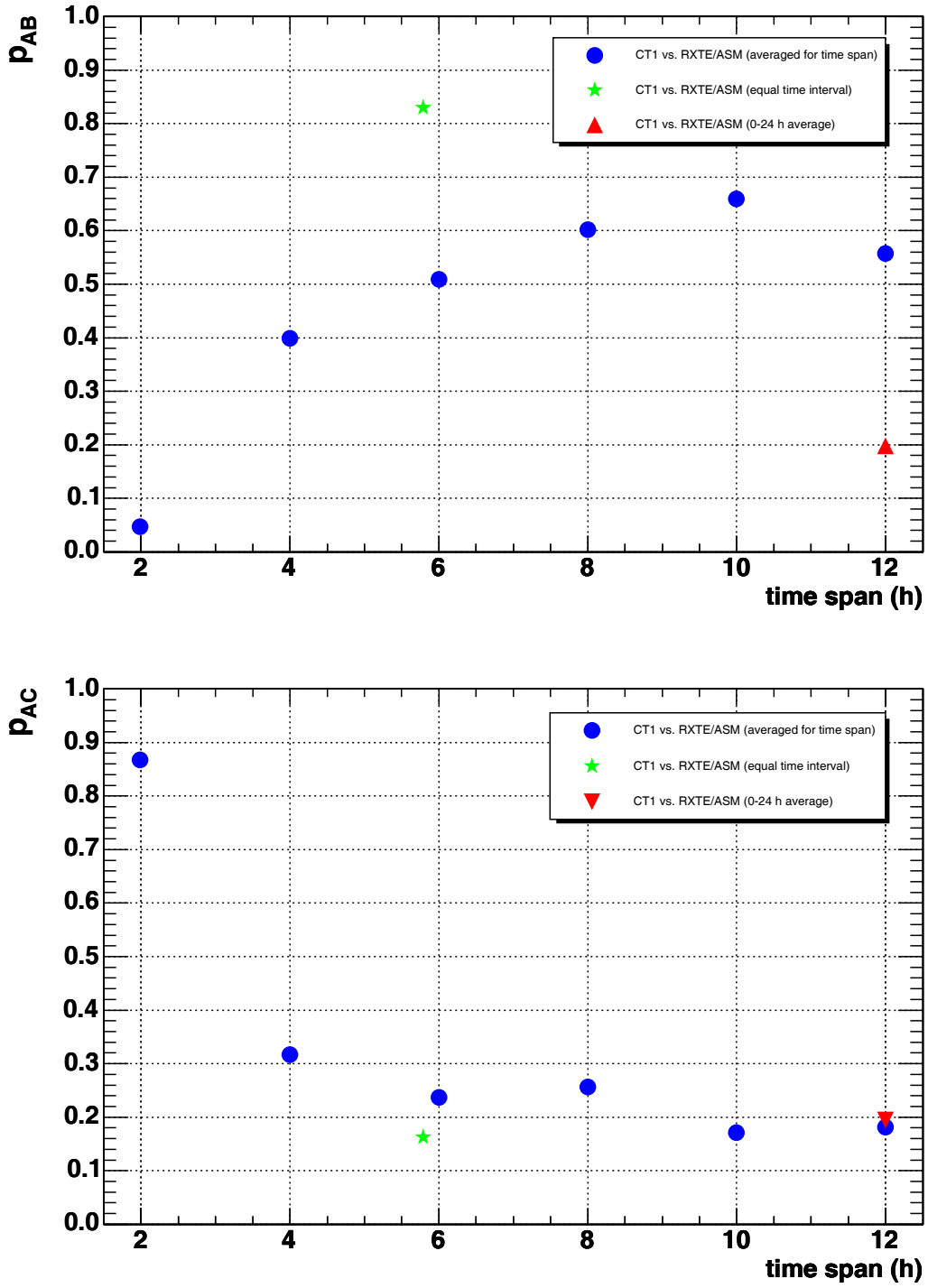

Figure 5.15: Probabilities p_{AB} and p_{AC} were calculated for each of 6 time spans from Figure 5.14 (RXTE/ASM data of Mkn 421 from 2003). Further, two more cases were added to be compared with (see text).

5.4.5 The KVA optical light curve

night (2003)	ΔMJD	<MJD>	$F_{\rm tot}$ (mJy)	F (mJy)
26/27 Feb	52696.96–52697.20	**52697.08**	20.4416 ± 0.0242	**12.3716 ± 0.4706**
27/28 Feb	52697.96–52698.20	**52698.08**	19.9280 ± 0.0238	**11.8580 ± 0.4706**
28 Feb/1 Mar	52698.95–52699.19	**52699.08**	18.9615 ± 0.0234	**10.8915 ± 0.4706**
1/2 Mar	52699.95–52700.19	**52700.07**	18.3009 ± 0.0229	**10.2309 ± 0.4706**
2/3 Mar	52700.95–52701.19	**52701.07**	18.6963 ± 0.0237	**10.6263 ± 0.4706**
3/4 Mar	52701.94–52702.18	**52702.05**	19.8592 ± 0.0261	**11.7892 ± 0.4707**
4/5 Mar	52702.95–52703.11	**52703.01**	20.5982 ± 0.0336	**12.5282 ± 0.4712**
5/6 Mar	52704.02–52704.18	**52704.10**	19.7740 ± 0.0268	**11.7040 ± 0.4708**

Table 5.6: KVA optical data of blazar Mkn 421 from the multiwavelength campaign in February and March 2003 (columns in bold are shown in Figure 5.16). $F_{\rm tot}$ is the total R-band flux and $F = F_{\rm tot} - F_{\rm host}$. The host galaxy flux is (**8.07 ± 0.47**) mJy (from very recent analysis of Kari Nilsson from Tuorla Observatory, Finland).

The correlation study of these data is presented in Section 6.2.2.

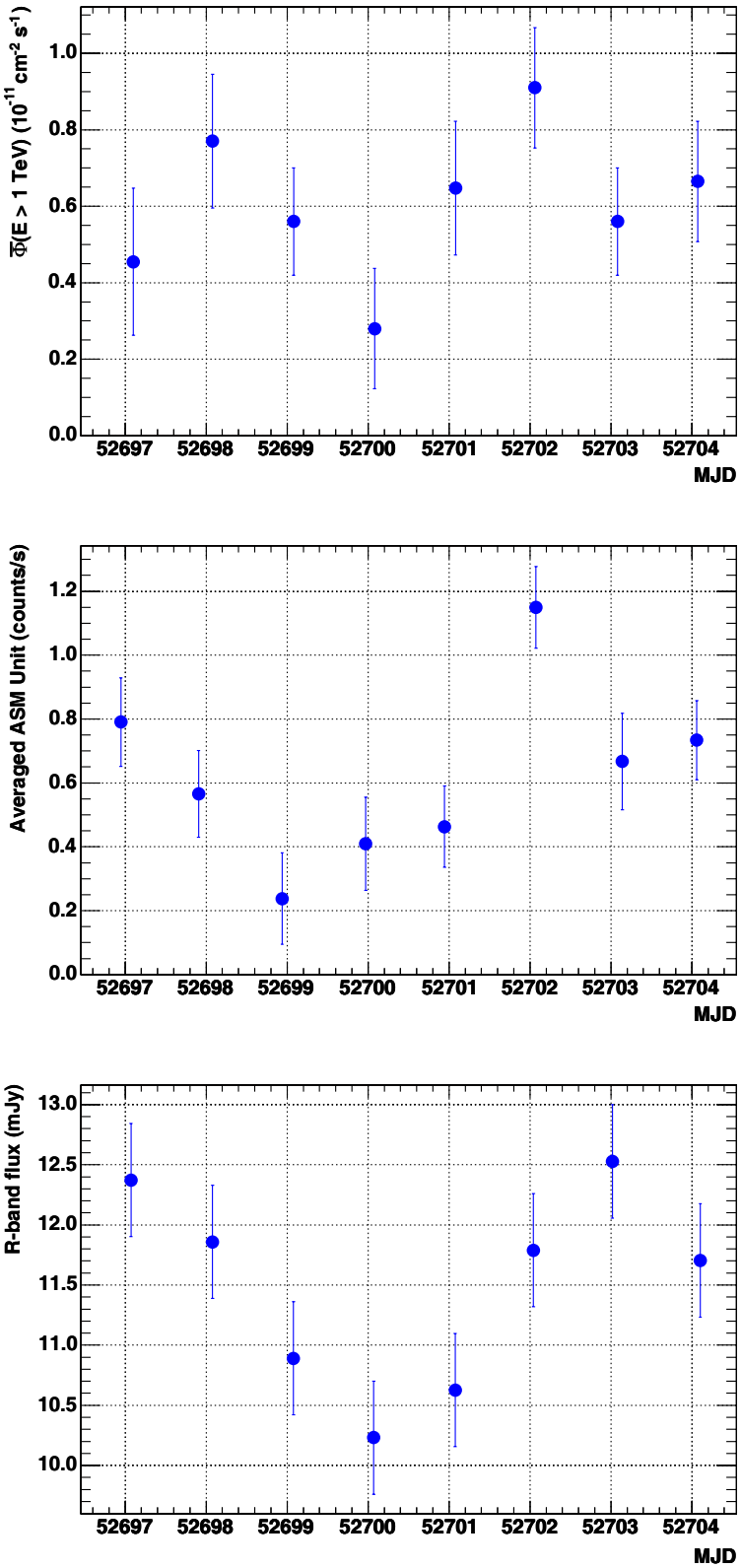

Figure 5.16: CT1 γ-ray flux above 1 TeV (upper panel), RXTE/ASM X-ray flux in ASM units (middle panel), and **KVA optical flux** in R-band (lower panel) from multi-wavelength campaign on Mkn 421 in February and March 2003.

5.5 Selected results from VAT simulations

We have generated 10 000 MC events of gamma-ray initiated EAS using *MAGIC Monte Carlo software* (Mmcs) [441], the Reflector v. 0.6 [360], and the Camera v. 0.7 [131].

In the Reflector code we have modified Elterman's aerosol data (Table 4.7) *in order to simulate clouds*. In principle, clouds are different from aerosols, but there is a strong connection between clouds and aerosols. Haze, some fogs, and **some clouds may be regarded as aerosols** [316] [456].

All events were generated for the CT1. The geometry of the CT1 reflector and camera were included as well as the telescope altitude and local geomagnetic[12] field value.

The events were generated in the energy range from 750 GeV to 10 TeV with the spectrum energy slope of -2.6. The impact parameter was up to 200 m, and ZA was 0^o (vertically incident showers). The trigger logic used in the simulations was the same as for the data analysis:
– a voltage **level** threshold equivalent to 13 photoelectrons (PE);
– two *next neighbor* (NN) pixels over the threshold in 6 ns (**topology**).

5.5.1 Trigger rate

In the study of the *trigger rate* (TR) we have chosen an altostratus cloud of 1000 m thickness. The relative trigger rate R means TR relative to the non-cloud (clear) conditions:

$$R = \frac{\mathrm{TR(cloud)}}{\mathrm{TR(clear)}}. \tag{5.70}$$

Figure 5.17 shows the dependence of R on the cloud base height h, for a fixed cloud water droplet density of 200 cm^{-3}. Each point represents 10 000 MC events. There is almost no dependence on the cloud base height.

h (km)	R (%)
3	83.7 ± 0.7
4	82.5 ± 0.7
5	82.8 ± 0.7
6	82.6 ± 0.9
7	82.9 ± 0.7

Table 5.7: The data shown in the Figure 5.17.

The Figure 5.18 shows the dependence of R on the cloud water droplet density of a 1000 m thick altostratus with the base height 4 km asl. Each point represents 10000 MC events. **The TR depends strongly on the water droplet density**. The droplet density is the most important cloud characteristic concerning VAT in the context of IACTs.

As far as we know, the only cloud study in the context of IACTs, done before ours, was the work of Badran [90] presented at 25^{th} ICRC in Durban. Badran claimed that a reasonable operating of CT may be around 500 m cloud thickness at which there is no dramatic change of its performance. Our VAT simulations have confirmed Badran's results. Although he was talking about *cirrus* clouds only, his LOWTRAN calculations

[12] The Earth's magnetic field values can be found at *http://www.ngdc.noaa.gov/seg/geomag/magfield.shtml*

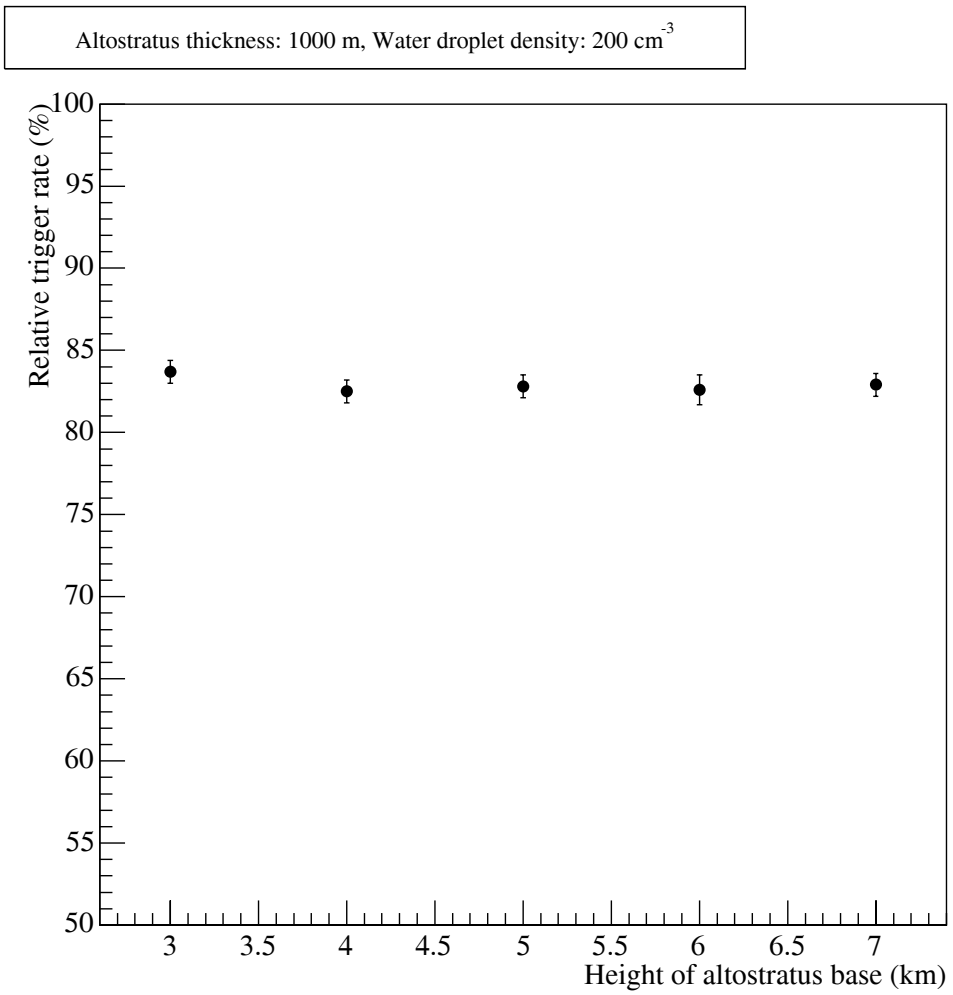

Figure 5.17: The height of an altostratus has no big impact on TR when the cloud is below the average Čerenkov light production height (about 10 km).

N (cm^{-3})	R (%)
100	91.3 ± 0.7
200	82.5 ± 0.7
300	73.5 ± 0.7
400	63.4 ± 1.0
500	52.1 ± 0.7
600	42.1 ± 0.8

Table 5.8: The data shown in the Figure 5.18.

refer to altostratus indeed[13].

These MC simulations have been used to show the reliability of the obtained results of VAT corrections.

[13]Cirrus clouds have thickness just about 100 m and base height above 6 km, while Badran's clouds have thickness up to 3500 m and base height only 2.6 km asl.

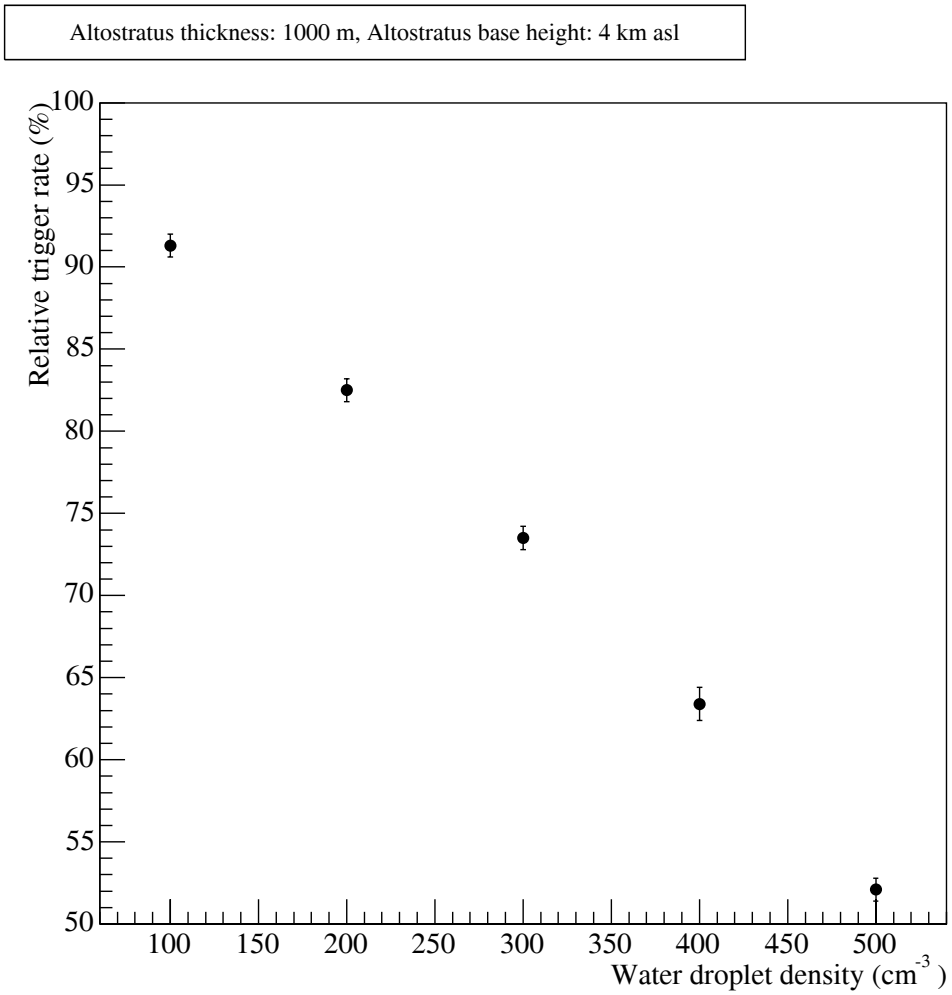

Figure 5.18: The trigger rate decreases almost linearly as the cloud droplet density increases.

5.6 VAT corrections on Mkn 421 (2001): the high state

In 2001, Mkn 421 underwent an extraordinary period of flaring activity. The source was observed by many ground-based telescopes (from radio to VHE $\gamma-$rays) and space-based telescopes (e.g. in X-rays).

The HEGRA CT1 observations of the 2001 flares of Mkn 421 were published [31] whereby 21 hours of data has been "excluded due to bad weather conditions". We found some of these data (14 hours in total) appropriate to test the throughput correction method. The observation times and conditions are listed in Table 5.9.

Evening date	**run#**	**obs. time/min**	$< \Delta TR_{rel} >$	**Extinction in r'**	**Comment**
February 14	12891, 12892 12897, 12898	80	-31 %	0.224	thin cloud most of night
February 20	13032, 13034	40	-41 %	0.150	some cloud
February 21	13058, 13067 13069, 13070 13072, 13074	120	-42 %	0.109	—
February 24	**13167**	**20**	$+6$ %	**0.102**	**reference data**
February 27	13244–13248 13252–13256 13259	220	-33 %	0.429	patchy cloud
March 1	13276–13279	80	-35 %	—	rain
March 26	13664–13667 13672, 13674	120	-29 %	—	some cloud
April 12	13856	20	-26 %	0.095	some cloud
April 14	13891	20	-29 %	0.112	—
April 15	13910, 13912 13917	60	-30 %	—	occasional cloud
April 17	13953, 13955	40	-31 %	0.112	rain at end of night
April 25	14055	20	-47 %	0.109	rain at start
May 14	14238	20	-39 %	0.134	—
		TOTAL: **14.0 h**			

Table 5.9: The CT1 data set of Mkn 421 from **February/May 2001** (12 nights + the reference night) with *variable atmospheric transmission* (VAT). Extinction values and comments on weather conditions are from *Carlsberg Meridian Telescope* (CMT).

The relative error of the mean trigger rate $< \Delta TR_{rel} >$ is

$$< \Delta TR_{rel} >= \frac{\frac{TR(\vartheta)}{\cos\vartheta} - TR_{nom}}{TR_{nom}} \tag{5.71}$$

where TR_{nom} is the nominal rate, the mean TR at zenith

$$TR_{nom} = < TR(\vartheta = 0^o) > = 3.48 \text{ Hz} \tag{5.72}$$

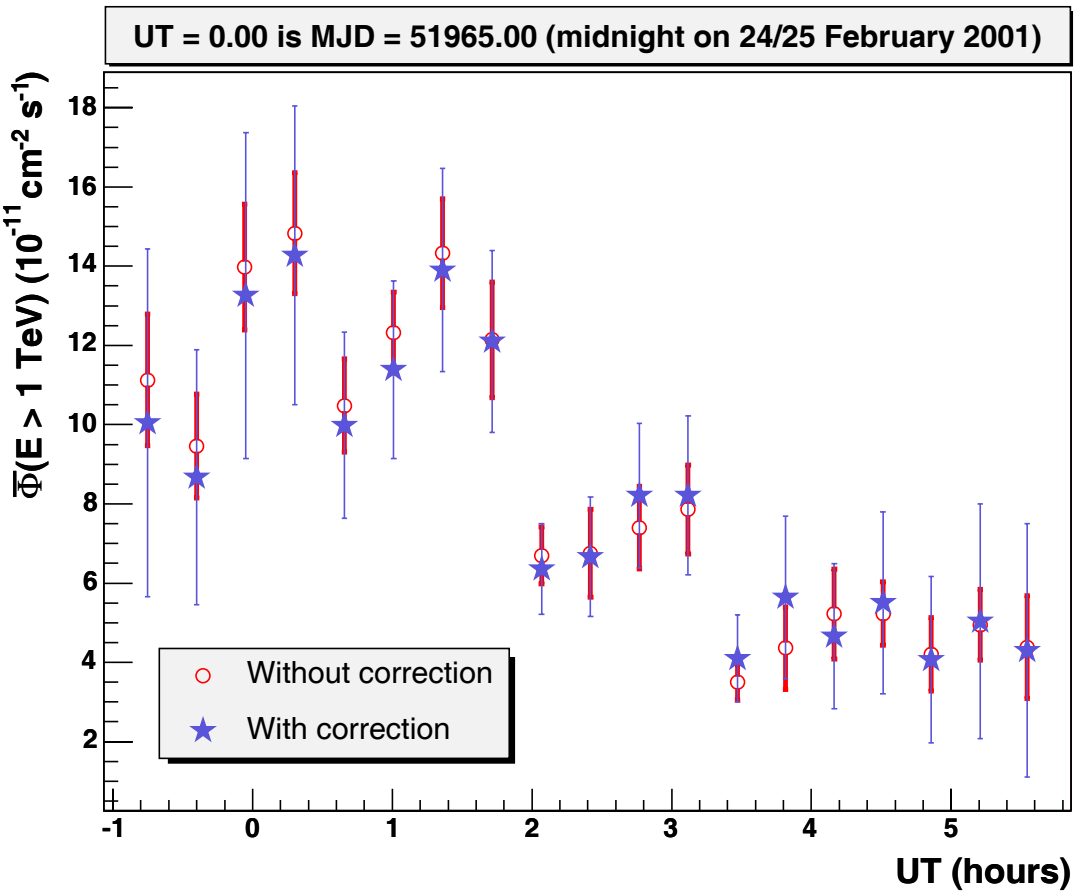

Figure 5.19: "Correction" of the reference night: the CT1 light curve of Mkn 421 for the observations on February 24/25, 2001 (19 runs in total).

MJD	$\overline{\Phi}$ (10^{-11}cm^{-2}s^{-1})	$\overline{\Phi}_{\rm corr}$ (10^{-11}cm^{-2}s^{-1})
51964.9687	11.13 ± 1.66	10.04 ± 4.39
51964.9833	9.46 ± 1.31	8.67 ± 3.21
51964.9980	13.94 ± 1.59	13.26 ± 4.12
51965.0126	14.83 ± 1.53	14.28 ± 3.77
51965.0274	10.48 ± 1.18	9.98 ± 2.35
51965.0421	12.32 ± 1.02	11.39 ± 2.24
51965.0567	14.33 ± 1.37	13.90 ± 2.56
51965.0715	12.14 ± 1.46	12.10 ± 2.29
51965.0862	6.70 ± 0.72	6.36 ± 1.15
51965.1008	6.75 ± 1.11	6.67 ± 1.50
51965.1154	7.40 ± 1.04	8.21 ± 1.83
51965.1299	7.86 ± 1.12	8.21 ± 2.01
51965.1446	3.50 ± 0.46	4.10 ± 1.10
51965.1590	4.36 ± 1.04	5.64 ± 2.05
51965.1735	5.22 ± 1.14	4.67 ± 1.83
51965.1880	5.23 ± 0.80	5.50 ± 2.30
51965.2024	4.20 ± 0.93	4.07 ± 2.10
51965.2170	4.95 ± 0.89	5.03 ± 2.96
51965.2310	4.38 ± 1.30	4.30 ± 3.20

Table 5.10: Data from Figure 5.19.

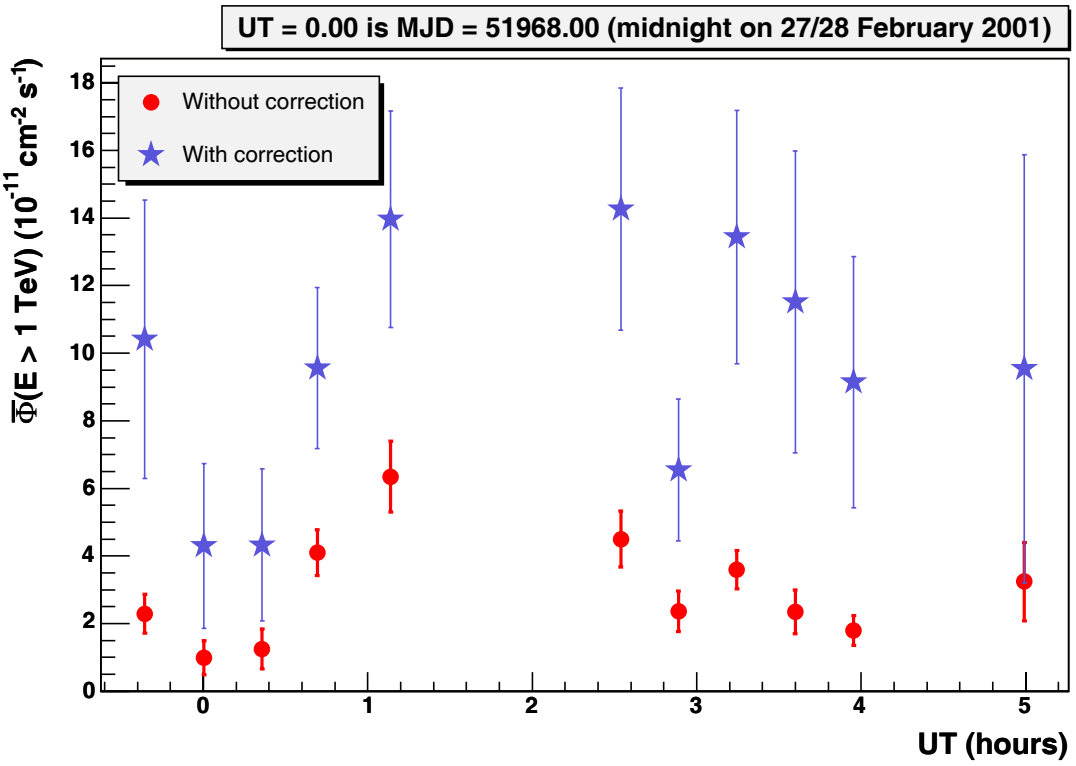

Figure 5.20: Correction of an example cloudy night: 11 runs of CT1 data set of Mkn 421 on February 27/28, 2001.

MJD	$\overline{\Phi}$ (10^{-11}cm^{-2}s^{-1})	$\overline{\Phi}_{\rm corr}$ (10^{-11}cm^{-2}s^{-1})
51967.9852	2.29 ± 0.58	10.41 ± 4.12
51968.0002	0.99 ± 0.50	4.30 ± 2.44
51968.0149	1.25 ± 0.59	4.33 ± 2.25
51968.0289	4.10 ± 0.68	9.56 ± 2.39
51968.0475	6.33 ± 1.05	13.97 ± 3.21
51968.1058	4.50 ± 0.83	14.27 ± 3.58
51968.1204	2.36 ± 0.60	6.55 ± 2.10
51968.1352	3.60 ± 0.57	13.44 ± 3.75
51968.1500	2.35 ± 0.65	11.52 ± 4.47
51968.1648	1.79 ± 0.44	9.14 ± 3.72
51968.2080	3.24 ± 1.16	9.54 ± 6.34

Table 5.11: Data from Figure 5.20.

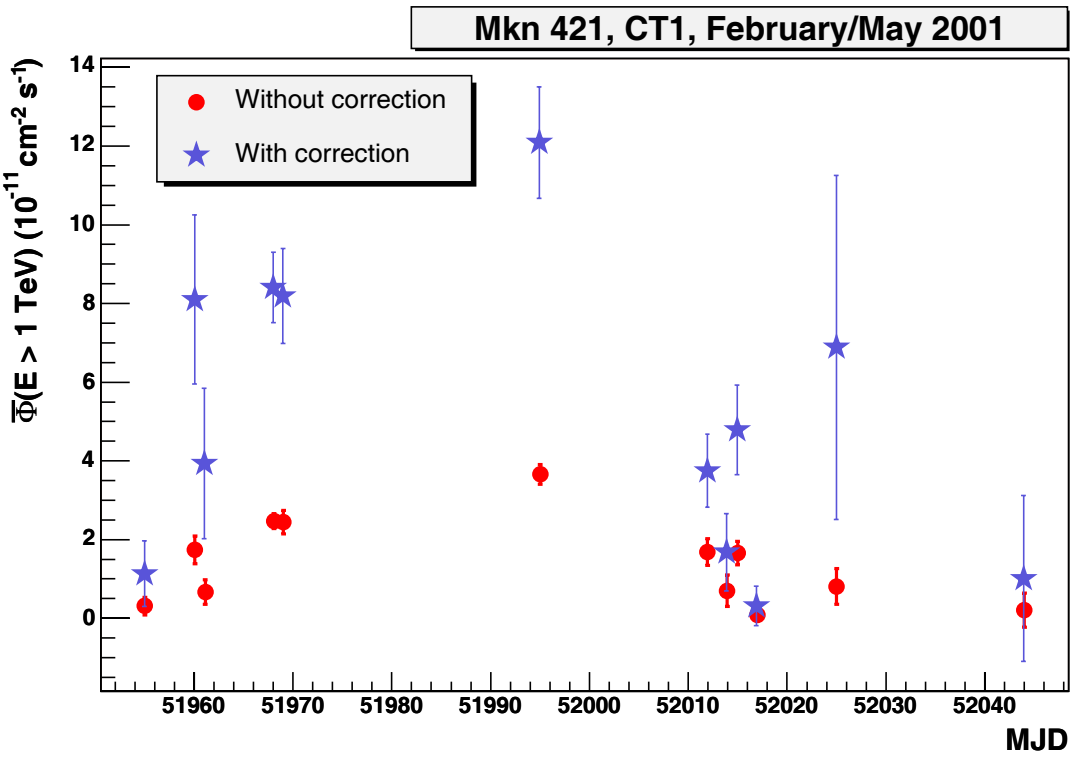

Figure 5.21: Nightly flux correction for CT1 data set of Mkn 421 in February/March 2001 (12 nights).

MJD	$\overline{\Phi}$ (10^{-11}cm^{-2}s^{-1})	$\overline{\Phi}_{\mathrm{corr}}$ (10^{-11}cm^{-2}s^{-1})
51955.01	0.31 ± 0.22	1.12 ± 0.83
51960.07	1.74 ± 0.35	8.09 ± 2.15
51961.13	0.67 ± 0.31	3.92 ± 1.91
51968.10	2.47 ± 0.19	8.40 ± 0.90
51969.09	2.43 ± 0.30	8.19 ± 1.21
51995.03	3.66 ± 0.25	12.07 ± 1.42
52011.95	1.68 ± 0.34	3.73 ± 0.93
52013.94	0.70 ± 0.40	1.66 ± 0.98
52014.99	1.66 ± 0.30	4.77 ± 1.14
52016.98	0.09 ± 0.16	0.30 ± 0.50
52025.00	0.81 ± 0.46	6.86 ± 4.37
52044.00	0.21 ± 0.43	0.99 ± 2.11

Table 5.12: Data from Figure 5.21.

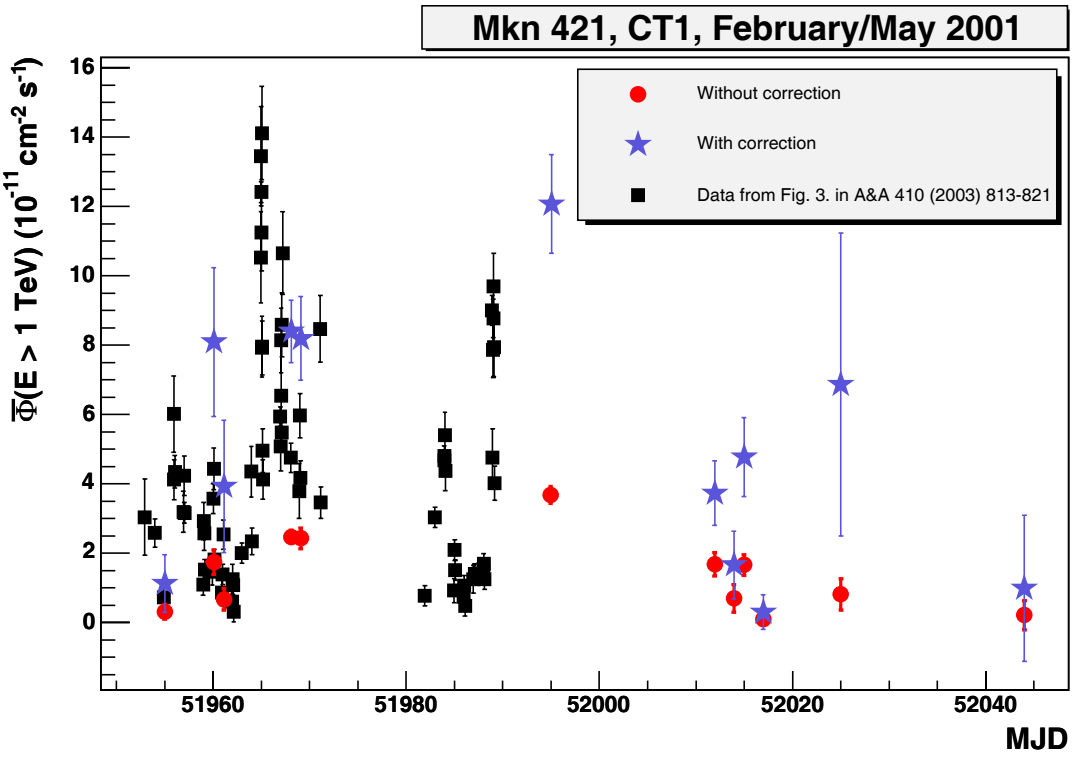

Figure 5.22: Combined plot: the data from Figure 5.21 (red circles and blue stars) altogether with the data published in [31] (black squares).

MJD	$\overline{\Phi}$ (10^{-11}cm^{-2}s^{-1})	MJD	$\overline{\Phi}$ (10^{-11}cm^{-2}s^{-1})
51952.9337	3.04 ± 1.10	51967.0105	5.07±0.70
51953.9679	2.58 ± 0.41	51967.0558	8.14±0.93
51954.9190	0.73 ± 0.34	51967.0739	6.55±1.43
51955.9442	6.02 ± 1.10	51967.0830	5.49±0.30
51955.9719	4.12 ± 0.57	51967.1192	8.58±0.92
51956.0548	4.34 ± 0.47	51967.2006	10.65±1.19
51956.9443	3.19 ± 0.59	51968.0515	4.75±0.43
51957.0211	4.24 ± 0.57	51968.9070	3.79±0.79
51957.0472	3.16 ± 0.30	51969.0019	5.97±0.64
51958.9643	1.09 ± 0.29	51969.0665	4.17±0.50
51959.0380	2.93 ± 0.54	51971.1139	8.47±0.96
51959.0791	2.57 ± 0.49	51971.1506	3.46±0.45
51959.1410	1.52 ± 0.29	51981.9261	0.77±0.29
51959.9318	1.46 ± 0.38	51982.9731	3.03±0.29
51960.0176	3.57 ± 0.43	51983.9507	4.80±0.29
51960.0729	4.43 ± 0.60	51983.9779	4.68±0.30
51960.1494	1.82 ± 0.30	51984.0105	5.40±0.66
51960.9395	0.86 ± 0.37	51984.0485	4.38±0.57
51961.0040	1.39 ± 0.29	51984.9556	0.92±0.34
51961.0743	2.53 ± 0.43	51985.0169	2.09±0.30
51961.9467	0.60 ± 0.29	51985.0851	1.51±0.30
51962.0170	1.25 ± 0.43	51985.9548	0.75±0.29
51962.0816	1.08 ± 0.29	51986.0254	1.07±0.29
51962.1402	0.31 ± 0.29	51986.1034	0.47±0.29
51962.9890	2.00 ± 0.29	51986.9621	1.25±0.40
51963.9631	4.35 ± 0.73	51987.0992	1.40±0.29
51964.0207	2.34 ± 0.38	51987.9647	1.53±0.29
51964.9561	10.53 ± 1.32	51988.0179	1.70±0.29
51964.9603	13.45 ± 1.43	51988.1057	1.25±0.29
51965.0076	12.42 ± 0.30	51988.9311	4.76±0.82
51965.0334	11.24 ± 1.10	51988.9753	8.97±0.43
51965.0407	14.12 ± 1.35	51989.0077	7.87±0.81
51965.0650	7.95 ± 0.88	51989.0116	8.77±0.56
51965.0931	7.92 ± 0.78	51989.0480	9.69±0.96
51965.1491	4.95 ± 0.63	51989.0843	7.93±0.84
51965.1682	4.12 ± 0.57	51989.1509	4.01±0.49
51966.9652	5.94 ± 0.28		

Table 5.13: Part of the data (black squares only) shown in Figure 5.22.

Chapter 6

Physics analysis

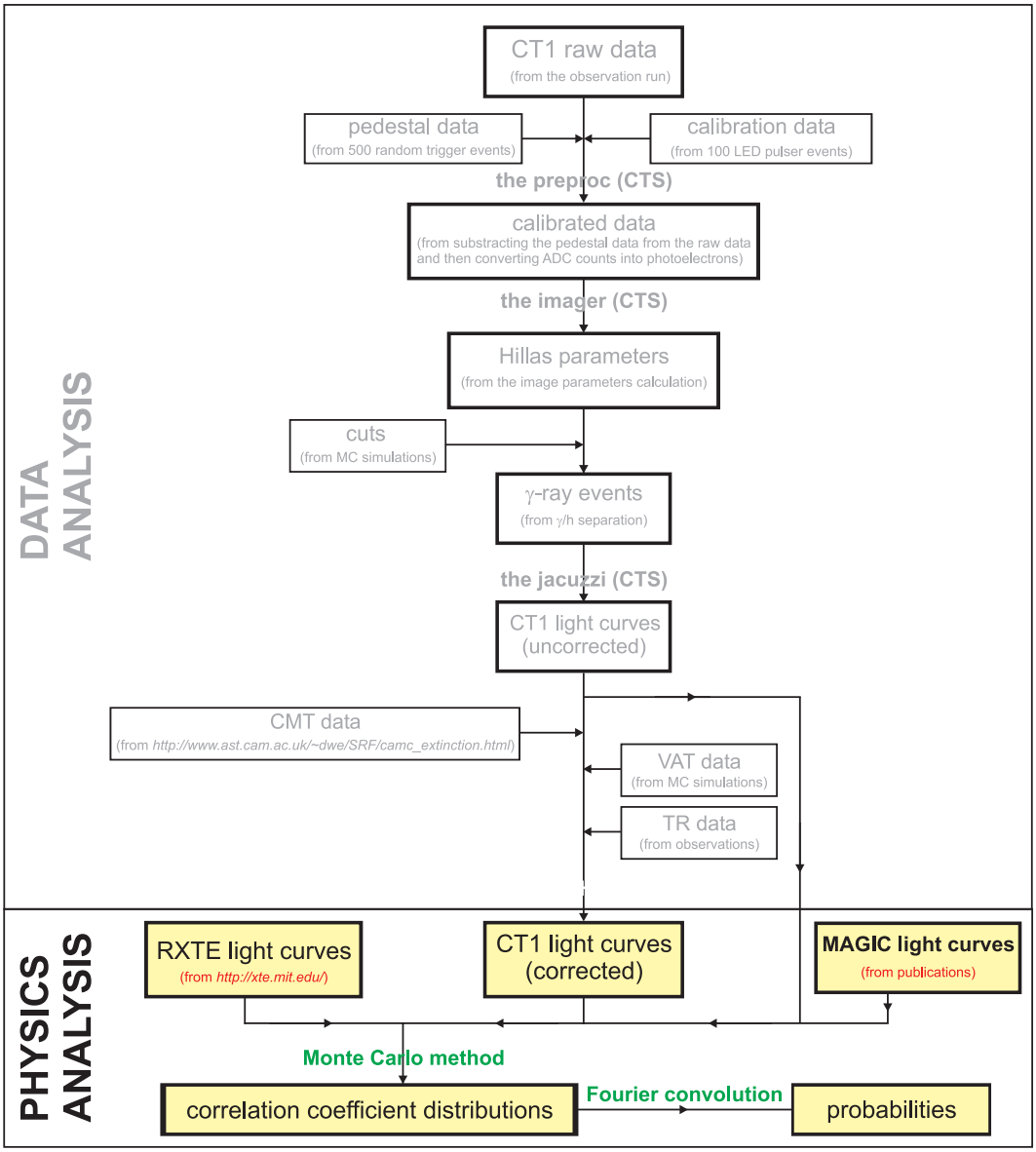

Figure 6.1: The analysis flowchart: the second part of the analysis (advanced analysis or hereafter **physics analysis**) includes all steps from the corrected light curves to the correlation coefficients and corresponding probabilities.

6A The analysis methods

6.1 New method for correlation analysis

6.1.1 Introduction to correlation study

Let x and y be two random variables. Correlation coefficient r is a dimensionless measure of the covariance σ_{xy} of x and y

$$r \stackrel{\text{def}}{=} \frac{\sigma_{xy}}{\sigma_x \sigma_y} \tag{6.1}$$

where σ_x and σ_y are standard deviations of x and y. The correlation coefficient r always lies in the interval $-1 \leq r \leq 1$. If x and y are independent then $r = 0$, but the opposite is not necessarily true [235]. Values of r close to ± 1 indicate a good correlation, while the values close to 0 show no correlation.

6.1.2 Common approach in ground-based γ-ray astronomy

The discrete correlation function

Linear correlation coefficient[1] of two data sets $(x_i, y_i) \quad \forall \quad i = 1, 2, 3, ..., n$ (from the definition above) is

$$r = \frac{\sum_i (x_i - \overline{x})(y_i - \overline{y})}{\sqrt{\sum_i (x_i - \overline{x})^2} \sqrt{\sum_i (y_i - \overline{y})^2}} \tag{6.2}$$

Edelson and Krolik [195] applied (6.2) to light curves, e.g. F_γ for TeV γ-rays and $R_{\rm X}$ for X-rays, introducing a possible time lag Δt between two data sets

$$r(\Delta t) = \frac{\sum_i \left(F_\gamma(t_i) - \overline{F_\gamma}\right)\left(R_{\rm X}(t_i + \Delta t) - \overline{R_{\rm X}}\right)}{\sqrt{\sum_i \left(F_\gamma(t_i) - \overline{F_\gamma}\right)^2 \sum_i \left(R_{\rm X}(t_i + \Delta t) - \overline{R_{\rm X}}\right)^2}}. \tag{6.3}$$

For the case of no time lag ($\Delta t = 0$), equation (6.3) coincides with the definition (6.2). This method is called the *discrete correlation function* (DCF). According to [195], the significance[2] is

$$S/\sigma = r \sqrt{\frac{n-2}{1-r^2}} \tag{6.4}$$

The standard deviation of the correlation coefficient r, according to [175], can be estimated as

$$\sigma_{\rm r} = \frac{1 - r^2}{\sqrt{n}} \tag{6.5}$$

Probabilities for correlation coefficients

For any given observed value $r_{\rm o}$, the probability $p_n(|r| \geq |r_{\rm o}|)$ means that n measurements of two uncorrelated variables x and y will give a correlation coefficient r as large as $r_{\rm o}$. If we obtain a coefficient $r_{\rm o}$ for which $p_n(|r| \geq |r_{\rm o}|)$ is small, then it is unlikely that our

[1] The extent to which n points fit a **straight line**.

[2] In normal English, *significant* means important, while in statistics *significant* means **probably true (not due to chance)**

variables are uncorrelated (it is likely that they are correlated). For example, if $p \leq 0.05$ the correlation is called *significant*, for $p \leq 0.01$ we call it *highly significant*.

The probability $p_n(|r| \geq |r_o|)$ can be calculated from the integral[3]

$$p_n(|r| \geq |r_o|) = \frac{2\Gamma(\frac{n-1}{2})}{\sqrt{\pi}\Gamma(\frac{n-2}{2})} \int_{r_o}^{1} (1-r^2)^{\frac{n-4}{2}} \mathrm{d}r \tag{6.6}$$

where Γ means gamma function (generalized factorial).

It is important to note that $p_n(|r| \geq |r_o|)$ depends strongly on n. For example, if the observed value of correlation coefficient is $r_o = 0.9$, but the number of measurements is just $n = 3$ then $p_3(|r| \geq 0.9) = 0.29$. It is not significant at all. We cannot claim that our variables are correlated although we have correlation coefficient 0.9. Otherwise, if $r_o = 0.9$, but $n = 7$ then $p_7(|r| \geq 0.9) = 0.006$. That is a highly significant result, and we can safely claim that our variables are correlated.

6.1.3 A new method for the correlation measurements of data with a finite variance in both dimensions

Motivation

A straightforward application of old formalism to data with finite measurement errors may lead to misleading conclusions. We have developed a numerical method that takes into account measurement errors, and reanalyzed the published data on X-ray and $\gamma-$ray correlations for blazars Mkn 180, Mkn 501 and Mkn 421 (data from 2001, 2003, and 2005) [207]. We found these data to be consistent with *realistic* expectations for complete correlation, even though the measured correlation coefficient would fall below 0.5 [207].

It is plausible that in a realistic measurement of a perfectly correlated phenomenon, performed with finite measurement precision, the correlation coefficient should always be smaller than one; the larger the error bars, the stronger the deviation of $|r|$ from unity. Knowing the measurement errors, one should be able to estimate the expectation value and the variance of r for any particular correlation case, including the perfectly correlated one [207].

We performed such an estimate using Monte Carlo simulations based on real data, modified to represent a hypothetical, perfectly correlated case. They demonstrated that, under realistic conditions of a typical X-ray/γ-ray correlation measurement, the expectation value for r should be significantly lower than 1 [207].

A perfectly correlated event that served as a seed in the Monte Carlo event generation was constructed by translation of each data point in the correlation plot (e.g. left panel in Figure 6.2) exactly to the straight line that fits the data[4], $F_\gamma = aF_x + b$, which results in the seed event shown in the right panel of Figure 6.2.

In this way, we have assured that the seed event has inherited most of the important features present in the data. The artificial points from the right panel of Figure 6.2 are then randomly smeared in both directions (up to 5σ) according to their individual error bars (assuming Gaussian statistics[5]), in a large ensemble of generated events (100,000 in

[3]For example, E.M. Pugh and G.H. Winslow, *The Analysis of Physical Measurements*, Addison-Wesley (1966).

[4]Each data point is translated to the line along the shortest path, measured in equal dimensionless intervals along x and y defined as $\Delta x/\sigma_x = \Delta y/\sigma_y$.

[5]Note that instead of the Gaussian function, some more realistic, either analytic or empirical function may be used.

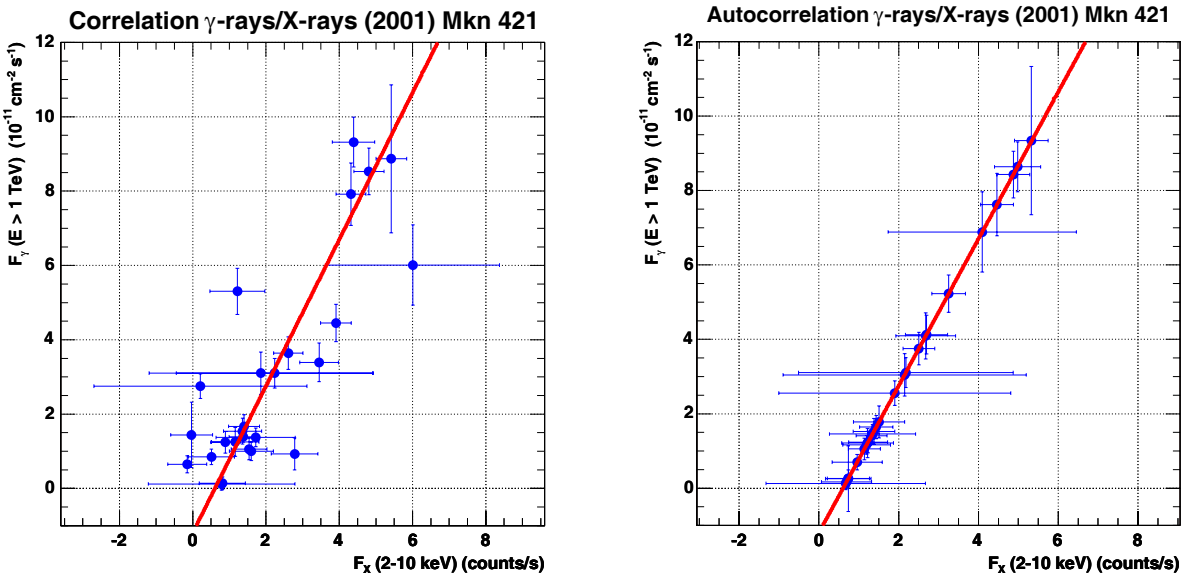

Figure 6.2: Left panel: an example of the correlation plot – data points from the HEGRA paper [31] (shown in Table 6.2 in this work). Right panel: a perfectly correlated event constructed by translation of each data point from left panel exactly to the straight line that fits the data.

the present analysis). The correlation coefficient is calculated for each of these events, and the probability density function $f_B(r)$ is formed, see Figure 6.5. We call $f_B(r)$ **autocorrelation** probability density function.

In the same way, but by smearing the actual data points, we calculated the probability density function $f_A(r)$ that represents the real measurement. Finally, to estimate the probability density function for the uncorrelated case, we created an ensemble of entirely randomized data points. The resulting distribution $f_C(r)$ (we call it **non-correlation** probability density function) is very similar to the analytically calculated distribution $f_D(r)$ that cannot take into account measurement errors (Figure 6.5). This is not surprising, since the smearing according to the error bars may add no more randomness to the already randomized seed events[6]. The width of the probability density distribution $f_D(r)$ depends exclusively on the number of points in the correlation plot (26 in Figure 6.5) [207].

The generation of the probability density distributions for the correlation coefficients

A *Monte Carlo* (MC) method is a numerical technique for calculating probabilities and relating quantities by using a sequence of random numbers[7]. MC is often the only practical way to sample random variables governed by complicated *probability density functions* (PDF) [498].

As a MC method, we have used von Neumann's acceptance-rejection technique[8] [498].

[6] In a modified approach, the fluctuations of fluxes to negative values may be rejected as unphysical. That has a visible consequence on all distributions including $f_C(r)$, which becomes asymmetric.

[7] A computer algorithm used to generate a sequence of uniformly distributed random numbers is called a *random number generator*.

[8] Original von Neumann's paper: J.Res.NBS Appl.Math.Ser. **12** (1951) 36

The method considers a PDF $f(x)$ which can be completely surrounded by a box between $x_{\min}$ and $x_{\max}$ and having height $f_{\max}$ as shown in Figure 6.3. A series of numbers

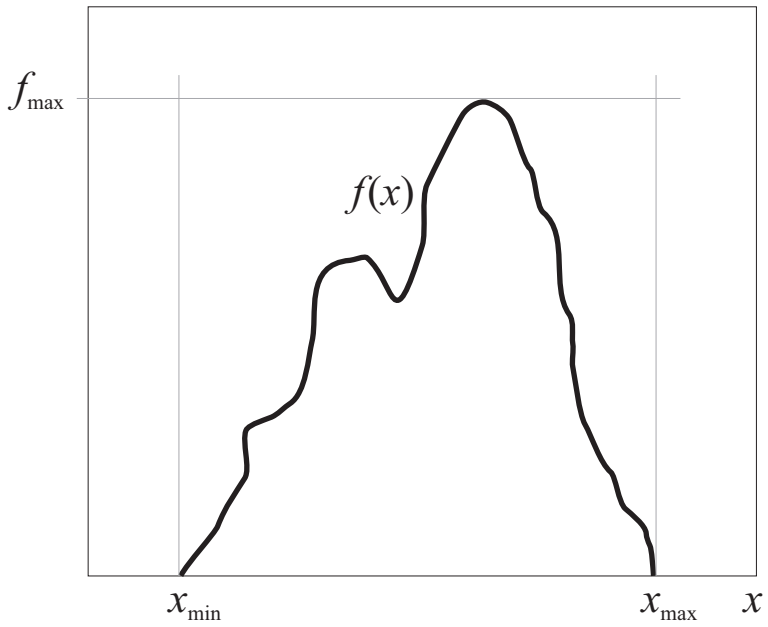

Figure 6.3: A *probability density function* (PDF) $f(x)$ enclosed by a box to generate random numbers using the acceptance-rejection (von Neumann) technique [498].

distributed according $f(x)$ can be generated using the following algorithm [175]:

- Generate a random number x, uniformly distributed between $x_{\min}$ and $x_{\max}$. For example, $x = x_{\min} + r_1(x_{\max} - x_{\min})$ where r_1 is uniformly distributed between 0 and 1.
- Generate a second independent random number u uniformly distributed between 0 and $f_{\max}$. For example, $u = r_2 f_{\max}$
- If $u < f(x)$, then accept x. If not, reject x.
- Repeat.

The efficiency of the algorithm (the fraction of x accepted) is the ratio of the area of the PDF to that of enclosing box $f_{\max}(x_{\max} - x_{\min})$ [175].

For the PDF $f(x)$, we have used Gaussian distribution. An example of our own C++ code can be found in the **Appendix C**.

Probability density functions

Let r be a *correlation coefficient* which can take any value from a continuous range from -1 to 1. We write $f(x)\mathrm{d}x$ as the probability that r lies between x and $x + \mathrm{d}x$. The function $f(x)$ is called *probability density function* (PDF) [235].

The measure of the correlation strength comes from the comparison of the probability density distribution $f_A(r)$ for the actual measurement with the distributions for the two extreme correlation cases, $f_B(r)$ (for perfectly correlated case) and $f_C(r)$ (for non-correlated case). For a quantitative comparison, we followed

the robust method from reference [387], based on the convolution of empirical probability density distributions; the comparison of a pair of probability density functions $f_X(r)$ and $f_Y(r)$ leads to **the probability that these two distributions are statistically consistent,** $P(f_X(r), f_Y(r))$. Hereafter, we use the following notation

$$p_{\mathrm{AB}} = P(f_A(r), f_B(r)) \tag{6.7}$$

$$p_{\mathrm{AC}} = P(f_A(r), f_C(r)) \tag{6.8}$$

Determination of the probability for the overlap of pairs of probaility density functions

We have used significance test for differences between two empirical distributions. It is based on the method of convolution which accommodates any form. This technique is used in mathematics and statistics to calculate the distribution of a sum of random variables. Such comparison has been often used by economists [388].

Let $f(x)$ and $g(y)$ be two PDFs where x and y are continuous, independent, random variables. Furthermore, let z be the difference (the distance between two distributions)

$$z = x + (-y) \tag{6.9}$$

The probability of the event z is defined as the union of all possible combinations of x and y which results is a difference of z [388]. For continuous function this relation is given as **Fourier convolution** of f an $-g$ [175] assuming that the distributions are ordered correctly (f is on the right of g)

$$h(z) = f \otimes (-g) = \int_{-\infty}^{\infty} f(x)g(-y)\mathrm{d}y = \int_{-\infty}^{\infty} f(z-(-y))g(-y)\mathrm{d}y \tag{6.10}$$

where $\otimes$ is used to denote the convolution operator, and $g(-y)$ indicate that the distribution of y is flipped around zero.

The corresponding cumulative distribution function of the difference of x and y is

$$H(z) = \int_{-\infty}^{z} h(z')\mathrm{d}z' \tag{6.11}$$

The one-sided probability for the null-hypothesis that there is no difference between probability density functions f and g is

$$H(0) = \int_{-\infty}^{0} h(z)\mathrm{d}z \tag{6.12}$$

The two-sided probability is

$$p = 2H(0) \tag{6.13}$$

which is 100% for full overlap and 0% for no overlap.

Equations (6.10)–(6.13) are generally not transparent to non-mathematicians, but the concept that they capture is both intuitive and simple. Basically, the convolution calculates the probability of each possible outcome, considering all possible combination of the two independent distributions [387].

The convolution integral (6.10) can be rewritten using the definition of integral

$$h(z) = f \otimes (-g) = \lim_{\Delta y \to 0} \sum_{-\infty}^{\infty} f(z-(-y))g(-y)\Delta y \tag{6.14}$$

When defined over a finite range, the above equation is sometimes referred to as a **one-dimensional discrete convolution** [387].

Concerning the discrete convolution, the associated cumulative distribution function is

$$H(z) = \sum_{-\infty}^{z} h(z')\Delta z' \tag{6.15}$$

We adapted this method to analyze discrete empirical distributions of correlation coefficients. Figure 6.5 shows an example of two CF distributions where $f(x)$ is *probability density function* (PDF) of correlation coefficients, and $g(x)$ is PDF for so called "auto correlation". Both distributions are just examples here, their origin and meaning will be explained in detail in the following sections.

An example: Fourier convolution applied to error propagation

Let us suppose that we have measured two independent quantities $x = \overline{a} + \sigma_{\mathrm{a}}$ and $y = \overline{b} + \sigma_{\mathrm{b}}$. The measurements x and y are normally distributed with mean values $\overline{a}$ and $\overline{b}$, and widths σ_{a} and σ_{b} as in Figure 6.4. Probability density functions $f(x)$ and $g(y)$ (from

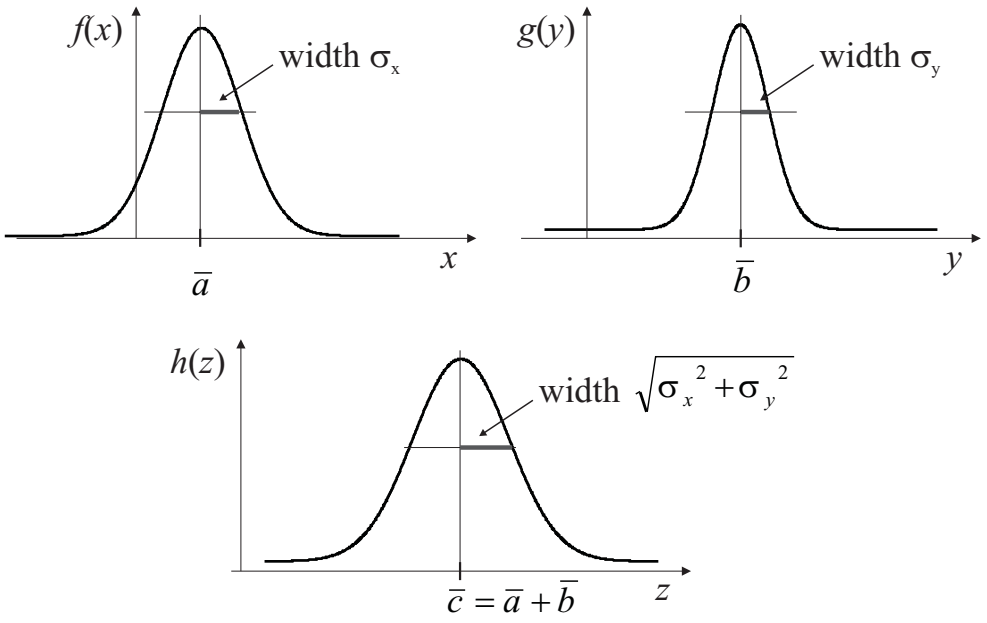

Figure 6.4: If the measurements of x and y are independent and normally distributed around $\overline{a}$ and $\overline{b}$, having widths σ_{a} and σ_{b}, then the calculated values of $z = x - y$ are normally distributed around $\overline{c} = \overline{a} - \overline{b}$, having width $\sigma_{\mathrm{c}} = \sqrt{\sigma_{\mathrm{a}}^2 + \sigma_{\mathrm{b}}^2}$.

Figure 6.4) are Gaussian functions

$$f(x) = \frac{1}{\sigma_a\sqrt{2\pi}} e^{-\frac{1}{2}\left(\frac{x-\overline{a}}{\sigma_a}\right)^2} \tag{6.16}$$

$$g(y) = \frac{1}{\sigma_b\sqrt{2\pi}} e^{-\frac{1}{2}\left(\frac{y-\overline{b}}{\sigma_b}\right)^2} \tag{6.17}$$

The values of the difference of two measured quantities $z = x - y$ are distributed according to a probability density function $h(z)$ which can be calculated **from Fourier convolution**

(6.10)

$$h(z) = \int_{-\infty}^{\infty} f(z+y)g(-y)\mathrm{d}y = \int_{-\infty}^{\infty} \frac{1}{\sigma_a\sqrt{2\pi}} e^{-\frac{1}{2}\left(\frac{z+y-\overline{a}}{\sigma_a}\right)^2} \frac{1}{\sigma_b\sqrt{2\pi}} e^{-\frac{1}{2}\left(\frac{-y+\overline{b}}{\sigma_b}\right)^2} \mathrm{d}y \tag{6.18}$$

$$h(z) = \frac{1}{2\pi\sigma_a\sigma_b} \int_{-\infty}^{\infty} e^{-\frac{1}{2}\left(\frac{z+y-\overline{a}}{\sigma_a}\right)^2 - \frac{1}{2}\left(\frac{y-\overline{b}}{\sigma_b}\right)^2} \mathrm{d}y \tag{6.19}$$

$$h(z) = \frac{1}{2\pi\sigma_a\sigma_b} e^{-\frac{1}{2}\frac{(z-\overline{a}+\overline{b})^2}{\sigma_a^2+\sigma_b^2}} \int_{-\infty}^{\infty} e^{-\frac{\sigma_a^2+\sigma_b^2}{2\sigma_a^2\sigma_b^2}\left(y-\frac{\overline{b}\sigma_a^2-(z-\overline{a})\sigma_b^2}{\sigma_a^2+\sigma_b^2}\right)^2} \mathrm{d}y \tag{6.20}$$

From the Gaussian integral

$$\int_{-\infty}^{\infty} e^{-x^2} \mathrm{d}x = \sqrt{\pi} \tag{6.21}$$

it follows that the values z are normally distributed according to probability density function $h(z)$

$$h(z) = \frac{1}{\sqrt{2\pi}\sqrt{\sigma_a^2+\sigma_b^2}} e^{-\frac{1}{2}\left(\frac{z-(\overline{a}-\overline{b})}{\sqrt{\sigma_a^2+\sigma_b^2}}\right)^2} \tag{6.22}$$

Finally, the center of the distribution $h(z)$ is

$$\overline{c} = \overline{a} - \overline{b} \tag{6.23}$$

and the width of the distribution $h(z)$ is

$$\sigma_c = \sqrt{\sigma_a^2 + \sigma_b^2} \tag{6.24}$$

We have justified the error-propagation formula for the special case of a difference, using Fourier convolution (6.10).

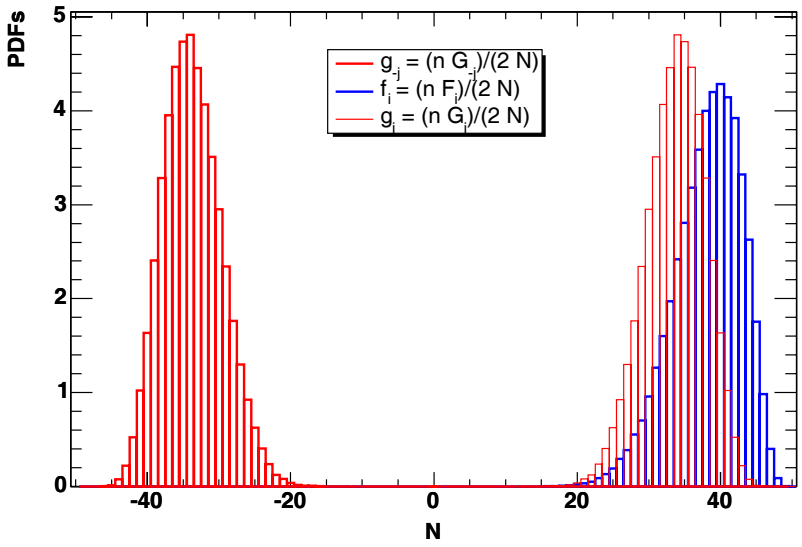

Figure 6.5: An example of two discrete empirical distributions f_i and g_j which have to be compared. The distributions are *probability density functions* (PDF). g_{-j} (bold red) is g_j (non-bold red) rotated around zero.

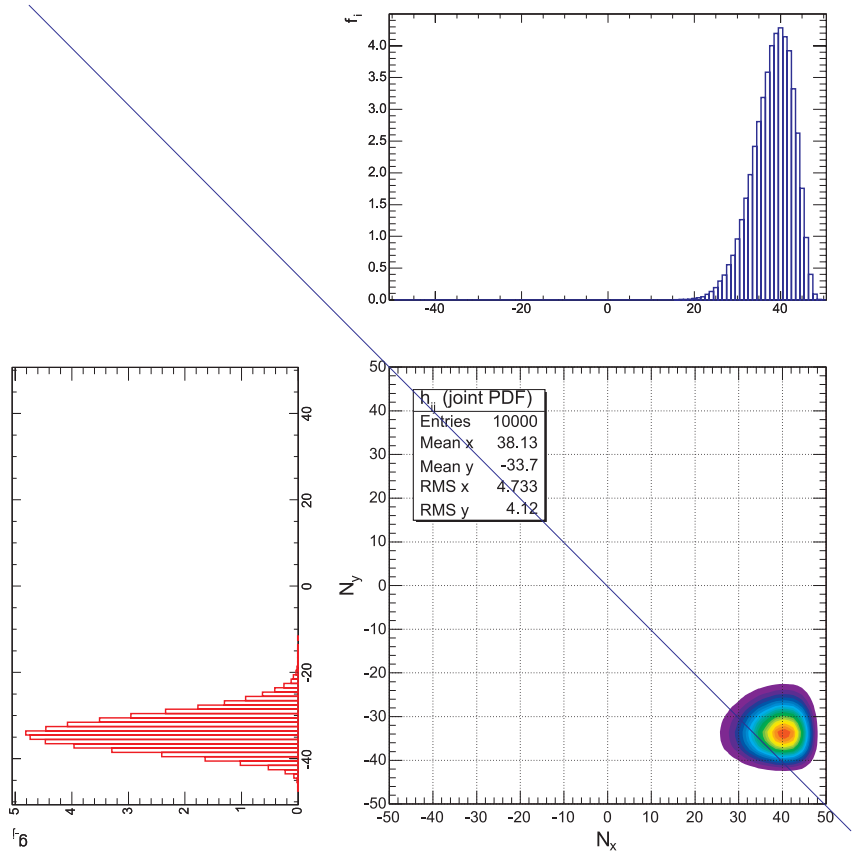

Figure 6.6: The joint *probability density function* (PDF) h_{ij} for discrete empirical distributions f_i and g_j from Figure 6.5.

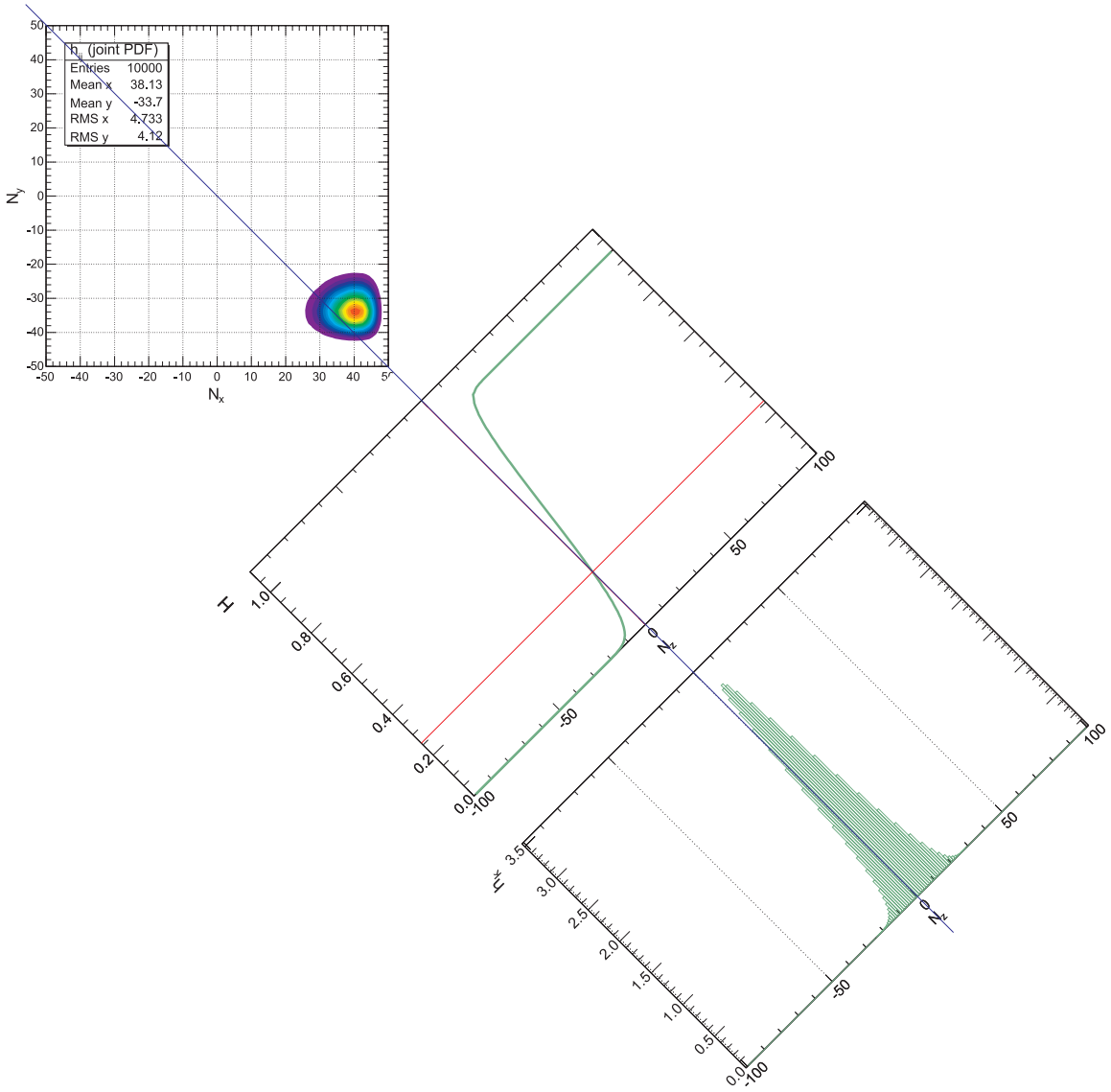

Figure 6.7: One-dimensional discrete convolution h_k and H distribution for two empirical discrete PDFs f_i and g_j defined in Figure 6.5.

The distributions are showed as histograms with n bins (100 in the example). Bin width is

$$\Delta x = \Delta y = \frac{r_{\max} - r_{\min}}{n} = \frac{2}{n} \tag{6.25}$$

where $r_{\max} = 1$ and $r_{\min} = -1$ are maximum and minimum value of CF.

F_i and G_j are number of events per bin which correspond to f and g distributions. Total number of events is N (100000 in the example)

$$N = \sum_i F_i = \sum_j G_j \tag{6.26}$$

Discrete PDFs are defined as

$$f_i = \frac{F_i}{N} \frac{n}{2} \tag{6.27}$$

$$g_j = \frac{G_j}{N}\frac{n}{2} \tag{6.28}$$

and they are normalized

$$\sum_i p_i = \sum_i f_i \Delta x = \sum_i \frac{F_i}{N} \cdot \frac{n}{2} \cdot \frac{2}{n} = \frac{1}{N}\sum_i F_i = 1 \tag{6.29}$$

$$\sum_j p_j = \sum_j g_j \Delta y = \sum_j \frac{G_j}{N} \cdot \frac{n}{2} \cdot \frac{2}{n} = \frac{1}{N}\sum_j G_j = 1 \tag{6.30}$$

The joint PDF h_{ij} (Figure 6.6) is

$$h_{ij} = f_i g_j \Delta y = \frac{2}{n} f_i g_j \tag{6.31}$$

The one-dimensional discrete convolution, corresponding to equation (6.14), is

$$\boxed{h_k = \sum_{j=1}^{k} h_{n-k+j,j}} \tag{6.32}$$

as shown in Figure 6.7. The one-sided probability, corresponding to equation (6.12), is

$$H(0) = \frac{2}{n}\sum_{k=1}^{n} h_k \tag{6.33}$$

Figure 6.7 shows also H distribution. $H(0)$ is denoted by a vertical line. The two-sided probability

$$p = 2H(0) \tag{6.34}$$

should be, in discrete form, corrected by subtracting one half of the main diagonal. Finally,

$$\boxed{p = \frac{2}{N^2}\left(\sum_{k=1}^{n}\sum_{j=1}^{k} F_j G_{n-k+j} - \frac{1}{2}\sum_{j=1}^{n} F_j G_j\right)} \tag{6.35}$$

In a case of two non-overlapping distributions, equation (6.35) gives $p \equiv 0$. Figure 6.8 illustrate such an example. For two equal distributions, equation (6.35) gives $p \equiv 1$. Such an example is shown in Figure 6.9.

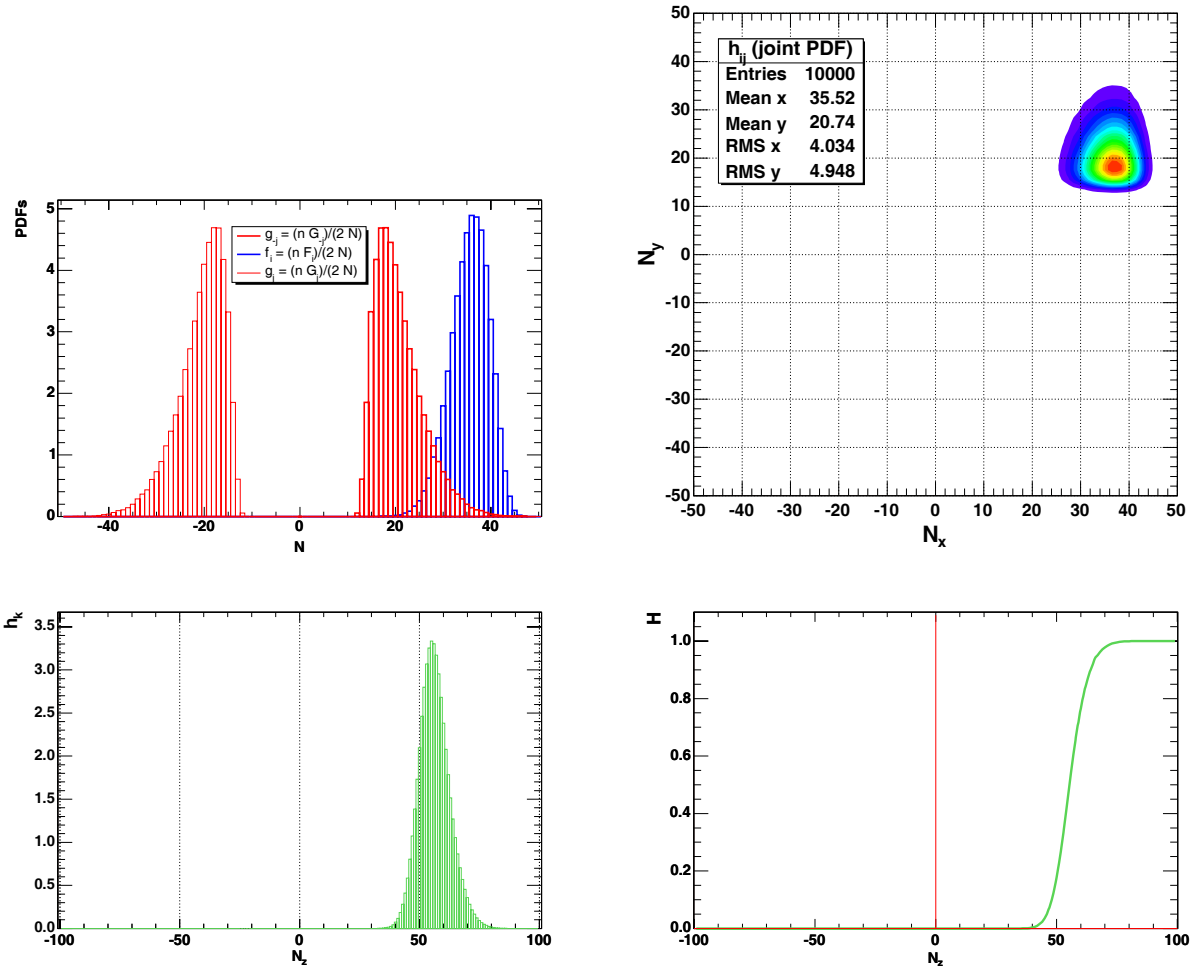

Figure 6.8: An example of two non-overlapping distributions. Upper panel: two discrete empirical distributions f_i and g_j, chosen to be **non-overlapping** (left) and corresponding joint PDF distribution (right). Lower panel: one-dimensional discrete convolution h_k (left) and H distribution (right). The probability is $p = 2H(0) \equiv 0$.

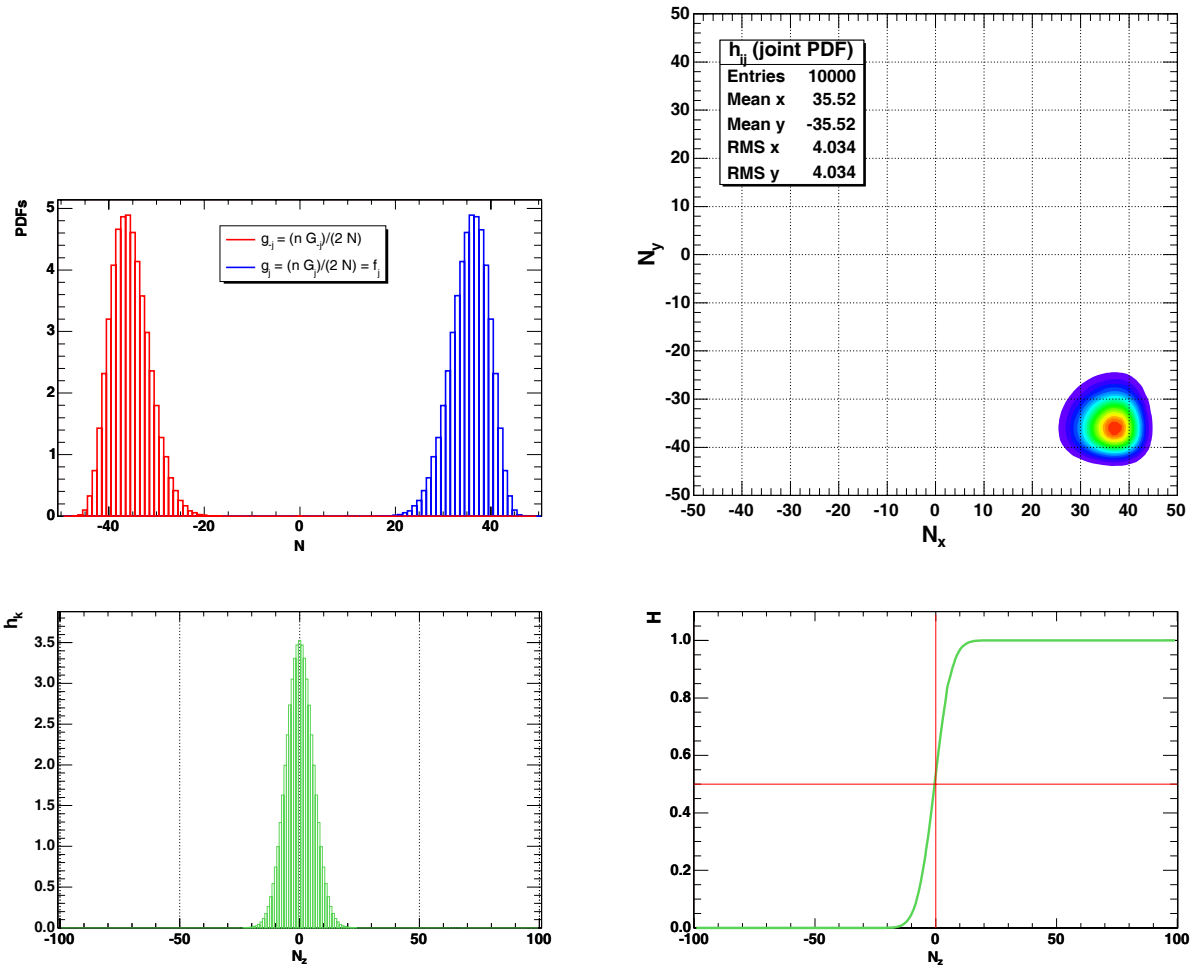

Figure 6.9: An example of two **equal** discrete distributions. Upper panel: two equal distributions $f_i = g_i$ (left) and corresponding joint PDF distribution (right). Lower panel: one-dimensional discrete convolution h_k (left) and H distribution (right). The probability is $p = 2H(0) \equiv 1$.

6.1.4 Discussion of the uncertainties in the determination of the probability for the overlap of pairs of probability density functions

Here we presented a study of several possible sources of systematic error in the determination of the probability for the overlap of pairs of *probability density functions* (PDF).

The influence of the choice of random numbers used in the formation of probability density functions on the overlap probability

We repeated, 50 times, the whole procedure of probability p_{AC} calculation for an example data set in order to study the influence of the choice of random numbers used in the formation of PDFs on the overlap probability. Each time we changed only the seed for random number generator for MC simulation of correlation coefficient distributions f_i and g_j. Both, histogram and fitted Gaussian (Figure 6.10) give an estimation of error Δ_p= **0.001**. Therefore, the influence of the choice of random numbers on the overlap probability is **negligible** compared to other sources (discussed below).

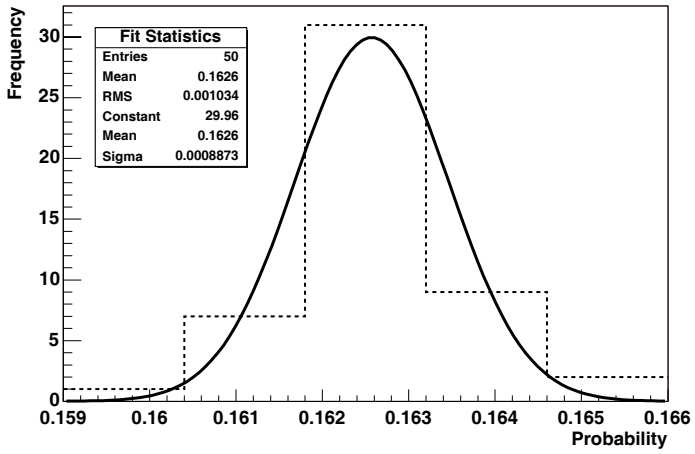

Figure 6.10: The solid red line is fitted Gaussian for 50 values of p_{AC}, which give an estimation of error $\Delta_p = 0.001$.

The influence of the statistical fluctuations of the data points and the method of the seed event formation, on the determination of the overlap probability

Another possible source of systematic errors in the determination of the probabilities p_{AB} and p_{AC} are statistical fluctuations of the data points and the method of the seed event formation. The seed event (e.g. right panel of Figure 6.2) is a hypothetical, perfectly correlated case which we construct by translation of each data point in the correlation plot exactly to the straight line that fits the data (as described in Section 6.1.3).

In order to obtain a large ensemble of MC generated events, we randomly smeared the artificial points in both directions (up to $\pm 5\sigma$) according to their individual error bars. This procedure sometimes gives negative value of fluxes. For all data sets analyzed in this thesis (in Chapter 6B), we allowed fluxes to be negative. In principle, we can request

positive fluxes only (what is resonable from a physical point of view). As a consequence, corresponding PDFs will be slightly deformed, and the overlap probabilities will be slightly different.

We calculated probabilities p_{AB} and p_{AC}, as defined in equations 6.7 and 6.8, for two example of data sets:
(1) Mkn 421 from 2001 as an example of flaring phase (Table 6.2);
(2) Mkn 421 from 2003 as an example of quiet phase (Tables 5.3 and 5.5);
We used the difference of the probabilities

$$\Delta p = \mid p(\text{negative fluxes allowed}) - p(\text{negative fluxes NOT allowed}) \mid \tag{6.36}$$

as an estimation of the uncertainty. For two data sets described above, we obtained the following values:
(1) $\Delta p_{\mathrm{AB}} = 0.018, \;\; \Delta p_{\mathrm{AC}} = 0.001$;
(2) $\Delta p_{\mathrm{AB}} = 0.014, \;\; \Delta p_{\mathrm{AC}} = 0.009$.

Therefore, we estimate that the influence of this effect on the overlap probability is up to $\Delta p = \mathbf{0.02}$.

Furthermore, we studied the overlap of no-correlation PDF and autocorrelation PDF (f_{B} and f_{C}, as described in Section 6.1.3). Corresponding probability p_{BC} is used as a good estimation of the error on probabilities p_{AB} and p_{AC}.

We also calculated a probability $p_{\mathrm{AE}} = P(f_{\mathrm{A}}, f_{\mathrm{E}})$, where f_{E} is a PDF formed analogusly to f_{B}: by translation of each data point in the correlation plot to the straight line **perpendicular** to the straight line that fits the data (Figure 6.11). Therefore, p_{AE} is

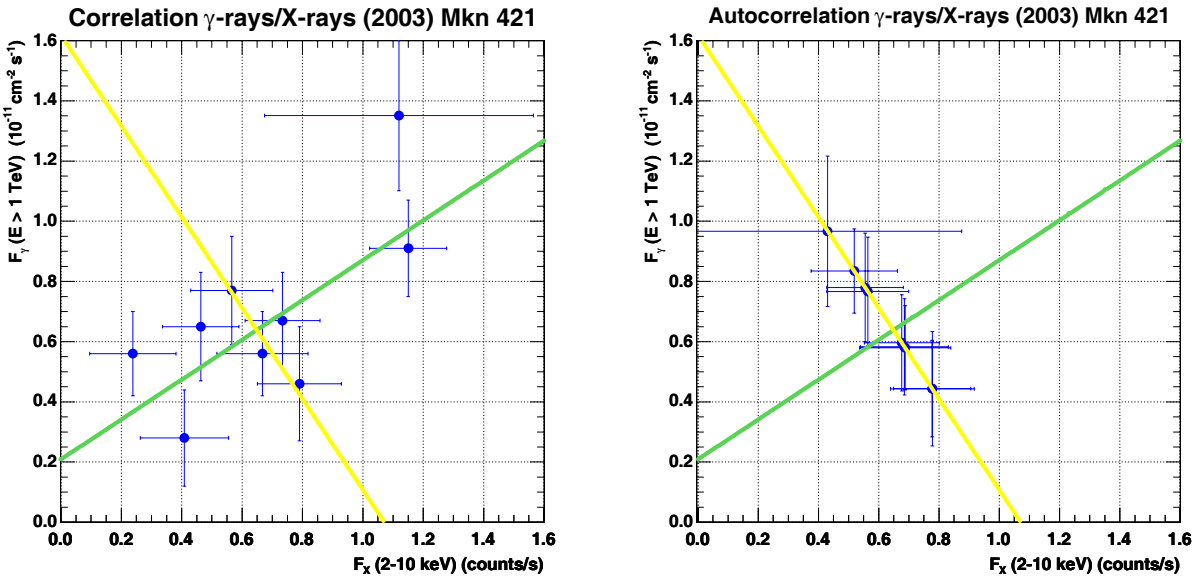

Figure 6.11: Correlation plot: 2003 – CT1/RXTE – Mkn 421. The green line is the straight line that fits the data (according equation (6.39)). The yellow line is a line perpendicular to the green one. It goes through the center of gravity of data points.

the overlap probability of PDFs f_{A} and f_{E} (Figure 6.12). We calculate probabilities p_{BC} and p_{AE} for all available data sets used in the thesis. Table 6.1 shows the results of this calculations as well as final estimations of maximum absolute errors on probability, Δp.

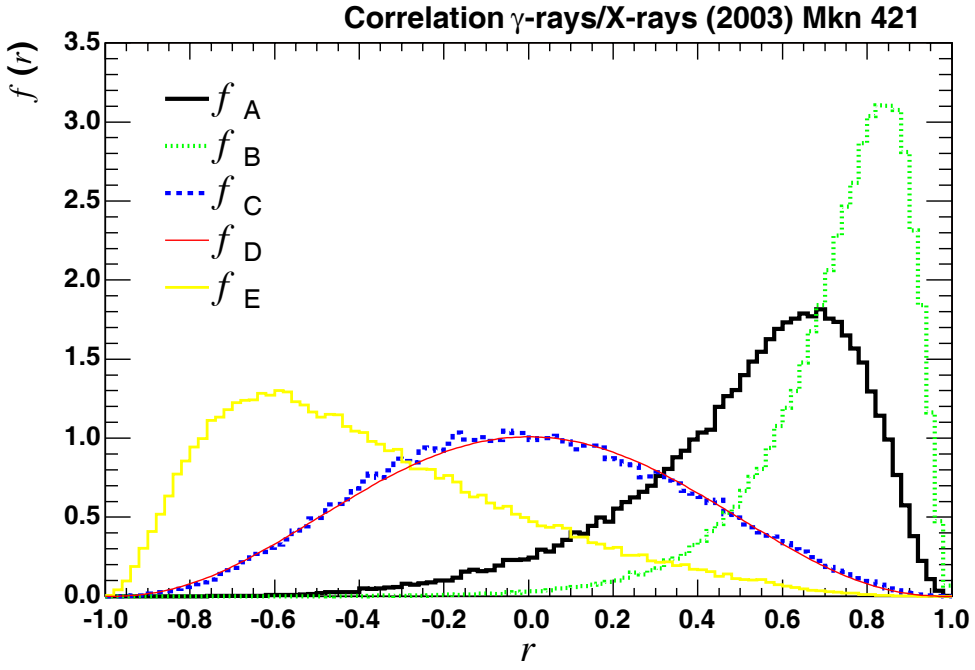

Figure 6.12: Correlation coefficient distribution: 2003 – CT1/RXTE – Mkn 421. The green distribution is an autocorrelation distribution formed by translation of the data points to the green line in Figure above. The yellow distribution is an autocorrelation distribution formed by translation of the data points to the yellow line in Figure above.

source	p_{AE}	p_{BC}	Δ_p
Mkn 421 (2001) γ/X	$\approx$0	0.0007	**0.01**
Mkn 421 (2003) γ/X	0.071	0.067	**0.07**
γ/o	0.53	0.31	**0.53**
X/o	0.15	0.05	**0.15**
Mkn 421 (2005) γ/X	0.001	0.038	**0.04**
γ/o	0.008	0.017	**0.02**
Mkn 180 (2006) γ/X	0.31	0.25	**0.31**
Mkn 501 (2005) γ/X	$\approx$0	0.07	**0.07**
γ/o	0.14	0.34	**0.34**

Table 6.1: Final estimations of maximum absolute errors Δ_p on probabilities p_{AB} and p_{AC}, for all data sets analyzed in the thesis.

The influence of the error bars and the slope of the fitted line on the overlap probability

Finally, we studied the influence of the error bars and the slope of the fitted line on the overlap probability. As an example, we took a set of 10 points: (1,1), (2,2),... (10,10) that lie on the straight line $y = x$ (red line in Figure 6.13).

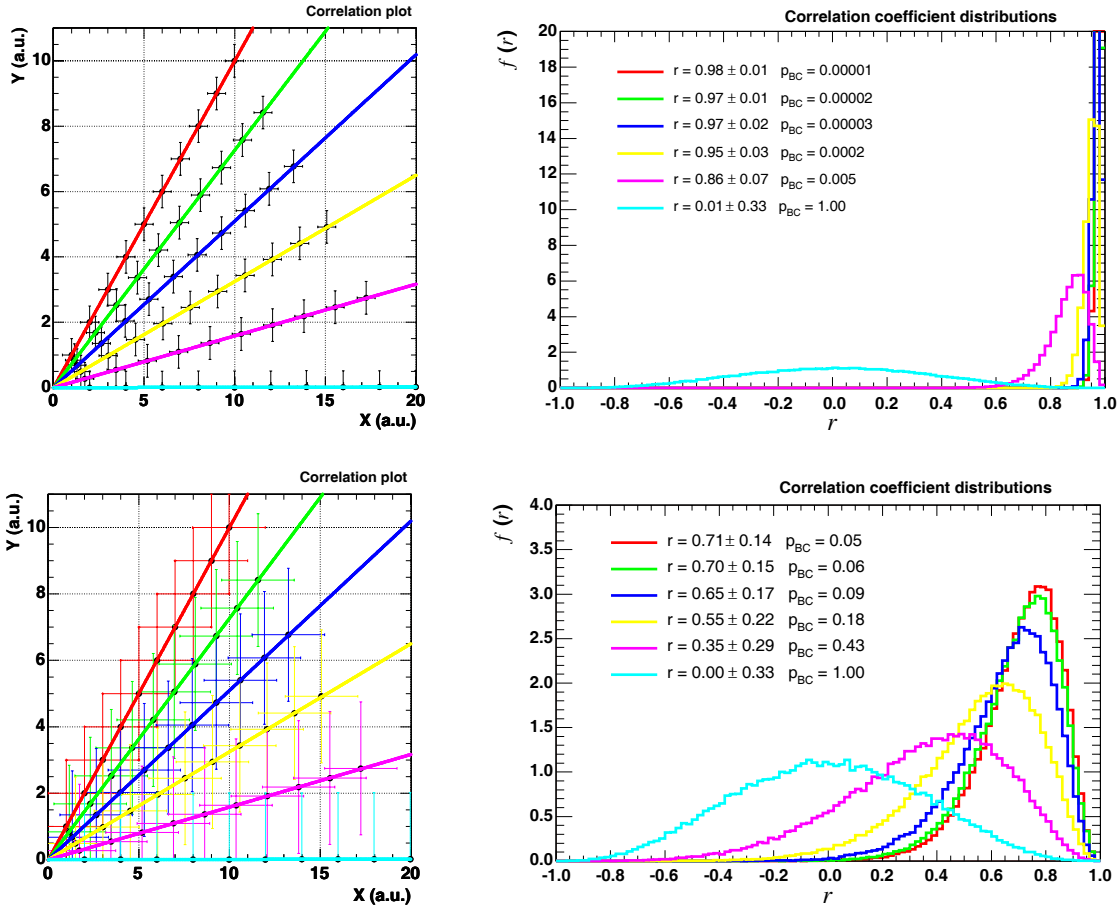

Figure 6.13: The influence of error bars and slope of a fitted line on the autocorrelation distribution (as defined in Section 6.1.3). In upper panels, the error bars are 0.5, and in lower panel they are 2.0.

If we ignore the error bars, correlation coefficient of these points is exactly one, as well as for point lying on the green, blue, yellow or pink line. Correlation coefficient for a set of points lying on the turquoise line is, however, zero. If we take into account the error bars, then correlation coefficients (according our MC generated PDFs) are lower than one, and depend strongly on the error bars and the slope of fitted line. In horizontal (or vertical) case we have $r \to 0$, as for the data points without errors.

Therefore, if the fitting line is far from being diagonal the corresponding correlation coefficient is small (in limit, goes to zero), even for so called "perfect" correlation. As a consequence of large error bars and high slope (almost horizontal or almost vertical), the probability p_{BC} (**our best estimation of the probability uncertainty**) is also large (in limit, goes to one). In such a case, no valid conclusion about correlation can be established.

6B Results and discussion

6.2 Correlations

We fitted all correlation plots (F_γ vs $F_{\rm X}$ and F_γ vs $F_{\rm opt}$) using both errors, vertical and horizontal. Therefore, instead of an usual definition of chi-square (using vertical errors only)

$$\chi^2 = \sum_i \left(\frac{y_i - f(x_i)}{\sigma_{{\rm y}i}} \right)^2 \tag{6.37}$$

here we have used generalized definition of chi-square (using both errors)

$$\chi^2 = \sum_i \frac{\left(y_i - f(x_i)\right)^2}{\sigma_{{\rm y}i}^2 + \left[\sigma_{{\rm x}i} f'(x_i)\right]^2} \tag{6.38}$$

For a linear fit $f(x) = ax + b$

$$\chi^2 = \sum_i \frac{\left(y_i - f(x_i)\right)^2}{\sigma_{{\rm y}i}^2 + \left[a\sigma_{{\rm x}i}\right]^2} \tag{6.39}$$

The probability $p(\chi^2, d)$ that a chi-square value, calculated for an experiment with d degrees of freedom, is due to chance is

$$p(\chi^2, d) = \left[2^{d/2}\Gamma(d/2)\right]^{-1} \int_{\chi^2}^{\infty} z^{d/2-1} e^{-z/2} {\rm d}z \tag{6.40}$$

where $\Gamma(x)$ is the gamma function, generalization of the factorial function to real and complex arguments:

$$\Gamma(x) = \int_0^{\infty} z^{x-1} e^{-z} {\rm d}z \tag{6.41}$$

We were calculating $p(\chi^2, d)$ numerically using the *Chi-Square Calculator*[9].

Furthermore, in order to find the fitting parameters a (slope) and b (intercept) we have used a standard *Minuit* fitting routine[10].

6.2.1 Mkn 421 (2001) CT1/RXTE

In the **Appendix C** we describe in detail how we produced correlation coefficient distributions (e.g. Figure 6.15). **Appendix C** also contains our full codes for calculation of corresponding probabilities $p_{\rm AB}$ and $p_{\rm AC}$.

[9]The Calculator is available on *http://www.fourmilab.ch/rpkp/experiments/analysis/chiCalc.html*
[10]The Minuit Home Page is *http://seal.web.cern.ch/seal/snapshot/work-packages/mathlibs/minuit/*

CT1 γ-ray flux $(10^{-11}\mathrm{cm}^{-2}\mathrm{s}^{-1})$	RXTE/ASM count rate (counts/s)
6.01 ± 1.08	6.01 ± 2.36
8.87 ± 1.99	5.42 ± 0.42
9.32 ± 0.67	4.39 ± 0.58
8.53 ± 0.63	4.81 ± 0.41
7.92 ± 0.84	4.32 ± 0.41
5.30 ± 0.62	1.22 ± 0.75
4.45 ± 0.50	3.91 ± 0.42
3.39 ± 0.52	3.45 ± 0.53
3.64 ± 0.44	2.61 ± 0.40
3.10 ± 0.40	2.24 ± 2.69
3.10 ± 0.57	1.86 ± 3.05
2.75 ± 0.33	0.21 ± 2.91
1.44 ± 0.88	−0.03 ± 0.57
0.65 ± 0.23	−0.15 ± 0.53
0.85 ± 0.21	0.51 ± 0.63
0.93 ± 0.43	2.78 ± 0.64
0.12 ± 0.17	0.79 ± 2.00
0.14 ± 0.17	0.81 ± 0.63
1.37 ± 0.25	1.72 ± 1.08
1.06 ± 0.29	1.54 ± 0.49
1.00 ± 0.25	1.60 ± 0.60
1.24 ± 0.29	0.89 ± 0.40
1.25 ± 0.39	1.16 ± 0.65
1.67 ± 0.31	1.40 ± 0.42
1.54 ± 0.35	1.36 ± 0.52
1.39 ± 0.15	1.38 ± 0.39

Table 6.2: Data shown in Figure 6.14 (26 data points) which we took from the HEGRA paper [31] (Figure 7 in the paper).

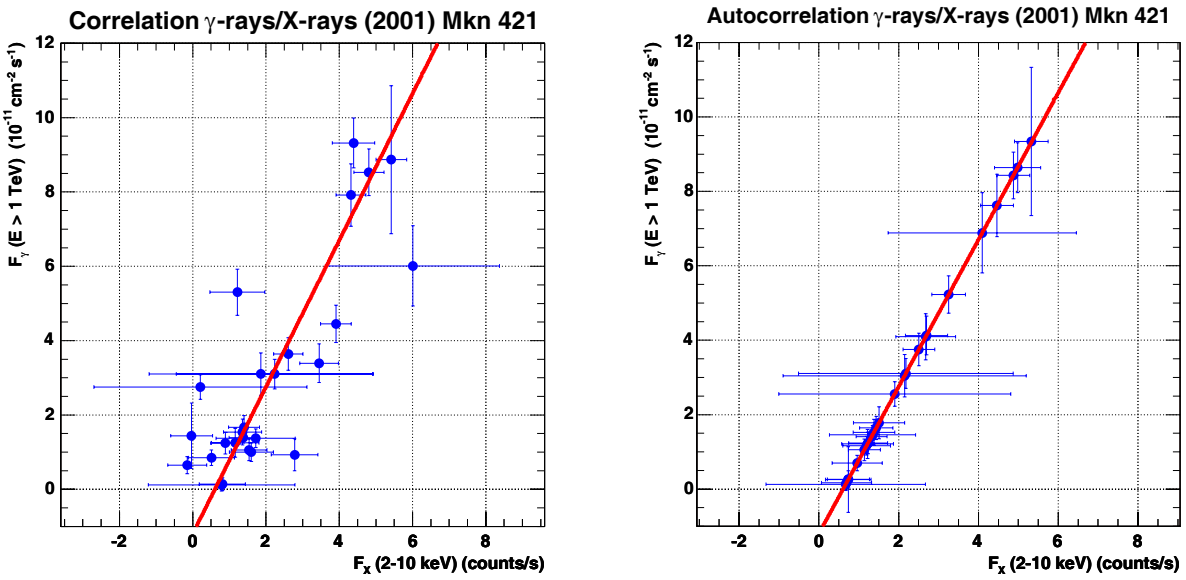

Figure 6.14: Correlation plot: 2001 – CT1 – Mkn 421. Data points from the HEGRA paper [31] (shown in Table 6.2 in this work). $\chi^2/\mathrm{ndf} = 35.2/24$ (Probability $= 0.065$) $F_\gamma = (1.97 \pm 0.18)\cdot 10^{-11}\mathrm{cm}^{-2}\mathrm{counts}^{-1} F_\mathrm{x} - (1.20 \pm 0.45)\cdot 10^{-11}\mathrm{cm}^{-2}\mathrm{s}^{-1}$

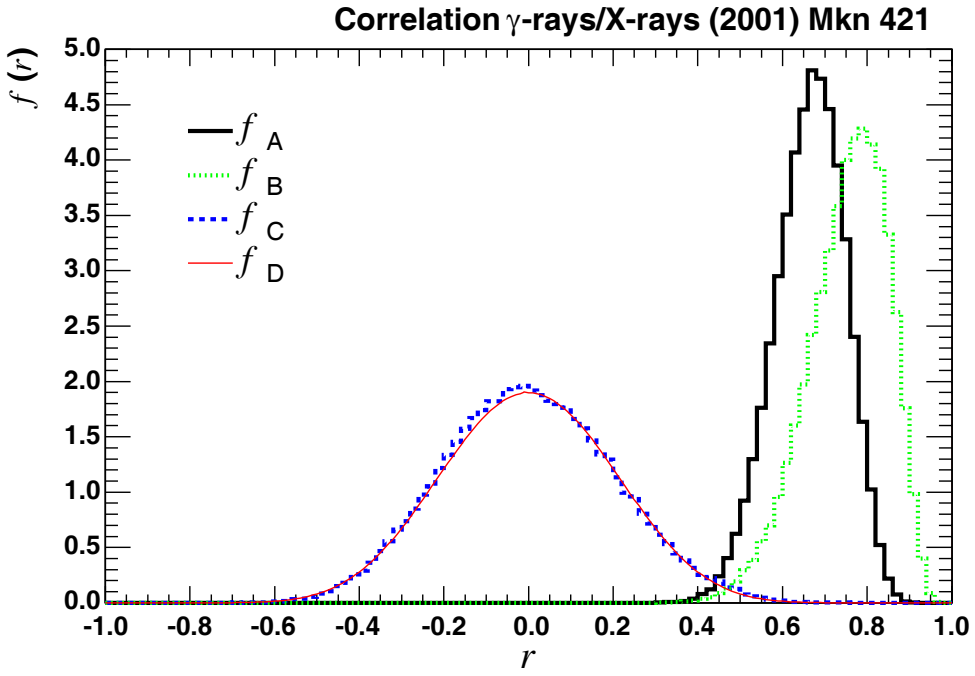

Figure 6.15: Correlation coefficient distribution: 2001 – CT1/RXTE – Mkn 421. Data points from the HEGRA paper [31] (Table 6.2). 100000 MC events were generated for each PDF. $r_\mathrm{MC} = 0.66 \pm 0.08$, $p_\mathrm{AB} = 0.47 \pm 0.01$, $p_\mathrm{AC} = 0.002^{+0.010}_{-0.002}$.

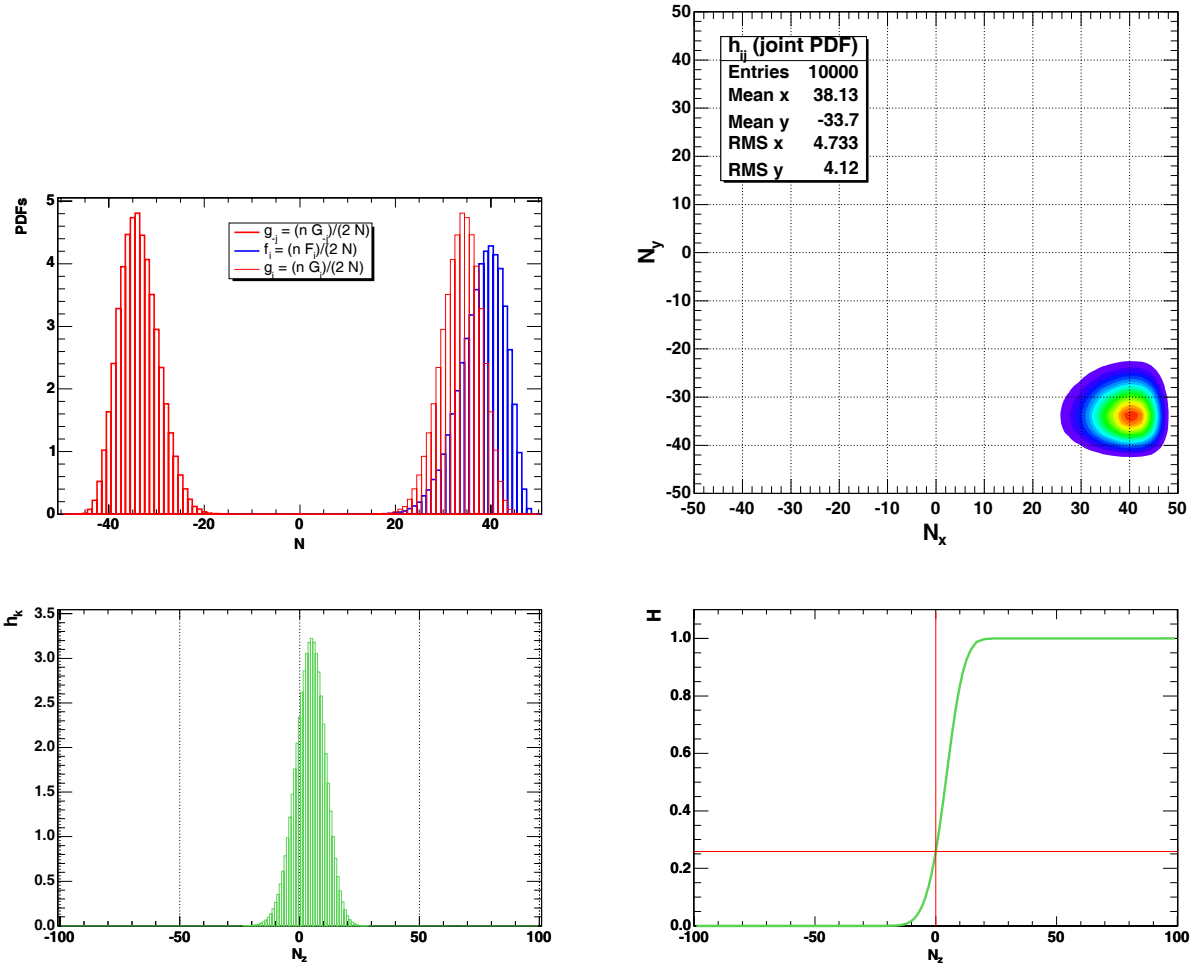

Figure 6.16: Upper panel: autocorrelation distribution f_i and distribution of randomized data g_j, both from Figure 6.15 (left) and corresponding joint PDF distribution (right). Lower panel: one-dimensional discrete convolution h_k (left) and H distribution (right). The probability is $p_{\mathrm{AB}} = 2H(0) = 0.47 \pm 0.01$. Source of data: [31].

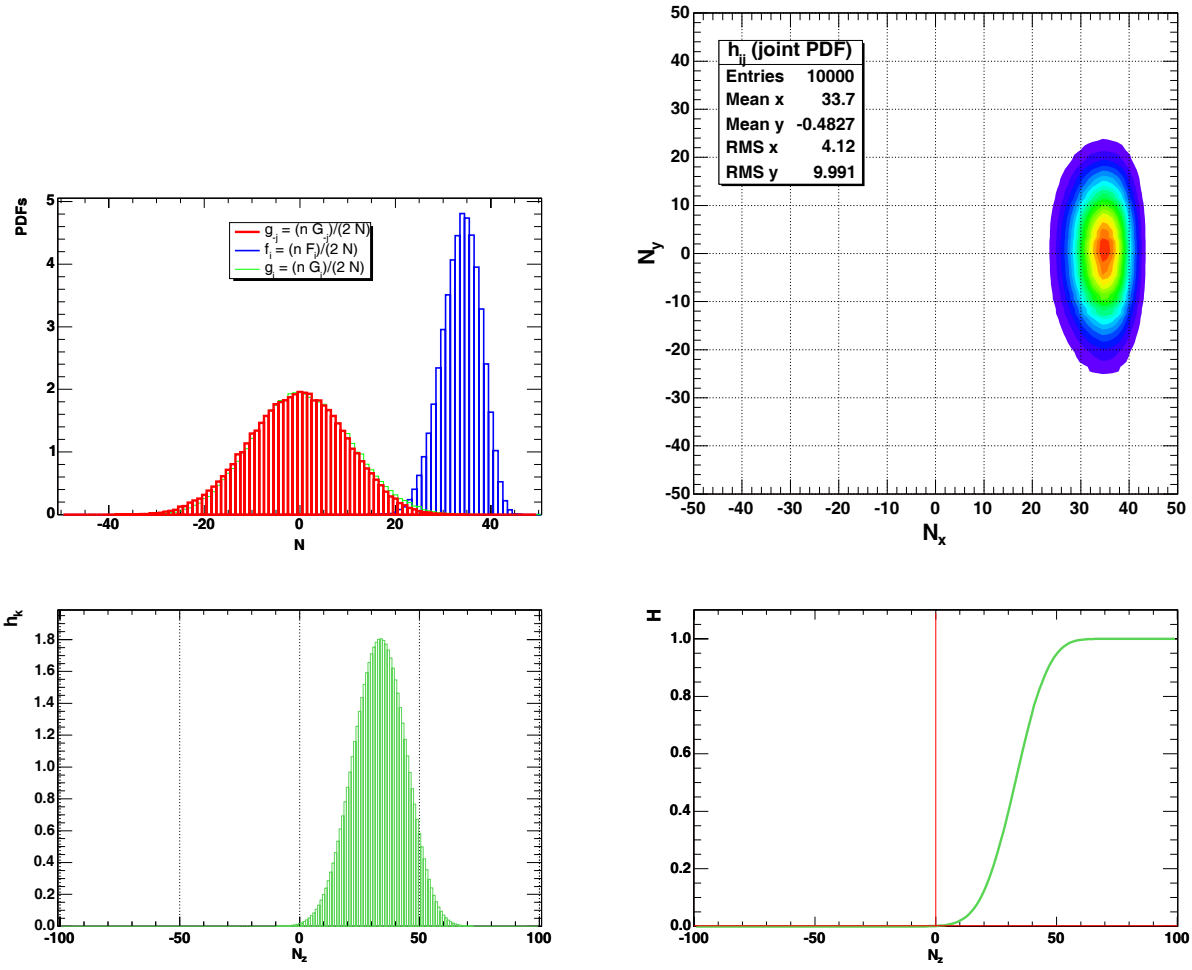

Figure 6.17: Upper panel: correlation coefficient distribution f_i and distribution of randomized data g_j, both from Figure 6.15 (left) and corresponding joint PDF distribution (right). Lower panel: one-dimensional discrete convolution h_k (left) and H distribution (right). The probability is $p_{\mathrm{AC}} = 2H(0) = 0.002 \pm {}^{0.010}_{0.002}$. Source of data: [31].

6.2.2 A study of the correlations of the fluxes X-rays, $\gamma-$rays, and optical radiation for Mkn 421 during 2003

We have been searching for linear correlation between light curves in three different wavebands: optical (KVA data), X-ray (RXTE/ASM data) and γ-ray (CT1 data).

γ/X correlations

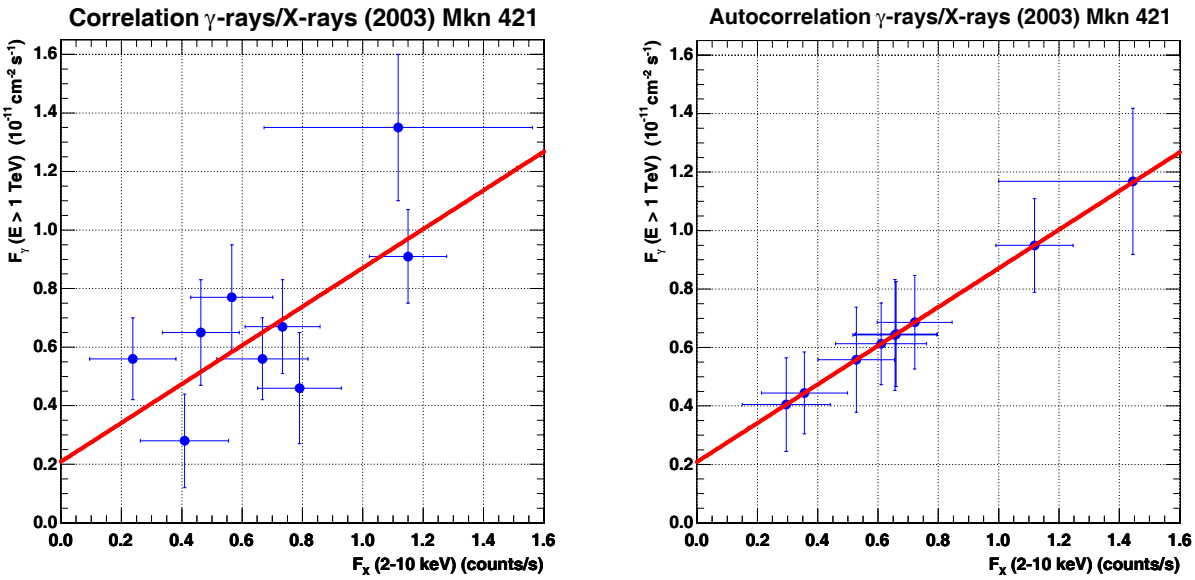

Figure 6.18: γ/X correlation plot: 2003 – CT1 – Mkn 421. Data from MWL campaign February/March 2003 (Tables 5.3 and 5.5). χ^2/ndf = 6.9/7 (Probability = 0.439) $F_\gamma = (0.66 \pm 0.23)\cdot 10^{-11}\mathrm{cm}^{-2}\mathrm{counts}^{-1} F_\mathrm{x} + (0.21 \pm 0.16)\cdot 10^{-11}\mathrm{cm}^{-2}\mathrm{s}^{-1}$

Figure 6.18 shows correlation plots between CT1 γ-ray integral flux above 1 TeV (data from Table 5.3) and RXTE/ASM X-ray flux in counts per second (data from Table 5.5). From equations (6.3), (6.4) and (6.5), the correlation coefficient is **0.71 ± 0.16** with significance of 2.7σ which is in good agreement with recent MAGIC results (0.64 ± 0.22 with significance of 2.4σ) [73].

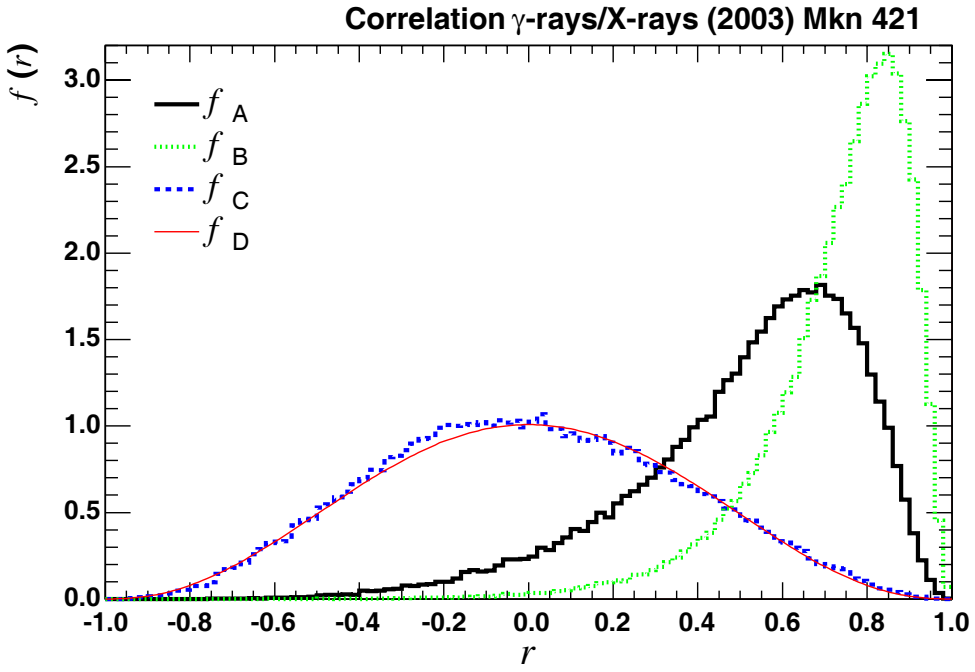

Figure 6.19: γ/X correlation coefficient distribution: 2003 – CT1/RXTE – Mkn 421. Data from MWL campaign February/March 2003 (Tables 5.3 and 5.5). 100000 MC events were generated for each PDF. $r_{\mathrm{MC}} = 0.52 \pm 0.27$, $p_{\mathrm{AB}} = 0.47 \pm 0.07$, $p_{\mathrm{AC}} = 0.25 \pm 0.07$.

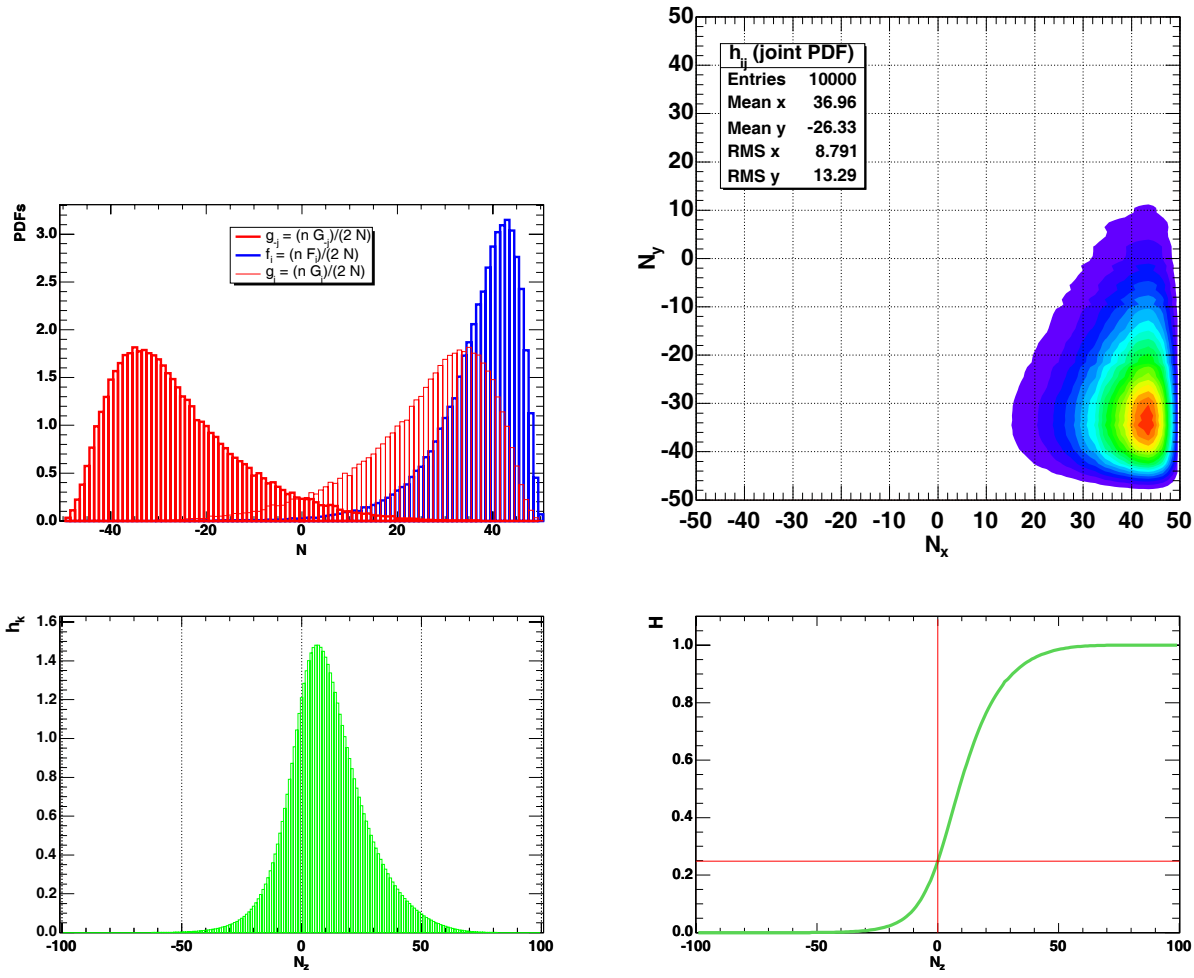

Figure 6.20: Upper panel: correlation coefficient distribution g_j and autocorrelation distribution f_i, both from Figure 6.19 (left) and corresponding joint PDF distribution (right). Lower panel: one-dimensional discrete convolution h_k (left) and H distribution (right). The probability is $p_{\mathrm{AB}} = 2H(0) = 0.47 \pm 0.07$. Data from MWL campaign February/March 2003 (Tables 5.3 and 5.5).

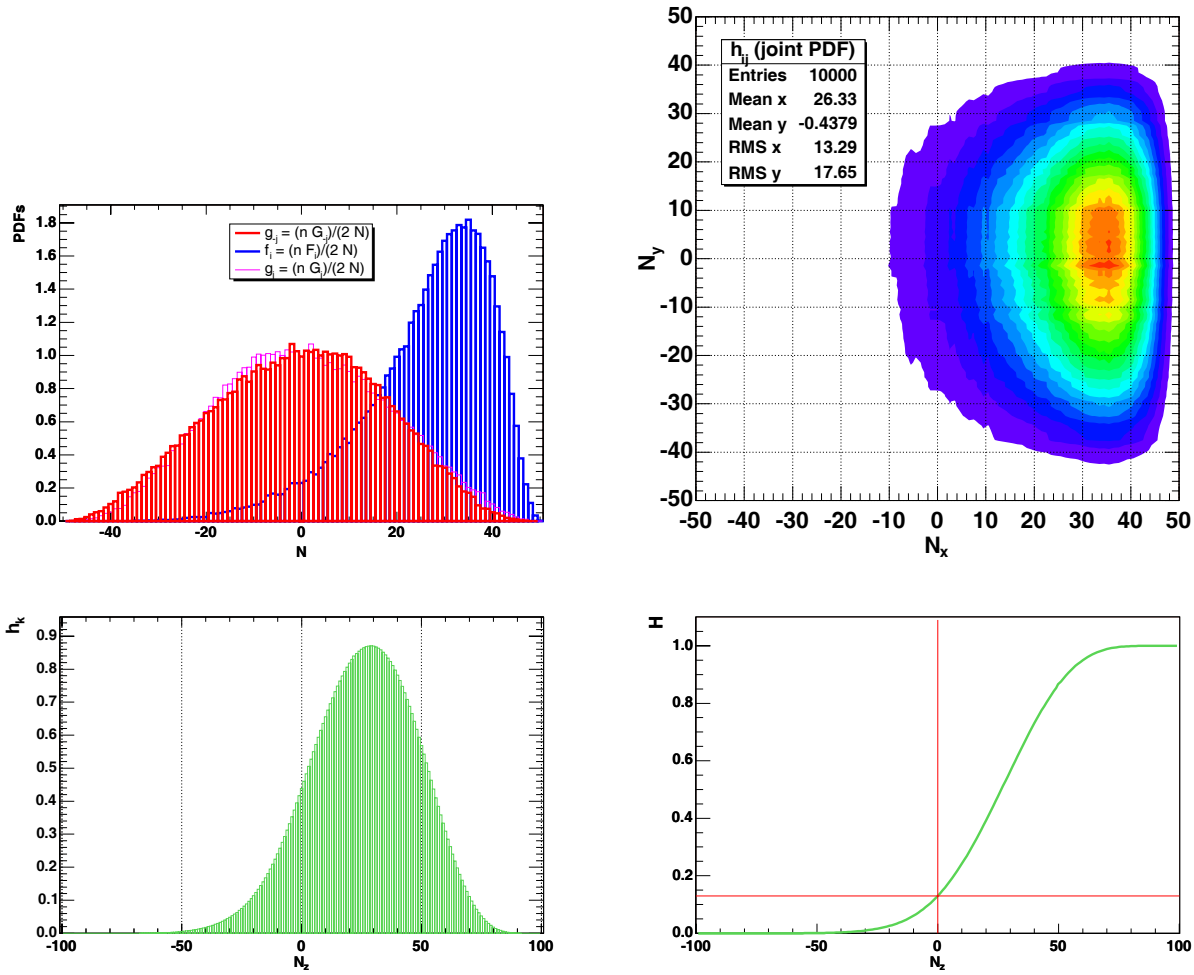

Figure 6.21: Upper panel: correlation coefficient distribution f_i and distribution of randomized data g_j, both from Figure 6.19 (left) and corresponding joint PDF distribution (right). Lower panel: one-dimensional discrete convolution h_k (left) and H distribution (right). The probability is $p_{\mathrm{AC}} = 2H(0) = 0.25 \pm 0.07$. Data from MWL campaign February/March 2003 (Tables 5.3 and 5.5).

γ/optical correlations

Figure 6.22 shows[11] a long-term optical light curve of Mkn 421.

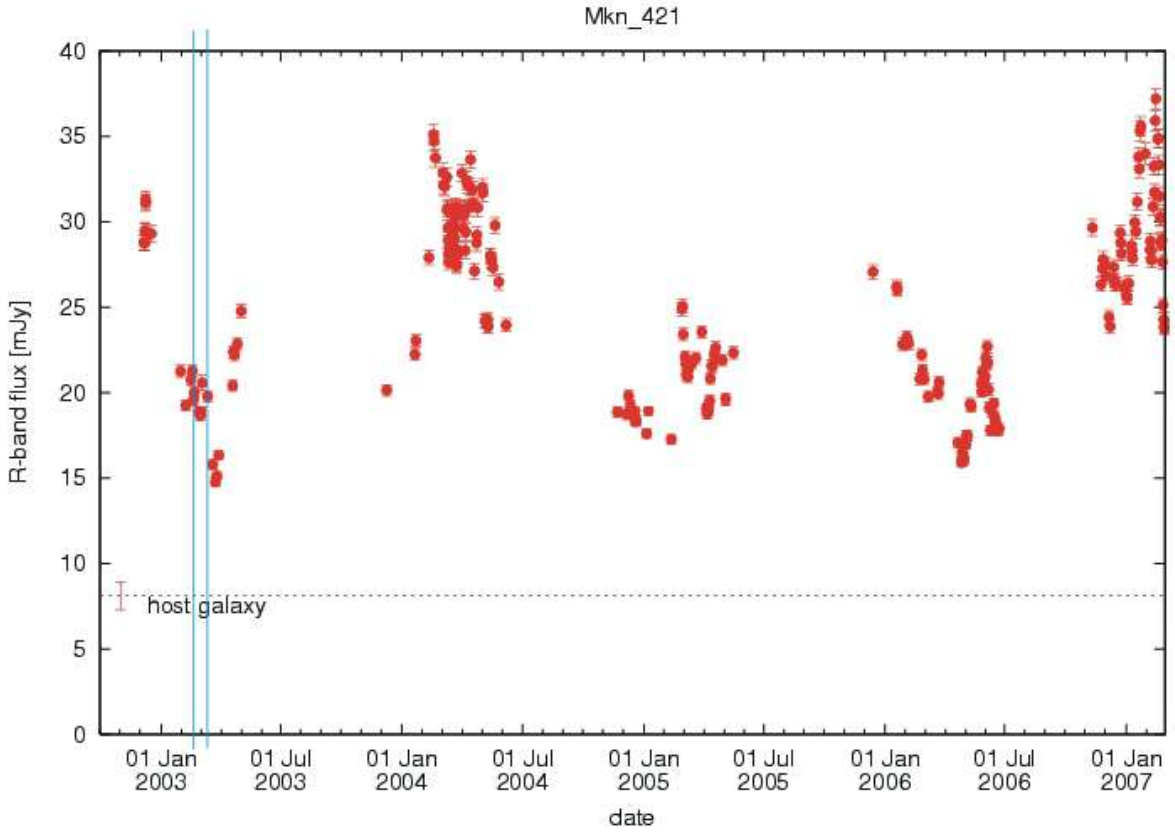

Figure 6.22: Long-term optical light curve of Mkn 421. Blue lines show a period of data that we analyzed here.

[11]Source: *http://users.utu.fi/kani/1m/Mkn_421_jy.html*

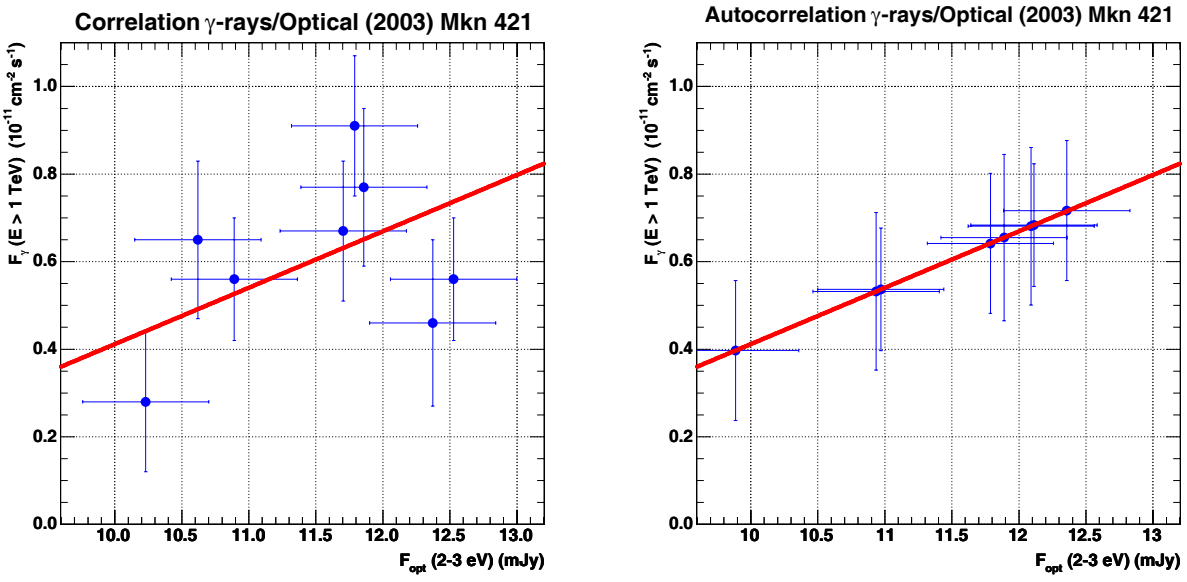

Figure 6.23: γ/optical correlation plot: 2003 – CT1/KVA – Mkn 421. Data from MWL campaign February/March 2003 (Tables 5.3 and 5.6). $\chi^2/\mathrm{ndf} = 7.53/6$ (Probability = 0.274) $F_\gamma = (+0.13 \pm 0.10)\cdot 10^{-11}\mathrm{cm}^{-2}\mathrm{s}^{-1}\mathrm{mJy}^{-1}$ $F_{\mathrm{opt}} - (0.88 \pm 1.1)\cdot 10^{-11}\mathrm{cm}^{-2}\mathrm{s}^{-1}$

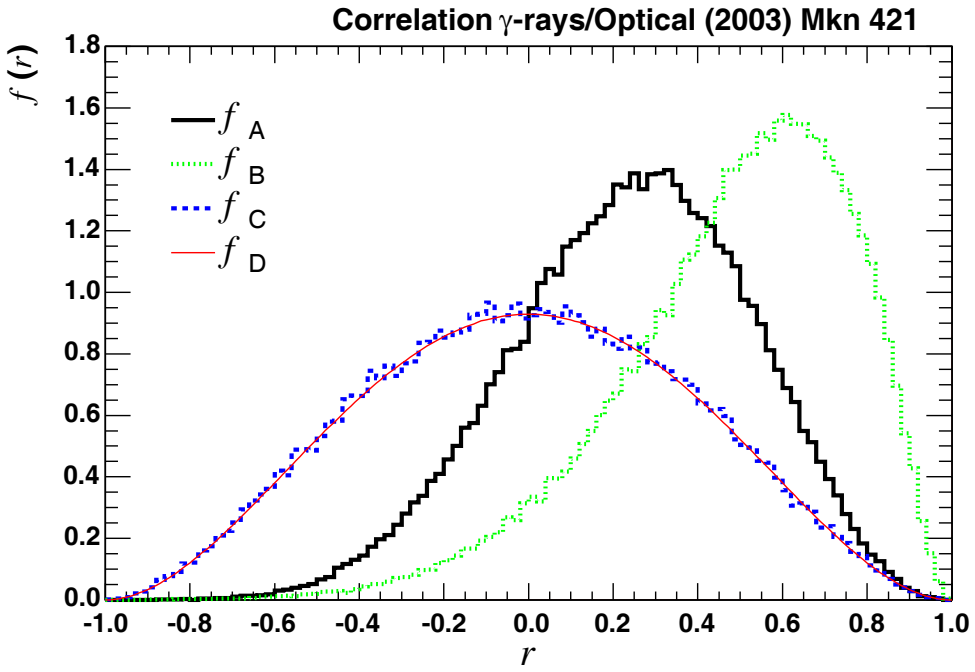

Figure 6.24: γ/optical correlation coefficient distribution: 2003 – CT1/KVA – Mkn 421. Data from MWL campaign February/March 2003 (Tables 5.3 and 5.6). 100000 MC events were generated for each PDF. $r_{\mathrm{MC}} = 0.24 \pm 0.28$, $p_{\mathrm{AB}} = 0.52 \pm^{0.48}_{0.53}$, $p_{\mathrm{AC}} = 0.63 \pm^{0.37}_{0.53}$.

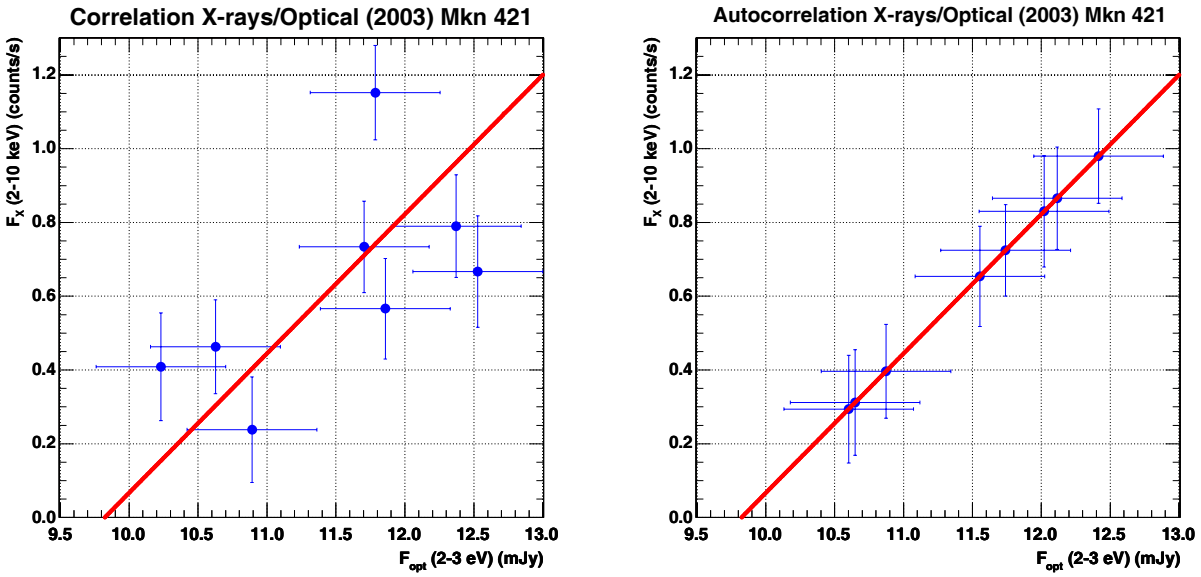

Figure 6.25: X/optical correlation plot: 2003 – RXTE/KVA – Mkn 421. Data from MWL campaign February/March 2003 (Tables 5.5 and 5.6). $\chi^2/\mathrm{ndf} = 9.47/6$ (Probability $= 0.1486$) $F_\mathrm{X} = (0.38 \pm 0.13)$ counts/s mJy^{-1} $F_\mathrm{opt} - (3.8 \pm 1.4)$ counts/s

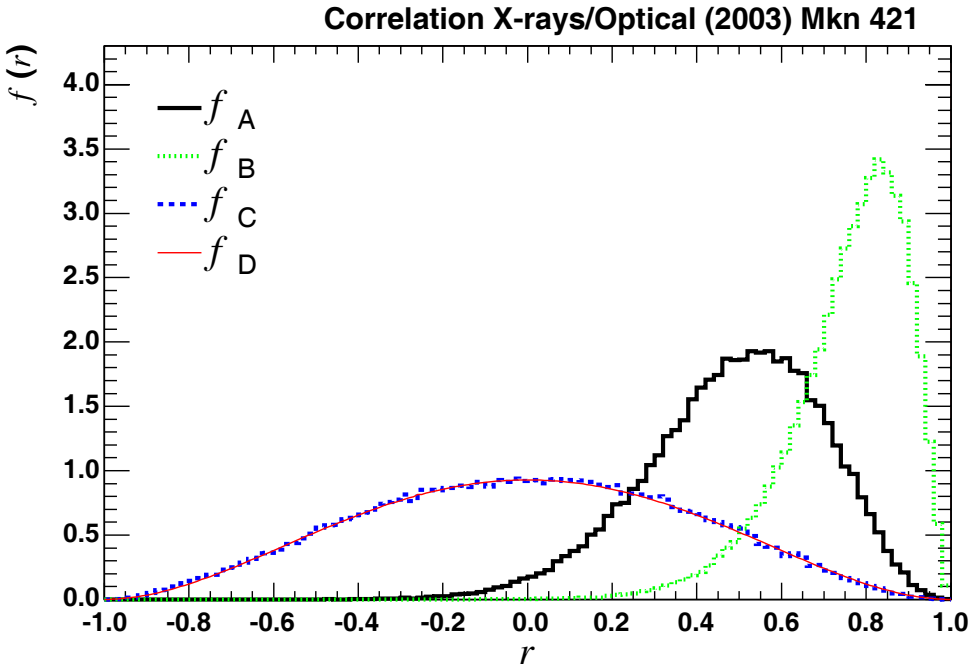

Figure 6.26: X/optical correlation coefficient distribution: 2003 – RXTE/KVA – Mkn 421. Data from MWL campaign February/March 2003 (Tables 5.5 and 5.6). 100000 MC events were generated for each PDF. $r_\mathrm{MC} = 0.49 \pm 0.21$, $p_\mathrm{AB} = 0.27 \pm 0.15$, $p_\mathrm{AC} = 0.27 \pm 0.15$.

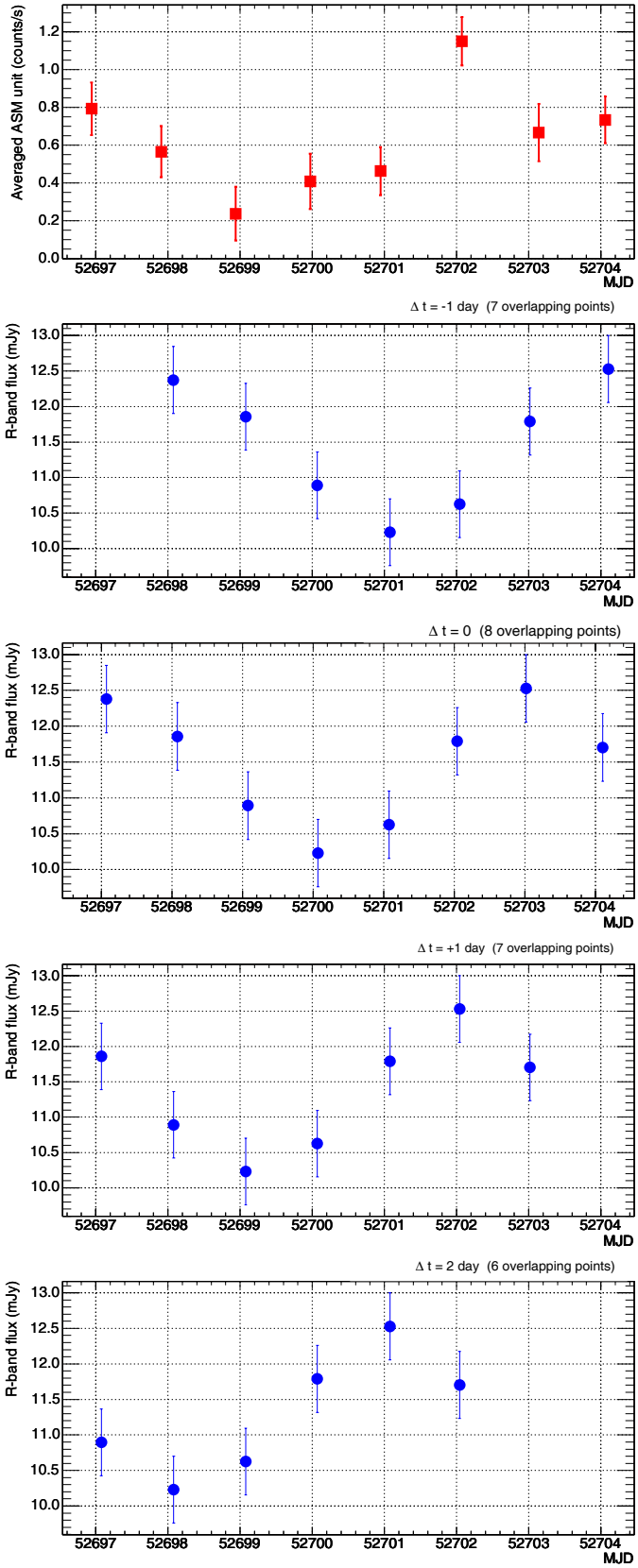

Figure 6.27: Possible time delay Δt of the KVA optical light curve relating to the RXTE/ASM X-ray light curve. Original X-ray light curve (third panel) has no time shift, $\Delta t = 0$. Data from MWL campaign February/March 2003 (Tables 5.5 and 5.6).

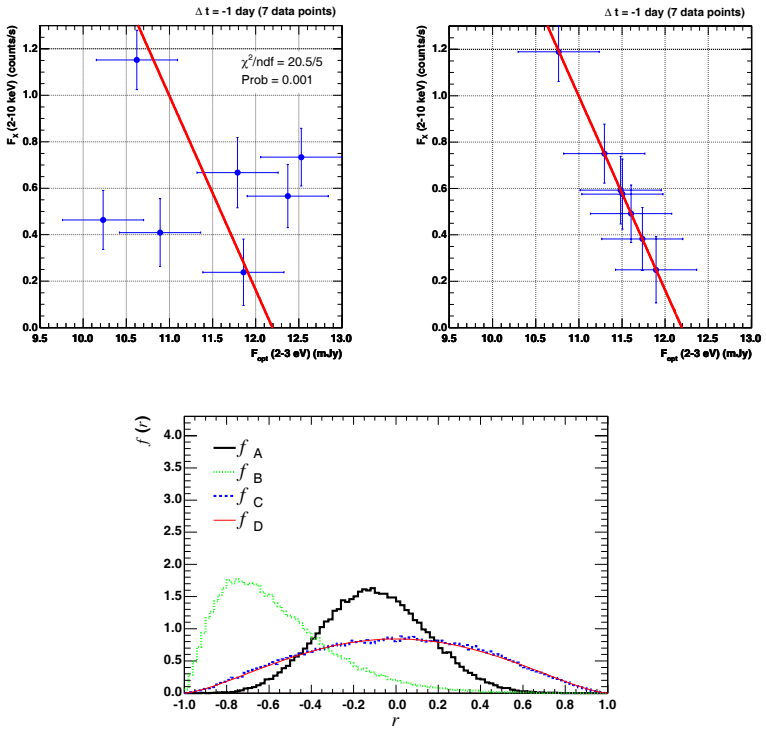

Figure 6.28: $\Delta t = -1$ day (7 data points) $r_{\rm MC} = -0.10 \pm 0.25$, $p_{\rm AB} = 0.21 \pm^{0.26}_{0.21}$, $p_{\rm AC} = 0.84 \pm^{0.16}_{0.26}$, $p_{\rm AB}(1-p_{\rm AC}) = 0.03 \pm^{0.07}_{0.03}$, $p_{\rm AC}(1-p_{\rm AB}) = 0.66 \pm 0.30$. Data from MWL campaign February/March 2003 (Tables 5.5 and 5.6).

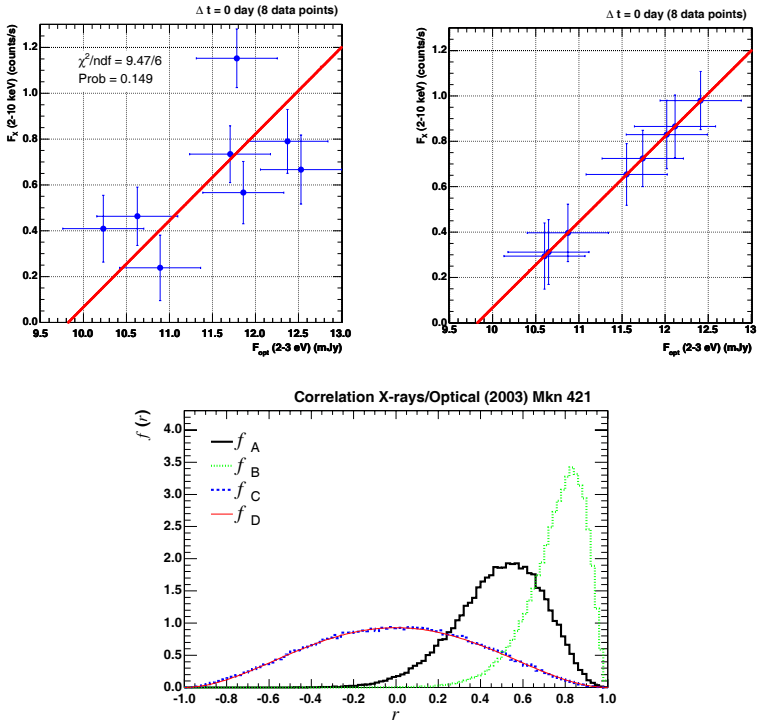

Figure 6.29: $\Delta t = 0$ (8 data points) $r_{\rm MC} = 0.49 \pm 0.21$, $p_{\rm AB} = 0.27 \pm 0.05$, $p_{\rm AC} = 0.27 \pm 0.05$, $p_{\rm AB}(1-p_{\rm AC}) = 0.19 \pm 0.04$, $p_{\rm AC}(1-p_{\rm AB}) = 0.20 \pm 0.04$. Data from MWL campaign February/March 2003 (Tables 5.5 and 5.6).

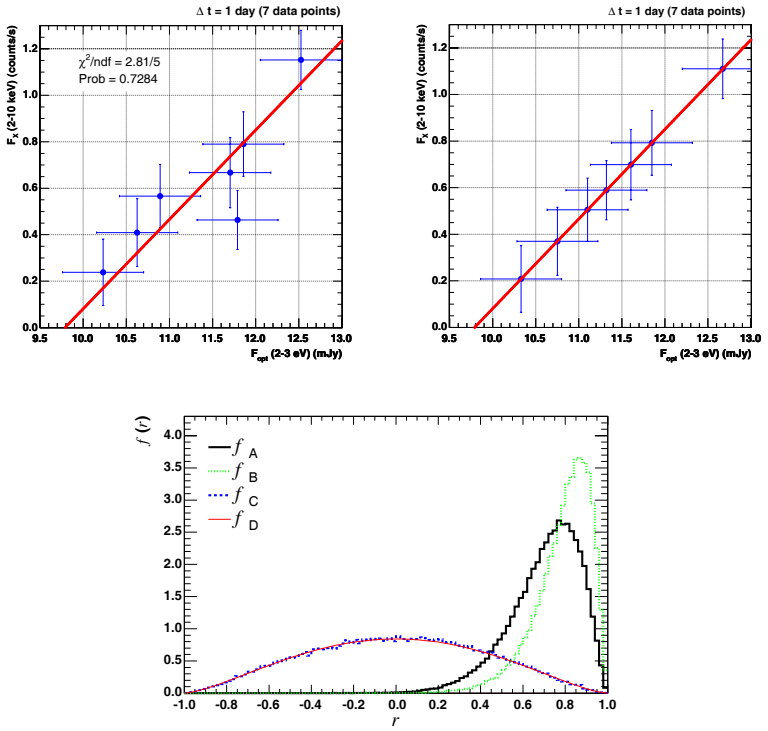

Figure 6.30: $\Delta t = +1$ day (7 data points) $r_{\rm MC} = 0.70 \pm 0.17$, $p_{\rm AB} = 0.67 \pm 0.05$, $p_{\rm AC} = 0.11 \pm 0.05$, $p_{\rm AB}(1 - p_{\rm AC}) = 0.59 \pm 0.06$, $p_{\rm AC}(1 - p_{\rm AB}) = 0.04 \pm 0.02$. Data from MWL campaign February/March 2003 (Tables 5.5 and 5.6).

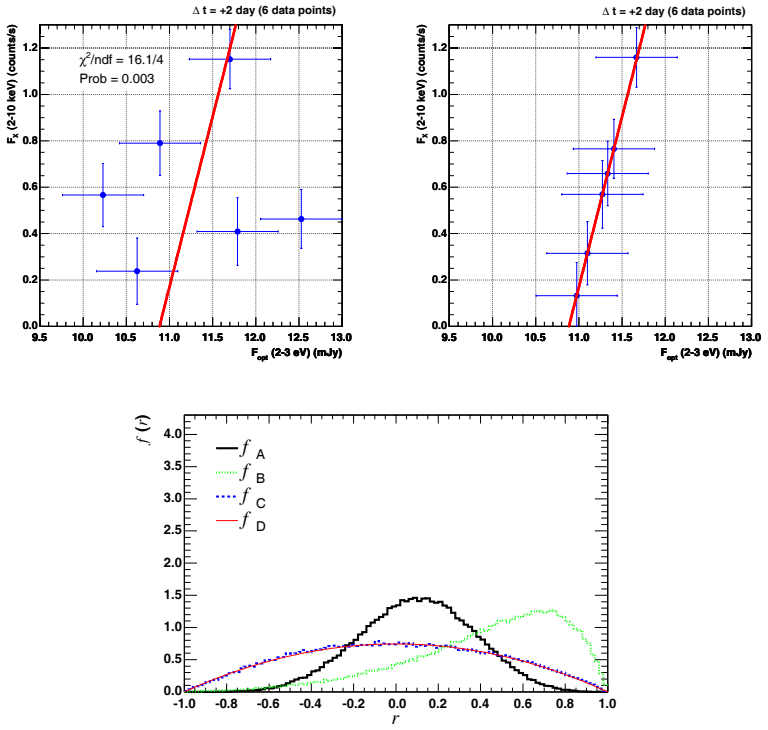

Figure 6.31: $\Delta t = +2$ day (6 data points) $r_{\rm MC} = 0.10 \pm 0.27$, $p_{\rm AB} = 0.44 \pm^{0.46}_{0.44}$, $p_{\rm AC} = 0.86 \pm^{0.14}_{0.46}$, $p_{\rm AB}(1 - p_{\rm AC}) = 0.06 \pm^{0.21}_{0.06}$, $p_{\rm AC}(1 - p_{\rm AB}) = 0.48 \pm 0.47$. Data from MWL campaign February/March 2003 (Tables 5.5 and 5.6).

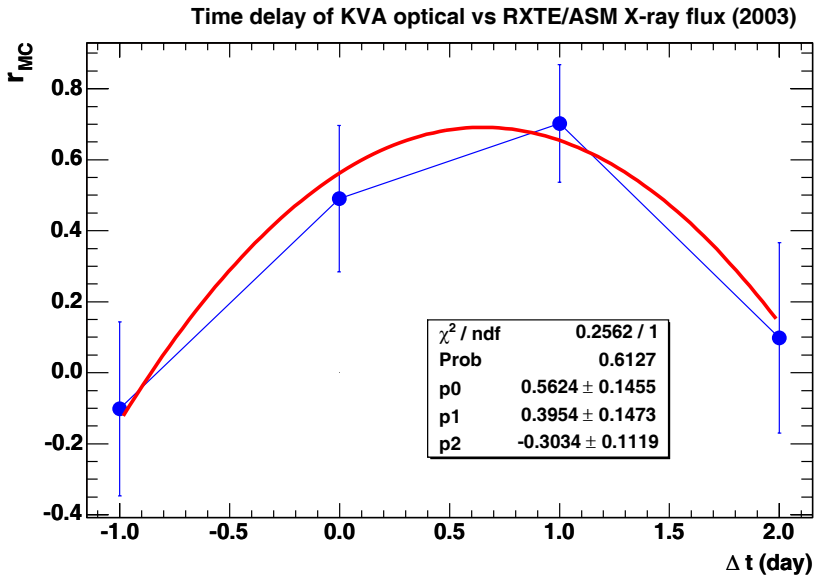

Figure 6.32: Correlation coefficient (from MC simulations) vs time delay. Data from MWL campaign February/March 2003 (Tables 5.5 and 5.6).

We fitted $r_{\rm MC}$ vs Δt (Figure 6.32) to second order polynomial $r_{\rm MC} = p_0 + p_1\Delta t + p_1\Delta t^2$. Extreme value of the parabola is

$$\overline{t_{\rm m}} = -\frac{\overline{p_1}}{2\overline{p_2}} = 0.65 \text{ day} \tag{6.42}$$

From the uncertainties σ_{p1} and σ_{p2} of the fitting parameters, error propagation gives us the value of $\sigma_{t\rm m}$

$$\sigma_{t\rm m} = \sqrt{(\partial_{p1} t_{\rm m}\sigma_{p1})^2 + (\partial_{p2} t_{\rm m}\sigma_{p2})^2} = \frac{1}{2\overline{p_2}}\sqrt{\sigma_{p1}^2 + (\frac{\overline{p_1}}{\overline{p_2}}\sigma_{p2})^2} = 0.26 \text{ day} \tag{6.43}$$

Δt/day	$p(\chi^2)$	$r_{\rm MC}$	$p_{\rm AB}$	$p_{\rm AC}$	$p_{\rm AB}(1-p_{\rm AC})$	$p_{\rm AC}(1-p_{\rm AB})$
-1	0.001	-0.10 ± 0.25	$0.21\pm^{0.26}_{0.21}$	$0.84\pm^{0.16}_{0.26}$	$0.03\pm^{0.07}_{0.03}$	0.66 ± 0.30
0	0.149	0.49 ± 0.21	0.27 ± 0.05	0.27 ± 0.05	0.19 ± 0.04	0.20 ± 0.04
1	0.728	0.70 ± 0.17	0.67 ± 0.05	0.11 ± 0.05	0.59 ± 0.06	0.04 ± 0.02
2	0.003	0.10 ± 0.27	$0.44\pm^{0.46}_{0.44}$	$0.86\pm^{0.14}_{0.46}$	$0.06\pm^{0.21}_{0.06}$	0.48 ± 0.47

Table 6.3: Correlation analysis parameters vs time shift. Data from MWL campaign February/March 2003 (Tables 5.5 and 5.6).

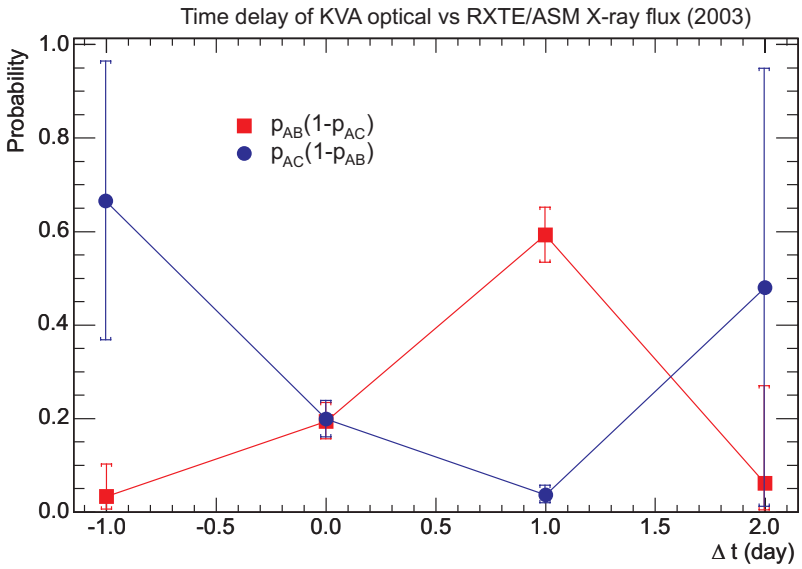

Figure 6.33: Combined probabilities (from Table 6.3) vs time delay. Data from MWL campaign February/March 2003 (Tables 5.5 and 5.6).

6.2.3 Mkn 421 (2005) MAGIC/RXTE/KVA

γ/X correlations

MJD	MAGIC γ-ray flux (10^{-10}cm^{-2}s^{-1})	RXTE/ASM X-ray flux (cts/s)
53325	1.46 ± 0.37	0.12 ± 0.45
53330	4.00 ± 0.34	1.85 ± 0.22
53357	2.78 ± 0.27	0.94 ± 0.33
53358	1.52 ± 0.21	1.5 ± 0.29
53359	2.37 ± 0.26	1.3 ± 0.31
53360	2.31 ± 0.39	1.69 ± 0.22
53377	1.54 ± 0.23	0.65 ± 0.25
53465	2.83 ± 0.31	1.9 ± 0.6
53466	2.06 ± 0.32	−0.06 ± 0.37
53467	1.79 ± 0.28	1.63 ± 0.57
53468	2.12 ± 0.26	1.2 ± 0.47
53469	1.42 ± 0.29	0.74 ± 0.43
53470	1.03 ± 0.24	0.83 ± 0.67

Table 6.4: The MAGIC data of Mkn 421, shown in Figure 6.34, we took from the MAGIC paper [73]. The RXTE/ASM data of Mkn 421, shown in Figures 6.34, we did not take from the MAGIC paper [73]. Instead, we calculated these points from raw data, available at *http://xte.mit.edu/ASM_lc.html*, in order to match the MAGIC data points better.

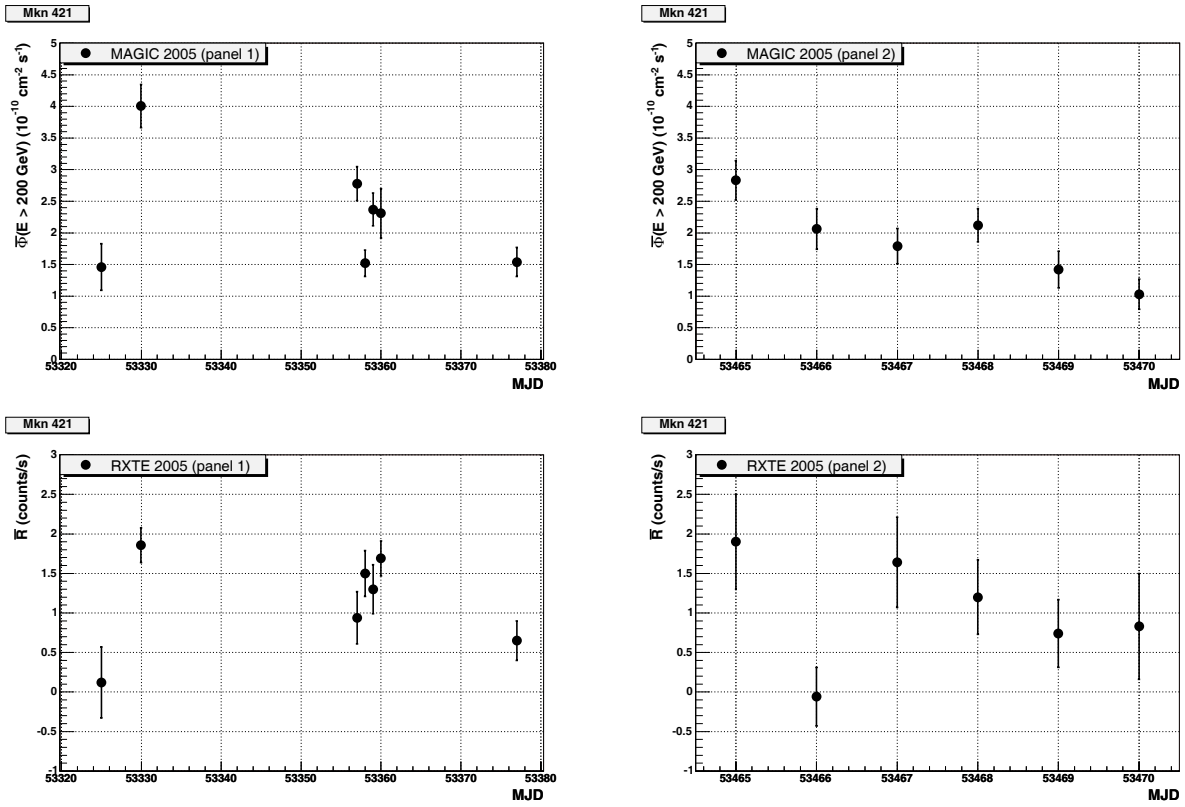

Figure 6.34: Light curves: 2005 – MAGIC/RXTE – Mkn 421. The MAGIC data points are from the paper [73] (**left** panel in Figure 5 in the paper) while RXTE/ASM data points are from Table 6.4.

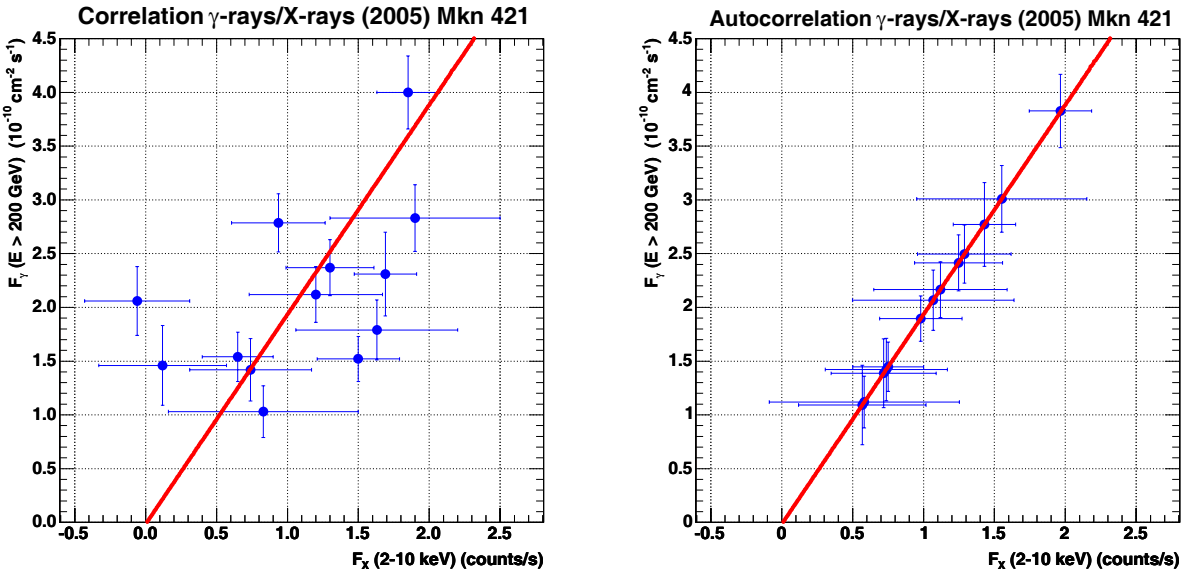

Figure 6.35: γ/X correlation plot: 2005 – MAGIC – Mkn 421. Data points (shown in Table 6.4 in this work) are from the MAGIC paper [73] (Figure 13 in the paper). $\chi^2/\mathrm{ndf} = 22.5/11$ (Probability $= 0.021$) $F_\gamma = (1.95 \pm 0.54) \cdot 10^{-10} \mathrm{cm}^{-2} \mathrm{counts}^{-1} F_\mathrm{x} - (0.02 \pm 0.66) \cdot 10^{-10} \mathrm{cm}^{-2} \mathrm{s}^{-1}$

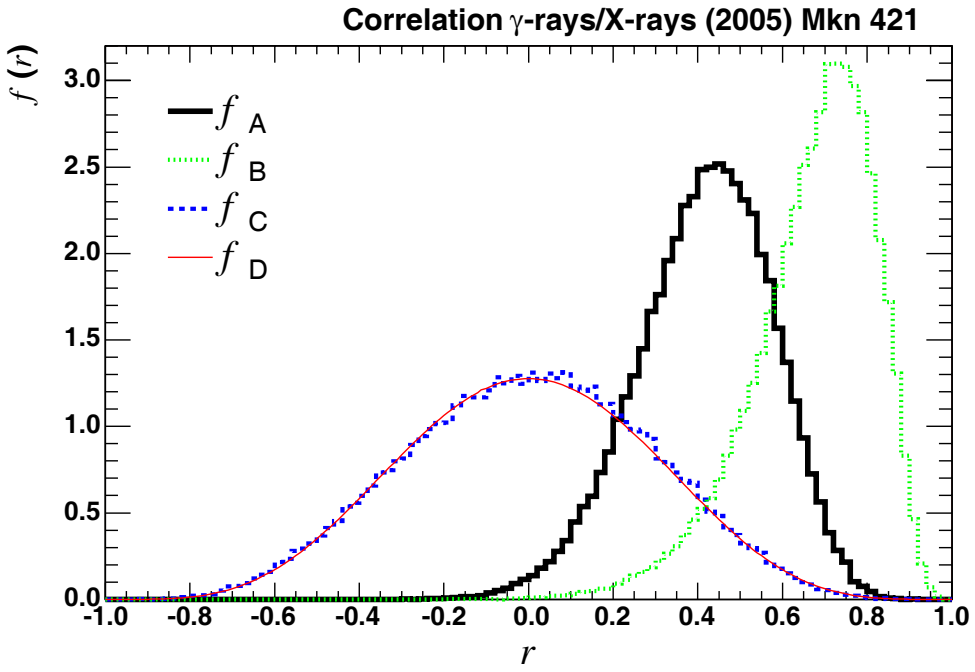

Figure 6.36: γ/X correlation coefficient distribution: 2005 – MAGIC – Mkn 421. Data points (Table 6.4) are from the MAGIC paper [73] (Figure 13 in the paper). 100000 MC events were generated for each PDF. $r_{\mathrm{MC}} = 0.42 \pm 0.16$, $p_{\mathrm{AB}} = 0.23 \pm 0.04$, $p_{\mathrm{AC}} = 0.22 \pm 0.04$.

MAGIC γ-ray flux (10^{-10}cm^{-2}s^{-1})	KVA optical flux (mJy)
2.38 ± 0.18	10.35 ± 0.04
2.80 ± 0.18	10.67 ± 0.04
1.73 ± 0.20	10.77 ± 0.09
2.01 ± 0.24	11.05 ± 0.07
2.06 ± 0.19	11.10 ± 0.10
1.54 ± 0.15	10.96 ± 0.10
1.37 ± 0.22	11.00 ± 0.12
1.52 ± 0.13	11.02 ± 0.15

Table 6.5: The KVA data and the corresponding MAGIC data for 8 nights which we took from the MAGIC paper [73] (Figure 14 in the paper).

Figure 6.37 shows[12] a long-term optical light curve of Mkn 421.

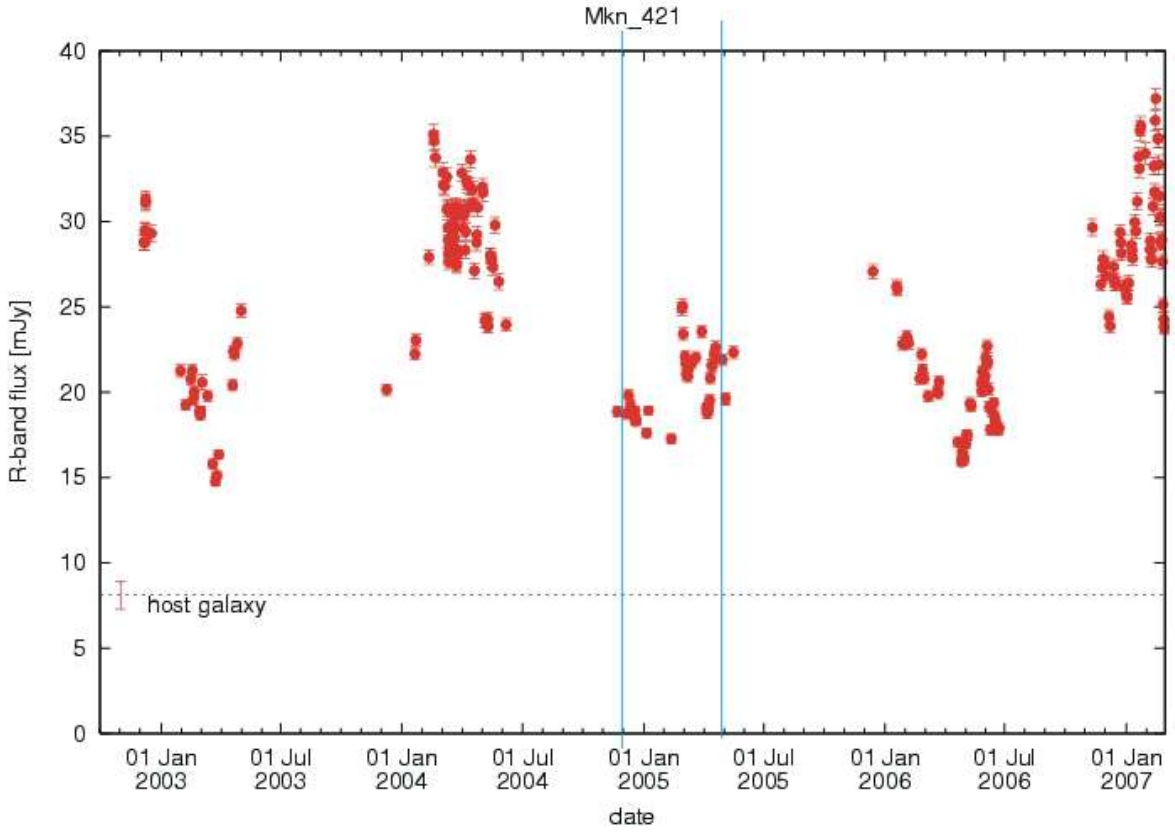

Figure 6.37: Long-term optical light curve of Mkn 421. Blue lines show a period of data that we analyzed here.

[12]Source: *http://users.utu.fi/kani/1m/Mkn_421_jy.html*

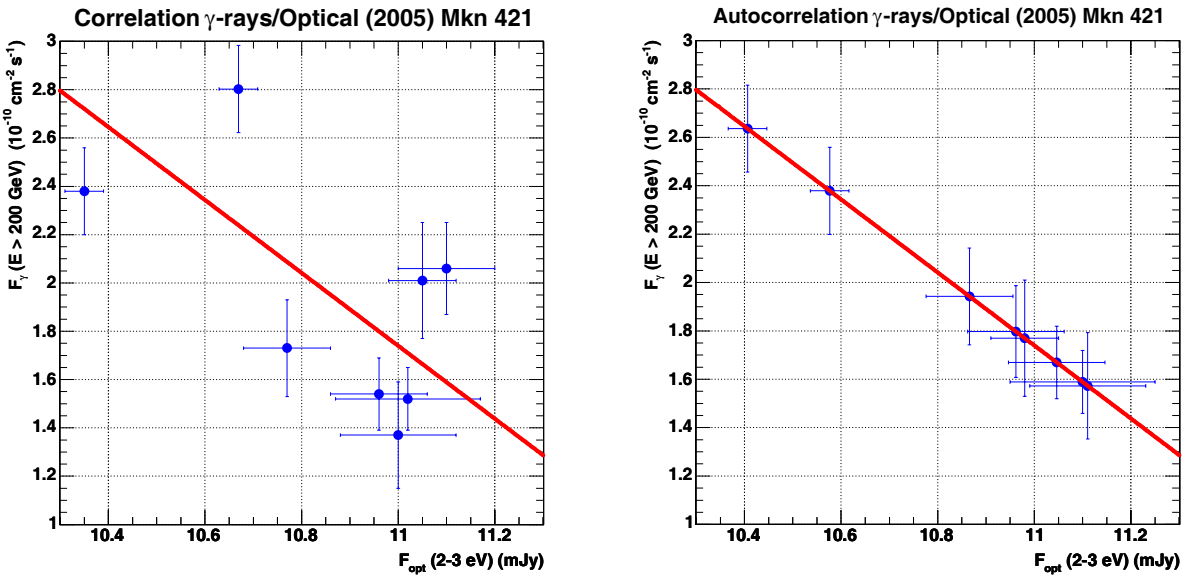

Figure 6.38: γ/optical correlation plot: 2005 – MAGIC – Mkn 421. Data points (shown in Table 6.5 in this work) are from the MAGIC paper [73] (Figure 14 in the paper). $\chi^2/\mathrm{ndf} = 23.4/6$ (Probability $= 0.001$) $F_\gamma = (-1.51 \pm 0.31)\cdot 10^{-10}\mathrm{cm}^{-2}\mathrm{s}^{-1}\mathrm{mJy}^{-1}\ F_{\mathrm{opt}} + (18.3 \pm 3.4)\cdot 10^{-10}\mathrm{cm}^{-2}\mathrm{s}^{-1}$

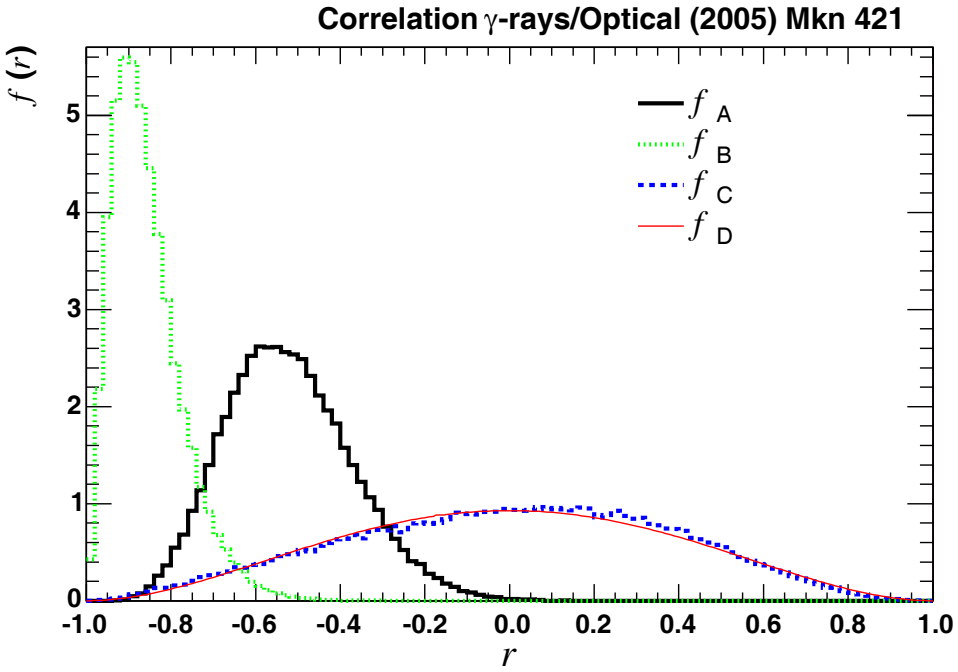

Figure 6.39: γ/optical correlation coefficient distribution: 2005 – MAGIC/KVA – Mkn 421. Data points (Table 6.5) are from the MAGIC paper [73] (Figure 14 in the paper). 100000 MC events were generated for each PDF. $r_{\mathrm{MC}} = -0.52 \pm 0.15$, $p_{\mathrm{AB}} = 0.05 \pm 0.02$, $p_{\mathrm{AC}} = 0.22 \pm 0.02$.

6.2.4 Mkn 180 (2006) MAGIC/RXTE

MJD	MAGIC γ-ray flux (10^{-11}cm^{-2}s^{-1})
53818	2.13 ± 1.84
53819	0.25 ± 1.82
53820	6.41 ± 1.87
53822	0.97 ± 1.84
53823	1.25 ± 1.77
53824	2.08 ± 1.65
53825	2.81 ± 1.67

Table 6.6: The MAGIC data on Mkn 180 shown in Figure 6.40 which we took from the MAGIC paper [66].

MJD	ASM X-ray flux (cts/s) 24-hour average	MJD	ASM X-ray flux (cts/s) nightly average (midnight ± 3h)
		53818.15	1.12 ± 0.80
53818.60	0.31 ± 0.54		
		53818.87	−0.28 ± 0.86
53819.50	0.32 ± 0.68		
		53819.99	1.51 ± 0.55
53820.50	1.63 ± 0.42		
		53821.99	−0.75 ± 0.49
53822.40	−0.40 ± 0.26		
		53822.97	0.51 ± 0.50
53823.50	0.33 ± 0.22		
		53824.00	0.01 ± 0.41
53824.50	−0.11 ± 0.23		
		53824.96	−0.31 ± 0.37
53825.40	0.21 ± 0.31		

Table 6.7: The RXTE/ASM data on Mkn 180 shown as light curve in Figure 6.41. Left aligned (blue) data are 24-hour averages taken from [66] (Figure 2 in the paper). Right aligned (red) data are nightly averages which we calculated from raw data available at *http://xte.mit.edu/ASM_lc.html*.

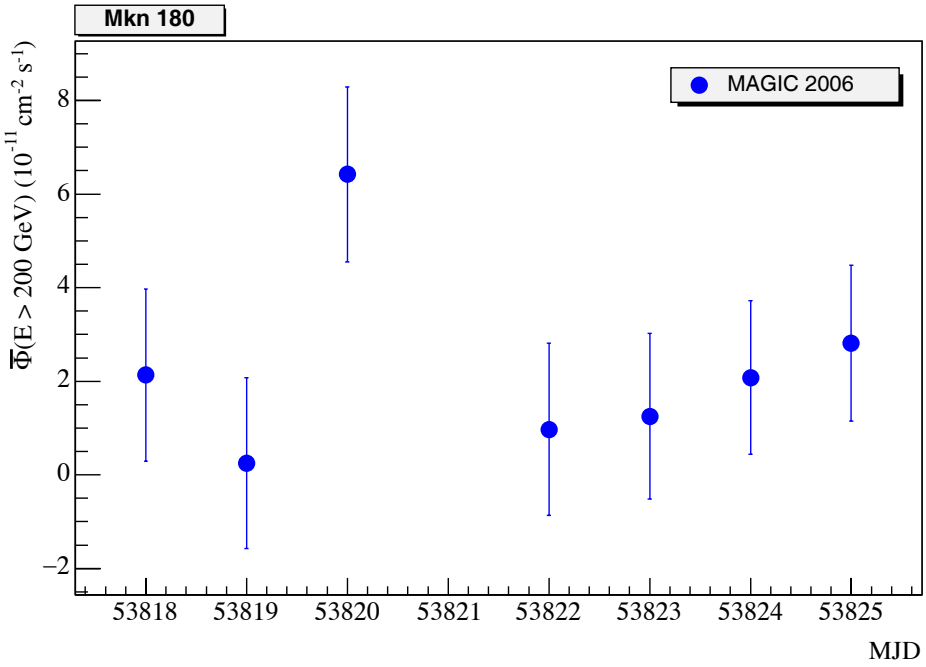

Figure 6.40: Light curve: 2006 – MAGIC – Mkn 180. Data points (Table 6.6) are from the MAGIC paper [66] (Figure 2 in the paper).

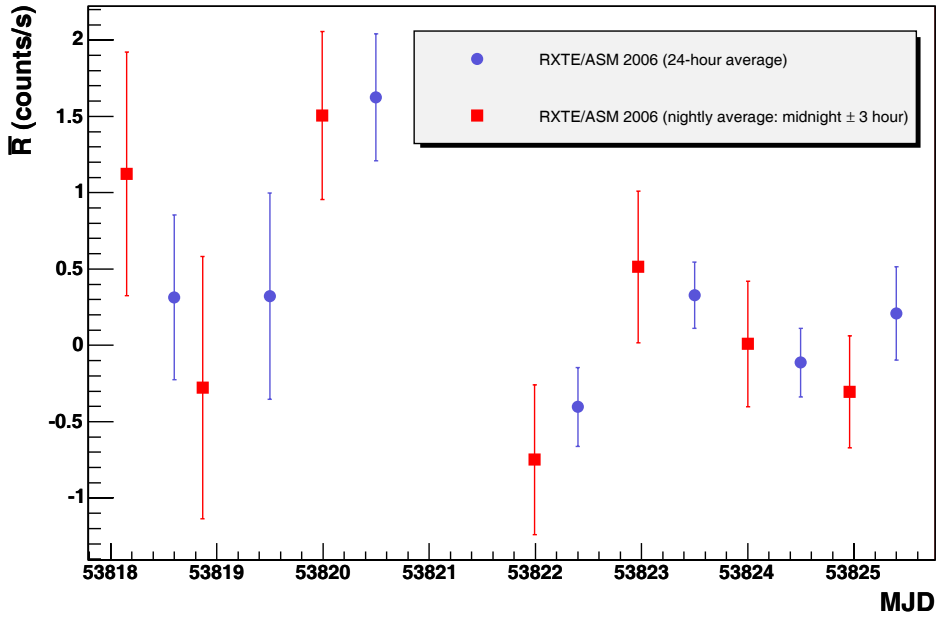

Figure 6.41: Light curve: 2006 – RXTE/ASM – Mkn 180. Data points are from Table 6.7.

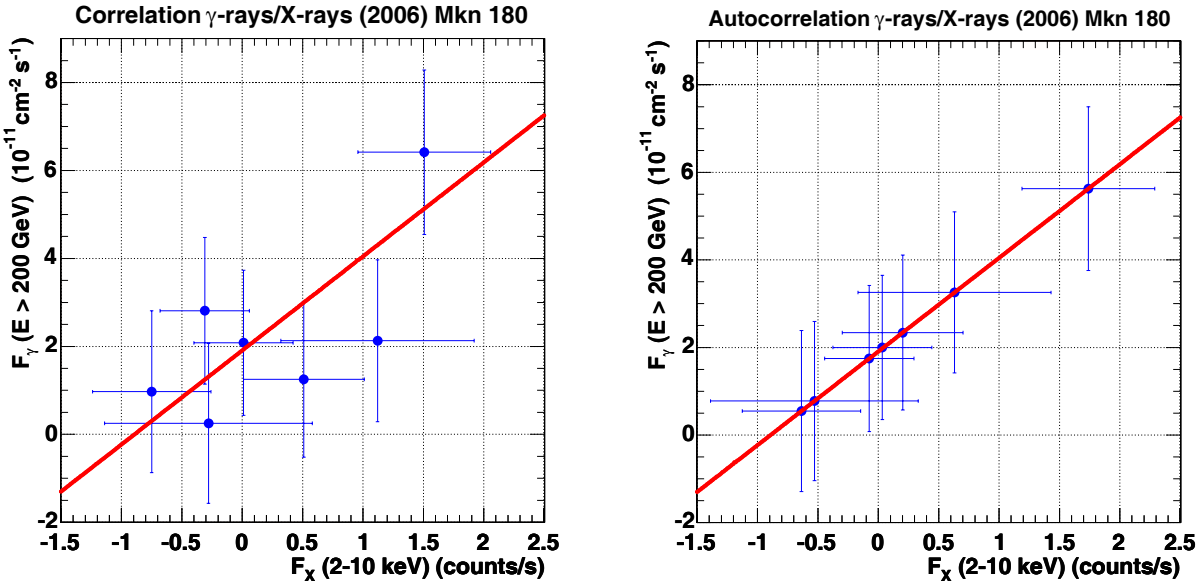

Figure 6.42: Correlation plot: 2006 – MAGIC – Mkn 180. Data points (shown in Tables 6.6 and 6.7 in this work) are from the MAGIC paper [66]. $\chi^2/\mathrm{ndf} = 2.8/5$ (Probability $= 0.733$) $F_\gamma = (2.14 \pm 1.22)\cdot 10^{-11}\mathrm{cm}^{-2}\mathrm{counts}^{-1} F_\mathrm{x} + (1.91 \pm 0.82)\cdot 10^{-11}\mathrm{cm}^{-2}\mathrm{s}^{-1}$

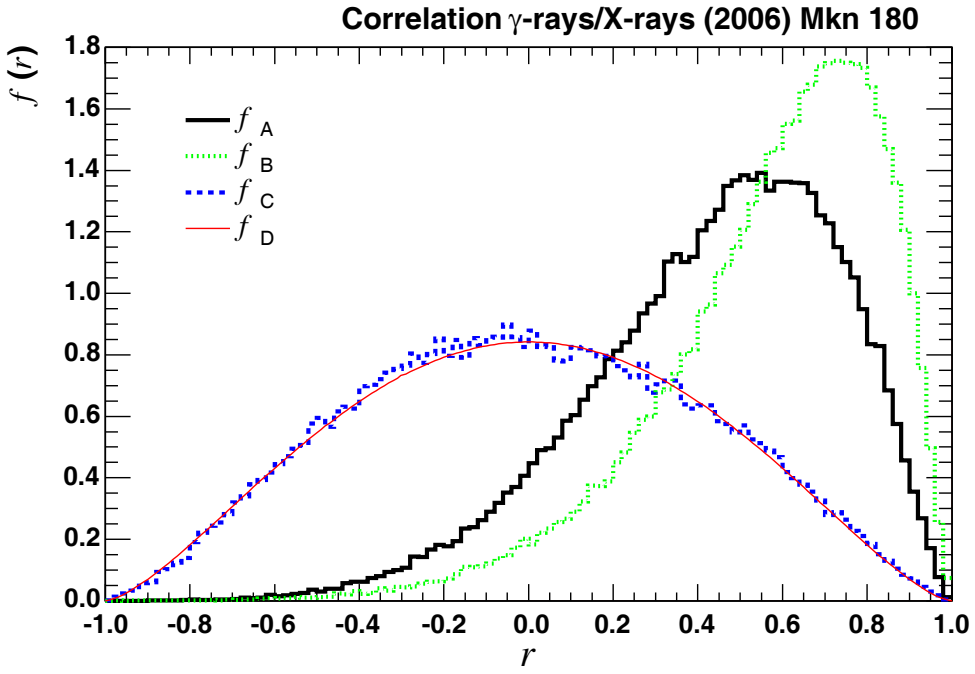

Figure 6.43: Correlation coefficient distribution: 2006 – MAGIC/RXTE – Mkn 180. Data points, shown in Tables 6.6 and 6.7, are from the MAGIC paper [66]. 100000 MC events were generated for each PDF. $r_\mathrm{MC} = 0.43 \pm 0.27$, $p_\mathrm{AB} = 0.71 \pm^{0.29}_{0.31}$, $p_\mathrm{AC} = 0.4 \pm 0.3$.

6.2.5 Mkn 501 (2005) MAGIC/RXTE/KVA

γ/X correlations

MAGIC γ-ray flux (10^{-10}cm^{-2}s^{-1})	RXTE/ASM X-ray flux (counts/s)
1.186 ± 0.251	0.293 ± 0.225
1.505 ± 0.173	0.046 ± 0.478
2.043 ± 0.295	0.496 ± 0.428
1.631 ± 0.217	0.843 ± 0.406
1.533 ± 0.324	-0.330 ± 0.396
1.502 ± 0.281	0.427 ± 0.687
1.441 ± 0.169	0.351 ± 0.645
1.433 ± 0.152	0.610 ± 0.374
2.693 ± 0.127	0.457 ± 0.507
0.750 ± 0.125	-0.327 ± 0.540
1.246 ± 0.104	1.240 ± 0.548
1.207 ± 0.251	0.625 ± 0.379
11.077 ± 0.322	1.280 ± 0.313
3.521 ± 0.300	0.700 ± 0.252
1.266 ± 0.339	0.829 ± 0.269
2.247 ± 0.321	-0.078 ± 0.248
1.852 ± 0.228	0.331 ± 0.292
9.933 ± 0.385	1.170 ± 0.501
2.192 ± 0.366	0.581 ± 0.260
5.525 ± 0.278	0.405 ± 0.382
2.890 ± 0.465	1.080 ± 0.425
1.707 ± 0.128	0.137 ± 0.204
1.329 ± 0.115	0.860 ± 0.270

Table 6.8: The MAGIC data and the RXTE/ASM data (**23** points) of Mkn 501 from 2005 [74].

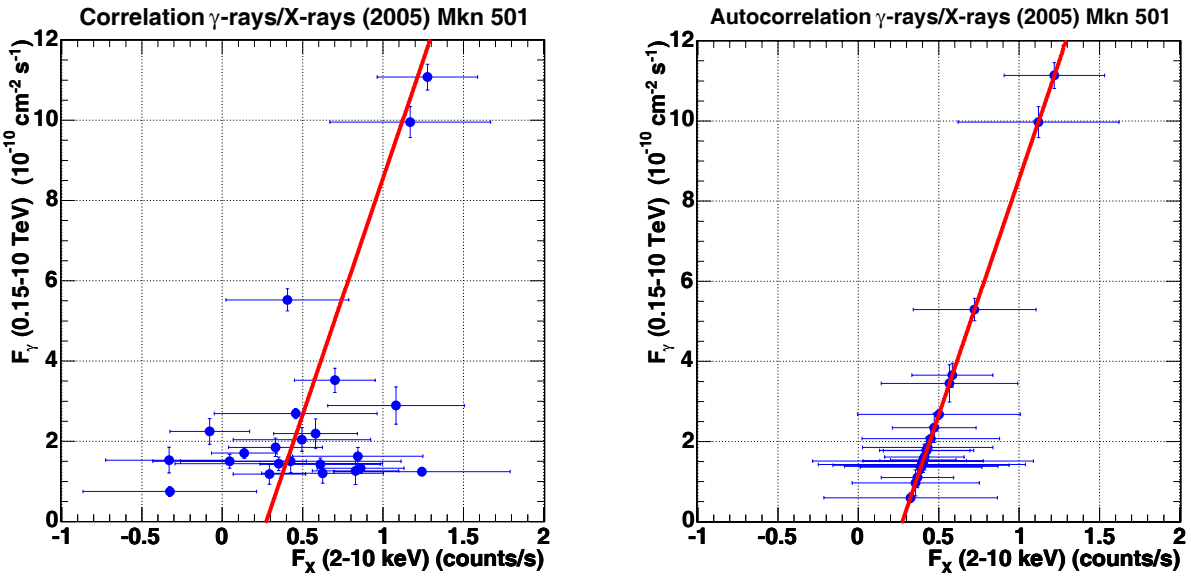

Figure 6.44: Correlation plots: 2005 – MAGIC/RXTE – Mkn 501 Data from [74] (shown in Table 6.8 in this work). $\chi^2/\mathrm{ndf} = 25.6/21$ (Probability $= 0.222$) $F_\gamma = (11.8 \pm 4.0)\cdot 10^{-10}\mathrm{cm}^{-2}\mathrm{counts}^{-1} F_\mathrm{x} - (3.23 \pm 2.14)\cdot 10^{-10}\mathrm{cm}^{-2}\mathrm{s}^{-1}$

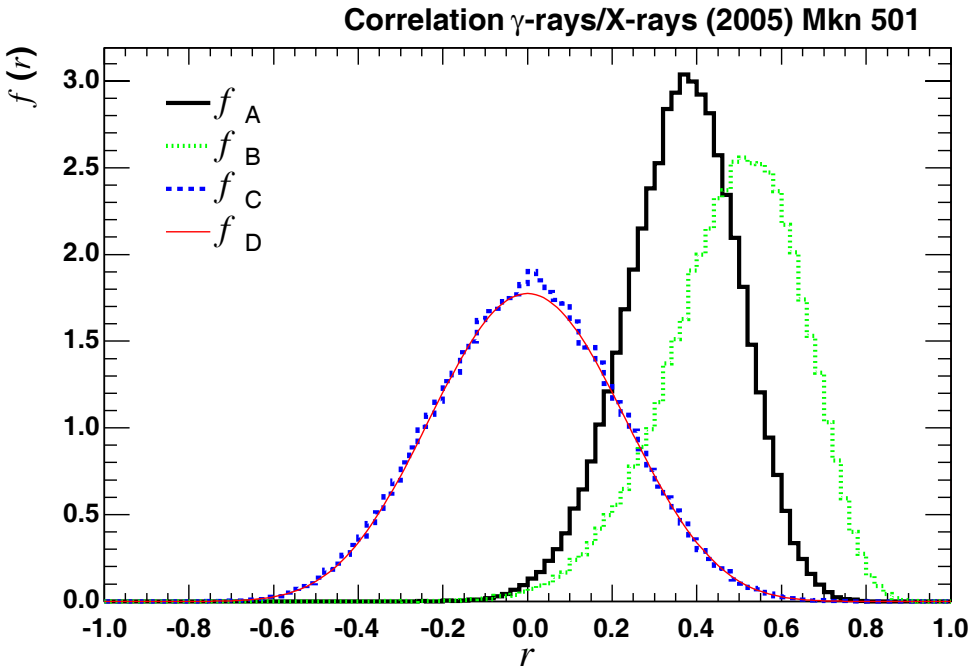

Figure 6.45: Correlation coefficient distributions: 2005 – MAGIC/RXTE – Mkn 501 [74]. 100000 MC events were generated for each PDF. $r_\mathrm{MC} = 0.36 \pm 0.13$, $p_\mathrm{AB} = 0.55 \pm 0.07$, $p_\mathrm{AC} = 0.15 \pm 0.07$.

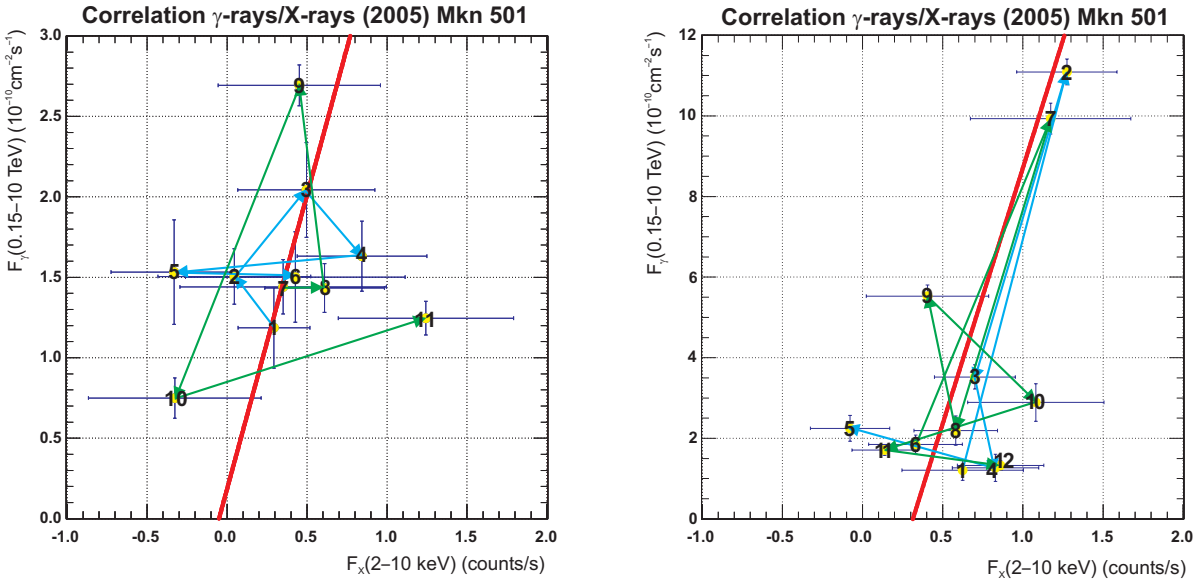

Figure 6.46: Correlation plots: 2005 – MAGIC/RXTE – Mkn 501. Left panel: first 11 points from Table 6.8 (quiet activity). Right panel: last 12 point from Table 6.8 (high activity).

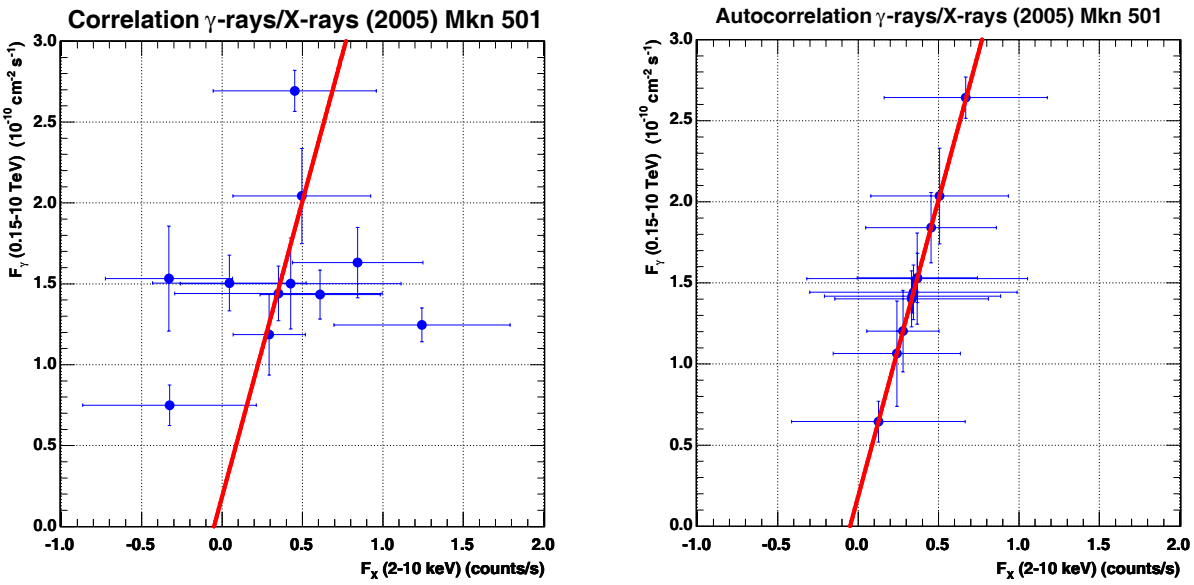

Figure 6.47: Correlation plots: 2005 – MAGIC/RXTE – Mkn 501 (**period of low activity**). Left panel in Figure 6.46. $\chi^2/\mathrm{ndf} = 9.13/9$ (Probability = 0.426) $F_\gamma = (3.7 \pm 4.5)\cdot 10^{-10}\mathrm{cm}^{-2}\mathrm{counts}^{-1} F_\mathrm{x} + (0.18 \pm 1.63)\cdot 10^{-10}\mathrm{cm}^{-2}\mathrm{s}^{-1}$

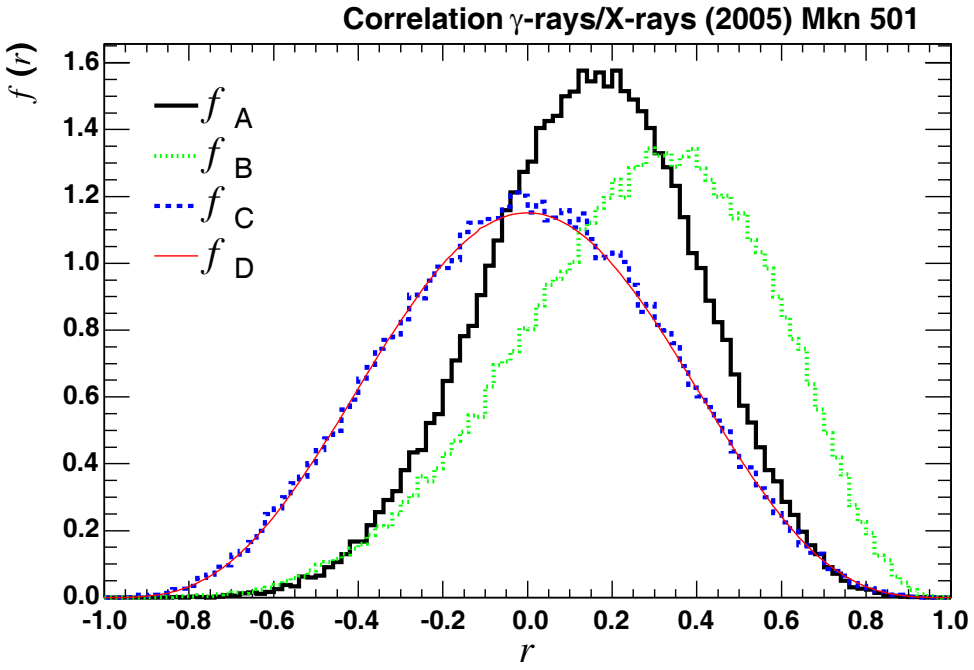

Figure 6.48: Correlation coefficient distributions: 2005 – MAGIC/RXTE – Mkn 501 [74] (**period of low activity**). Left panel in Figure 6.46. 100000 MC events were generated for each PDF. $r_\mathrm{MC} = 0.14 \pm^{0.25}_{0.14}$, $p_\mathrm{AB} = 0.75 \pm^{0.25}_{0.55}$, $p_\mathrm{AC} = 0.73 \pm^{0.27}_{0.55}$.

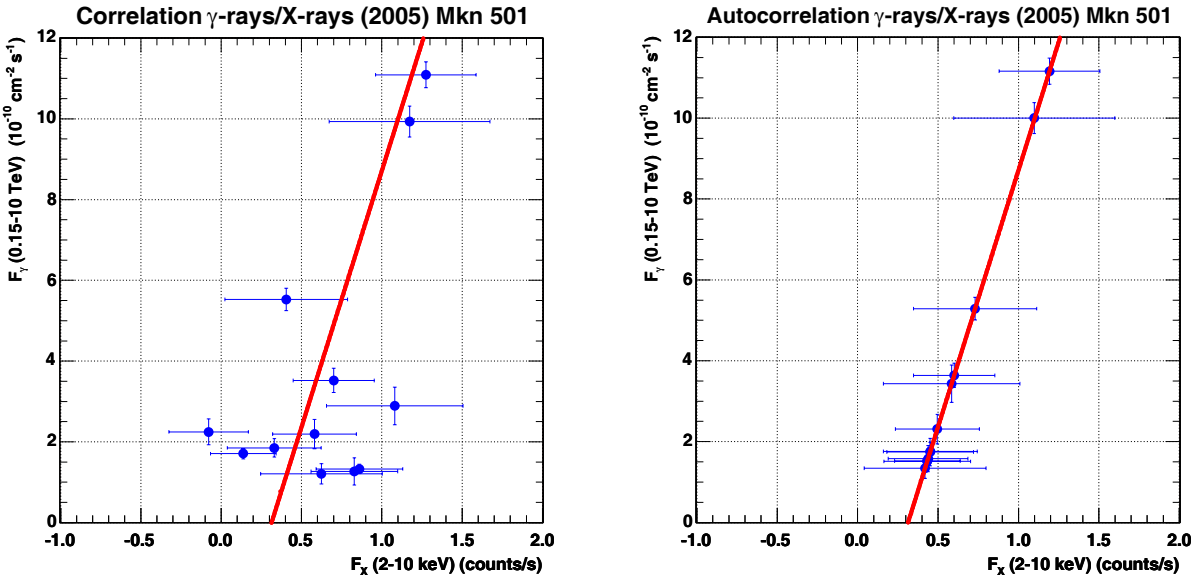

Figure 6.49: Correlation plots: 2005 – MAGIC/RXTE – Mkn 501 (**period of high activity**). Right panel in Figure 6.46. $\chi^2/\mathrm{ndf} = 15.9/10$ (Probability = 0.102) $F_\gamma = (12.7 \pm 4.9)\cdot 10^{-10}\mathrm{cm}^{-2}\mathrm{counts}^{-1} F_\mathrm{x} - (4.0 \pm 2.9)\cdot 10^{-10}\mathrm{cm}^{-2}\mathrm{s}^{-1}$

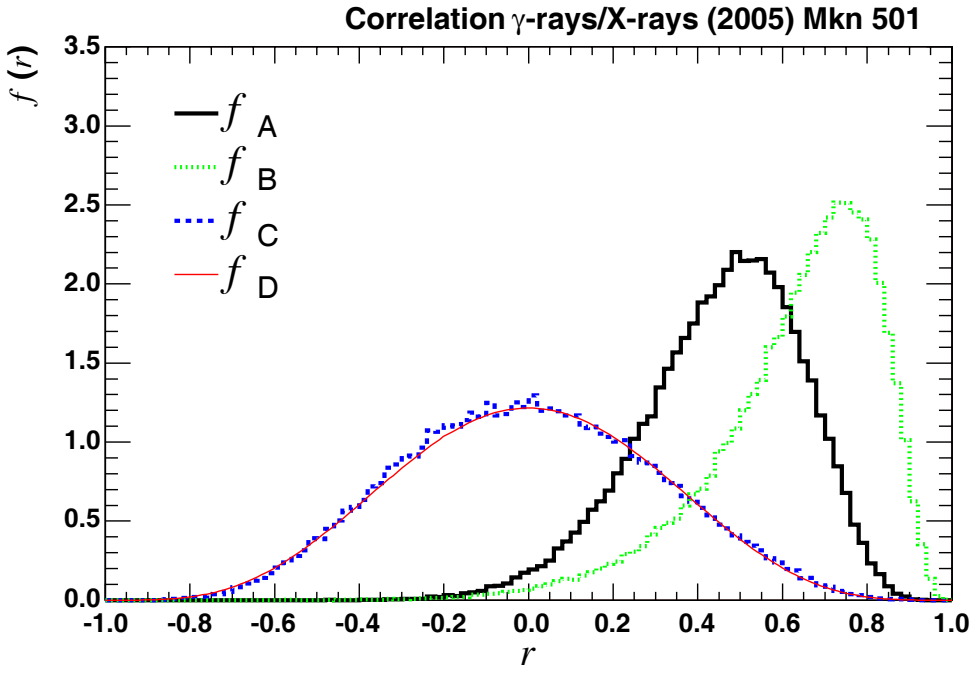

Figure 6.50: Correlation coefficient distributions: 2005 – MAGIC/RXTE – Mkn 501 [74] (**period of high activity**). Right panel in Figure 6.46. 100000 MC events were generated for each PDF. $r_\mathrm{MC} = 0.45 \pm 0.19$, $p_\mathrm{AB} = 0.47 \pm 0.09$, $p_\mathrm{AC} = 0.21 \pm 0.09$.

F_γ (10^{-10}cm^{-2}s^{-1})	$F_{\rm opt}^{\rm TOT}$ (mJy)	$F_{\rm opt}$ (mJy)
1.505 ± 0.173	18.020 ± 0.198	5.720 ± 0.824
1.631 ± 0.217	17.874 ± 0.229	5.574 ± 0.832
1.533 ± 0.324	17.748 ± 0.195	5.448 ± 0.823
1.289 ± 0.236	17.724 ± 0.275	5.424 ± 0.846
1.502 ± 0.281	17.610 ± 0.274	5.310 ± 0.845
2.693 ± 0.127	17.352 ± 0.270	5.052 ± 0.844
0.750 ± 0.125	17.626 ± 0.274	5.326 ± 0.846
1.207 ± 0.251	17.513 ± 0.272	5.213 ± 0.845
11.077 ± 0.322	17.448 ± 0.271	5.148 ± 0.845
3.521 ± 0.300	17.320 ± 0.269	5.020 ± 0.844
1.852 ± 0.228	17.020 ± 0.264	4.720 ± 0.843
5.525 ± 0.278	17.161 ± 0.267	4.861 ± 0.843
1.707 ± 0.128	17.082 ± 0.265	4.782 ± 0.843
1.329 ± 0.115	17.561 ± 0.273	5.261 ± 0.845

Table 6.9: The MAGIC data F_γ and the KVA data $F_{\rm opt}^{\rm TOT}$ (**14** points) of Mkn 501 from 2005 [74]. Subtracted flux $F_{\rm opt}$ is $F_{\rm opt} = F_{\rm opt}^{\rm TOT} - F_{\rm host}$ where $F_{\rm host} = (12.3 \pm 0.8)$ mJy. $F_{\rm host}$ is the Mkn 501 host galaxy flux from Figure 6.51.

Figure 6.51 shows[13] a long-term optical light curve of Mkn 501.

[13]Source: *http://users.utu.fi/kani/1m/Mkn_501_jy.html*

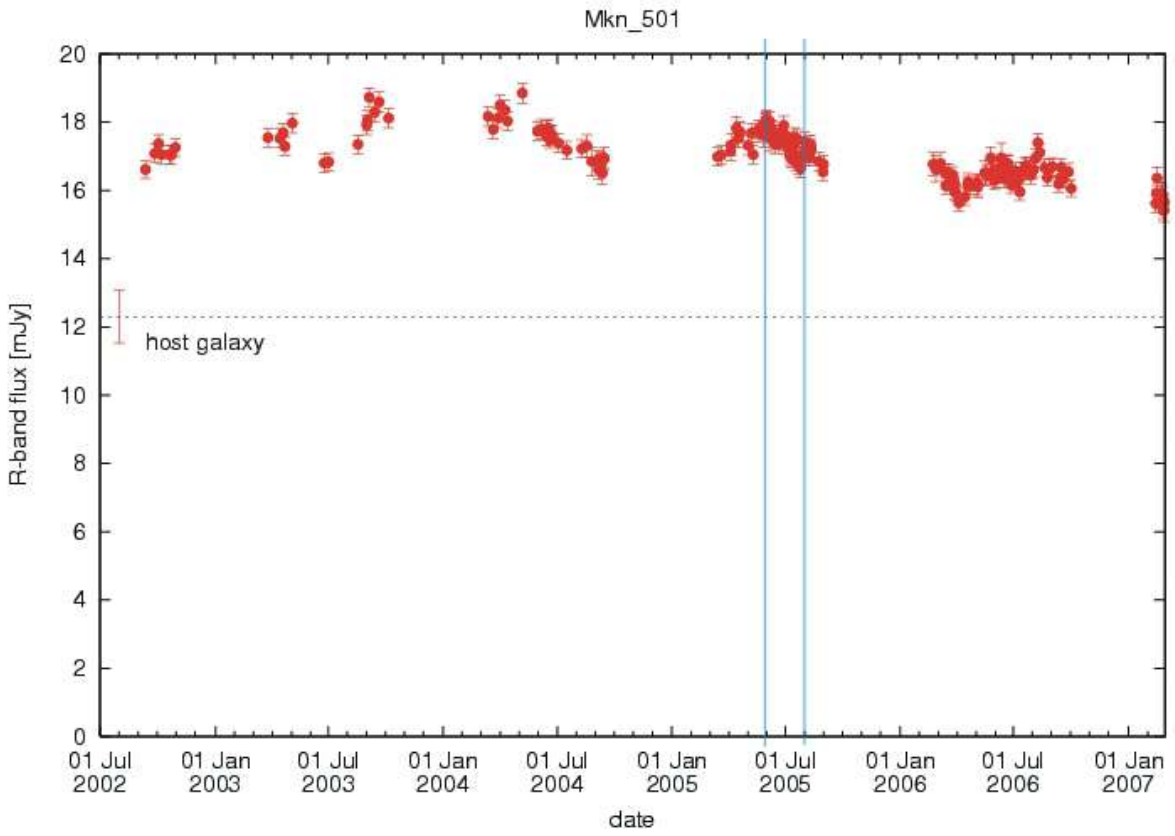

Figure 6.51: Long-term optical light curve of Mkn 501. Blue lines show a period of data that we analyzed here.

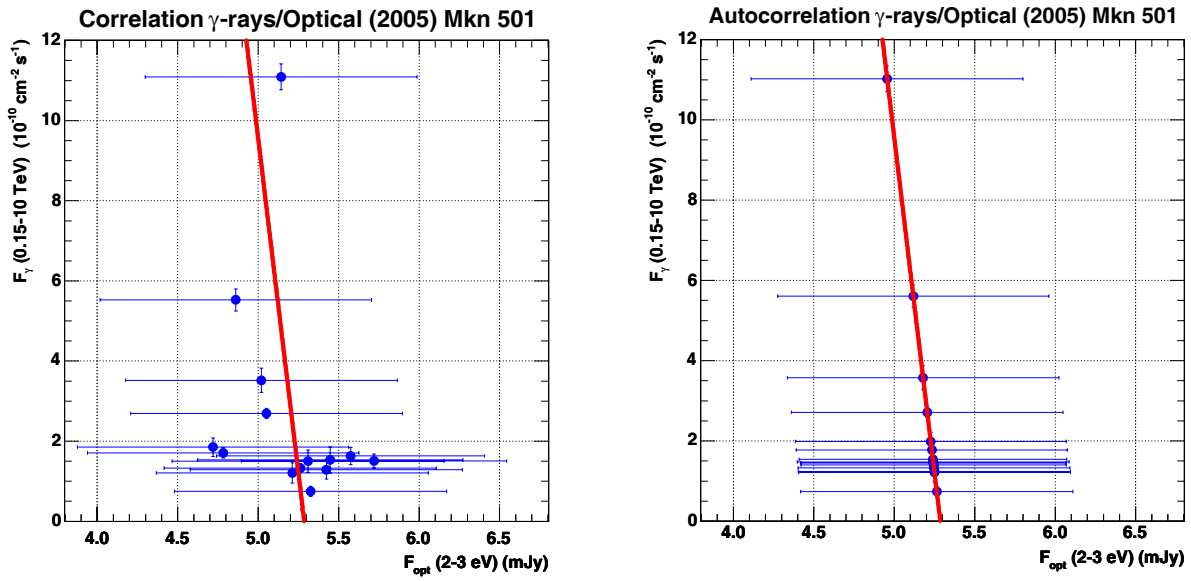

Figure 6.52: Correlation plots: 2005 – MAGIC/KVA – Mkn 501 [74]. (shown in Table 6.9 in this work). $\chi^2/\mathrm{ndf} = 1.49/12$ (Probability $= 0.999$) $F_\gamma = (-33.4 \pm 290)\cdot 10^{-10}\mathrm{cm}^{-2}\mathrm{s}^{-1}\mathrm{mJy}^{-1}\ F_{\mathrm{opt}} + (176 \pm 1511)\cdot 10^{-10}\mathrm{cm}^{-2}\mathrm{s}^{-1}$

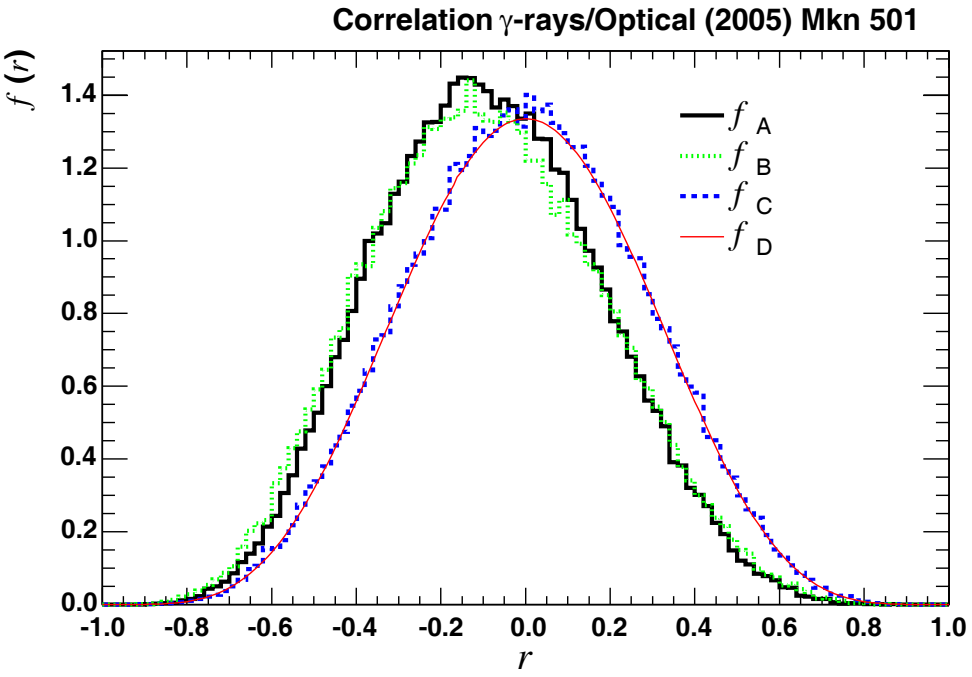

Figure 6.53: Correlation coefficient distributions: 2005 – MAGIC/KVA – Mkn 501 [74]. 100000 MC events were generated for each PDF. $r_{\mathrm{MC}} = 0.66 \pm 0.08$, $p_{\mathrm{AB}} = 0.98\pm^{0.02}_{0.30}$, $p_{\mathrm{AC}} = 0.82\pm^{0.18}_{0.30}$.

γ/γ correlations (Energy-dependent time delay in peak flare emission)

The MAGIC observations of blazar Mkn 501 in 2005 were in the energy range from 250 GeV (the energy threshold of the analysis) to approximately 10 TeV. Apart from total integral flux ϕ(>250 GeV), partial fluxes in different energy regions were studied too, especially for the flares (periods of sudden change in the flux).

It is the very first time that a time delay between the two peaks was clearly seen. Figure 6.54 shows the light curves (during the July 9 flare) in two energy regions: the flux of low energy γ-rays ϕ(250−600 GeV) and the flux of high energy γ-rays ϕ(1.2−10 TeV). The flux in the middle energy was not analyzed here and its light curve can be found in [74]. Under the assumption that the shape of the flares is the same in the two energy ranges, the time delay was found to be $\Delta t = (4 \pm 1)$ min [74].

In our independent analysis, based on γ/γ correlations study, we found $\Delta t = (3.4\pm2.6)$ (Figure 6.60 and Table 6.10).

The physics of blazars can accommodate physical mechanisms which would produce a time delay between emitted photons at different energies. In particular, gradual electron acceleration in the emitting plasma could explain the delay observed in the flare from July 9th [74].

A more speculative explanation is that blazar emission allows exploring some new physics. Different approaches to quantum gravity lead to similar quantification of a violation in the Lorentz symmetry. Such violation should cause **a dependence of the speed of light on the photon energy** [74]. This extremely interesting new result is currently under intensive discussion [75], but beyond the scope of this work.

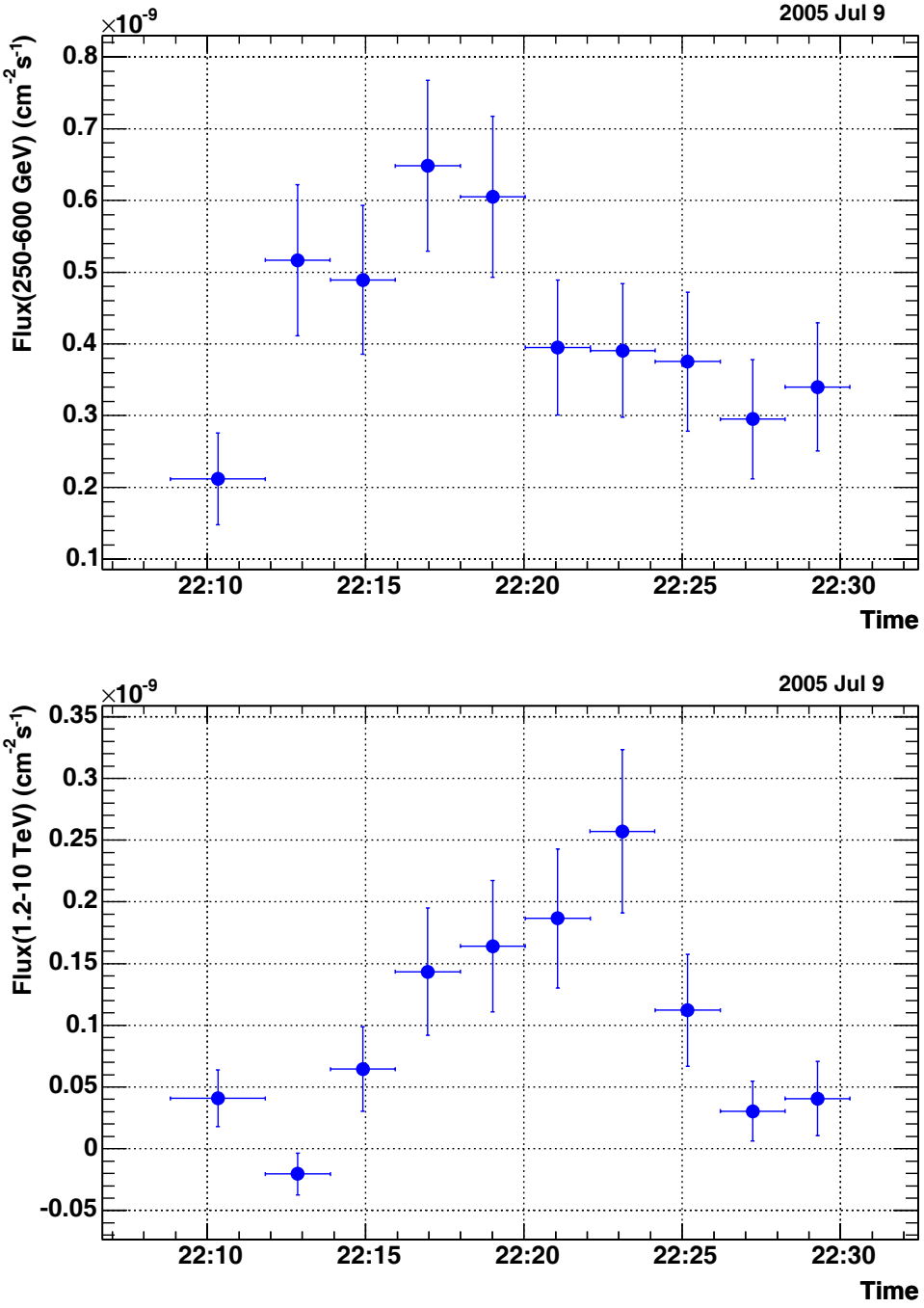

Figure 6.54: Variable part of the light curve ot the flare "2005 July 9" (2 minute binning).

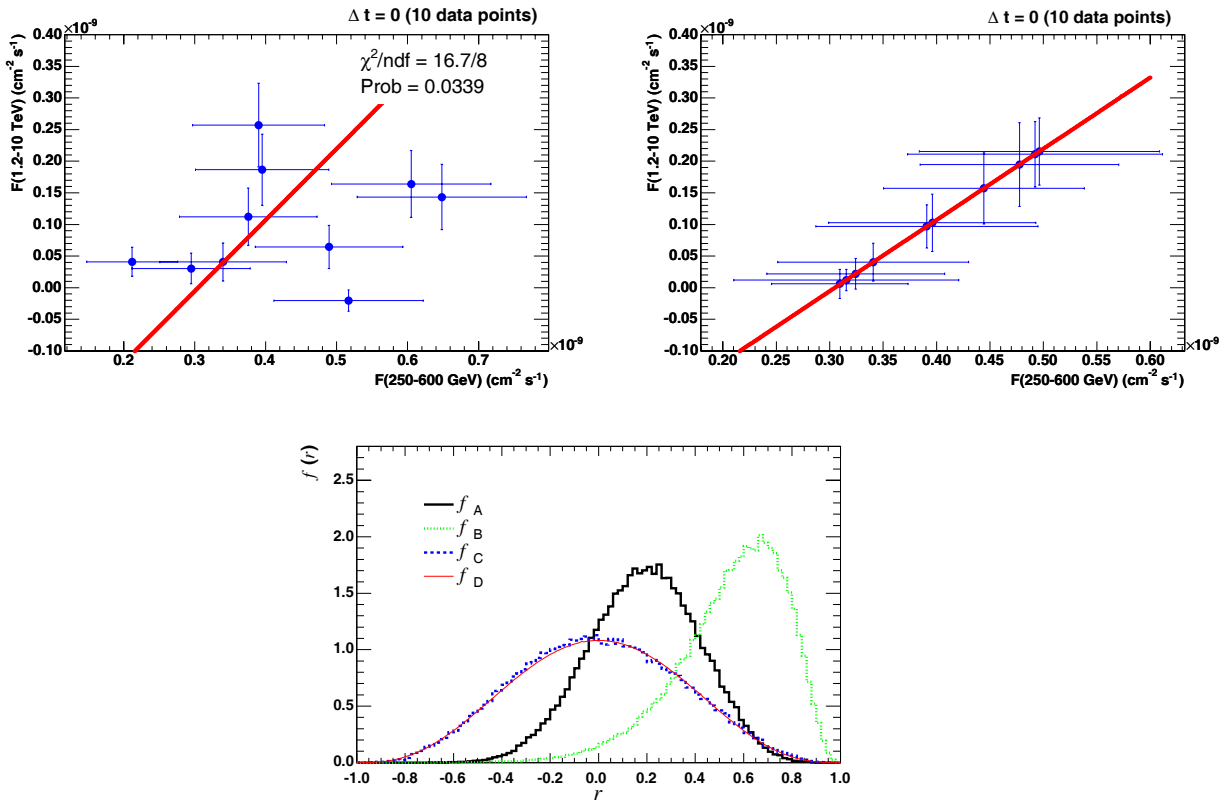

Figure 6.55: $\Delta t = 0$ (10 data points) $r_{\mathrm{MC}} = 0.19 \pm 0.23$, $p_{\mathrm{AB}} = 0.26 \pm 0.18$, $p_{\mathrm{AC}} = 0.65 \pm 0.18$

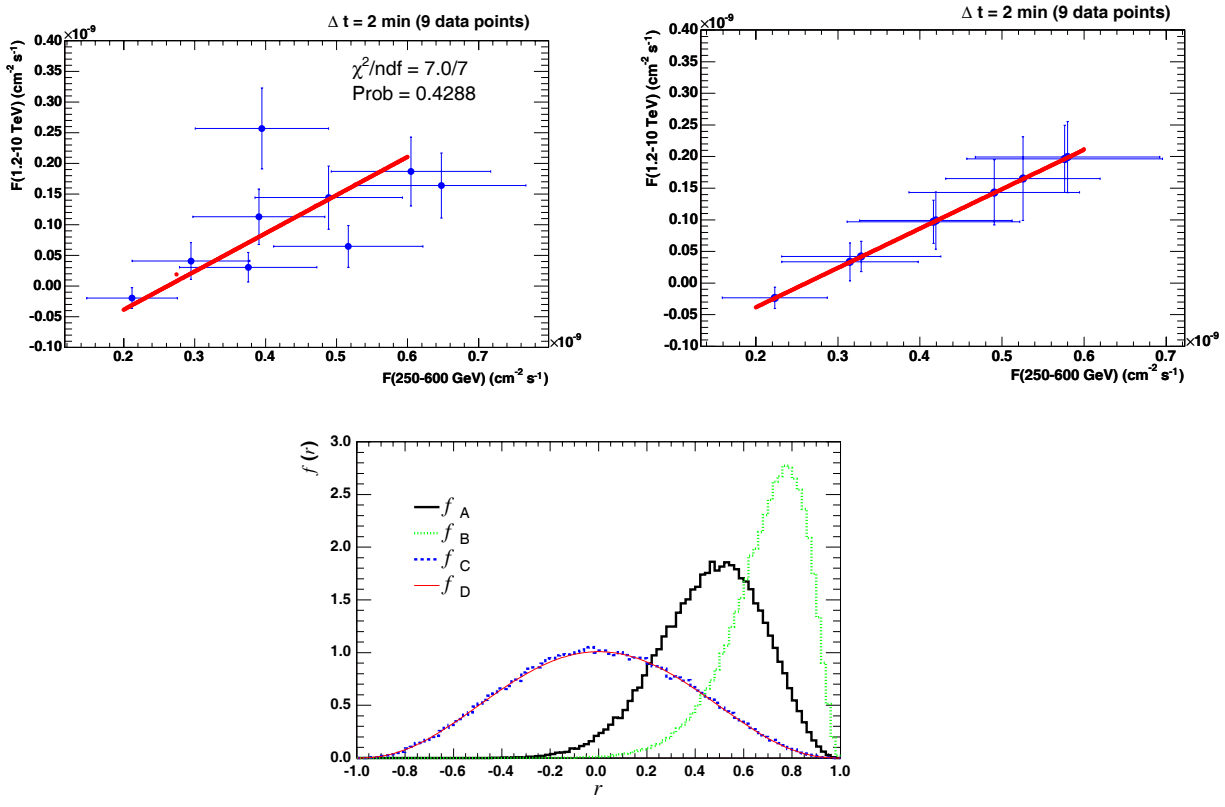

Figure 6.56: $\Delta t = 2$ min (9 data points) $r_{\mathrm{MC}} = 0.46 \pm 0.21$, $p_{\mathrm{AB}} = 0.38 \pm 0.08$, $p_{\mathrm{AC}} = 0.28 \pm 0.08$

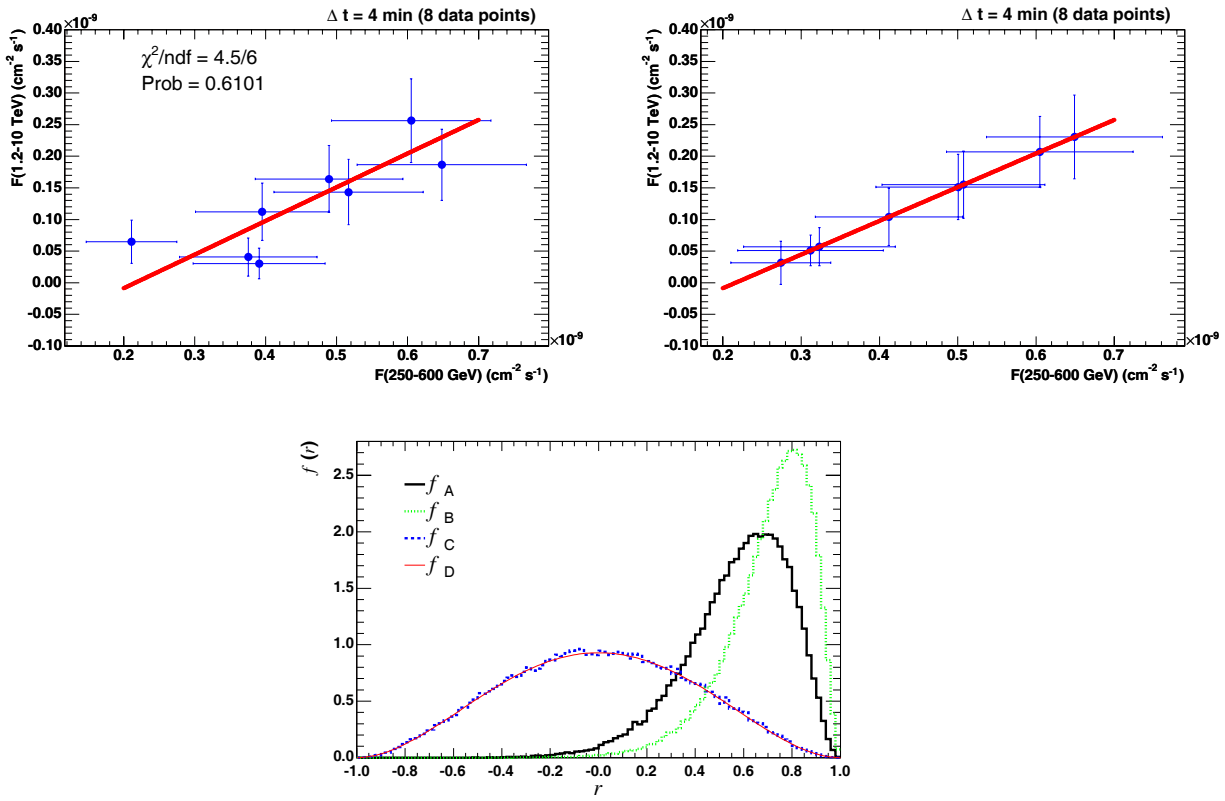

Figure 6.57: $\Delta t = 4$ min (8 data points) $r_{\mathrm{MC}} = 0.58 \pm 0.21$, $p_{\mathrm{AB}} = 0.62 \pm 0.09$, $p_{\mathrm{AC}} = 0.19 \pm 0.09$

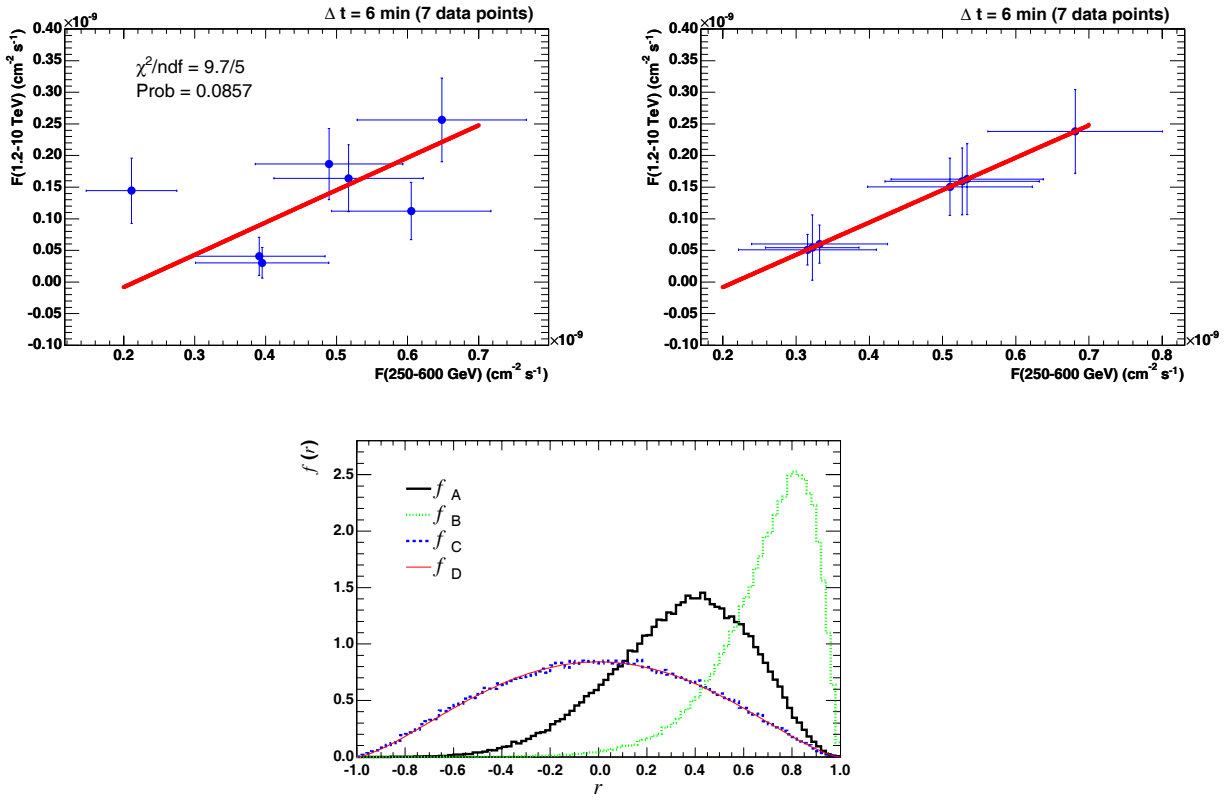

Figure 6.58: $\Delta t = 6$ min (7 data points) $r_{\mathrm{MC}} = 0.34 \pm 0.28$, $p_{\mathrm{AB}} = 0.29 \pm 0.13$, $p_{\mathrm{AC}} = 0.51 \pm 0.13$

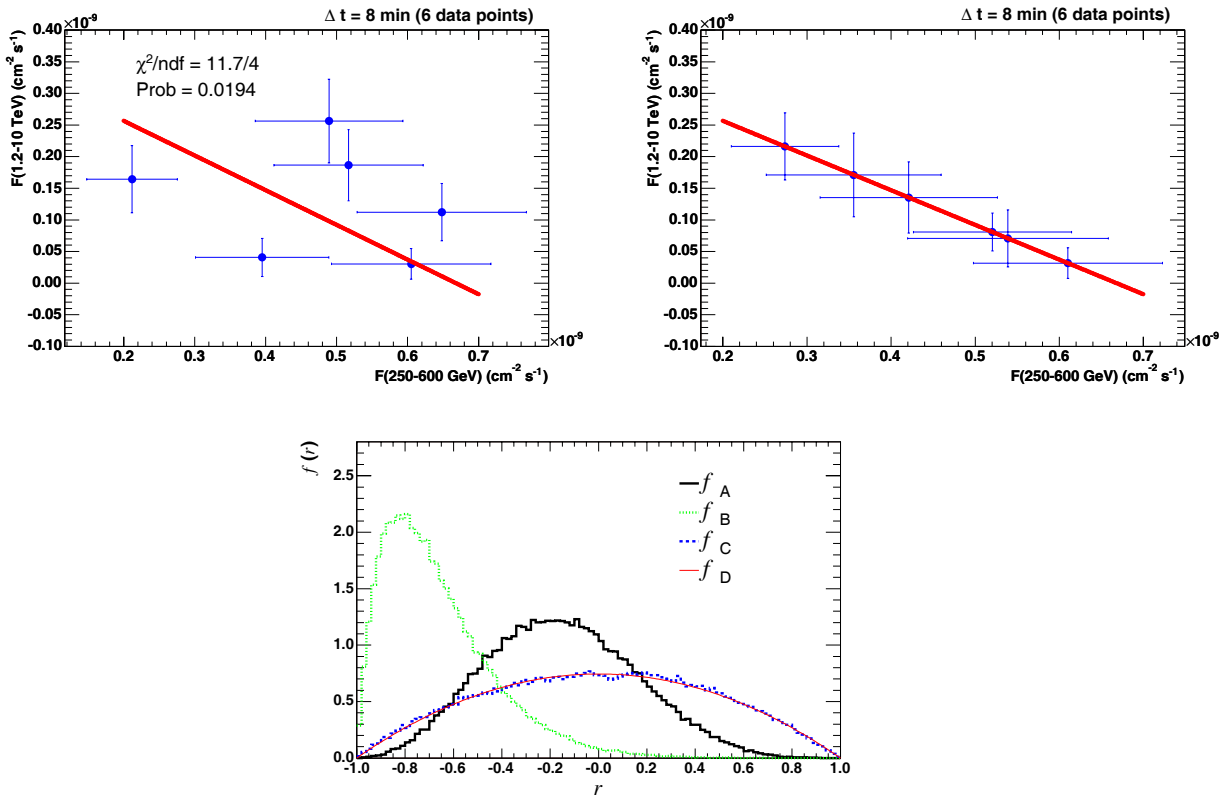

Figure 6.59: Δt = 8 min (6 data points) $r_{\rm MC} = -0.15 \pm 0.31$, $p_{\rm AB} = 0.18 \pm^{0.20}_{0.18}$, $p_{\rm AC} = 0.79 \pm 0.20$

Δt/min	$p(\chi^2)$	$r_{\rm MC}$	$p_{\rm AB}$	$p_{\rm AC}$	$p_{\rm AB}(1-p_{\rm AC})$	$p_{\rm AC}(1-p_{\rm AB})$
0.0	0.03	0.19 ± 0.23	0.26 ± 0.18	0.65 ± 0.18	0.09 ± 0.08	0.48 ± 0.18
2.0	0.43	0.46 ± 0.21	0.38 ± 0.08	0.28 ± 0.08	0.27 ± 0.07	0.17 ± 0.05
4.0	0.61	0.58 ± 0.21	0.62 ± 0.09	0.19 ± 0.09	0.50 ± 0.09	0.07 ± 0.04
6.0	0.09	0.34 ± 0.28	0.29 ± 0.13	0.51 ± 0.13	0.14 ± 0.07	0.37 ± 0.11
8.0	0.02	-0.15 ± 0.31	$0.18 \pm ^{0.20}_{0.18}$	0.79 ± 0.20	$0.04 \pm ^{0.06}_{0.04}$	0.65 ± 0.23

Table 6.10: Correlation analysis parameters vs time shift.

We fitted $r_{\rm MC}$ vs Δt (upper right corner of Figure 6.60) to second order polynomial $r_{\rm MC} = p_0 + p_1\Delta t + p_1\Delta t^2$. The extreme value of the parabola is

$$\overline{t_{\rm m}} = -\frac{\overline{p_1}}{2\overline{p_2}} = 3.4 \text{ min} \tag{6.44}$$

The uncertainties σ_{p1} and σ_{p2} of the fitting parameters are large, therefore error propagation probably overestimates the value of $\sigma_{t\rm m}$

$$\sigma_{t\rm m} = \sqrt{(\partial_{p1} t_{\rm m}\sigma_{p1})^2 + (\partial_{p2} t_{\rm m}\sigma_{p2})^2} = \frac{1}{2\overline{p_2}}\sqrt{\sigma_{p1}^2 + (\frac{\overline{p_1}}{\overline{p_2}}\sigma_{p2})^2} = 2.6 \text{ min} \tag{6.45}$$

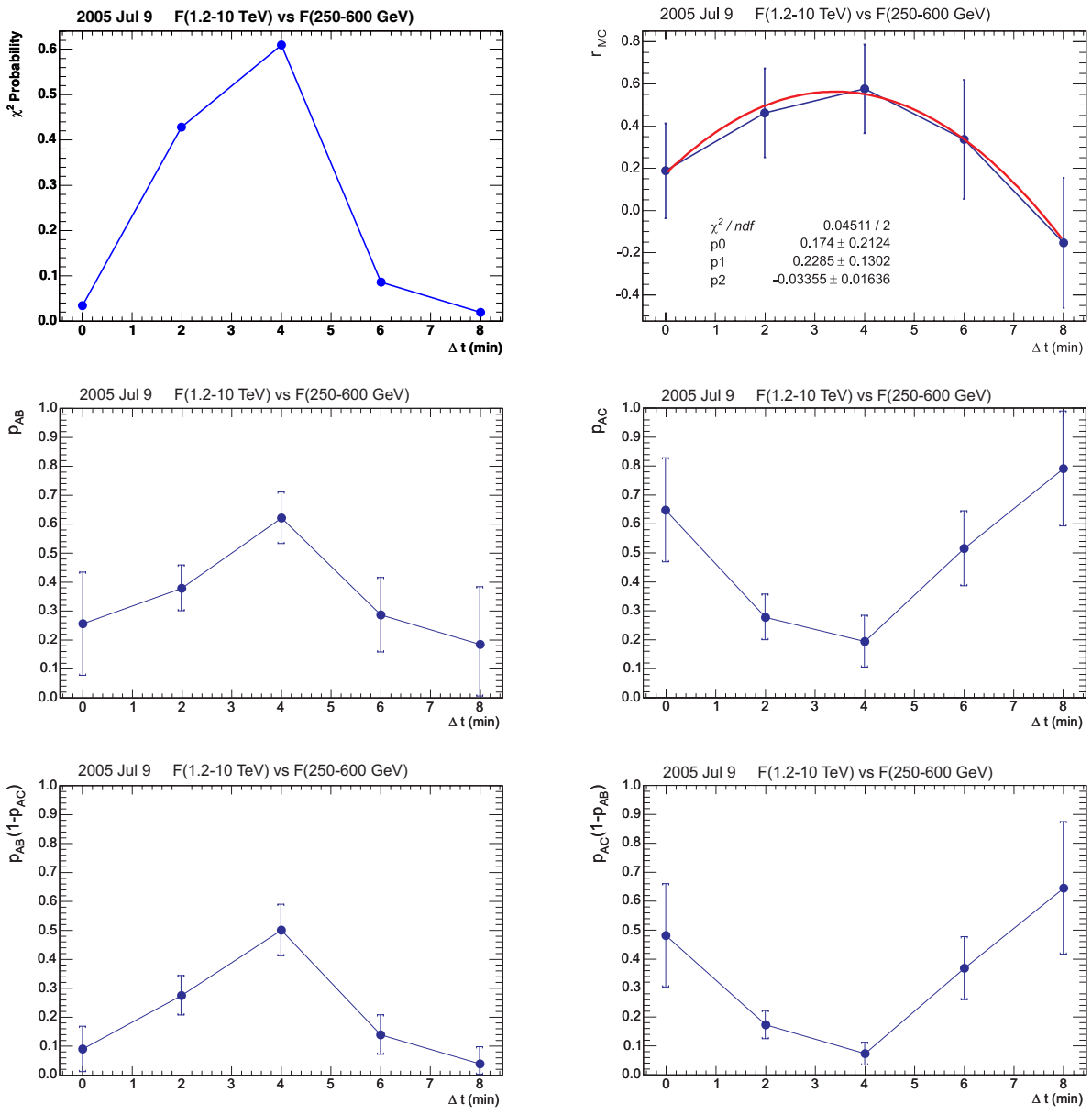

Figure 6.60: Correlation analysis parameters vs time shift.

6.2.6 Comparative results

Tables 6.11, 6.12 and 6.13 show γ/X correlation coefficients and γ/optical correlation coefficients as well as their corresponding probabilities for all data sets that have been analyzed.

The correlated observations of X-ray and TeV γ-ray are naturally explained in the *synchrotron self-Compton* (SSC) scenario (see Section 2.2.6) and strongly support this model [26].

source	Mkn 421	Mkn 421	Mkn 180
data set	2001	2003	2006
data points	26	9	7
telescope	CT1	CT1	MAGIC
r_{DCF}	0.83±0.06	0.71±0.16	0.70±0.19
S	7.3σ	2.7σ	2.2σ
slope/10^{-11}cm^{-2}counts^{-1}	(1.97 ± 0.18)	(0.66 ± 0.23)	(2.14 ± 1.22)
activity	**flaring**	**quiet**	**quiet**
r_{MC}	0.66 ± 0.08	0.52 ± 0.27	0.43 ± 0.29
p_{AB}	0.47 ± 0.01	0.47 ± 0.07	$0.71 \pm {}^{0.29}_{0.31}$
p_{AC}	$0.002 \pm {}^{0.010}_{0.002}$	0.25 ± 0.07	0.40 ± 0.31
$p_{\mathrm{AB}}(1-p_{\mathrm{AC}})$	0.47 ± 0.01	0.35 ± 0.06	0.42 ± 0.29
$p_{\mathrm{AC}}(1-p_{\mathrm{AB}})$	$0.001 \pm {}^{0.010}_{0.001}$	0.13 ± 0.04	$0.12 \pm {}^{0.15}_{0.12}$

Table 6.11: A comparative overview of the γ/**X** correlation (**PART 1**). r_{DCF} and S are correlation coefficient and significance according the old formalism: equations (6.2) and (6.4). r_{MC} is correlation coefficient from our Monte Carlo approach and p_{AB} and p_{AC} are corresponding probabilities as defined in Section 6.1.3.

source	Mkn 421	Mkn 501	Mkn 501	Mkn 501
data set	2005	2005	2005	2005
data points	13	23	11 (of 23)	12 (of 23)
telescope	MAGIC	MAGIC	MAGIC	MAGIC
r_{DCF}	0.53 ± 0.20	0.49 ± 0.16	$0.23 \pm {}^{0.29}_{0.23}$	0.58 ± 0.19
S	2.1σ	2.6σ	0.7σ	2.3σ
slope/10^{-11}cm^{-2}counts^{-1}	(19.5 ± 5.4)	(118 ± 40)	(37 ± 45)	(127 ± 49)
activity	**quiet**	**flaring**	**quiet**	**flaring**
r_{MC}	0.42 ± 0.16	0.36 ± 0.13	$0.14 \pm {}^{0.25}_{0.14}$	0.45 ± 0.19
p_{AB}	0.23 ± 0.04	0.55 ± 0.07	$0.75 \pm {}^{0.25}_{0.55}$	0.47 ± 0.09
p_{AC}	0.22 ± 0.04	0.15 ± 0.07	$0.73 \pm {}^{0.27}_{0.55}$	0.21 ± 0.09
$p_{\mathrm{AB}}(1-p_{\mathrm{AC}})$	0.18 ± 0.03	0.47 ± 0.07	$0.21 \pm {}^{0.44}_{0.21}$	0.37 ± 0.08
$p_{\mathrm{AC}}(1-p_{\mathrm{AB}})$	0.17 ± 0.03	0.07 ± 0.03	$0.18 \pm {}^{0.42}_{0.18}$	0.11 ± 0.05

Table 6.12: A comparative overview of the γ/**X** correlation (**PART 2**). r_{DCF} and S are correlation coefficient and significance according the old formalism: equations (6.2) and (6.4). r_{MC} is correlation coefficient from our Monte Carlo approach and p_{AB} and p_{AC} are corresponding probabilities as defined in Section 6.1.3.

source	Mkn 421	Mkn 421	Mkn 501
data set	2003	2005	2005
data points	8	8	14
telescope	CT1	MAGIC	MAGIC
r_{DCF}	$+0.35 \pm 0.31$	-0.59 ± 0.23	-0.27 ± 0.25
S	0.9σ	1.8σ	1.0σ
slope/ $10^{-10}\mathrm{cm}^{-2}\mathrm{s}^{-1}\mathrm{mJy}^{-1}$	(-0.013 ± 0.010)	(-1.51 ± 0.31)	(-33 ± 290)
activity	**quiet**	**quiet**	**flaring**
r_{MC}	$+0.24 \pm 0.28$	-0.52 ± 0.15	-0.09 ± 0.26
p_{AB}	$0.52 \pm {}^{0.48}_{0.53}$	0.05 ± 0.02	$0.98 \pm {}^{0.02}_{0.30}$
p_{AC}	$0.63 \pm {}^{0.37}_{0.53}$	0.22 ± 0.02	$0.82 \pm {}^{0.18}_{0.30}$
$p_{\mathrm{AB}}(1-p_{\mathrm{AC}})$	$0.19 \pm {}^{0.34}_{0.19}$	0.04 ± 0.02	$0.18 \pm {}^{0.30}_{0.18}$
$p_{\mathrm{AC}}(1-p_{\mathrm{AB}})$	$0.30 \pm {}^{0.42}_{0.30}$	0.21 ± 0.02	$0.01 \pm {}^{0.25}_{0.01}$

Table 6.13: A comparative overview of the γ/**optical** correlation. r_{DCF} and S are correlation coefficient and significance according the old formalism: equations (6.2) and (6.4). r_{MC} is correlation coefficient from our Monte Carlo approach and p_{AB} and p_{AC} are corresponding probabilities as defined in Section 6.1.3.

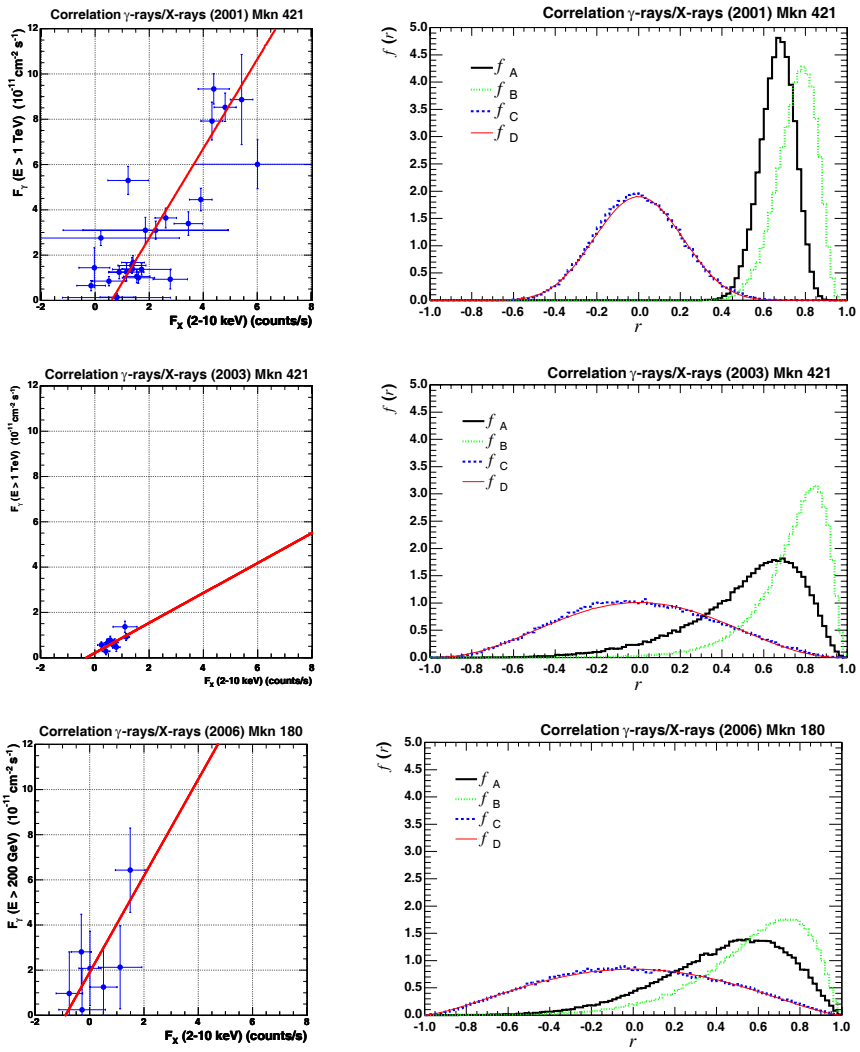

Figure 6.61: Summary of γ-X correlation analysis (**PART 1**). In order to compare different data sets, the same axes-range was used.

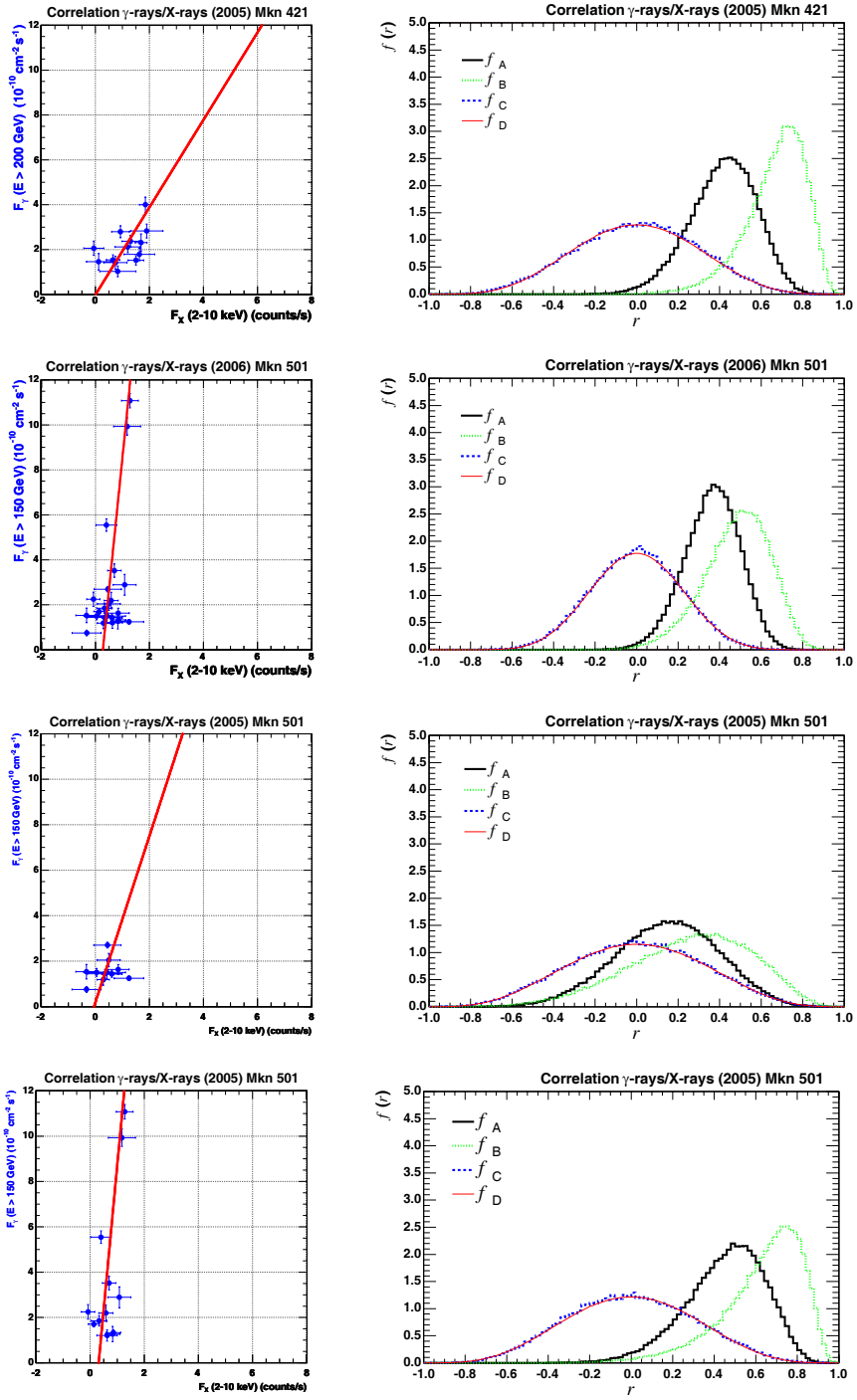

Figure 6.62: Summary of γ-X correlation analysis (**PART 2**). In order to compare different data sets, the same axes-range was used.

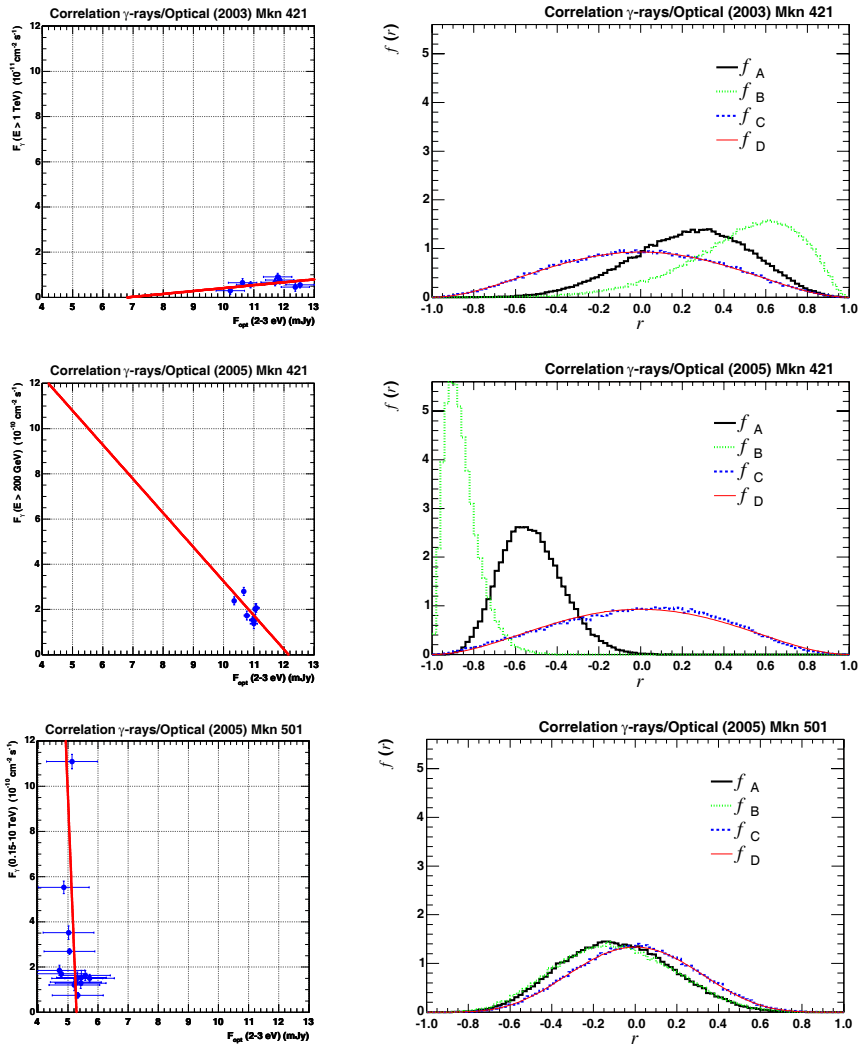

Figure 6.63: Summary of γ-optical correlation analysis. In order to compare different data sets, the same axes-range was used.

Chapter 7

Summary

This thesis presents a study of variable high-energy radiation from three nearby blazars; Mkn 421, Mkn 501, and Mkn 180. Blazars are a subclass of radio-loud active galactic nuclei whose orientation in space is such that one of their two relativistic jets points towards us. The observed high-energy radiation from blazars is most likely produced within the relativistic jets, close to the black hole.

Two different classes of models have been proposed to explain the physics of jets, but currently neither may be safely excluded. According to the so-called hadronic model, the high-energy gamma-rays originate in the decays of relativistic neutral pions. It is well known that in high-energy collisions of hadrons, neutral and charged pions are created together. Since charged pions eventually decay into muons and neutrinos, a rather safe signature of the hadronic scenario would be a simultaneous detection of high-energy neutrinos and gamma-rays. One of the main goals of the recently commissioned IceCube neutrino experiment at the Antarctica is precisely to detect cosmic neutrinos from blazars, preferably in coincidence with gamma-rays detected by telescopes in the northern hemisphere. The goal of the future gamma-ray observatory CROATEA has been precisely to provide such measurements by constantly monitoring the gamma-ray activity of the nearby Markarian galaxies. According to the leptonic model, the dominant source of gamma-rays are relativistic electrons that scatter off the low-energy photons within the jet (Inverse Compton (IC) scattering), effectively transmitting their energy to a photon. The low-energy photons (visible, UV, X-ray) are created by the same population of electrons, through Synchrotron Radiation (SR). Since SR feeds photons to IC, and nearly the same population of electrons may be involved in both processes, the observed SR and IC fluxes should be strongly correlated.

The main focus of this thesis has been precisely on the study of X-ray and gamma-ray correlations as a test of the emission mechanism. Our contribution is twofold. First, we have developed a new method for the extension of the time base of continuous gamma-ray observations. The study of the correlations of the rapidly variable fluxes of X-rays and gamma-rays crucially relies on simultaneous and continuous observations. One of the reasons why Čerenkov telescopes sometimes lack continuity are periods of imperfect weather conditions, i.e. periods of limited atmospheric transparency. So far, data taken during cloudy skies have been commonly discarded. We have demonstrated that the observations during cloudy weather may be still feasible, provided that an appropriate correction is applied. Our new correction method indirectly monitors the atmospheric transparency through the measurements of the hadronic background data, and then calculates and applies a correction to the gamma-ray data. This method was inspired by the simple idea of the so-called throughput factor, originally developed by the Whipple Collaboration. The correction method was tested using the set of Mkn 421 data taken by the HEGRA-CT1

telescope during bad weather conditions in 2001. The results for the recovered data agree with the complementary data taken during the same period of time, but during periods of good weather. Our correction method might significantly increase the duty cycle of virtually all gamma-ray telescopes. But it is of particular importance for telescopes installed at lower elevations, such as CANGAROO and CROATEA. This development may be therefore viewed as a direct contribution to the CROATEA Observatory.

Soon after we had engaged in the analysis of the correlations of the X-ray and gamma-ray fluxes, we realized that the universally accepted method - the standard calculation of a linear correlation coefficient - must be incorrect if applied to data sets with a finite variance on data points. Note that this is a completely general statement. However, in gamma-ray astronomy this mistake has been particularly devastating. It has repeatedly lead to misleading conclusions regarding the strength of the correlation - the correlation was underestimated. The reason is very simple - the expectation value for the correlation factor in the case of perfectly correlated data with a finite variance should in reality be always smaller than unity; the larger the error bars on data points, the smaller the expectation for the correlation coefficient. We have developed a new method for correlation analysis, which properly takes into account the finite variance and compares the measured correlations to different expectations. The application of the method to various available data leads to the conclusion that the gamma-ray flux is in general significantly more correlated with the X-ray flux than previously thought, which speaks in favour of the leptonic model.

We have applied this method to all available data for Mkn 421, Mkn 501, and Mkn 180. In particular, we performed a complete analysis of data from the multiwavelength measurement of Mkn 421 (measured by the CT1 telescope in the gamma-ray band, the RXTE satellite-borne detector in the X-ray band, and by the KVA telescope in the optical band). During February and March 2003, we participated in data taking at La Palma, in the framework of a specially organized 'multi-wavelength campaign.' Despite the low level of flux during the campaign, we were able to detect the variability of the VHE gamma-ray flux, and find positive correlation with the X-ray flux. Other analysed data include the most recent measurements of the Mkn 421, Mkn 501 and Mkn 180 galaxies performed by the MAGIC Telescope in 2005, 2006, and 2006, respectively. In some cases the measurement significance was very low and inconclusive, mainly due to large relative errors, and due to a rather small number of data points. The strong flares have invariably demonstrated a high level of correlation. The majority of measurements are consistent with positive correlations between X-rays and gamma-rays, again in support of the leptonic model.

Using our correlation analysis technique, we have also observed two other interesting phenomena. First, we observed positive correlations of the optical and X-ray fluxes, provided that a one day time delay of the optical light curve is assumed. This effect came up in the analysis of the Mkn 421 data from February/March 2003, and presents the first observation of positive correlation among the X-ray and optical fluxes. Second, we have independently confirmed a very interesting recent observation - the energy-dependent four minute time delay within the strong flare in the gamma-ray emission, found in the Mkn 501 data by the MAGIC Collaboration. Both phenomena may shed new light on the mechanism of the emission processes in blazar jets. However, the latter result has already created a lot of attention, since it may provide the means to test one of the most fundamental predictions of quantum gravity - the dependence of the speed of light on the photon energy.

Bibliography

[1] R.U. Abbasi. A Measurement of Time-Averaged Aerosol Optical Depth using Air-Showers Observed in Stereo by HiRes. *Astroparticle Physics*, **25**:93–97, 2006. [arXiv:astro-ph/0601091].

[2] R. Abbasi et al. Techniques for measuring atmospheric aerosols at the High Resolution Fly's Eye experiment. *Astroparticle Physics*, **25**:74–83, 2006. [arXiv:astro-ph/0512423].

[3] T. Abu-Zayyad, C.C.H. Jui, and E.C. Loh. The Effect of Clouds on Air Showers Observation from Space. *Astroparticle Physics*, **21**:163–182, 2004. [arXiv:astro-ph/0310810].

[4] F. Aharonian. *Very High Energy Cosmic Gamma Radiation - A Crucial Window on the Extreme Universe*. World Scientific Publishing, 2004.

[5] F. Aharonian. Next generation of IACT arrays: scientific objectives versus energy domain. *arXiv:astro-ph/0511139*, November 2005.

[6] F. Aharonian and C.W. Akerlof. Gamma-Ray Astronomy with Imaging Atmospheric Čerenkov Telescopes. *Annual Review of Nuclear and Particle Science*, **47**:273–314, 1997.

[7] F. Aharonian et al. On the optimization of multichannel cameras for imaging atmospheric Cherenkov telescopes. *Journal of Physics G: Nuclear and Particle Physics*, **21**:985–993, 1995.

[8] F. Aharonian et al. Measurement of the flux, spectrum, and variability of TeV γ-rays from Mkn 501 during a state of high activity. *Astronomy and Astrophysics*, **327**:L5–L8, 1997. [arXiv:astro-ph/9706019].

[9] F. Aharonian et al. Cosmic ray proton spectrum determined with the imaging atmospheric Cherenkov technique. *Physical Review D*, **59**:092003, 1999. [arXiv:astro-ph/9901160].

[10] F. Aharonian et al. Measurement of the radial distribution of Cherenkov light generated by TeV γ-ray air showers. *Astroparticle Physics*, **10**:21–29, 1999. [arXiv:astro-ph/9807119].

[11] F. Aharonian et al. Observations of Mkn 421 during 1997 and 1998 in the energy range above 500 GeV with the HEGRA stereoscopic Cherenkov telescope system. *Astronomy and Astrophysics*, **350**:757–764, 1999. [arXiv:astro-ph/9905032].

[12] F. Aharonian et al. Phase-resolved TeV Gamma-Ray Characteristics of the Crab and Geminga pulsars. *Astronomy and Astrophysics*, **346**:913–921, 1999.

[13] F. Aharonian et al. The temporal characteristics of the TeV γ-emission from Mkn 501 in 1997 – Part II. Results from HEGRA CT1 and CT2. *Astronomy and Astrophysics*, **349**:29–44, 1999. [arXiv:astro-ph/9901284].

[14] F. Aharonian et al. The temporal characteristics of the TeV gamma-radiation from Mkn 501 in 1997 – Part I. Data from stereoscopic imaging atmospheric Cherenkov telescope system of HEGRA. *Astronomy and Astrophysics*, **342**:69–86, 1999. [arXiv:astro-ph/9808296].

[15] F. Aharonian et al. The time averaged TeV energy spectrum of Mkn 501 of the extraordinary 1997 outburst as measured with the stereoscopic Cherenkov telescope system of HEGRA. *Astronomy and Astrophysics*, **349**:11–28, 1999. [arXiv:astro-ph/9903386].

[16] F. Aharonian et al. HEGRA search for TeV emission from BL Lacertae objects. *Astronomy and Astrophysics*, **353**:847–852, 2000. [arXiv:astro-ph/9903455].

[17] F. Aharonian et al. Optimizing the angular resolution of the HEGRA telescope system to study the emission region of VHE gamma rays in the Crab Nebula. *Astronomy and Astrophysics*, **361**:1073–1078, 2000. [arXiv:astro-ph/0007367].

[18] F. Aharonian et al. Rejection of the hypothesis that Markarian 501 TeV photons are pure Bose-Einstein condensates. *The Astrophysical Journal*, **543**:L39–L42, 2000. [arXiv:astro-ph/0006092].

[19] F. Aharonian et al. The energy spectrum of TeV gamma rays from the Crab Nebula as measured by the HEGRA system of imaging air Cherenkov telescopes. *The Astrophysical Journal*, **539**:317–324, 2000. [arXiv:astro-ph/0003182].

[20] F. Aharonian et al. 5@5 – a 5 GeV energy threshold array of imaging atmospheric Cherenkov telescopes at 5 km altitude. *Astroparticle Physics*, **15**:335–356, 2001. [arXiv:astro-ph/0006163].

[21] F. Aharonian et al. A search for gamma-ray emission from the Galactic plane in the longitude range between 37° and 43°. *Astronomy and Astrophysics*, **375**:1008–1017, 2001. [arXiv:astro-ph/0106528].

[22] F. Aharonian et al. A study of Tycho's SNR at TeV energies with the HEGRA CT-System. *Astronomy and Astrophysics*, **373**:292–300, 2001. [arXiv:astro-ph/0107044].

[23] F. Aharonian et al. Evidence for TeV gamma ray emission from Cassiopeia A. *Astronomy and Astrophysics*, **370**:112–120, 2001. [arXiv:astro-ph/0102391].

[24] F. Aharonian et al. Reanalysis of the high energy cutoff of the 1997 Mkn 501 TeV energy spectrum. *Astronomy and Astrophysics*, **366**:62–67, 2001. [arXiv:astro-ph/0011483].

[25] F. Aharonian et al. Search for a TeV gamma-ray halo of Mkn 501. *Astronomy and Astrophysics*, **366**:746–751, 2001. [arXiv:astro-ph/0012401].

[26] F. Aharonian et al. The TeV energy spectrum of Markarian 501 measured with the stereoscopic telescope system of HEGRA during 1998 and 1999. *The Astrophysical Journal*, **546**:898–902, 2001. [arXiv:astro-ph/0008211].

[27] F. Aharonian et al. A search for TeV gamma-ray emission from SNRs, pulsars and unidentified GeV sources in the Galactic plane in the longitude range between -2^o and 85^o. *Astronomy and Astrophysics*, **395**:803–811, 2002. [arXiv:astro-ph/0209360].

[28] F. Aharonian et al. TeV gamma rays from the blazar H 1426+428 and the diffuse extragalactic background radiation. *Astronomy and Astrophysics*, **384**:L23–L26, 2002. [arXiv:astro-ph/0202072].

[29] F. Aharonian et al. Un unidentified TeV source in the vicinity of Cygnus OB2. *Astronomy and Astrophysics*, **393**:L37–L40, 2002. [arXiv:astro-ph/0207528].

[30] F. Aharonian et al. Variation of the TeV energy spectrum at different flux levels of Mkn 421 observed with the HEGRA system of Cherenkov telescopes. *Astronomy and Astrophysics*, **393**:89–100, 2002. [arXiv:astro-ph/0205499].

[31] F. Aharonian et al. TeV γ-ray light curve and energy spectrum of Mkn 421 during its 2001 flare as measured with HEGRA CT1. *Astronomy and Astrophysics*, **410**:813–821, 2003.

[32] F. Aharonian et al. Calibration of cameras of the HESS detector. *Astroparticle Physics*, **22**:109–125, 2004. [arXiv:astro-ph/0406658].

[33] F. Aharonian et al. Observation of 54 Active Galactic Nuclei with the HEGRA system of Cherenkov telescopes. *Astronomy and Astrophysics*, **421**:529–537, 2004. [arXiv:astro-ph/0401301].

[34] F. Aharonian et al. The Crab nebula and pulsar between 500 GeV and 80 TeV: observations with the HEGRA stereoscopic air Cerenkov telescopes. *The Astrophysical Journal*, **614**:897–913, 2004. [arXiv:astro-ph/0407118].

[35] F. Aharonian et al. A new population of very high energy γ-ray sources in the Milky Way. *Science*, **307**:1938–1942, 2005. [arXiv:astro-ph/0504380].

[36] F. Aharonian et al. A possible association of the new VHE γ-ray source HESS J1825-137 with the pulsar wind nebula H 18.0-0.7. *Astronomy and Astrophysics*, **442**:L25–L30, 2005. [arXiv:astro-ph/0510394].

[37] F. Aharonian et al. A search for very high energy gamma-ray emission from the starburst galaxy NGC 253 with H.E.S.S. *Astronomy and Astrophysics*, **442**:177–184, 2005. [arXiv:astro-ph/0507370].

[38] F. Aharonian et al. Detection of TeV γ-ray emission from the shell-type supernova remnant RX J0852.0-4622 with HESS. *Astronomy and Astrophysics*, **437**:L7–L10, 2005. [arXiv:astro-ph/0505380].

[39] F. Aharonian et al. Discovery of the binary pulsar PSR B1259-63 in very-high-energy gamma rays around periastron with H.E.S.S. *Astronomy and Astrophysics*, **442**:1–10, 2005. [arXiv:astro-ph/0506280].

[40] F. Aharonian et al. Discovery of very high energy gamma-rays associated with an X-ray binary. *Science*, **309**:746–749, 2005. [arXiv:astro-ph/0508298].

[41] F. Aharonian et al. Discovery of VHE gamma rays from PKS 2005-489. *Astronomy and Astrophysics*, **436**:L17–L20, 2005. [arXiv:astro-ph/0504520].

[42] F. Aharonian et al. H.E.S.S. Observations of PKS 2155-304. *Astronomy and Astrophysics*, **430**:865–875, 2005. [arXiv:astro-ph/0411582].

[43] F. Aharonian et al. Multi-wavelength observations of PKS 2155-304 with H.E.S.S. *Astronomy and Astrophysics*, **442**:895–908, 2005. [arXiv:astro-ph/0506593].

[44] F. Aharonian et al. Observations of Mkn 421 in 2004 with H.E.S.S. at large zenith angles. *Astronomy and Astrophysics*, **437**:95–100, 2005. [arXiv:astro-ph/0506319].

[45] F. Aharonian et al. Observations of Selected AGN with H.E.S.S. *Astronomy and Astrophysics*, **441**:465–472, 2005. [arXiv:astro-ph/0507207].

[46] F. Aharonian et al. Search for TeV emission from the region around PSR B1706-44 with the H.E.S.S. experiment. *Astronomy and Astrophysics*, **432**:L9–L12, 2005. [arXiv:astro-ph/0501512].

[47] F. Aharonian et al. Serendipitous discovery of the unidentified extended TeV γ-ray source HESS J1303-631. *Astronomy and Astrophysics*, **439**:1013–1021, 2005. [arXiv:astro-ph/0505219].

[48] F. Aharonian et al. TeV gamma-ray observations of SS-433 and a survey of the surrounding field with the HEGRA IACT-System. *Astronomy and Astrophysics*, **439**:635–643, 2005.

[49] F. Aharonian et al. The unidentified TeV source (TeV J2032+4130) and surrounding field: Final HEGRA IACT-System results. *Astronomy and Astrophysics*, **431**:197–202, 2005. [arXiv:astro-ph/0501667].

[50] F. Aharonian et al. Upper Limits to the SN1006 multi-TeV gamma-ray flux from HESS observation. *Astronomy and Astrophysics*, **437**:135–139, 2005. [arXiv:astro-ph/0502239].

[51] F. Aharonian et al. Very high energy gamma rays from composite SNR G 0.9+0.1. *Astronomy and Astrophysics*, **432**:L25–L29, 2005. [arXiv:astro-ph/0501265].

[52] F. Aharonian et al. A detailed spectral and morphological study of the gamma-ray supernova remnant RX J1713.7-3946 with H.E.S.S. *Astronomy and Astrophysics*, **449**:223–242, 2006. [arXiv:astro-ph/0511678].

[53] F. Aharonian et al. A low level of extragalactic background light as revealed by γ-rays from blazars. *Nature*, **440**:1018–1021, 2006.

[54] F. Aharonian et al. Discovery of Very High Energy Gamma-Ray Emission from the BL Lac Object H2356-309 with the H.E.S.S. Cherenkov Telescopes. *Astronomy and Astrophysics*, **455**:461–466, 2006. [arXiv:astro-ph/0607569].

[55] F. Aharonian et al. Discovery of very-high-energy γ-rays from the Galactic Centre ridge. *Nature*, **439**:695–698, 2006. [arXiv:astro-ph/0603021].

[56] F. Aharonian et al. Evidence for VHE Gamma-ray Emission from the Distant BL Lac PG 1553+113. *Astronomy and Astrophysics*, **448**:L19–L24, 2006. [arXiv:astro-ph/0601545].

[57] F. Aharonian et al. First detection of a VHE gamma-ray spectral maximum from a Cosmic source: H.E.S.S. discovery of the Vela X nebula. *Astronomy and Astrophysics*, **448**:L43–L47, 2006. [arXiv:astro-ph/0601575].

[58] F. Aharonian et al. H.E.S.S. observations of the Galactic Center region and their possible dark matter interpretation. *Physical Review Letters*, **97**:221102, 2006. [arXiv:astro-ph/0610509].

[59] F. Aharonian et al. Observations of 14 young open star clusters with the HEGRA system of Cherenkov telescopes. *Astronomy and Astrophysics*, **454**:775–779, 2006.

[60] F. Aharonian et al. Observations of the Crab nebula with HESS. *Astronomy and Astrophysics*, **457**:899–915, 2006. [arXiv:astro-ph/0607333].

[61] F.A. Aharonian et al. High-energy particle acceleration in the shell of a supernova remnant. *Nature*, **432**:75–77, 2004. [arXiv:astro-ph/0411533].

[62] M. Ahlers. Strongly Interacting Astrophysical Neutrinos. *arXiv:astro-ph/0511483*, November 2005.

[63] E.J. Ahn. Modeling extensive air showers from TeV black holes. *Proceedings of the Very High Energy Phenomena in the Universe (La Thuile)*, March 2005.

[64] J. Albert. Variable Very-High-Energy Gamma-Ray Emission from the Microquasar LS I +61 303. *Science*, **312**:1771–1773, 2006.

[65] J. Albert et al. Physics and Astrophysics with a ground-based gamma-ray telescope of low energy threshold. *Astroparticle Physics*, **23**:493–509, 2005.

[66] J. Albert et al. Discovery of very high energy γ-rays from Markarian 180 triggered by an optical outburst. *The Astrophysical Journal Letters*, **648**:L105–L108, 2006. [arXiv:astro-ph/0606630].

[67] J. Albert et al. Discovery of VHE gamma-ray emission from 1ES 1218+304. *The Astrophysical Journal*, **642**:L119–L122, 2006. [arXiv:astro-ph/0603529].

[68] J. Albert et al. Flux upper limit of gamma-ray emission by GRB050713a from MAGIC Telescope observations. *The Astrophysical Journal*, **641**:L9–L12, 2006. [arXiv:astro-ph/0602231].

[69] J. Albert et al. MAGIC observations of very high energy gamma-rays from HESS J1813-178. *The Astrophysical Journal*, **637**:L41–L44, 2006. [arXiv:astro-ph/0512283].

[70] J. Albert et al. Observation of Gamma Rays from the Galactic Center with the MAGIC Telescope. *The Astrophysical Journal*, **638**:L101–L104, 2006. [arXiv:astro-ph/0512469].

[71] J. Albert et al. Observation of VHE Gamma Radiation from HESS J1834-087/W41 with the MAGIC Telescope. *The Astrophysical Journal*, **643**:L53–L56, 2006. [arXiv:astro-ph/0604197].

[72] J. Albert et al. Observation of VHE gamma-ray emission from the Active Galactic Nucleus 1ES1959+650 using the MAGIC telescope. *The Astrophysical Journal*, **639**:761–765, 2006. [arXiv:astro-ph/0508543].

[73] J. Albert et al. Observations of Mkn 421 with the MAGIC Telescope. *The Astrophysical Journal*, accepted, 2006. [arXiv:astro-ph/0603478].

[74] J. Albert et al. **Variable VHE gamma-ray emission from Markarian 501**. *The Astrophysical Journal*, **669**:862–883, 2007. [arXiv:astro-ph/0702008].

[75] J. Albert et al. (for the MAGIC Collaboration), John Ellis, D.V. Mavromatos, D. Nanopoulos, A.S. Sakharov, and E.K.G. Sarkisyan. Probing Quantum Gravity using Photons from a Mkn 501 Flare Observed by MAGIC. *Physical Review Letters*, submitted, 2007. [arXiv:0708.2889].

[76] D. Allard et al. Extragalactic cosmic-ray source composition and interpretation of the ankle. *Proceedings of the 29th ICRC (Pune)*, August 2005. [arXiv:astro-ph/0508465].

[77] O.C. Allkofer. *Introduction to Cosmic Radiation*. Verlag Karl Thiemig, 1975.

[78] M. Amenomori et al. A Northen Sky Survey for Steady TeV Gamma-Ray Point Sources Using the Tibet Air Shower Array. *ArXiv:astro-ph/0502039*, February 2005.

[79] F.C. Andres, F. Arqueros, D.M. Borque, and C.E. Portocarrero. Atmospheric effect on Cherenkov light from extensive air showers. *Proceedings of the 16th European Cosmic Ray Symposium (Alcalá de Henares)*, 1998.

[80] D.G. Andrews. *An Introduction to Atmospheric Physics*. Cambridge University Press, 2000.

[81] D. Ardouin et al. Radiodetection of Cosmic Ray Extensive Air Showers: Present Status of the CODALEMA Experiment. *ArXiv:astro-ph/0412211*, December 2004.

[82] F. Arqueros et al. A technique for the optical characterization of imaging air-Cherenkov telescopes. *Astroparticle Physics*, **24**:137–145, 2005.

[83] S. Asano and M. Sato. Light scattering by randomly oriented spheroidal particles. *Applied Optics*, **19**:962–974, 1980.

[84] Astroparticle Physics European Coordination. Astroparticle Physics in Europe: A Roadmap. ApPEC, January 2007. Draft.

[85] R. Atkins. Search for Cygnus Arm Diffuse TeV Gamma Ray Emission with the Whipple 10 m Telescope. *Proceedings of the 29th ICRC (Pune)*, August 2005. [arXiv:astro-ph/0507446].

[86] A. Atoyan, J. Buckley, and H. Krawczynski. A gamma-ray burst remnant in our Galaxy: HESS J1303-631. *arXiv:astro-ph/0509615*, September 2005.

[87] A. Atoyan, J. Patera, V. Sahakian, and A. Akhperjanian. Fourier Transform method for imaging atmospheric Cherenkov Telescopes. *Astroparticle Physics*, **23**:79–95, 2005. [arXiv:astro-ph/0409388].

[88] V. Aynutdinov et al. Baikal neutrino telescope NT200+: Upgrade of data acquisition and time calibration systems. *Proceedings of the 29th ICRC (Pune)*, August 2005. [arXiv:astro-ph/0507715].

[89] V. Aynutdinov et al. The Baikal neutrino experiment: from NT200 to NT200+. *Proceedings of the 29th ICRC (Pune)*, August 2005. [arXiv:astro-ph/0507709].

[90] H.M. Badran. Atmospheric effect on Cherenkov light generated by air showers. *Proceedings of the 25th ICRC (Durban)*, 1997.

[91] C. Baixeras et al. Commissioning and first tests of the MAGIC telescope. *Nuclear Instruments and Methods in Physics Research A*, **518**:188–192, 2004.

[92] C. Baixeras et al. Design studies for a European Gamma-ray Observatory. *arXiv:astro-ph/0403180*, March 2004.

[93] C. Baixeras et al. MAGIC Phase II. *Proceedings of the 29th ICRC (Pune)*, August 2005. [arXiv:astro-ph/0508273].

[94] M.B. Baker. Cloud Microphysics and Climate. *Science*, **276**:1072–1078, 1997.

[95] P. Barber and C. Yeh. Scattering of electromagnetic waves by arbitrarily shaped dielectric bodies. *Applied Optics*, **14**:2864–2872, 1975.

[96] H.M.J. Barbosa et al. Determination of the calorimetric energy in extensive air showers. *Astroparticle Physics*, **22**:159–166, 2004. [arXiv:astro-ph/0310234].

[97] R. Barlow. *STATISTICS A Guide to the Use of Statistical Methods in the Physical Sciences*. John Wiley & Sons, 1989.

[98] J.A. Barrio et al. The MAGIC Telescope Design Study for the construction of a 17 Cherenkov telescope for Gamma-Astronomy above 10 GeV. Technical Report MPI-PhE/98-5. Max-Planck-Institut für Physik (Werner-Heisenberg-Institut), Munich, March 1998.

[99] S.D. Barthelmy et al. An origin for short γ-ray bursts unassociated with current star formation. *Nature*, **438**:994–996, 2005. [arXiv:astro-ph/0511579].

[100] H. Bartko et al. Observation of VHE Gamma Radiation from HESS J 1813-178 with the MAGIC Telescope. *Proceedings of the 29th ICRC (Pune)*, August 2005. [arXiv:astro-ph/0508244].

[101] H. Bartko et al. Search for Gamma Rays from the Galactic Center with the MAGIC Telescope. *Proceedings of the 29th ICRC (Pune)*, August 2005. [arXiv:astro-ph/0508244].

[102] H. Bartko et al. Test of a Prototype Multiplexed Fiber-Optic Ultra-fast FADC Data Acquisition System for the MAGIC Telescope. *Proceedings of the 29th ICRC (Pune)*, August 2005. [arXiv:astro-ph/0508273].

[103] H. Bartko et al. Toward Dark Matter Searches with the MAGIC Telescope. *Proceedings of the 29th ICRC (Pune)*, August 2005. [arXiv:astro-ph/0508273].

[104] S. W. Barwick et al. Constraints on Cosmic Neutrino Fluxes from the ANITA Experiment. *arXiv:astro-ph/0512265*, December 2005.

[105] D. Bastieri. The MAGIC Telescope. *Proceedings of the Science with the New Generation of High Energy Gamma-ray Experiments (Cividale del Friuli)*, June 2005.

[106] D. Bastieri et al. The MAGIC experiment and its first results. *Proceedings of the 6th International Symposium Frontiers of Fundamental and Computational Physics (Udine)*, 2004. [arXiv:astro-ph/0503534].

[107] D. Bastieri et al. The MAGIC Telescope and the Observation of Gamma Ray Bursts. *Proceedings of the 4th Workshop Gamma-Ray Bursts in the Afterglow Era (Rome)*, October 2004. [arXiv:astro-ph/0504310].

[108] D. Bastieri et al. The Mirrors for the MAGIC Telescope. *Proceedings of the 29th ICRC (Pune)*, August 2005. [arXiv:astro-ph/0508274].

[109] D. Bastieri et al. Using the photons from the Crab nebula seen by GLAST to calibrate MAGIC and the imaging air Cherenkov telescopes. *Astroparticle Physics*, **23**:572–576, 2005.

[110] L.J. Battan. *Cloud physics and cloud seeding.* Anchor Books, 1962.

[111] G. Baym and F.K. Lamb. Neutron Stars. *arXiv:physics/0503245*, April 2005.

[112] D. Beasley, S. Roy, and M. Watzke. Cosmic X-rays Reveal Evidence for New Form of Matter. *Chandra Press Release: 02-65*, April 2002.

[113] W. Bednarek and R.J. Protheroe. Modulation of AGN gamma-rays by interaction with X-rays from an accretion disc hotspot. *Monthly Notices of the Royal Astronomical Society*, **290**:139–144, 1997. [arXiv:astro-ph/9612211].

[114] M. Begelman and M. Ress. *Gravity's Fatal Attraction: Black Holes in the Universe.* Scientific American Library, 1998.

[115] L. Bergstrom et al. Gamma Rays from Kaluza-Klein Dark Matter. *arXiv:astro-ph/0410359*, October 2004.

[116] K. Bernlöhr. Impact of atmospheric parameters on the atmospheric Cerenkov technique. *Astroparticle Physics*, **12**:255–268, 2000.

[117] K. Bernlöhr. Cherenkov Light in CORSIKA. *VIHKOS CORSIKA School, Lauterbad, Germany*, June 2005.

[118] K. Bernlöhr. Simulation for H.E.S.S. *VIHKOS CORSIKA School, Lauterbad, Germany*, June 2005.

[119] D. Bertone, G. Hooper and J. Silk. Particle dark matter: evidence, candidates and constrains. *Physics Reports*, **405**:279–390, 2005. [arXiv:hep-ph/0404175].

[120] G. Bertone, A.R. Zentner, and J. Silk. Gamma-Rays from Intermadiate-Mass Black Holes. *arXiv:astro-ph/0509565*, September 2005.

[121] H.A. Bethe, G.E. Brown, and C.-H. Lee. And Don't Forget the Black Holes. *arXiv:astro-ph/0510103*, October 2005.

[122] S. Bhattacharyya, S. Sahayanathan, and N. Bhatt. Particle acceleration procces and temporal behaviour of non-thermal emission from blazar. *New Astronomy*, **11**:17–26, 2005.

[123] P.L. Biermann. Dark energy-dark matter-and black holes: The music of the universe. *arXiv:astro-ph/0510024*, October 2005.

[124] C. Bigongiari. The MAGIC Telescope. *arXiv:astro-ph/0512184*, December 2005.

[125] D. Bigongiari et al. The MAGIC telescope reflecting surface. *Nuclear Instruments and Methods in Physics Research A*, **518**:193–194, 2004.

[126] N. Bilić. Black-Hole Phenomenology. *School on Particle Physics, Gravity and Cosmology (Dubrovnik)*, 2006. [arXiv:astro-ph/0610657].

[127] S.D. Biller et al. Calibration Techniques for Air-Cherenkov Telescopes. *Proceedings of the 24th ICRC (Rome)*, pages 412–415, 1995.

[128] O. Blanch and M. Martinez. Exploring the gamma ray horizon with the next generation of gamma ray telescopes. Part 1: Theoretical prediction. *Astroparticle Physics*, **23**:588–597, 2005. [arXiv:astro-ph/0107582].

[129] O. Blanch and M. Martinez. Exploring the gamma-ray horizon with the next generation of gamma ray telescopes. Part 2: Extracting cosmological parameters from the observation of gamma-ray sources. *Astroparticle Physics*, **23**:598–607, 2005. [arXiv:astro-ph/0406061].

[130] O. Blanch and M. Martinez. Exploring the gamma-ray horizon with the next generation of gamma ray telescopes. Part 3: Opimizing the observation schedule of gamma-ray sources for the extraction of cosmological parameters. *Astroparticle Physics*, **23**:608–615, 2005. [arXiv:astro-ph/0409591].

[131] O. Blanch and A. Moralejo. How to use the Camera Simulation Program 0.7. MAGIC-TDAS 04-07 040906/OBlanch, 2004.

[132] M. Błażejowski et al. A Multi-wavelength View of the TeV Blazar Markarian 421: Correlated Variability, Flaring, and Spectral Evolution. *The Astrophysical Journal*, **630**:130–141, 2005. [arXiv:astro-ph/0505325].

[133] J. Blumberg, S. Roy, and M. Watzke. Tycho's Remnant Provides Shocking Evidence for Cosmic Rays. *Chandra Press Release: CXC 05-07*, September 2005.

[134] P. Boinne et al. Neural networks for gamma-hadron separation in MAGIC. *Proceedings of the 6th International Symposium Frontiers of Fundamental and Computational Physics (Udine)*, March 2005. [arXiv:astro-ph/0503539].

[135] D. Bose. Observation of AGNs with PACT. *Proceedings of the 29th ICRC (Pune)*, 2005.

[136] M. Böttcher. Modeling the Emission Processes in Blazars. *Astrophysics and Space Science*, submitted, 2006. [arXiv:astro-ph/0608713].

[137] M. Bradac et al. Strong and Weak Lensing United III: Measuring the Mass Distribution of the Merging Galaxy Cluster 1E0657-56. *The Astrophysical Journal*, **652**:937–947, 2006. [arXiv:astro-ph/0608408].

[138] F.-M. Bréon, D. Tanré, and S. Generoso. Aerosol Effect on Cloud Droplet Size Monitored from Satellite. *Science*, **295**:834–838, 2002.

[139] T. Bretz et al. Comparison of On-Off and Wobble mode observations for MAGIC. *Proceedings of the 29th ICRC (Pune)*, August 2005. [arXiv:astro-ph/0508274].

[140] E. Brion. Mrk 421 and 501 above 60 GeV: the influence of CELESTE's energy scale on the study of flares and spectra. *arXiv:astro-ph/0410205*, October 2004.

[141] E. Brion. Study of Mrk 501 above 60 GeV with CELESTE. *arXiv:astro-ph/0509498*, September 2005.

[142] A.M. Brown. Active Atmospheric Calibration for H.E.S.S. Applied to PKS 2155-304. *Proceedings of the 29th ICRC (Pune)*, 2005.

[143] A.M. Brown. Atmospheric monitoring for the H.E.S.S. Cherenkov telescope array by transmissometer and LIDAR. *Proceedings of the 29th ICRC (Pune)*, 2005.

[144] R. Brun et al. ROOT An Object-Oriented Data Analysis Framework. Users Guide 5.12, July 2006. [ftp://root.cern.ch/root/doc/Users_Guide_5_12.pdf].

[145] E.V. Bugaev and P.A. Klimai. Neutrino from extragalactic cosmic ray interactions in far infrared background. *Proceedings of the 29th ICRC (Pune)*, August 2005. [arXiv:astro-ph/0507366].

[146] N. Bulian et al. Characteristics of the multi-telescope coincidence trigger of the HEGRA IACT system. *Astroparticle Physics*, **8**:223–233, 1998. [arXiv:astro-ph/9712063].

[147] R.D. Cadle. *Particles in the atmosphere and space.* Reinhold Publishing Corporation, 1966.

[148] A. Cafarella, C. Coriano, and T.N. Tomaras. Searching for extra dimensions in High Energy Cosmic Rays. *arXiv:astro-ph/0410190*, October 2004.

[149] I. de la Calle Peréz. A study of the polarization of Cherenkov Radiation in Extensive Air Showers of Energy around 1 TeV. Diploma thesis. Facultad de Ciencias Físicas, Univesidad Complutense, Madrid, 1999.

[150] I. de la Calle Peréz and S.D. Biller. Extending the sensitivity of air Čerenkov telescopes. *Astroparticle Physics*, **26**:69–90, 2006. [arXiv:astro-ph/0602284].

[151] A. Cappa. Cherenkov Light Measurements for the EUSO Experiment. *Proceedings of the Very High Energy Phenomena in the Universe (La Thuile)*, March 2005.

[152] V. Cardoso et al. Microscopic black hole detection in UHECR: the double bang signature. *Astroparticle Physics*, **22**:399–407, 2005.

[153] B. Carr. Primordial Black Holes: Do They Exist and Are They Useful? *arXiv:astro-ph/0511743*, November 2005.

[154] B.J. Carr. Primordial Black Holes-Recent Developments. *Proceedings of the 22th Texas Symposium (Stanford)*, 2004. [arXiv:astro-ph/0504034].

[155] B.W. Carroll and D.A. Ostlie. *An Introduction to Modern Astrophysics*. Addison-Wesley, 2006.

[156] K.S. Carslaw, R.G. Harrison, and J. Kirkby. Cosmic Rays, Clouds, and climate. *Science*, **298**:1732–1737, 2002.

[157] J. Carson. The Spectrum of Markarian 421 above 100 GeV with STACEE. *Proceedings of the 29th ICRC (Pune)*, 2005.

[158] M. Catanese and T. Weekes. Very High Energy Gamma-Ray Astronomy. *Publication of the Astronomical Society of the Pacific*, **111**:1193–1222, 1999. [arXiv:astro-ph/9906501].

[159] M. Chantell et al. Gamma-ray Observations in Moonlight with the Whipple Atmospheric Cherenkov Hybrid Camera. *Proceedings of the 24th ICRC (Rome)*, pages 544–547, 1995.

[160] P. Charlot, D.C. Gabuzda, H. Sol, B. Degrange, and F. Piron. Simultaneous radio-interferometric and high-energy TeV observations of the gamma-ray blazar Mkn 421. *Astronomy and Astrophysics*, **457**:455–465, 2006. [arXiv:astro-ph/0607258].

[161] S. Chaty. The role of microquasars in astroparticle physics. *Proceedings of the Frontier Objects in Astrophysics and Particle Physics (Vulcano)*, 2006. [arXiv:astro-ph/0607668].

[162] A. Cho. Long-Awaited Data Sharpen Picture of Universe's Birth. *Science*, **311**:1689, 2006.

[163] S. Ciprini et al. Optical Monitoring of PKS 2155-304 during August-September 2004 with the KVA telescope. *arXiv:astro-ph/0509023*, September 2005.

[164] D.H. Clark. *The quest for SS433*. Adam Hilger, 1986.

[165] D. Clery. Telescopes Break New Ground in Quest for Cosmic Rays. *Science*, **305**:1393–1395, 2004.

[166] D. Clery. Dwarf Galaxies May Help Define Dark Matter. *Science*, **311**:758–759, 2006.

[167] D. Clowe et al. A direct empirical proof of the existence of dark matter. *The Astrophysical Journal Letters*, **648**:L109–L113, 2006. [arXiv:astro-ph/0608407].

[168] J.A. Coarasa et al. The Data Acquisition of the MAGIC II Telescope. *Proceedings of the 29th ICRC (Pune)*, August 2005. [arXiv:astro-ph/0508274].

[169] P. Cogan. Observation of AGN with the First VERITAS Telescope. *Proceedings of the 29th ICRC (Pune)*, August 2005. [arXiv:astro-ph/0507441].

[170] M. Coleman Miller. Constraints on Alternatives to Supermassive Black Holes. *Monthly Notices of the Royal Astronomical Society*, **367**:L32–L36, 2006. [arXiv:astro-ph/0512194].

[171] P. Coppi. AGN, Blazars and microquasars. *Proceedings of the Towards a Network of Atmospheric Cherenkov Detectors VII (Palaiseau)*, April 2005.

[172] J. Cortina, F. Arqueros, and E. Lorenz. Methods for determining the primary energy of cosmic-ray showers. *Journal of Physics G: Nuclear and Particle Physics*, **23**:1733–1749, 1997.

[173] J. Cortina and J.C. González. The cosmic electron background in low energy imaging atmospheric Cherenkov telescopes: effect of geomagnetic field. *Astroparticle Physics*, **15**:203–210, 2001. [arXiv:astro-ph/0010329].

[174] J. Cortina et al. Technical Performance of the MAGIC Telescope. *Proceedings of the 29th ICRC (Pune)*, August 2005. [arXiv:astro-ph/0508274].

[175] G. Cowan. *Statistical Data Analysis*. Clarendon Press, 1998.

[176] R. Cowsik et al. A Possible High Altitude High Energy Gamma Ray Observatory in India. *arXiv:astro-ph/0108392*, August 2001.

[177] J.W. Cronin, K.G. Gibbs, and T.C. Weekes. The search for discrete astrophysical sources of energetic gamma radiation. *Annual Review of Nuclear and Particle Science*, **43**:883–925, 1993.

[178] W. Cui. TeV Astrophysics, A Review. *Proceedings of the Frontier Objects in Astrophysics and Particle Physics (Vulcano)*, 2006. [arXiv:astro-ph/0608042].

[179] W. Cui et al. News from a Multi-Wavelength Monitoring Campaign on Mrk 421. *arXiv:astro-ph/0410160*, October 2004.

[180] G. Cusumano et al. Detection of a huge explosion in the early Universe. *arXiv:astro-ph/0509737*, September 2005.

[181] M. Daniel. Status of VERITAS. *Proceedings of the Science with the New Generation of High Energy Gamma-ray Experiments (Cividale del Friuli)*, June 2005.

[182] M. Daniel et al. Spectrum of Very High Energy Gamma-Rays from the blazar 1ES 1959+650 during flaring activity in 2002. *ArXiv:astro-ph/0503085*, March 2005.

[183] A. Daum et al. First results on the performance of the HEGRA IACT array. *Astroparticle Physics*, **8**:1–11, 1997. [arXiv:astro-ph/9704098].

[184] A. Dekel et al. Lost and found dark matter in elliptical galaxies. *Nature*, **437**:707–710, September 2005. [arXiv:astro-ph/0501622].

[185] C.D. Dermer and A. Atoyan. Collapse of Neutron Stars to Black Holes in Binary Systems: A Model for Short Gamma Ray Bursts. *arXiv:astro-ph/0601142*, January 2006.

[186] C.D. Dermer and R. Schlickeiser. Model for the High-energy Emission from Blazars. *The Astrophysical Journal*, **416**:458–484, 1993.

[187] G. Deutsch, E. Hupp, S. Hendrix, and M. Watzke. In a Flash, NASA Helps Solve 35-Year-Old Cosmic Mystery. *Chandra Press Release: 05-334*, October 2005.

[188] T. Di Matteo, V. Springel, and L. Hernquist. Energy input from quasars regulates the growth and activity of black holes and their host galaxies. *Nature*, **433**:604–607, February 2005. [arXiv:astro-ph/0502199].

[189] E. Domingo-Santamara et al. The DISP analysis method for point-like or extended γ source searches/studies with the MAGIC Telescope. *Proceedings of the 29th ICRC (Pune)*, August 2005. [arXiv:astro-ph/0508274].

[190] D. Dorner et al. Data Management and Processing for the MAGIC Telescope. *Proceedings of the 29th ICRC (Pune)*, August 2005. [arXiv:astro-ph/0508274].

[191] A. Drago, A. Lavagno, and G. Pagliara. Gamma Ray Bursts and the transition to Quark Matter in Compact Stars. *arXiv:astro-ph/0510018*, October 2005.

[192] M. Drees and G. Gerbier. DARK MATTER (Review of Particle Physics). *Journal of Physics G: Nuclear and Particle Physics*, **33**:233–237, 2006.

[193] I. Dutan. Jets driven by accretion onto rotating black holes. *Proceedings of the Very High Energy Phenomena in the Universe (La Thuile)*, March 2005.

[194] H.F. Ebel, C. Bliefert, and W.E. Russey. *The Art of Scientific Writing: From Student Reports to Professional Publications in Chemistry and Related Fields*. Wiley-VCH, 2$^{\text{th}}$ edition, 2004.

[195] R.A. Edelson and J.H. Krolik. The discrete correlation function - A new method for analyzing unevenly sampled variability data. *The Astrophysical Journal*, **333**:646–659, 1988.

[196] D. Eichler and G. Beskin. Optical SETI with Air Cherenkov Telescopes. *arXiv:astro-ph/0111081*, November 2001.

[197] D. Elsässer and K. Mannheim. MAGIC and the search for signatures of supersymmetric dark matter. *New Astronomy Reviews*, **49**:297–301, 2005. [arXiv:astro-ph/0409563].

[198] L. Elterman. Parameters for Attenuation in the Atmospheric Windows for Fifteen Wavelengths. *Applied Optics*, **3**:745–749, 1964.

[199] R. Engel. Very High Energy Cosmic Rays and Their Interactions. *arXiv:astro-ph/0504358*, April 2005.

[200] R. Enomoto et al. A Search for sub-TeV Gamma-rays from the Vela Pulsar Region with CANGAROO-III. *arXiv:astro-ph/0510300*, October 2005.

[201] H. Falcke et al. Detection and imaging of atmospheric radio flashes from cosmic ray air showers. *Nature*, **435**:313–316, 2005. [arXiv:astro-ph/0505383].

[202] D. Fargion. Blazing Cherenkov Flashes at the Horizons by Cosmic Rays and neutrino induced air-showers. *ArXiv:astro-ph/0412582*, December 2004.

[203] D. Fargion. Cosmic Rays Astrophysics and Neurtrino Astronomy beyond and beneath the Horizons. *ArXiv:astro-ph/0502017*, February 2005.

[204] D.J. Fegan. The art and power of Cherenkov imaging. *Space Science Reviews*, **75**:137–151, 1996.

[205] D.J. Fegan. γ/hadron separation at TeV energies. *Journal of Physics G: Nuclear and Particle Physics*, **23**:1013–1060, 1997.

[206] D. Ferenc. The MAGIC gamma-ray observatory. *Nuclear Instruments and Methods in Physics Research A*, **553**:274–281, 2005.

[207] D. Ferenc and D. Hrupec. In preparation. 2007.

[208] F. Ferrer. TeV Dark Matter Detection by Atmospheric Čerenkov Telescopes. *ArXiv:astro-ph/0505414*, May 2005.

[209] R. Firpo. *Study of MAGIC Telescope sensitivity for Large Zenith Angle observations*. PhD thesis, Institut de Física d'Altes Energies (Universitat Autònoma de Barcelona), 2006.

[210] M.C. Forbes, R.J. Dodd, and D.J. Sullivan. A Detailed Investigation of Atmospheric Extinction via Vilnius Photometry. *Baltic Astronomy*, **5**:281–295, 1996.

[211] A. Forti et al. Grid services for the MAGIC experiment. *Proceedings of the 6^{th} International Symposium Frontiers of Fundamental and Computational Physics (Udine)*, March 2005. [arXiv:astro-ph/0503541].

[212] D.B. Fox et al. The afterglow of GRB 050709 and the nature of the short-hard gamma-ray bursts. *Nature*, **437**:845–850, 2005.

[213] L. Fuhrmann et al. A rapid and dramatic outburst in Blazar 3C 454.3 during May 2005. *arXiv:astro-ph/0511829*, November 2005.

[214] Y. Fukuda et al. Evidence for Oscillation of Atmospheric Neutrinos. *Physical Review Letters*, **81**:1562–1567, 1998.

[215] S. Funk et al. The trigger system of the HESS telescope array. *Astroparticle Physics*, **22**:285–296, 2004. [arXiv:astro-ph/0408375].

[216] J.A. Gaidos et al. Extremely radid bursts of TeV photons from the active galaxy Markarian 421. *Nature*, **383**:319–320, 1996.

[217] T.K. Gaisser. Cosmic-ray cascades in the atmosphere. *VIHKOS CORSIKA School, Lauterbad, Germany*, June 2005.

[218] T.K. Gaisser and T. Stanev. High-energy Cosmic Rays. *arXiv:astro-ph/0510321*, October 2005.

[219] T.K. Gaisser, T. Stanev, P.V. Sokolsky, and R.E. Streitmatter. COSMIC RAYS (Review of Particle Physics). *Journal of Physics G: Nuclear and Particle Physics*, **33**:245–251, 2006.

[220] E. Gallo and R.P. Fender. Accretion modes and jet production in black hole X-ray binaries. *arXiv:astro-ph/0509172*, September 2005.

[221] E. Gallo et al. A dark jet dominates the power output of the stellar black hole Cygnus X-1. *Nature*, **436**:819–821, August 2005. [arXiv:astro-ph/0508228].

[222] H. Gaug et al. Calibration of the MAGIC Telescope. *Proceedings of the 29th ICRC (Pune)*, August 2005. [arXiv:astro-ph/0508274].

[223] N. Gehrels et al. Swift detects a remarkable gamma-ray burst, GRB 060614, that introduces a new classification scheme. *Nature*, **444**:1044–1046, 2006. [arXiv:astro-ph/0610635].

[224] M. Georganopoulos, E.S. Perlman, D. Kazanas, and B. Wingert. How is the blazar GeV emission really produced? *arXiv:astro-ph/0506567*, June 2005.

[225] S. Gibilisco. *Astronomy Demystified: A self-teaching guide*. McGraw-Hill, 2003.

[226] B. Giebels, G. Dubus, and B. Khelifi. Unveiling the X-ray/TeV engine in Mkn 421. *Astronomy and Astrophysics*, **462**:29–41, 2007. [arXiv:astro-ph/0610270].

[227] S. Gillessen and H.L. Harney. Significance in gamma-ray astronomy - the Li & Ma problem in Bayesian statistics. *Astronomy and Astrophysics*, **430**:355–362, 2005. [ArXiv:astro-ph/0411660].

[228] T. Gneiting and A.E. Raftery. ATMOSPHERIC SCIENCE: Weather Forecasting with Ensemble Methods. *Science*, **310**:248–249, October 2005.

[229] F. Goebel et al. Absolute energy scale calibration of the MAGIC telescope using muon images. *Proceedings of the 29th ICRC (Pune)*, August 2005. [arXiv:astro-ph/0508274].

[230] J. Goodman. Neutrino Astronomy. *Proceedings of the Very High Energy Phenomena in the Universe (La Thuile)*, March 2005.

[231] P.W. Gorham. Planet-sized Detectors for Ultra-high Energy Neutrinos and Cosmic Rays. *ArXiv:astro-ph/0411510*, November 2004.

[232] A.M. Green. WIMP direct detection: astrophysical input. *New Astronomy Reviews*, **49**:181–184, 2005.

[233] B. Greene. *The Elegant Universe: Superstrings, Hidden Dimensions, and the Quest for the Ultimate Theory*. Vintage, 2000.

[234] J. Gribbin. *Companion to the Cosmos*. Phoenix Giant, 1997.

[235] D.E. Groom, F. James, R. Cousins, and G. Cowan. PROBABILITY (Review of Particle Physics). *Journal of Physics G: Nuclear and Particle Physics*, **33**:297–300, 2006.

[236] A. Groß. Recent Results from the AMANDA-II neutrino telescope. *arXiv:astro-ph/0505278*, May 2005.

[237] J. Grube. Spectral Monitoring of Mrk 421 during 2004. *Proceedings of the 29th ICRC (Pune)*, August 2005. [arXiv:astro-ph/0507447].

[238] M.A. Guerrero et al. Extinction over the Canarian Observatories: the limited influence of Saharan dust. *New Astronomy Reviews*, **42**:529–532, 1998.

[239] A.C. Gupta. Simultaneous Multi-wavelength Variability of the TeV Blazar Mrk 421. *Proceedings of the 29th ICRC (Pune)*, 2005.

[240] K. Gutierrez et al. Multiwavelength Observations of 1ES 1959+650, One Year After the Strong Outburst of 2002. *The Astrophysical Journal*, **644**:742–747, 2006. [arXiv:astro-ph/0603013].

[241] A. Habig. High-Energy Neutrino Astronomy with the Super-Kamiokande Detector. *Proceedings of the 29th ICRC (Pune)*, July 2005. [arXiv:astro-ph/0506758].

[242] J.B. Haislip et al. A photometric redshift of $z = 6.39 \pm 0.12$ for GRB 050904. *Nature*, **440**:181–183, 2006.

[243] J. Hall. Search for TeV Radiation from Selected Local Group Galaxies. *Proceedings of the 29th ICRC (Pune)*, August 2005. [arXiv:astro-ph/0507448].

[244] F. Halzen. Lectures on High-Energy Neutrino Astronomy. *arXiv:astro-ph/0506248*, June 2005.

[245] F. Halzen and D. Hooper. High Energy Neutrinos from the TeV Blazar 1ES 1959+650. *Astroparticle Physics*, **23**:537–542, 2005. [arXiv:astro-ph/0502449].

[246] F. Halzen, E. Zas, J.H. MacGibbon, and T.C. Weekes. Gamma rays and energetic particles from primordial black holes. *Nature*, **353**:807–815, 1991.

[247] A. Haungs et al. KASKADE: Astrophysical results and tests of hadronic interaction models. *ArXiv:astro-ph/0412610*, December 2004.

[248] M. Hayashida et al. Development of HPDs with an 18-mm-diameter GaAsP photo cathode for the MAGIC-II project. *Proceedings of the 29th ICRC (Pune)*, August 2005. [arXiv:astro-ph/0508273].

[249] N. Hayashida et al. Observations of TeV gamma-ray flares from Markarian 501 with the telescope array prototype. *The Astrophysical Journal*, **504**:L71–L74, 1998.

[250] D.S. Hayes and D.W. Latham. A Rediscussion of the atmospheric extinction and the absolute spectral-energy distribution of Vega. *The Astrophysical Journal*, **197**:593–601, 1975.

[251] D. Heck. Introduction to CORSIKA and Historical Review. *VIHKOS CORSIKA School, Lauterbad, Germany*, June 2005.

[252] D. Heck, J. Knapp, and M. Risse. The automated Air Shower Generation with CORSIKA at the Computing Center of IN2P3 (Lyon). Auger Technical Note GAP-2001-059, 2001.

[253] D. Heck and T. Pierog. Extensive Air Showers Simulations with CORSIKA: A User's Guide Version 6.6. Forschungszentrum Karlsruhe, April 2007.

[254] D. Heck et al. CORSIKA: A Monte Carlo Code to Simulate Extensive Air Showers. Technical Report FZKA 6019. Forschungszentrum Karlsruhe, 1998.

[255] G. Hermann et al. A Smart Pixel Camera for future Cherenkov Telescopes. *arXiv:astro-ph/0511519*, November 2005.

[256] A.M. Hillas. The origin of ultra-high-energy cosmic rays. *Annual Review of Astronomy and Astrophysics*, **22**:425–444, 1984.

[257] A.M. Hillas. Differences between gamma-ray and hadronic showers. *Space Science Reviews*, **75**:17–30, 1996.

[258] A.M. Hillas and J.R. Patterson. Characteristics and brightness of Cherenkov shower images for gamma ray astronomy near 1 TeV. *Journal of Physics G: Nuclear and Particle Physics*, **16**:1271–1281, 1990.

[259] H.L. Hirsch. *Essential Communication Strategies for Scientists, Engineers, and Technology Professionals*. John Wiley & Sons, 2$^{\text{th}}$ edition, 2003.

[260] C.M. Hoffman, C. Sinnis, P. Fleury, and M. Punch. Gamma-ray Astronomy at high energies. *Review of Modern Physics*, **71**:897–936, 1999.

[261] W. Hofmann. HESS I: Status report. *Proceedings of the Towards a Network of Atmospheric Cherenkov Detectors VII (Palaiseau)*, April 2005.

[262] W. Hofmann et al. On the optimum spacing of stereoscopic imaging atmospheric Cherenkov telescopes. *Astroparticle Physics*, **13**:253–258, 2000. [arXiv:astro-ph/9910443].

[263] J. Holder. Exploiting VERITAS Timing Information. *Proceedings of the 29th ICRC (Pune)*, August 2005. [arXiv:astro-ph/0507450].

[264] J. Holder, P. Ashworth, S. LeBohec, H.J. Rose, and T.C. Weekes. Optical SETI with Imaging Cherenkov Telescope. *Proceedings of the 29th ICRC (Pune)*, July 2005. [arXiv:astro-ph/0506758].

[265] J. Holder et al. Status and Performance of the First VERITAS telescope. *Proceedings of the 29th ICRC (Pune)*, August 2005. [arXiv:astro-ph/0507451].

[266] J. Holder et al. The First VERITAS Telescope. *Astroparticle Physics*, **25**:391–401, 2006. [arXiv:astro-ph/0604119].

[267] D. Horan and T. Weekes. Extragalactic sources of TeV gamma rays: a summary. *New Astronomy Reviews*, **48**:527–535, 2004.

[268] D. Horan and T.C. Weekes. Extragalactic Sources of TeV Gamma Rays: A Summary. *New Astronomy Reviews*, **48**:527–535, 2004. [arXiv:astro-ph/0310391].

[269] D. Horns. Performance of a prototype system of Cherenkov telescopes at high altitude. *Proceedings of the 29th ICRC (Pune)*, 2005.

[270] D. Horns et al. Nucleonic gamma-ray production in Vela X. *Astronomy and Astrophysics*, **451**:L51–L54, 2006.

[271] D. Hrupec. Doprinos razvoju teleskopa MAGIC za detekciju gama zračenja iz kompaktnih kozmičkih objekata. Diploma thesis. Faculty of Science, University of Zagreb, 1997.

[272] S. Hsu and A. Zee. Message in the Sky. *arXiv:physics/0510102*, October 2005.

[273] T. Huege and H. Falcke. Simulation and parameterization of radio emission from cosmic ray air shower. *Proceedings of the 29th ICRC (Pune)*, July 2005. [arXiv:astro-ph/0507051].

[274] T.B. Humensky. Calibration of VERITAS Telescope 1 via Muons. *Proceedings of the 29th ICRC (Pune)*, August 2005. [arXiv:astro-ph/0507449].

[275] S. Hundertmark. Results from the AMANDA Neutrino telescope and Status of the IceCube Neutrino Observatory. *Proceedings of the Very High Energy Phenomena in the Universe (La Thuile)*, March 2005.

[276] K. Hurley. Cosmic Gamma-Ray Bursts: The Current Status. *Proceedings of the Very High Energy Phenomena in the Universe (La Thuile)*, 2005.

[277] A. Ibarra Ibaibarriaga. Study of the Gamma ray induced showers at High Zenith Angles. Diploma thesis. Facultad de Ciencias Físicas, Univesidad Complutense, Madrid, 1999.

[278] M. Iye et al. A galaxy at a redshift $z = 6.96$. *Nature*, **443**:186–188, 2006. [arXiv:astro-ph/0609393].

[279] F. James. A review of pseudorandom generators. *Computer Physics Communications*, **60**:329–344, 1990.

[280] F. James, R. Cousins, and G. Cowan. STATISTICS (Review of Particle Physics). *Journal of Physics G: Nuclear and Particle Physics*, **33**:301–310, 2006.

[281] J.V. Jelley. Čerenkov radiation and its applications. *British Journal of Applied Physics*, **6**:227–232, 1955.

[282] J.V. Jelley. *Čerenkov radiation and its application*. Pergamon Press, 1958.

[283] K.-H. Kampert. The Pierre Auger Observatory - Status and Prospects. *ArXiv:astro-ph/0501074*, January 2005.

[284] K. Katarzyński et al. Correlation between the TeV and X-ray emission in high–energy peaked BL Lac objects. *Astronomy and Astrophysics*, **433**:479–496, 2005. [arXiv:astro-ph/0412405].

[285] B. Keilhauer. Impact of varying atmospheric profiles on extensive air shower observation: atmospheric density and primary mass reconstruction. *Astroparticle Physics*, **22**:249–261, 2004. [arXiv:astro-ph/0405048].

[286] B. Keilhauer. Atmospheric Description in CORSIKA. *VIHKOS CORSIKA School, Lauterbad, Germany*, June 2005.

[287] B. Keilhauer. Impact of varying atmospheric profiles on extensive air shower observation: Fluorescence light emission and energy reconstruction. *Astroparticle Physics*, **25**:259–268, 2006. [arXiv:astro-ph/0511153].

[288] M. Kestel. The upgrade of the HEGRA CT1 telescope with new mirrors and new Trigger system. *Proceedings of the 16th European Cosmic Ray Symposium (Alcalá de Henares)*, 1998.

[289] M. Kestel. *TeV γ-Flux and Spectrum of Markarian 421 in 1999/2000 with HEGRA CT1 using refined Analysis Methods*. PhD thesis, Max-Planck-Institut für Physik (Werner-Heisenberg-Institut), Munich, 2001.

[290] D.L. King. Atmospheric Extinction at the Roque de los Muchachos Observatory, La Palma. RGO/La Palma technical note no 31, September 1985.

[291] J. Knapp. Physics Capabilities of CORSIKA. *VIHKOS CORSIKA School, Lauterbad, Germany*, June 2005.

[292] A. Konopelko. Design studies for the future 50 GeV arrays of imaging air Čerenkov telescopes. *Astroparticle Physics*, **11**:263–266, 1999. [arXiv:astro-ph/9901365].

[293] A. Konopelko. Altitude effect in Čerenkov light flashes of low energy gamma-ray-induced atmospheric showers. *Journal of Physics G: Nuclear and Particle Physics*, **30**:1835–1846, 2004. [arXiv:astro-ph/0409514].

[294] A. Konopelko. STEREO ARRAY of 30 m imaging atmospheric Čerenkov telescopes: A next-generation detector for ground-based high energy gamma-ray astronomy. *Astroparticle Physics*, **24**:191–207, 2005. [arXiv:astro-ph/0506465].

[295] A. Konopelko, A. Mastichiadis, and F.W. Stecker. TeV Gamma-Ray Spectra Unfolded for IR Absorption for a Sample of Low and High Red-Shifted AGN. *Proceedings of the 29th ICRC (Pune)*, August 2005. [arXiv:astro-ph/0507479].

[296] A.K. Konopelko and A.V. Plyasheshnikov. ALTAI: computational code for the simulations of TeV air showers as observed with the ground-based imaging atmospheric Cherenkov telescopes. *Nuclear Instruments and Methods in Physics Research A*, **450**:419–429, 2000.

[297] A. Konopelko et al. Performance of the stereoscopic system of the HEGRA imaging air Čerenkov telescopes: Monte Carlo simulations and observations. *Astroparticle Physics*, **10**:275–289, 1999. [arXiv:astro-ph/9901199].

[298] R. Koul. MACE gamma-ray telescope. *Proceedings of the Towards a Network of Atmospheric Cherenkov Detectors VII (Palaiseau)*, April 2005.

[299] C. Kouveliotou, R.C. Duncan, and C. Thompson. Magnetars. *Scientific American*, **288**:24–31, 2003.

[300] D. Kranich. *Temporal and spectral characteristics of the active galactic nucleus Mkn 501 during a phase of high activity in the TeV range*. PhD thesis, Max-Planck-Institut für Physik (Werner-Heisenberg-Institut), Munich, 2001.

[301] D. Kranich et al. Evidence for a QPO structure in the TeV and X-ray light curve during the 1997 high state gamma emission of Mkn 501. *Proceedings of the 26th ICRC (Salt Lake City)*, **3**:358, 1999. [arXiv:astro-ph/9907205].

[302] D. Kranich et al. TeV γ-ray observations of the Crab and Mkn 501 during moonshine and twilight. *Astroparticle Physics*, **12**:65–74, 1999. [arXiv:astro-ph/9901330].

[303] H. Krawczynski. Observations of Active Galactic Nuclei with Ground-Based Cherenkov Telescopes. *arXiv:astro-ph/0508621*, November 2006.

[304] H. Krawczynski et al. Simultaneous X-ray and TeV gamma-ray observation of the TeV blazar Markarian 421 during February and May 2000. *The Astrophysical Journal*, **559**:187–195, 2001. [arXiv:astro-ph/0105331].

[305] H. Krawczynski et al. Gamma-Hadron Separation Methods for the VERITAS Array of Four Imaging Atmospheric Cherenkov Telescopes. *Astroparticle Physics*, **25**:380–390, 2006. [arXiv:astro-ph/0604508].

[306] F. Krennrich, S. Le Bohec, and T.C. Weekes. Detection techniques of microsecond gamma-ray bursts using ground-based telescopes. *The Astrophysical Journal*, **529**:506–512, 2000. [arXiv:astro-ph/9909078].

[307] F. Krennrich et al. Discovery of Spectral Variability of Markarian 421 at TeV Energies. *The Astrophysical Journal*, **575**:L9–L14, 2002. [arXiv:astro-ph/0207184].

[308] H. Langenberg. Inside information. *Nature*, **437**:468–469, September 2005.

[309] S. LeBohec, C. Duke, and P. Jordan. Minimal stereoscopic analysis for imaging atmospheric Cherenkov telescope arrays. *Astroparticle Physics*, **24**:26–31, 2005.

[310] S. LeBohec and J. Holder. The cosmic ray background as a tool for relative calibration of atmospheric Cherenkov telescopes. *Astroparticle Physics*, **19**:221–233, 2003. [arXiv:astro-ph/0208396].

[311] M. Lemoine-Goumard, B. Degrange, and M. Tluczykont. Selection and 3D-Reconstruction of Gamma-Ray-induced Air Showers with a Stereoscopic System of Atmospheric Cherenkov Telescopes. *Astroparticle Physics*, **25**:195–211, 2006. [arXiv:astro-ph/0601373].

[312] T.-P. Li and Y.-Q. Ma. Analysis methods for results in gamma-ray astronomy. *The Astrophysical Journal*, **272**:317–324, 1983.

[313] J. Liberty and D.B. Horvath. *C++ for Linux in 21 Days*. Sams Publishing, 2000.

[314] A.S. Lidvansky. Air Cherenkov Methods in Cosmic Rays: A Review and Some History. *ArXiv:astro-ph/0504269*, April 2005.

[315] C.H. Lineweaver and T.M. Davis. Misconceptions about the big bang. *Scientific American*, pages 36–45, March 2005.

[316] K.N. Liou. *Radiation and Cloud Processes in the Atmosphere: Theory, Observation, and Modeling*. Oxford University Press, 1992.

[317] Z. Liu et al. A cloud-aerosol discrimination algorithm for CALIPSO lidar observations: algorithm test. *Proceedings of 22nd International Laser Radar Conference (Matera)*, pages 987–990, 2004.

[318] G. Lombardi et al. El Roque de Los Muchachos site characteristics, I.Temperature analysis. *The Publications of the Astronomical Society of the Pacific*, **118**:1198–1204, 2006. [arXiv:astro-ph/0606723].

[319] M.S. Longair. *High Energy Astrophysics: Particles, photons and their detection*, volume 1. Cambridge University Press, 1992.

[320] M.S. Longair. *High-Energy Astrophysics: Stars, the Galaxy and the interstellar medium*, volume 2. Cambridge University Press, 1994.

[321] N. López et al. Search for pulsed VHE Gamma ray emission from the Crab Pulsar. *Proceedings of the 29th ICRC (Pune)*, August 2005. [arXiv:astro-ph/0508244].

[322] M. López Moya. Estudio de la Influencia del Campo Geomagnético Terrestre Sobre el Fondo de Electrones Cósmicos. Diploma thesis. Facultad de Ciencias Físicas, Univesidad Complutense, Madrid, 2001.

[323] E. Lorenz. Atmospheric Transmission Measurements for the MAGIC Telescope Operation. MAGIC note 99-3, March 1999.

[324] E. Lorenz. Status of ground-based GeV/TeV gamma-ray astronomy. *Journal of Physics G: Nuclear and Particle Physics*, **27**:1675–1690, 2001.

[325] E. Lorenz. Very High Energy Gamma-Ray Astronomy. *Nuclear Physics B*, **114**:217–232, 2003.

[326] E. Lorenz. Ground-Based Gamma-Ray Astronomy. *Acta Physica Polonica B*, **35**:1991–2006, 2004.

[327] E. Lorenz. Status of the 17 m MAGIC telescope. *New Astronomy Reviews*, **48**:339–344, 2004.

[328] E. Lorenz. Ideas on long-term observations with small Cherenkov telescopes. *Multi-messenger Workshop (DESY Zeuthen)*, 2005. [http://www-zeuthen.desy.de/astro-workshop/].

[329] E. Lorenz. High-energy astroparticle physics. *Nuclear Instruments and Methods in Physics Research A*, **567**:1–11, 2006.

[330] F. Lucarelli et al. Observations of the Crab Nebula with the HEGRA system of IACTs in convergent mode using a topological trigger. *Astroparticle Physics*, **19**:339–350, 2003. [arXiv:astro-ph/0209447].

[331] F. Lucarelli et al. Development and first results of the MAGIC central pixel system for optical observations. *Proceedings of the 29th ICRC (Pune)*, August 2005. [arXiv:astro-ph/0508273].

[332] M.C. Maccarone et al. GAW, Gamma Air Watch - A Large Field of View Imaging Atmospheric Cherenkov. *arXiv:astro-ph/0509706*, September 2005.

[333] P. Madau. Trouble at first light. *Nature*, **440**:1002, 2006. [arXiv:astro-ph/0604448].

[334] P. Magain et al. Discovery of a bright quasar without a massive host galaxy. *Nature*, **437**:381–394, September 2005. [arXiv:astro-ph/0509433].

[335] G. Maier. Monte Carlo Studies of the first VERITAS telescope. *Proceedings of the 29th ICRC (Pune)*, August 2005. [arXiv:astro-ph/0507445].

[336] P. Majumdar et al. Angular Resolution of the Pachmarhi Array of Cerenkov Telescopes. *Astroparticle Physics*, **18**:333–349, 2003. [arXiv:astro-ph/0204112].

[337] P. Majumdar et al. Monte Carlo simulations for the MAGIC telescope. *Proceedings of the 29th ICRC (Pune)*, August 2005. [arXiv:astro-ph/0508274].

[338] R.D.R. Mandal. Strange Pulsar Hypothesis. *arXiv:astro-ph/0511106*, November 2005.

[339] L. Maraschi et al. Correlated variability of Mkn 421 at X-ray and TeV wavelengths on time scales of hours. *Astroparticle Physics*, **11**:189–192, 1999. [arXiv:astro-ph/9902224].

[340] M. Mariotti. MAGIC: Status report. *Proceedings of the Towards a Network of Atmospheric Cherenkov Detectors VII (Palaiseau)*, April 2005.

[341] M. Marklund, G. Brodin, L. Stenflo, and P.K. Shukla. Cherenkov radiation in a photon gas. *ArXiv:astro-ph/0502092*, February 2005.

[342] N.D. Marsh and H. Svensmark. Low cloud properties influenced by cosmic rays. *arXiv:physics/0005072*, November 2000.

[343] M. Martinez. VHE gamma-ray astronomy: observations. *Proceedings of the Topics in Astroparticle and Underground Physics (Barcelona)*, 2005.

[344] S. Martinez et al. Monte Carlo simulations of the HEGRA cosmic ray detector performance. *Nuclear Instruments and Methods in Physics Research A*, **357**:567–579, 1995.

[345] D. Mazin. Observation of the AGN Markarian 421 with the MAGIC telescope. *Proceedings of the Very High Energy Phenomena in the Universe (La Thuile)*, March 2005.

[346] D. Mazin. Observations of Extragalactic Sources with the MAGIC Telescope. *Proceedings of the Multi-messenger approach to high-energy gamma-ray sources (Barcelona)*, 2006. [arXiv:astro-ph/0609152].

[347] D. Mazin et al. Concept of a Global Network of Cherenkov Telescopes and first joint observations with H.E.S.S. and MAGIC. *Proceedings of the 29th ICRC (Pune)*, August 2005. [arXiv:astro-ph/0508273].

[348] D. Mazin et al. Observation of Mkn 421 with the MAGIC Telescope. *Proceedings of the 29th ICRC (Pune)*, August 2005. [arXiv:astro-ph/0508244].

[349] B. McBreen et al. Gamma-ray bursts and other sources of giant lighting discharges in protoplanetary systems. *Astronomy and Astrophysics*, **429**:L41–L45, 2005.

[350] J. McEnery. GLAST Mission Overview. *Proceedings of the 29th ICRC (Pune)*, 2005.

[351] B. McKernan, M.J. Carson, T. Yaqoob, and D.J. Fegan. Short timescale variability in the broadband emission of the blazars Mkn 421 and Mkn 501. *Astroparticle Physics*, **14**:131–140, 2000. [arXiv:astro-ph/9906200].

[352] M. Meyer et al. MAGIC observations of high-peaked BL Lacertae objects. *Proceedings of the 29th ICRC (Pune)*, August 2005. [arXiv:astro-ph/0508273].

[353] I.F. Mirabel. Very Energetic γ-Rays from Microquasars and Binary Pulsars. *Science*, **312**:1759–1760, 2006.

[354] R. Mirzoyan. Cherenkov light observation with the HEGRA detector at the Roque de los Muchachos Observatory. *New Astronomy Reviews*, **42**:547–551, 1998.

[355] R. Mirzoyan. Status report on the 17 m Diameter MAGIC Telescope Project. *Proceedings of the 29th ICRC (Pune)*, August 2005. [arXiv:astro-ph/0508274].

[356] A.L. Mishev et al. Ground based Gamma Ray Studies based on Atmosferic Cherenkov technique at high mountin altitude. *arXiv:astro-ph/0410118*, October 2004.

[357] S. Mizobuchi et al. Reconstruction methods of energy spectra for high redshift sources with the MAGIC Telescope. *Proceedings of the 29th ICRC (Pune)*, August 2005. [arXiv:astro-ph/0508274].

[358] D.L. Moché. *Astronomy: A Self-teaching Guide*. John Wiley & Sons, 5$^{\text{th}}$ edition, 2002.

[359] T. Montaruli. IceCube: The state of the art. *Proceedings of the Frontier Objects in Astrophysics and Particle Physics (Vulcano)*, 2006. [arXiv:astro-ph/0608140].

[360] A. Moralejo. The Reflector Simulation Program v. 0.6. MAGIC-TDAS 02-11 030120/AMoralejo, 2003.

[361] A. Moralejo et al. The MAGIC telescope for gamma-ray astronomy above 30 GeV. *Chinese Journal of Astronomy and Astrophysics Supplement*, **3**:531–538, 2003.

[362] M. Mori. CANGAROO. *Proceedings of the Science with the New Generation of High Energy Gamma-ray Experiments (Cividale del Friuli)*, June 2005.

[363] M. Mori. CANGAROO-III: Status report. *Proceedings of the Towards a Network of Atmospheric Cherenkov Detectors VII (Palaiseau)*, April 2005.

[364] I.V. Moskalenko and A.W. Strong. Diffuse γ-ray emission: lessons and perspectives. *arXiv:astro-ph/0509414*, September 2005.

[365] R. Nahnhauer. Alternative detection methods for highest energy neutrinos. *Proceedings of the Very High Energy Phenomena in the Universe (La Thuile)*, March 2005.

[366] F. Nerling et al. Universality of electron distributions in high-energy air showers - Description of Cherenkov light production. *Astroparticle Physics*, **24**:421–437, 2006. [arXiv:astro-ph/0506729].

[367] P. Nieβen. Use of CORSIKA in AMANDA, SPACE, Ice Cube and IceTop. *VIHKOS CORSIKA School, Lauterbad, Germany*, June 2005.

[368] E. Oña–Wilhelmi et al. First pulsar observation with the MAGIC telescope. *Proceedings of the 29th ICRC (Pune)*, August 2005. [arXiv:astro-ph/0508244].

[369] J. Oehlschläger. Air Shower Physics with Computer Animations. *VIHKOS CORSIKA School, Lauterbad, Germany*, June 2005.

[370] The University of Chicago Press. *The Chicago Manual of Style*. The University of Chicago Press, 15$^{\text{th}}$ edition, 2003.

[371] P.M. O'Neill et al. The relationship between X-ray variability amplitude and black hole mass in active galactic nuclei. *ArXiv:astro-ph/0501471*, January 2005.

[372] R. Ong. The Status of VHE Gamma-Ray Astronomy. *Proceedings of the 29th ICRC (Pune)*, 2005. [arXiv:astro-ph/0605191].

[373] R.A. Ong. Very high-energy gamma-ray astronomy. *Physics Reports*, **305**:93–202, 1998.

[374] J.A. Ortiz, G. Medina-Tanco, and V. de Souza. Longitudinal Development of Extensive Air Showers: Hybrid Code SENECA and Full Monte Carlo. *ArXiv:astro-ph/0411421*, November 2004.

[375] S. Osone. Study of 23 day periodicity of Blazar Mkn501 in 1997. *Astroparticle Physics*, **26**:209–218, 2006. [arXiv:astro-ph/0506328].

[376] S. Ostapchenko. QGSJET-II: results for extensive air showers. *ArXiv:astro-ph/0412591*, December 2004.

[377] A.N. Otte et al. Status of Silicon Photomultiplier Developments as optical Sensors for MAGIC/EUSO-like Detectors. *Proceedings of the 29th ICRC (Pune)*, August 2005. [arXiv:astro-ph/0508273].

[378] B. Paczynski and P. Haensel. Gamma-Ray Bursts from quark stars. *ArXiv:astro-ph/0502297*, March 2005.

[379] E. Pakštiene. The dependence of atmospheric extinction on meteorological conditions and aerosol size distribution (Paper III). *Baltic Astronomy*, **10**:651–669, 2001.

[380] N. Palanque-Delabrouille. Overview of astroparticle physics and cosmology. *LHC days (Split)*, 2006.

[381] C. Palomares. The Alpha Magnetic Spectrometer on the International Space Station. *Proceedings of the Very High Energy Phenomena in the Universe (La Thuile)*, March 2005.

[382] J. van Paradijs et al. Transient optical emission from the error box of the gamma-ray burst of 28 February 1997. *Nature*, **386**:686–689, 1997.

[383] J.M. Paredes. High-energy γ-ray emission in AGNs and microquasars. *Proceedings of the Frontier Objects in Astrophysics and Particle Physics (Vulcano)*, 2006. [arXiv:astro-ph/0609168].

[384] D.H. Perkins. *Particle astrophysics*. Oxford University Press, 2003.

[385] D. Petry et al. Detection of VHE γ-rays from Mkn 421 with the HEGRA Cherenkov Telescopes. *Astronomy and Astrophysics*, **311**:L13–L16, 1996. [arXiv:astro-ph/9606159].

[386] L. Piro. Short-burst sources. *Nature*, **437**:822–823, October 2005.

[387] G.L. Poe, K.L. Giraud, and J.B. Loomis. Computational Methods for Measuring the Difference of Empirical Distributions. *American Journal of Agricultural Economics*, **87** (2):353–365, 2005.

[388] G.L. Poe, E.K. Severance-Lossin, and M.P. Welsh. Measuring the Difference $(X - Y)$ of Simulated Distributions: A Convolutions Approach. *American Journal of Agricultural Economics*, **76** (4):904–915, 1994.

[389] M. Pohl. Hadronic models for blazars and AGN neutrinos. *Proceedings of the Very High Energy Phenomena in the Universe (La Thuile)*, March 2005.

[390] N.A. Porter. The atmospheric Cherenkov technique in the search for PBH. *Space Science Reviews*, **75**:67–69, 1996.

[391] N.A. Porter and T.C. Weekes. A search for high energy gamma-ray bursts from primordial black holes or other astronomical objects. *The Astrophysical Journal*, **404**:206–218, 1993.

[392] K. Postnov. Stellar explosions: from supernovae to gamma-ray bursts. *arXiv:astro-ph/0410349*, October 2004.

[393] J.R. Primack, J.S. Bullock, and R.S. Somerville. Observational Gamma-ray Cosmology. *ArXiv:astro-ph/0502177*, February 2005.

[394] G. Pühlhofer et al. The technical performance of the HEGRA system of imaging air Cherenkov telescopes. *Astroparticle Physics*, **20**:267–291, 2003. [arXiv:astro-ph/0306123].

[395] M. Punch. Results from Observations of AGNs with the HESS Telescope System and Future Plans. *ArXiv:astro-ph/0501115*, January 2005.

[396] M. Punch et al. Detection of TeV photons from the active galaxy Markarian 421. *Nature*, **358**:477–478, 1992.

[397] C.M. Raiteri et al. Multifrequency variability of the blazar AO 0235+164. The WEBT campaign in 20042005 and long-term SED analysis. *Astronomy and Astrophysics*, **459**:731–743, 2006. [arXiv:astro-ph/0608627].

[398] R.C. Rannot. TeV gamma-ray Observations of the Blazar Markarian 421 from January to April 2004 with TACTIC Imaging Element. *Proceedings of the 29th ICRC (Pune)*, 2005.

[399] G. Rauterberg, N. Müller, and T. Deckers. A New 127 Pixel Camera for Cherenkov Telescopes of the HEGRA Array on La Palma. *Proceedings of the 24th ICRC (Rome)*, **3**:460–463, 1995.

[400] A. Razdan et al. Factorial moment studies of Cherenkov images. *Proceedings of the 29th ICRC (Pune)*, August 2005. [arXiv:astro-ph/0509012].

[401] P.F Rebillot et al. Multiwavelength Observations of the Blazar Mrk 421 in December 2002 and January 2003. *The Astrophysical Journal*, **641**:740–751, 2006. [arXiv:astro-ph/0512628].

[402] T. Reichhardt. Two telescopes join hunt for ET. *Nature*, **440**:853, 2006.

[403] A. Reimer, M. Böttcher, and S. Postnikov. Neutrino Emission in the Hadronic Synchrotron Mirror Model: The "Orphan" TeV Flare from 1ES 1959+650. *The Astrophysical Journal*, **630**:186–190, 2005. [arXiv:astro-ph/0505233].

[404] R. de los Reyes López. Análisis y simulación de datos de telescopios Cherenkov atmosféricos. Diploma thesis. Facultad de Ciencias Físicas, Univesidad Complutense, Madrid, 2002.

[405] P.T. Reynolds et al. Survey of candidate gamma-ray sources at TeV energies using a high-resolution Cherenkov imaging system: 1988-1991. *The Astrophysical Journal*, **404**:206–218, 1993.

[406] J. Rico et al. Study of the MAGIC sensitivity for off-axis observation. *Proceedings of the 29th ICRC (Pune)*, August 2005. [arXiv:astro-ph/0508273].

[407] I. Ridpath, editor. *A Dictionary of Astronomy*. Oxford University Press, 1997.

[408] B. Riegel et al. A tracking monitor for the MAGIC Telescope. *Proceedings of the 29th ICRC (Pune)*, August 2005. [arXiv:astro-ph/0508274].

[409] F.M. Rieger. Supermassive binary black holes among cosmic gamma-ray sources. *Astrophysics and Space Science*, accepted, 2006. [arXiv:astro-ph/0611224].

[410] F.M. Rieger and K. Mannheim. Implications of a possible 23 day periodicity for binary black hole models in Mkn 501. *Astronomy and Astrophysics*, **359**:948–952, 2000. [arXiv:astro-ph/0005478].

[411] A.G. Riess et al. (Supernova Search Team). Observational Evidence from Supernovae for an Accelerating Universe and a Cosmological Constant. *The Astronomical Journal*, **116**:1009–1038, 1998. [arXiv:astro-ph/9805201].

[412] L. Rochester. Status of GLAST - The Gamma-Ray Large Area Space Telescope. *Proceedings of the Science with the New Generation of High Energy Gamma-ray Experiments (Cividale del Friuli)*, June 2005.

[413] B. Rossi. *Cosmic Rays*. McGraw-Hill, 1964.

[414] G. Rowell, F. Aharonian, and A. Plyasheshnikov. Ground-Based Gamma-Ray Astronomy at Energies above 10 TeV: Searching for Galactic PeV Cosmic-Ray Accelerators. *arXiv:astro-ph/0512523*, December 2005.

[415] S. Roy and M. Watzke. X-rays Signal Presence of Elusive Intermediate-Mass Black Hole. *Chandra Press Release: CXC 05-04*, March 2005.

[416] V. Ruhlmann-Kleider. The SuperNova Legacy Survey. *LHC days (Split)*, 2006.

[417] Y. Sakamoto. Search for Very High Energy Gamma-Rays from Active Galactic Nuclei with the CANGAROO-III Telescope. *Proceedings of the 29th ICRC (Pune)*, 2005.

[418] M. Salvati, M. Spada, and F. Pacini. Rapid variability of gamma-ray blazars: A model for Markarian 421. *The Astrophysical Journal*, **495**:L19–L21, 1998. [arXiv:astro-ph/9801049].

[419] R.M. Sambruna et al. Correlated intense X-ray and TeV activity of Markarian 501 in 1998 June. *The Astrophysical Journal*, **538**:127–133, 2000. [arXiv:astro-ph/0002215].

[420] M. Sasano et al. Atmospheric monitoring in Utah using Back Scatter Lidar method. *Proceedings of the 27th ICRC (Hamburg)*, 2001.

[421] G. Schilling. *Flash! The hunt for the biggest explosions in the universe*. Cambridge University Press, 2002.

[422] G. Schilling. ASTROPHYSICS: Short Gamma Ray Bursts: Mystery Solved. *Science*, **310**:37, October 2005.

[423] G. Schilling. ASTROPHYSICS: Surprise Neutron Star Suggest Black Holes Are Hard to Make. *Science*, **310**:956–957, 2005.

[424] A. Schliesser and R. Mirzoyan. Wide-field prime-focus imaging atmospheric Cherenkov telescopes: A systematic study. *Astroparticle Physics*, **24**:382–390, 2005. [arXiv:astro-ph/0507617].

[425] R. Schwarz. Development of a LIDAR for Measuring the Atmospheric Transmission for GeV-TeV γ-Astronomy with the 17 m MAGIC Telescope. Diploma thesis. Max-Planck-Institut für Physik (Werner-Heisenberg-Institut), Munich, 2002.

[426] R. Schwarz et al. A LIDAR for atmospheric studies for the 17 m diameter MAGIC telescope. *Proceedings of the 27th ICRC (Hamburg)*, 2001.

[427] T. Schweizer. *Analysis of the Large Gamma Ray Flares of Mkn 421 as Observed with HEGRA CT1 on the Island La Palma in 2001*. PhD thesis, Institut de Física d'Altes Energies (Universitat Autònoma de Barcelona), Barcelona, 2002.

[428] D. Scott and J.P. Zibin. The Real Message in the Sky. *arXiv:physics/0511135*, November 2005.

[429] D. Seckel and T. Stanev. Neutrinos: the key to UHE Cosmic Rays. *ArXiv:astro-ph/0502244*, February 2005.

[430] G. Sembroski et al. Very High Resolution Whipple Gamma Ray Camera. *Proceedings of the 24th ICRC (Rome)*, pages 428–431, 1995.

[431] C. Shapiro and M.S. Turner. What Do We Really Know About Cosmic Acceleration? *arXiv:astro-ph/0512586*, December 2005.

[432] Z.-Q. Shen et al. A size of 1 AU for the radio source Sgr A* at the centre of the Milky Way. *Nature*, **438**:62–64, 2005. [arXiv:astro-ph/0512515].

[433] N. Shepherd et al. Absolute calibration of imaging atmospheric Cherenkov telescopes. *Proceedings of the 29th ICRC (Pune)*, July 2005. [arXiv:astro-ph/0507083].

[434] M. Shibata. Magnetized hypermassive neutron star collapse: a central engine for short gamma–ray bursts. *arXiv:astro-ph/0511142*, November 2005.

[435] J.M. Shull. Hot pursuit of missing matter. *Nature*, **433**:465–466, 2005.

[436] N. Sidro. First results of galactic observations with MAGIC. *Proceedings of VII reunion cientifica de la SEA 2006 (Barcelona)*, 2006. [arXiv:astro-ph/0610945].

[437] M. Sikora et al. Are Quasar Jets Matter or Poynting Flux Dominated? *arXiv:astro-ph/0509685*, September 2005.

[438] P.O. Slane, D.J. Helfand, and S.S. Murray. New Constrains on Neutron Star Cooling from Chandra Observations of 3C58. *The Astrophysical Journal*, **571**:L45–L49, 2002. [arXiv:astro-ph/0204151].

[439] D.A. Smith. Review of the "Solar Array" Cherenkov telescopes. *Proceedings of the Towards a Network of Atmospheric Cherenkov Detectors VII (Palaiseau)*, April 2005.

[440] D.A. Smith et al. Mrk 421, Mrk 501, and 1ES 1426+428 at 100 GeV with the CELESTE Cherenkov Telescope. *Astronomy and Astrophysics*, **459**:453–464, 2006. [arXiv:astro-ph/0608247].

[441] D. Sobczyńska. Mmcs from CORSIKA 6.014. MAGIC-TDAS 02-10 020730/D.Sobczynska, 2002.

[442] D. Sobczyńska and E. Lorenz. Simulations of the trigger performance of air Cherenkov telescopes for γ-astronomy. *Nuclear Instruments and Methods in Physics Research A*, **490**:124–131, 2002.

[443] P. Sokolsky and J. Krizmanic. Effect of clouds on apertures of space-based air fluorescence detectors. *Astroparticle Physics*, **20**:391–403, 2004. [arXiv:astro-ph/0302501].

[444] V. de Souza et al. A Monte Carlo method to generate fluorescence light in extensive air showers. *Astroparticle Physics*, **22**:263–273, 2004.

[445] M. Spada. Rapid variability of gamma-ray blazars: a model for Mkn 421. *Astroparticle Physics*, **11**:59–61, 1999. [arXiv:astro-ph/9801049].

[446] C. Spiering. Neutrino Astrophysics in the cold: Amanda, Baikal and IceCube. *ArXiv:astro-ph/0503122*, March 2005.

[447] V. Springel et al. Simulation of the formation, evolution and clustering of galaxies and quasars. *Nature*, **435**:629–636, 2005. [arXiv:astro-ph/0504097].

[448] F.W. Stecker. A Note on High Energy Neutrinos from AGN Cores. *arXiv:astro-ph/0510537*, November 2005.

[449] Y.V. Stenkin. Power Law Spectra in the Nature: Analogies with the Cosmic Ray Spectrum. *Proceedings of the 29th ICRC (Pune)*, July 2005. [arXiv:astro-ph/0507019].

[450] G.L. Stephens et al. The CloudSat mission and the A-train: A new dimension of space-based observations of cloud and precipitation. *Bulletin of the American Meteorological Society*, **83**:1771–1790, 2002.

[451] J.A. Stratton and G.H. Houghton. A theoretical investigation of the transmission of light through fog. *Physical Review*, **38**:159–165, 1931.

[452] W. Strunk and E.B. White. *The Elements of Style*. Wiley-VCH, 4$^{\text{th}}$ edition, 2004.

[453] I. Tada. Detection of Atmospheric Cherenkov Images of Air Showers using High-Resolution and High-Speed Camera System with Image Intensifiers. *Proceedings of the 29th ICRC (Pune)*, 2005.

[454] N.R. Tanvir et al. An origin in the local Universe for some short γ-ray bursts. *Nature*, **438**:991–993, 2005. [arXiv:astro-ph/0509167].

[455] M. Tegmark and N. Bostrom. Is doomsday catastrophe likely? *Nature*, **438**:754, 2005. [arXiv:astro-ph/0512204].

[456] W.I. Thompson. *Atmospheric transmission handbook: A survey of electromagnetic wave transmission in the Earth's atmosphere over the frequency (wavelength) range 3 kHz (100 km) 3.000 THz (0.1 μm)*. Cambridge: Transportation Systems Center, Report No. Dot-Tsc-NASA-71-6, 1971.

[457] K.S. Thorne. *Black Holes and Time Warps: Einstein's Outrageous Legacy*. W.W. Norton, 1994.

[458] M.G. Tomasko et al. Rain, winds and haze during the Huygens probe's descent to Titan's surface. *Nature*, **438**:765–778, 2005.

[459] N. Tonello. *Study of the VHE γ-ray emission from the Active Galactic Nucleus 1ES1959+650*. PhD thesis, Max-Planck-Institut für Physik (Werner-Heisenberg-Institut), Munich, 2006.

[460] N. Tonello et al. Observation of γ-ray emission above 200 GeV from the AGN 1ES1959+650 during low X-ray and optical activity. *Proceedings of the 29th ICRC (Pune)*, August 2005. [arXiv:astro-ph/0508244].

[461] D.F. Torres, T.M. Dame, and S.W. Digel. High-Latitude Molecular Clouds as gamma ray Sources for GLAST. *ArXiv:astro-ph/0501385*, January 2005.

[462] Y. Uchiyama et al. Shedding New Light on the 3C 273 Jet with the Spitzer Space Telescope. *The Astrophysical Journal*, **648**:910–921, 2006. [arXiv:astro-ph/0605530].

[463] M. Ulrich, A. Daum, and W. Hofmann. An improved technique for the determination of shower geometry from single and stereo IACT images. *Journal of Physics G: Nuclear and Particle Physics*, **24**:883–897, 1998. [arXiv:astro-ph/9708003].

[464] P. Uttley. The relation between optical and X-ray variability in Seyfert galaxies. *ArXiv:astro-ph/0501157*, January 2005.

[465] S.V. Vadawale et al. Monte-Carlo simulations of the expected imaging performance of the EXIST high-energy telescope. *arXiv:astro-ph/0509757*, September 2005.

[466] V. Vasilev and S. Fegan. High Energy All Sky Transient Radiation Observatory. *arXiv:astro-ph/0511342*, November 2005.

[467] V. Venema et al. Cloud boundary height measurements using lidar and radar. *Physics and Chemistry of the Earth*, **24**:129–134, 2000.

[468] R. Villard. The weirdest star in the sky. *Astronomy*, pages 34–39, March 2005.

[469] P. Vincent. H.E.S.S. *Proceedings of the Science with the New Generation of High Energy Gamma-ray Experiments (Cividale del Friuli)*, June 2005.

[470] P.R. Vishwanath. Possible bursts of TeV gamma rays in PACT from Mkn 421 in April 2004. *Proceedings of the 29th ICRC (Pune)*, 2005.

[471] V. Vitale. *Search for multi-TeV gamma ray emission from the SN1006 remnant with the HEGRA CT1 telescope*. PhD thesis, Max-Planck-Institut für Physik (Werner-Heisenberg-Institut), Munich, 2004.

[472] H.J. Völk. New Results from High Energy Gamma-Ray Astronomy. *arXiv:astro-ph/0603501*, March 2006.

[473] R.M. Wagner et al. Observation of the Crab nebula with the MAGIC telescope. *Proceedings of the 29th ICRC (Pune)*, August 2005. [arXiv:astro-ph/0508244].

[474] L. Wai. Search for WIMP annihilation with GLAST. *New Astronomy Reviews*, **49**:307–310, 2005.

[475] P. Wallace, S. Bloom, and M. Lewis. A multiwavelength investigation of undefined EGRET sources. *ArXiv:astro-ph/0501193*, January 2005.

[476] F.M. Walter and J.M. Lattimer. A Revised Parallax and its Implication for RX J185635-3754. *The Astrophysical Journal*, **576**:L145–L148, 2002. [arXiv:astro-ph/0204199].

[477] J.S. Warren et al. Cosmic-Ray Acceleration at the Forward Shock in Tycho's Supernova Remnant: Evidence from Chandra X-Ray Observations. *The Astrophysical Journal*, **634**:376–389, 2005. [arXiv:astro-ph/0507478].

[478] E. Waxman. Extragalactic sources of high energy neutrinos. *ArXiv:astro-ph/0502159*, February 2005.

[479] F. Weber. Strangeness in neutron stars. *Journal of Physics G: Nuclear and Particle Physics*, **27**:465–474, 2001. [arXiv:astro-ph/0008376].

[480] T.C. Weekes. Very high energy gamma-ray astronomy. *Physics Reports*, **160**:1–121, 1988.

[481] T.C. Weekes. TeV radiation from galactic sources. *Space Science Reviews*, **59**:315–364, 1992.

[482] T.C. Weekes. The atmospheric Cherenkov technique in very high energy gamma-ray astronomy. *Space Science Reviews*, **75**:1–15, 1996.

[483] T.C. Weekes. *Very High Energy Gamma Ray Astronomy*. The Institute of Physics, 2003.

[484] T.C. Weekes. The Atmospheric Cherenkov Imaging Technique for Very High Energy Gamma-ray Astronomy. *arXiv:astro-ph/0508253*, August 2005.

[485] T.C. Weekes. VERITAS: Status report. *Proceedings of the Towards a Network of Atmospheric Cherenkov Detectors VII (Palaiseau)*, April 2005.

[486] T.C. Weekes et al. Obseravtions of TeV Gamma Rays from the Crab Nebula using the Atmospheric Cerenkov Imaging Technique. *The Astrophysical Journal*, **342**:379–395, 1989.

[487] M.C. Weisskopf. Five Years of observations with the Chandra X-Ray Observatory. *ArXiv:astro-ph/0503091*, March 2005.

[488] B.A. Whitney. How to make a massive star. *Nature*, **437**:37–38, September 2005.

[489] P.J. Wiita. Active Galactic Nuclei: Unification, Blazar Variability and the Radio Galaxy/Cosmology Interface. *arXiv:astro-ph/0603728*, March 2006.

[490] B. Wilczynska. Variation of atmospheric depth profile on different time scales. *Astroparticle Physics*, **25**:106–117, 2006. [arXiv:astro-ph/0603088].

[491] D. Winker et al. CALIOP: The CALIPSO lidar. *Proceedings of 22nd International Laser Radar Conference (Matera)*, pages 941–944, 2004.

[492] J.N. Winn. The life of a Neutron Star. *Sky & Telescope*, **98**:30–38, 1999.

[493] R. Wischnewski. NT200+ The Baikal Neutrino Telescope. *VIHKOS CORSIKA School, Lauterbad, Germany*, June 2005.

[494] R. Wischnewski. The Baikal Neutrino Telescope - Results and Plans. *arXiv:astro-ph/0507698*, August 2005.

[495] R. Wischnewski et al. Search for relativistic magnetic monopoles with the Baikal neutrino telescope NT200. *Proceedings of the 29th ICRC (Pune)*, August 2005. [arXiv:astro-ph/0507713].

[496] K.K. Yadav et al. Real-time data acquisition and control system for the 349-pixel TACTIC atmospheric Cherenkov imaging telescope. *Nuclear Instruments and Methods in Physics Research A*, **527**:411–422, 2004.

[497] S. Young et al. The retrieval of extinction profiles in optically-inhomogeneous cloud and aerosol layers detected by CALIPSO lidar. *Proceedings of 22nd International Laser Radar Conference (Matera)*, pages 999–1002, 2004.

[498] S. Youssef, R. Cousins, F. James, G. Cowan, and R. Miquel. MONTE CARLO TECHNIQUES (Review of Particle Physics). *Journal of Physics G: Nuclear and Particle Physics*, **33**:311–313, 2006.

[499] A. Zakharov. Measuring parameters of Supermassive Black Holes. *Proceedings of the Very High Energy Phenomena in the Universe (La Thuile)*, March 2005.

[500] K. Zdanavičius and E. Pakštiene. Determination of the spectral transmittance of the Earth atmosphere and its parameters from Vilnius multicolor photometry (Paper I). *Baltic Astronomy*, **6**:421–443, 1997.

[501] K. Zdanavičius, E. Pakštiene, and S. Bartašiute. A study of atmospheric extinction by stellar photometry in the Vilnius system (Paper II). *Baltic Astronomy*, **10**:439–460, 2001.

[502] J.-L. Zhang, X.-J. Bi, and H.-B. Hu. VHE γ ray absorption by galactic interstellar radiation field. *arXiv:astro-ph/0508236*, August 2005.

[503] J.A. Zweerink et al. The TeV gamma-ray spectrum of Markarian 421 during an intense flare. *The Astrophysical Journal*, **490**:L141–L144, 1997.

[504] Y.L. Zyskin, A.A. Stepanian, and A.P. Kornienko. On the optimal characteristics of the multichannel imaging camera for TeV gamma ray observations. *Journal of Physics G: Nuclear and Particle Physics*, **20**:1851–1858, 1994.

List of Figures

List of Tables

Prošireni sažetak na hrvatskome jeziku

1. Uvod

1.1 Zračenje odozgo

Kozmičke su zrake visokoenergijske čestice izvanzemaljskog podrijetla. Tradicionalno, to su stabilne nabijene čestice – uglavnom protoni ($\approx 90\%$) i α-čestice ($\approx 9\%$). Ostatak čine teže jezgre čiji je poluživot iznad 10^6 godina [219]. Elektroni, γ-zrake i neutrini čine tek manji dio ($< 10^{-4}$) zračenja koje dopire do Zemlje. Ponekad se i oni ubrajaju u kozmičko zračenje, no većinom se termin kozmičke zrake odnosi samo na nabijene čestice. Kinetička energija kozmičkih zraka proteže se 14 redova veličine (od 10^6 do 10^{20} eV i više), a njihov tok pri vrhu atmosfere opada približno s trećom potencijom energije (slika 1.2). Ovakav oblik spektra potvrđuje netermičko podrijetlo kozmičkih zraka.

Otkriće kozmičkih zraka pripisuje se Victoru Hessu koji je u nizu istraživačkih letova balonom, 1912. godine konačno pokazao da postoji neprekidno zračenje "odozgo" [413]. Izraz *kozmičke zrake* skovao je 1925. godine Robert Andrews Millikan.

1938. godine, Pierre Auger opazio je gotovo simultane ionizacijske događaje na međusobno udaljenim položajima. Zaključio je da je riječ o visokoenergijskim česticama koje su potaknule nastanak kaskada sekundarnih čestica. Danas su takve kaskade poznate kao pljuskovi čestica u atmosferi odnosno Augerovi pljuskovi.

Opće je prihvaćeno da su ostaci supernova glavni izvori galaktičkih kozmičkih zraka [4] kroz akceleracijski mehanizam udarnog vala [23]. Mnoga su opažanja potvrdila tu teoriju.

Izvori kozmičkih zraka najviših energija još nisu poznati. Nova bi opažanja mogla razotkriti još nepoznate akceleracijske mehanizme kao i fiziku iza Standardnog modela [84].

Iznad 10^{14} eV pljuskovi sekundarnih čestica, stvoreni upadom kozmičke zrake u atmosferu, dovoljno su veliki da se mogu detektirati na površini Zemlje nizovima detektora čestica (PDA). Takvi detektori, čiji je radni ciklus gotovo 100%, koriste velike rezervoare vode u kojima nabijene čestice stvaraju Čerenkovljevu svjetlost. PDA imaju veliki kut opažanja (FoV) pa su pogodni za pretraživanje neba. S druge strane, imaju malu osjetljivost pa teško mogu doseći signifikantnost od 5σ potrebnu za potvrdu detekcije izvora. Neki od postojećih eksperimentata tog tipa (ili eksperimenata u gradnji) su: KASCADE Grande, Tibet III Air Shower Array, EAS-TOP i TUNKA.

Sekundarne čestice u velikim pljuskovima u atmosferi stvaraju i fluorescentnu svjetlost koja se može opažati detektorima smještenim na površini Zemlje (npr. Auger) ili na satelitima (npr. EUSO). Takvi eksperimenti mogu opažati događaje najviših mogućih energija: UHE i EHE (tablica 1.2).

Foton, kvant elektromagnetskog zračenja, tradicionalna je čestica-prenositelj u astronomiji. Njegovo pravocrtno širenje omogućuje opažanje pojedinačnih astrofizičkih izvora. Većina znanja o svemiru proizlazi iz opažanja elektromagnetskog zračenja – od radiovalova do γ-zraka (tablica 1.1). γ-zrake protežu se preko 15 redova veličine u energijskom spektru, stoga je za opažanje γ-neba potrebno mnoštvo različitih detekcijskih tehnika i uređaja. Prirodno se nameće i potreba za dodatnom podjelom γ-spektra (tablica 1.2).

Među mnoštvom različitih detekcijskih tehnika koje su do sada razvijene za detekciju kozmičkih γ-zraka, dvije su se pokazale iznimno uspješnima: eksperimenti u orbiti (γ-detektori na satelitima) te eksperimenti na površini Zemlje (Čerenkovljevi teleskopi).

γ-detektori na satelitima koriste vrlo učinkovitu metodu razdvajanja γ-zraka od nabijenih čestica: anti-koincidentne brojače koji potpuno okružuju aktivni detekcijski volumen. No istovremeno, ti detektori imaju vrlo malu detekcijsku površinu (do 1 m^2, često svega nekoliko cm^2) pa stoga imaju gornji energijski prag od oko 10 GeV (GLAST će podići taj prag na oko 300 GeV). Značajni γ-detektori na satelitima bili su npr. *Small Astronomy Satellite 2* (SAS-2) i *COsmic ray Satellite B* (COS-B) te iznimno uspješni *Compton Gamma Ray Observatory* (CGRO) koji je nosio: *Energetic Gamma Ray Experiment Telescope* (EGRET), *Compton Telescope* (COMPTEL), *Burst and Transient Source Experiment (BATSE)* i *Oriented Scintillation Spectrometer Experiment (OSSE)*. Trenutno su u orbiti *International Gamma-Ray Astrophysics Laboratory* (INTEGRAL) i *Swift*, a uskoro se očekuje lansiranje malog talijanskog satelita *Astro-rivelatore Gamma a Immagini LEggero* (AGILE) i velikog obećavajućeg γ-opservatorija *Gamma-ray Large Area Space Telescope* (GLAST). GLAST će nositi tri instrumenta: *GLAST Burst Monitor* (GBM), *Large Area Telescope* (LAT) i *Anti-Coincidence Detector* (ACD).

γ-zrake viših energija (iznad desetak GeV) mogu se detektirati posredno, s površine Zemlje. Postoji nekoliko vrsta eksperimenata s različitim pristupima: vodeni Čerenkovljevi detektori (npr. MILAGRO i HAWC); solarne elektrane u službi Čerenkovljevih teleskopa (npr. CELESTE i STACEE); tehnika sampliranja valne fronte (npr. PACT i HAGAR); razne kombinirane tehnike (npr. ASHRA) te konačno Čerenkovljevi atmosferski imaging-teleskopi (npr. CT1, MAGIC, HESS, VERITAS i CANGAROO III).

Čerenkovljevi atmosferski teleskopi (IACT) koriste zrcala za refleksiju Čerenkovljeve svjetlosti (nastale u pljusku sekundarnih čestica) u kameru teleskopa. Kamera je obično matrica fotomultiplikatora smještena u žarišnoj ravnini. Brza elektronika potrebna je kako bi bljesak Čerenkovljeve svjetlosti (koji traje svega nekoliko ns) razlučila od pozadinske svjetlosti noćnog neba [266]. Neki od prethodnih IACT su npr. Whipple, CAT, i HEGRA. Od trenutno aktivnih Čerenkovljevih teleskopa, vodeći su europski instrumenti MAGIC i HESS, zatim američki VERITAS i japanski CANGAROO III. Tablica 1.3 prikazuje njihove usporedne karakteristike. Neki od istaknutijih budućih Čerenkovljevih atmosferskih imaging-teleskopa su: MAGIC II, HESS II, *European Čerenkov Observatory 1000* (ECO-1000), *Major Atmospheric Čerenkov Experiment* (MACE), *5@5*, *Gamma Air Watch* i *High Altitude Telescope System* (HATS).

X-astronomija je opažanje X-zračenja s nebeskih objekata. Prvo takvo opažanje zabilježeno 1949. godine kad je X-zračenje sa Sunca otkriveno u eksperimentima postavljenim na raketama [407]. X-astronomija bila je tako prva "nova astronomija" svemirskog doba. Godine 1962., otkriven je prvi izvor X-zračenja izvan Sunčeva sustava. Danas je poznato obilje nebeskih izvora X-zračenja: Sunčev sustav (Sunčeva korona, Jupiter, kometi), zvijezde, kompaktni objekti (bijeli patuljci, neutronske zvijezde, crne rupe), supernove i njihovi ostaci galaksije, grozdovi galaksija te konačno aktivne galaktičke jezgre. S obzirom da atmosfera apsorbira kozmičko X-zračenje, instrumenti kojima se ono opaža moraju biti na velikim visinama. Prvi su eksperimenti bili postavljani na balone i rakete. Danas je većina eksperimenata iz područja X-astronomije smještena na satelitima, no i dalje postoje i eksperimenti s balonima kao npr. HEXIT. Za razvoj X-astronomije važni su bili sateliti: Uhuru (poznat i kao SAS-1), *High Energy Astrophysical Observatory* (HEAO) i *Röntgensatellit* (ROSAT). Danas su vodeći: Chandra X-ray Observatory, *X-ray Multi-Mirror* (XMM) te *Rossi X-ray Timing Explorer* (RXTE) koji je detaljnije opisan u odlomku 3.1.2.

Opažanje astrofizičkih neutrina otvara novi prozor u svemir. Od svih astrofizičkih prenositelja informacija, neutrini su savršene probe (gustih područja, izvora na koz-

mološkim udaljenostima i akceleracijskih procesa) s obzirom da nemaju naboja te da imaju izuzetno slabo međudjelovanje. Neutrinska astronomija pri energijama od 1 TeV komplementarna je visokoenergijskoj γ-astronomiji [480]. Istovremena detekcija neutrina i γ-zraka iz blazara dala bi uvjerljivu potvrdu hadronskog modela akceleracije [480]. Jedini zasad potvrđeni izvori astrofizičkih neutrina su Sunce i SN 1987A. Mjesta velikih ubrzavanja nabijenih nabijenih čestica (izvori kozmičkih zraka) ujedno su i potencijalni izvori neutrina. Drugi mogući neutrinski izvori su mikrokvazari (dvojni akrecijski sustavi koji sadrže neutronsku zvijezdu ili crnu rupu) i provale gama-zraka (GRB). Trenutno u svijetu postoje četiri velika neutrinska eksperimenta smještena na velikim dubinama (mora ili jezera): BAIKAL, AMANDA II, NESTOR and ANTARES. Ostali važniji eksperimenti su: Super-KAMIOKANDE u Japanu i *Large Volume Detector* (LVD) u Gran Sasso laboratoriju u Italiji te *ANtarctic Impulsive Transient Antenna* (ANITA). ANITA ne koristi vodu kao medij nego atmosferu te detektira radiovalove nastale u pljuskovima čestica koje iniciraju astrofizički neutrini. Neutrinski eksperimenti iduće generacije su IceCube na Južnom polu (koji je djelomično dovršen te već prikuplja podatke), zatim *NEutrino Mediterranean Observatory* (NEMO) i KM3NeT.

Idući astrofizički prenositelj informacija koji ima ogromni potencijal su gravitacijski valovi. Njihovo je postojanje predvidio Einstein još 1916. godine na temelju opće teorije relativnosti. Prema općoj relativnosti, gravitacija se može izraziti kao zakrivljenost prostor-vremena. Promjena u raspodjeli mase uzrokuje nabore u prostor-vremenu koji se šire od izvora brzinom svjetlosti. Gravitacijski su valovi opaženi posredno kroz gubitak energije u dvojnom sustavu pulsara PSR 1913+16. Neposredno opažanje gravitacijskih valova veliki je izazov za eksperimentalnu fiziku, no nakon 40 godina razvoja detekcijskih uređaja danas smo na pragu neposredne detekcije [84]. Gravitacijski valovi koji bi mogli biti opaženi očekuju se tamo gdje su velike mase podložne snažnim ubrzanjima. Tipični galaktički izvori očekuju se stoga pri spajanjima dvojnih sustava kompaktnih objekata [114]. Eksplozije supernova također bi trebale emitirati snažno gravitacijsko zračenje u kratkom vremenskom periodu. Spajanje supermasivnih crnih rupa očekivani je tipični izvangalaktički izvor gravitacijskih valova. Prvi i trenutno najveći detektor gravitacijskih valova je *Laser Interferometer Gravitational-wave Observatory* (LIGO). U gradnji su još eksperimenti VIRGO, GEO 600, TAMA i AIGO. Intenzivno se priprema i *Laser Interferometer Space Antenna* (LISA) – opservatorij za direktnu detekciju gravitacijskih valova koji će se sastojati od tri svemirske letjelice, udaljene oko $5 \cdot 10^6$ km, u orbiti oko Sunca.

1.2 Astronomija visokoenergijskih γ-zraka

Astronomija visokoenergijskih γ-zraka je istraživanje neba u području γ-zraka visokih energija. To je opservacijska znanost i trenutno jedno od najaktivnijih područja fizike astročestica [329]. Dva su glavna područja astronomije visokoenergijskih γ-zraka: visokoenergijska astrofizika i opservacijska kozmologija [472].

Visokoenergijska astrofizika bavi se najenergetskijim i najsilovitijim procesima u svemiru, posebice njihovom netermičkom prirodom. Neki od galaktičkih $\gamma-$izvora visokih energija (HE) i vrlo visokih energija (VHE) su: pulsari, ostatci supernova i mikrokvazari. Primjeri izvangalaktičkih $\gamma-$izvora su: aktivne galaktičke jezgre (AGN), provale $\gamma-$zraka (GRB), radiogalaksije, zvjezdorodne galaksije i grozdovi galaksija.

Opservacijska kozmologija istražuje nastanak kozmičkih struktura, između ostalog preko izvangalaktičke pozadinske svjetlosti (EBL). Drugi važni kozmološki vid astronomije visokoenergijskih γ-zraka je posredno traženje tamne tvari (DM) kroz opažanje anihilacijskog zračenja najlakše supersimetrične (SUSY) čestice zvane neutralino.

1.3 Kozmički visokoenergijski γ-izvori

Kozmički visokoenergijski γ-izvori (u energijskom području od par desetaka GeV do par desetaka TeV) su galaktičkog i izvangalaktičkog podrijetla. Svi izvangalaktički izvori su točkasti, dok galaktički mogu biti točkasti, prošireni i difuzni. Prvi visokoenergijski γ-izvor uopće (Rakovica) otkriven je Čerenkovljevim teleskopom Whipple 1989. godine [486]. Danas je poznato oko stotinu kozmičkih γ-izvora (slika 1.5).

Rakovica (poznata i kao M1) ostatak je supernove čiju su eksploziju zabilježili kineski astronomi 1954. godine (slika 1.6). Leži u zviježđu Bik na udaljenosti od oko 6500 svjetlosnih godina (približno 2 kiloparseka). U središtu maglice nalazi se pulsar perioda 33.3 ms koji usporava 36.4 ns na dan. Zbog takvog usporavanja vrtnje pulsar ima luminozitet $L = 5 \cdot 10^{38}$ erg s^{-1} i uzrokuje neprestano sinkrotronsko zračenje okolnog medija. Ubrzani elektroni inverznim Comptonovim procesom iz sinkrotronskog zračenja stvaraju visokoenergijske γ-zrake [60]. Zbog stabilnog i relativno visokog toka visokoenergijskih γ-zraka u području TeV, Rakovica je standardna svijeća zemaljske γ-astronomije. Svaki Čerenkovljev teleskop dio svojih opažanja posvećuje Rakovici [266].

Galaktička ravnina i posebice **galaktičko središte** snažni su izvori γ-zraka. Galaktička ravnina zamišljeni je krug na nebu koji nastaje zbog najgušće koncentracija zvijezda u galaksiji. Galaktičko središte je središnji dio naše vlastite galaksije koji se sa Zemlje vidi u smjeru zviježđa Strijelac. Samo je središte zasjenjeno plinom i prašinom pa nije vidljivo optičkim teleskopima. To, međutim, ne vrijedi za γ-astronomiju. Prva γ-opažanja galaktičke ravnine provela je HEGRA 1997. i 1998. godine bez pozitivnih rezultata [27]. 2004. godine HESS je proveo detaljniji pregled galaktičke ravnine sa znatno boljom osjetljivošću te pronašao osam prethodno nepoznatih izvora γ-zraka u području TeV [35]. Kasnije je HESS otkrio još izvora u galaktičkoj ravnini, zasad nepoznate prirode [47].

Ostaci supernova važni su galaktički izvori γ-zraka (ujedno i izvori galaktičkih kozmičkih zraka tj. nabijenih čestica). Postoje dvije vrste ostataka supernova: plerioni i ljuskasti tip. Plerioni su rjeđi. Poznati primjeri su Rakovica i Jedra. Ljuskasti tip ostataka supernova izvor je γ-zraka u nižem području (ispod TeV) [483]. Primjeri su SN1006, Kasiopeja A (koja je ujedno najjači radioizvor na nebu) te RXJ1713 [471].

Pulsari su prvi astrofizički izvori γ-zraka koji su otkriveni (detektorima na satelitima u području MeV i GeV). Pulsar je brzorotirajuća neutronska zvijezda, kompaktni kozmički objekt (tablica 2.1), teorijski predviđen još 1934. godine. Prvi je pulsar otkriven 1967. godine, a danas ih je poznato preko 650 u našoj galaksiji. Tipični parametri pulsara su $M = 1.4\ M_\odot$, $R = 10$ km i $B = 10^{12}$ gauss [483]. Većina ih je nastala implozijom središta pri eksploziji supernove. Pulsari su izvori sinkrotronskog zračenja (poznatog i kao magneto-bremsstrahlung) čiji se kontinuirani spektar jako razlikuje od spektra crnog tijela te se proteže od radiovalova do γ-zraka. Sinkrotronsko zračenje emitiraju relativističke nabijene čestice (većinom elektroni) koje se gibaju u snažnom magnetskom polju. Neki su pulsari izvori iznimno snažnih magnetskih polja, najjačih ikad izmjerenih, više od 10^8 T [299]. Takvi se pulsari zovu magnetari.

Mikrokvazari su iznimno zanimljivi galaktički izvori γ-zraka, otkriveni 1994. godine. Mikrokvazari su dvojni sustavi koji se sastoje od jednog kompaktnog objekta (neutronske zvijezde ili crne rupe) te pratitelja koji je izvor akrecijskog materijala (npr. zvijezda u fazi crvenog diva). Kao i kod kvazara (i općenito kod aktivnih galaktičkih jezgara), okomito na ravninu akrecijskog diska izlaze, u suprotnim smjerovima, dva relativistička mlaza. Mikrokvazari su stoga umanjene verzije kvazara te su, zbog relativne blizine, iznimno važni za razumijevanje aktivnih galaktičkih jezgara. Neki su od poznatih mikrokvaza-

ra: GRS 1915+105 (čiji mlazovi imaju $\beta = 0.98$ [483]), Labud X-3 i SS433. Kad je SS433 prvi put opažen (prije 25 godina) slovio je kao najneobičniji objekt na nebu [164]. Mehanička snaga njegovih mlazova dostatna je za stvaranje ukupnog galaktičkog toka kozmičkih zraka [4]. Nedavno je teleskopom MAGIC otkriven mikrokvazar LS I +61 303 koji emitira γ-zrake periodički. Period od 26 dana odgova orbitalnom gibanju dvojnog sustava [64].

Provale γ-zraka (GRB) su iznenadne snažne emisije γ-zraka izvangalaktičkog podrijetla. Otkrivene su 1967. godine i punih su trideset godina bile jedna od najvećih zagonetki astrofizike. Mnogi su teorijski modeli predvidjeli perzistenciju – iščezavajuću emisiju na većim valnim duljinama (u X-području, ultraljubičastom, optičkom i infracrvenom području te u području radiovalova) koja se javlja nakon provale γ-zraka. Perzistencija (engl. afterglow) je otkrivena tek 1997. godine u X-području satelitom BeppoSAX. Tada su dugotrajne provale γ-zračenja neupitno povezane s implozijama središta velikih supernova na kozmološkim udaljenostima [382]. Nedavno je otkriveno da kratkotrajne provale γ-zračenja većinom nastaju kao rezultat stapanja dvojnih sustava kompatknih objekata (neutronskih zvijezda ili crnih rupa) [212] [422] [386]. Energijski spektar provala γ-zraka uglavnom je u području MeV do GeV. Vjeruje se da bi se spektar mogao protezati i do par desetaka GeV. U tom bi slučaju provale γ-zraka bile opazive i Čerenkovljevim teleskopima niskog energijskog praga. Predviđa se da bi teleskop MAGIC mogao opažati u prosjeku jednu provalu γ-zraka godišnje [68]. U 2005. godini teleskop MAGIC reagirao je na dojavu provale γ-zraka GRB050713a te proveo prvo opažanje u visokoenergijskom γ-području. Međutim, γ-signal nije opažen [68].

Zvjezdorodne galaksije su nepravilne galaksije u čijim se većim područjima rađaju nove zvijezde. Po vrsti galaksija, one su između normalnih galaksija (npr. Mliječni put ili Andromedina galaksija) i aktivnih galaksija (npr. Markarian 421) Zvjezdorodne galaksije (npr. NGC 253) i općenito sva područja u kojima nastaju nove zvijezde, očekivani su izvori visokoenergijskih γ-zraka.

Aktivne galaktičke jezgre (AGN) glavni su izvangalaktični izvori visokoenergijskih γ-zraka [483]. AGN je općeniti pojam kojim se označuje postojanje fenomena iznimne snage u središnjim područjima pojedinih galaksija. AGN su vrlo kompaktni objekti čiji je luminozitet 10.000 puta veći od okolne galaksije. Procesi u kojima nastaje takva ogromna količina energije očito su različiti od procesa u normalnim zvijezdama. Pretpostavka da je svaka aktivna galaktička jezgra pogonjena supermasivnom crnom rupam, koja se nalazi u njezinom središtu, danas je općeprihvaćena [489]. Slika 1.7 prikazuje ključne elemente jedne aktivne galaktičke jezgre: supermasivnu crnu rupu, akrecijski disk, zasjenjujući torus, dva relativistička mlaza i područja snažne radioemisije. Prema ujedinjavajućem modelu aktivnih galaktičkih jezgara, klasifikacija proizlazi iz kuta pod kojim se sa Zemlje vide mlazovi ili ravnina torusa (slika 1.8). Tako su različite vrste aktivnih galaktičkih jezgara rezultat geometrije, a ne fizike [483].

Egzotični izvori izuzetno su zanimljiva mogućnost nastanka visokoenergijskih γ-zraka. Umjesto scenarija "odozdo-gore" u kojem visokoenergijske čestice nastaju kao rezultat ubrzavanja nabijenih čestica, moguć je i scenarij "odozgo-dolje" u kojem visokoenergijske čestice nastaju raspadom iznimno teških, egzotičnih čestica koje su izvan Standardnog modela. Takve bi čestice mogle biti ostaci Velikog praska kao npr. topološki defekti (magnetski monopoli, kozmičke strune, domenski zidovi ili kozmičke teksture) ili hladna tamna tvar. Dok su topološki defekti još uvijek samo hipoteza, postojanje je tamne tvari pouzdano utvrđeno [192] [167] [137]. Tipični kandidati za nebarionsku tamnu tvar su aksioni i slabo međudjelujuće masivne čestice (WIMP). Barionsku tamnu tvar mogli

bi sačinjavati masivni kompaktni halo-objekti (MACHO). Svi su oni, u principu, opazivi sa sadašnjom tehnologijom ili tehnologijom bliske budućnosti. MACHO su masivni tamni objekti poput smeđih patuljaka. Crne rupe također bi mogle biti MACHO-objekti, osobito praiskonske crne rupe. Masa WIMP-čestica teorijski je predviđena u intervalu između 10 GeV i nekoliko desetaka TeV [192]. To je upravo područje osjetljivosti Čerenkovljevih teleskopa. Najbolji kandidat za WIMP-česticu je najlakša supersimetrična (SUSY) čestica – neutralino [384]. WIMP bi se mogao opaziti posredno kroz anihilaciju pri kojoj nastaju dvije γ-zrake. U tom bi smislu satelit GLAST [474] ili Čerenkovljevi teleskopi (MAGIC ili HESS) [192] bili pogodni za testiranje supersimetričnih modela.

1.4 Blazari

Blazar je aktivna galaktička jezgra (AGN) koju karakterizira vremenski vrlo promjenljivo netermičko zračenje iz relativističkih mlazova od kojih je jedan usmjeren prema Zemlji (slika 1.7). Mlaz je uski snop plazme i zračenja koji se giba od središnje crne rupe relativističkom brzinom, a može se protezati stotinama kiloparseka. Izraz *blazar* skovao je 1978. godine astronom Ed Spiegel kako bi označio kombinaciju objekata: **BL** Lac i kv**azar**. BL Lac je izvangalaktički objekt, jako promjenljiva aktivna galaktička jezgra. Prototip je originalno klasificiran kao pekulijarna promjenljiva zvijezda, kojoj je dodjeljena dvoslovna oznaka **BL**, u zvježđu Gušterica (Lacreta, skraćeno **Lac**). BL Lac objekti uključuju *low-frequency peaked BL Lac* (LBL) i *high-frequency peaked BL Lac* (HBL). HBL emitiraju γ-zrake u području TeV (spektar im se proteže i do 20 TeV). Do sada je poznato 13 izvangalaktičkih γ-izvora u području TeV (tablica 1.4). Svi su ti izvori tipa HBL, s izuzetkom M87, aktivne galaktičke jezgre tipa *Fanaroff-Riley I* (FRI). Smatra se da γ-zrake iz M87 nastaju inverznim Comptonovim procesom, kao u blazara, ali mlaz nije usmjeren točno prema Zemlji. Prema tome, M87 je "pomaknuti" blazar [178].

1.5 Pljuskovi čestica u atmosferi

Pljusak čestica u atmosferi (EAS) potaknut je pojedinačnom kozmičkom zrakom (nabijenom česticom) ili kozmičkom γ-zrakom koja ima dovoljno veliku energiju da je njezinu kaskadu (sekundarne nabijene čestice i fotone) moguće detektirati na tlu. Primarna visokoenergijska kozmička čestica, koja pogađa gornji sloj atmosfere, međudjeluje s jednom molekulom zraka na visini između 10 i 15 km [373]. U takvim sudarima nastaje mnoštvo novih čestica koje se gibaju kroz atmosferu prema tlu. Ako je primarna čestica hadron (proton ili jezgra) tada su sekundarne čestice većinom pioni (oko 90 %), ali također i kaoni, anti-protoni te dijelovi jezgara. Nabijeni pioni raspadaju se na mione (te stvaraju atmosferske neutrine) dok se neutralni pioni raspadaju na dva fotona koji induciraju nove electromagnetske pljuskove. Slike 1.11 i 1.12 prikazuju razvoj pljuska sekundarnih čestica u atmosferi.

Primarna kozmička γ-zraka započinje pljusak tvorbom para elektron-pozitron (u polju jezgre). Visokoenergijski elektroni i pozitroni ($E > 10$ GeV) gube energiju zakočnim zračenjem (bremsstrahlung) i tako stvaraju nove visokoenergijske fotone odnosno sekundarne $\gamma-$zrake. Sekundarni fotoni mogu ponovo stvarati parove elektron-pozitron i tako se razvija elektromagnetski pljusak čija veličina ovisi o energiji primarne γ-zrake.

1.6 Atmosfera kao ogromni kalorimetar

Za opažanje visokoenergijskih čestica potreban je kalorimetrijski princip [329]. Prirodni kalorimetar za kozmičke visokoenergijske čestice je *atmosfera*. Dok je za većinu astronoma atmosfera samo problematični filter koji otežava opažanja, za astronome koji opažaju

$\gamma-$zrake s površine Zemlje atmosfera je prijeko potreban dio detektora [483].

Izraz *ekstinkcija* znači smanjivanje intenziteta svjetlosti s nebeskog tijela pri prolasku kroz atmosferu. Ekstinkcija nastaje zbog atenuacije (apsorpcije i raspršenja) u atmosferi i proporcionalna je zračnoj masi i atmosferskom tlaku. Glavni uzrok ekstinkciji je raspršenje, a najkritičnije je Mievo raspršenje (ili raspršenje na aerosolima i oblacima). Ono može biti vrlo promjenljivo, čak na vremenskoj skali manjoj od sata [323]. Slika 1.13 prikazije ekstinkcijsku krivulju $\mathcal{A}_{\rm total}$ za nebo iznad opservatorija Roque de los Muchachos (ORM) na La Palmi [290]. Ekstinkcija je izražena u magnitudama po zračnoj masi, jedinici uobičajenoj u optičkoj astronomiji. Zračna masa (engl. *airmass*) je relativna debljina atmosfere kroz koju prolazi zvjezdana svjetlost. Na primjer, $airmass = 1$ u zenitu ($ZA = 0^{\rm o}$), a $airmass \approx 2$ za $ZA = 60^{\rm o}$ [407]. Magnituda (ili zvjezdana veličina) mjera je sjajnosti nebeskog objekta. Apsolutna magnituda M je vlastiti sjaj, a prividna magnituda m je sjaj kakav se vidi sa Zemlje. Prividna magnituda ovisi o apsolutnoj, ali i o udaljenosti objekta od Zemlje. Neki optički teleskopi redovito mjere pojednine zvijezde poznatog sjaja i na taj način prate promjenljivu atmosfersku transparentnost (VAT). Opservatorij HEGRA koristio je takva opažanja teleskopom Carlsberg Meridian Telescope (CMT). Tipična vrijednost ekstinkcije u području r' za La Palmu iznosi 0.09 mag. Glavni nedostatak primjene ekstinkcijskih koeficijenata za praćenje atmosferske transparentnosti je taj što se raspoložive vrijednosti odnose na cijelu noć, odnosno predstavljaju prosječne vrijednosti. Za Čerenkovljeve teleskope bili bi idealni ektinkcijski koeficijenti mjereni na vremenskoj skali jednog opažanja (npr. 20 minuta). Drugi mogući način da se uzmu u obzir karakteristike atmosfere je daljinsko ispitivanje (meteorološkim balonima ili aktivnim uređajima smještenim na tlu – radarima i lidarima). Radarima se mogu opažati veće čestice, npr. kapljice kiše, dok su lidari osjetljiviji na manje čestice, npr. kapljice vode od kojih se sastoje oblaci. Lidar (*Light detection and ranging*) radi na istom principu kao i radar. Sastoji se od lasera i malog teleskopa za detekciju raspršene svjetlosti. Tipična valna duljina lidara je nekoliko stotina nanometara (npr. 532 nm), dok radar ima tipičnu valnu duljinu od nekoliko centimetara. Lidari mogu mjeriti gustoću atmosfere po visini pa čak i koncentraciju aerosoli kao funciju visine [80]. Također mogu detektirati udaljene tanke oblake [425]. Kombinacijom lidara i radara mogu se dobiti pouzdane procjene granica oblaka pri čemu radar određuje gornju, a lidar donju granicu [467].

Detaljno poznavanje svojstava atmosfere važno je za simulacije razvoja pljuskova sekundarnih čestica u atmosferi izazvanih upadom visokoenergijske kozmičke γ-zrake.

2. Aktivna galaktička jezgra Markarian 421

2.1 Uvod

Markarian 421 (Mkn 421) velika je eliptična galaksija koja sadrži aktivnu galaktičku jezgru, blazar tipa HBL. Slika 2.1 prikazuje položaj Mkn 421 na nebu, odnosno njegove nebeske koordinate: rektascenziju (RA or α) i deklinaciju (DEC or δ).

Mkn 421 jedan je od Zemlji najbližih blazara i najbliži blazar opažen u TeV-području te ujedno jedan od najsjajnijih kvazara na nebu. S obzirom na prosječnu magnitudu od 13.3, vidljiv je i boljim amaterskim teleskopom. Kozmološki crveni pomak Markariana 421 je $z = 0.031$ iz čega proizlazi brzina udaljavanja od 9000 km/s odnosno udaljenost od 130 Mpc (ili 420 milijuna svjetlosnih godina).

2.2 Fizika Markariana 421

Luminozitet L (energija oslobođena u jedinici vremena, odnosno snaga) unutrašnje je svojstvo svakog astrofizičkog izvora. Luminozitet Sunca je $L_\odot = 3.826 \cdot 10^{33}$ erg/s, gdje je 1 erg = 0.1 μJ. Normalne galaksije poput našeg Mliječnog puta imaju L približno 10^{43} erg/s, odnosno 10^9 $L_\odot$. No, luminozitet aktivnih galaktičkih jezgara (posebice nekih kvazara) kreće se od 10^{45} do više od 10^{48} erg/s. Tako su kvazari 100.000 puta snažniji izvori od normalnih galaksija ili čak milijardu puta snažniji od Rakovice. Što je izvor takve izuzetne snage? Može li se on objasniti u okvirima poznate fizike?

Većina astrofizičara danas vjeruje da se na ta pitanja može odgovoriti u okviru modela međudjelovanja crne rupe i okolne tvari [114]. Općeprihvaćeno je vjerovanje da su aktivne galaktičke jezgre pogonjene akrecijom tvari na supermasivnu crnu rupu [126], kao što se normalne zvijezde pogone nuklearnom fuzijom.

Postoje snažni dokazi da se supermasivne crne rupe nalaze u središtima većina, vjerojatno svih, spiralnih i eliptičnih galaksija [155]. Postojanje supermasivne crne rupe u središtu naše vlastite galaksije danas je potvrđeno izvan svake sumnje [114].

Akrecija na supermasivnu crnu rupu najefikasniji je poznati energijski izvor: oko 10% mase koja pada prema crnoj rupi može se pretvoriti u energiju (za usporedbu, samo 0.7% mase pretvara se u energiju kod nuklearne fisije). Kod maksimalno rotirajuće crne rupe efikasnost se penje na čak 42%! Većina energije oslobađa se u obliku relativističkih mlazova.

Crna je rupa kompaktni astrofizički objekt čije je gravitacijsko polje toliko jako da potpuno zakrivi prostor-vrijeme, tako da ni svjetlost ne može pobjeći [234]. Danas postoji oko 20 potvrđenih kandidata za crne rupe u području masa 5–20 $M_\odot$ (rendgenski dvojni sustavi) te oko 30 kandidata za supermasivne crne rupe u području masa 10^6–$10^{9.5}$ $M_\odot$ (u galaktičkim središtima) [126].

Kad neka tvar, npr. međuzvjezdani oblak plina, prolazi dovoljno blizu crne rupe, ona počinje kružiti oko crne rupe i tako stvara akrecijski disk. Unutrašnje orbite rotiraju brže od vanjskih pa postoji trenje odnosno brojni međusobni sudari. Mnoštvo čestica pri tome biva izbačeno u suprotnom smjeru od središta crne rupe. Zbog debelog akrecijskog diska, čestice koje su izbačene pod pravim kutom u odnosu na ravninu akrecijskog diska mogu lakše napustiti područje crne rupe. Kao rezultat toga, nastaju dva relativistička mlaza (uska snopa tvari i zračenja) koji se šire u suprotnim smjerovima kao što prikazuje slika 1.7. U slučaju blazara (npr. Markariana 421), jedan od mlazova usmjeren je prema Zemlji. Mlazovi su najznačajnije obilježje supermasivnih crnih rupa u aktivnim galaktičkim jezgrama.

Spektar γ-zraka iz aktivnih galaktičkih jezgara jasno se razlikuje od spektra običnih zvijezda (spektra crnog tijela) [155]. Blazare, poput Markarijana 421, karakterizira snažno polarizirano zračenje čiji spektar opada eksponencijalno, a proteže se od radiovalova do visokoenergijskih γ-zraka. Slika 2.4 prikazuje teorijski primjer spektra blazara Mkn 421, a slika 2.5 daje primjer stvarnih podataka.

Spektar γ-zraka blazara može biti rezultat različitih astrofizičkih procesa [483]. Modeli koji se temelje na ubrzavanju nabijenih čestica mogu se podijeliti na *hadronske* i *leptonske* (slika 2.6). Hadronski (ili protonski) modeli emisije visokoenergijskih γ-zraka u mlazovima blazara zahtijevaju ubrzavanje protona do energija od čak 10^{20} eV. U protivnom, protoni ne bi mogli s dovoljnom efikasnošću stvarati γ-zrake u mlazovima blazara [4]. Hadronski modeli motivirani su željom da objasne oboje: stvaranje visokoenergijskih γ-zraka u aktivnim galaktičkim jezgrama i podrijetlo kozmičkih zraka najviših energija (UHECR) [483]. Hadronski modeli, s druge strane, zapadaju u teškoće kad trebaju objasniti kratke

promjene intenztiteta (od sat vremena ili manje) emisije u blazara. Tako, opažanja kratkotrajnih varijacija favoriziraju leptonske modele. U leptonskim (ili elektronskim) modelima γ-zrake nastaju u interakcijama visokoenergijskih elektrona s fotonima niže energije. Leptonski modeli podrazumijevaju da X-zračenje i visokoenergijske $\gamma-$zrake nastaju u relativističkim mlazovima blazara u sinkrotronskom i inverznom Comptonovom procesu.

2.3 Prethodna opažanja Markariana 421 u području energija TeV

Mkn 421 otkriven je kao prvi izvangalaktički visokoenergijski izvor $\gamma-$zraka 1992. godine teleskopom Whipple [396]. Iste je godine s opažanjima počeo i CT1, prvi Čerenkovljev teleskop kolaboracije HEGRA. Nakon početnih opažanja Rakovice, CT1 je bio posvećen opažanjima blazara Mkn 421 od 1994. godine [385].

Brza vremenska promjenljivost emisije γ-zraka svojstvena je aktivnim galaktičkim jezgrama [114]. Objekte BL Lac karakterizira iznimna varijabilost na vremenskoj skali od par minuta do nekoliko godina [483]. Godine 1994., prvi je put jasno opažena pojava bljeskova (nagle i intenzivne promjene emisije) blazara Mkn 421. U tim opažanjima, teleskopom Whipple, uočena je promjena toka za red veličine [216]: od 0.15 crab do 1.5 crab, gdje je 1 crab $= 1.75 \cdot 10^{-11}$ cm^{-2}s^{-1}. Mkn 421 bio je iznimno aktivan tjekom tri mjeseca 2001. godine [483]. Dio podataka iz tog perioda, prikupljenih Čerenkovljevim teleskopom CT1, analizirali smo u ovom radu. Promjenljivost emisije blazara Mkn 421 prisutna je na svim valnim duljinama, od radiovalova do $\gamma-$zraka. U $\gamma-$području opažena je vrlo brza promjenljivost, od svega 15 minuta. Iz takve brze promjenljivosti može se zaključiti da je emisijsko područje mnogo manje od veličine galaksije. Na primjer, varijacija u luminozitetu koja je kraća od jedan sat pokazuje da je emisijsko područje manje od jednog svjetlosnog sata (što je približno udaljenost Saturna od Sunca).

Jedno od prvih viševalnih opažanja, organizirano 1995. godine, imalo je za cilj blazar Mkn 421. Tada je prvi put utvrđena korelacija između X-zračenja i visokoenergijskih γ-zraka [483]. Prva jasna potvrda da je X-zračenje iz Mkn 421 dobro korelirano s $\gamma-$zrakama u području TeV, na vremenskoj skali od jednog sata, objavljeno je 1999. godine [339].

Cilj je ovog rada proučiti korelacije u optičkom, X$-$ i $\gamma-$području za sve dostupne podatke, uključivši nedavna opažanja opservatorija MAGIC i satelita RXTE. Istraživali smo uglavnom najbliže blazare Mkn 421 i Mkn 501, ali i nedavno otkriveni (u $\gamma-$području) blazar Mkn 180. Kao što je prikazano u odlomku 6.2, primjenjujući našu **novu metodu** za istraživanje korelacija pronašli smo da su, u nekim slučajevima, korelacije X/γ toliko jake koliko bismo očekivali u savršeno koreliranom slučaju. Naši rezultati potvrđuju da su emisije u X$-$ i $\gamma-$području blisko povezane odnosno da je SCC (Synchrotron Self-Compton) glavni emisijski model za objekte tipa BL Lac. Do sada, nisu bile opažane korelacije optičke emisije blazara s emisijom u $\gamma-$području [483]. Vrlo nedavno, našli smo, po prvi put uopće, γ/optičke i X/optičke korelacije u podatcima CT1/KVA iz 2003. godine. Također, detaljnom korelacijskom studijom pronašli smo kašnjenje (od oko jedan dan) vremenskih promjena optičke krivulje sjaja u odnosu na promjene u X- i γ-području. To bi moglo biti izuzetno važno za razumijevanje detalja mehanizma emisije u mlazovima blazara.

3. Opažanja Markariana 421

3.1 Opis detektora

Čerenkovljev teleskop 1 (CT1) bio je samostalni Čerenkovljev atmosferski *imaging*-teleskop (IACT) smješten na opservatoriju Roque de los Muchachos (ORM) na kanarskom otoku La Palmi u Španjolskoj (28°45'30" sjeverno, 17°52'48" zapadno, 2200 m nad morem). Taj je opservatorij jedno od ponajboljih mjesta na svijetu za astronomska opažanja. CT1 bio je dio eksperimenta *High Energy Gamma Ray Astronomy* (HEGRA), prethodnik današnjeg projekta *Major Atmospheric Gamma-ray Imaging Čerenkov detector* (MAGIC). Imao je ekvatorijalnu montažu i pozicijsku točnost bolju od 0.1°. CT1 je počeo s opažanjima 1992., a završio 2003. godine.

Reflektor teleskopa bio je sfernog oblika (Davis-Cotton) koji na najmanju mjeru svodi sferne aberacije. Slika 3.2 prikazuje geometriju reflektora teleskopa CT1 sastavljenog od 33 aluminijska zrcala. Promjer reflektora bio je 3.6 m, a njegova ukupna površina 10 m^2.

Kamera teleskopa CT1 sastojala se od 127 fotomultiplikatora smještenih u heksagonalne prstene, ukupnog promjera 273 mm (slika 3.4). Korišteni su fotomultiplikatori s bialkalnom fotokatodom osjetljivi u području od 300 do 600 nm, kvantne efikasnosti do 25%. Ispred svakog fotomultiplikatora korišten je Winstonov konus kako bi se smanjila neosjetljiva površina (slika 3.3). Kutna širina pojedinog piksela bila je 0.24°, a ukupno vidno polje kamere 3.12°.

Triger teleskopa zahtijevao je dva susjedna piksela iznad praga (50 mV, odnosno oko 13 fotoelektrona) unutar 13 ns. Učestalost trigera za kozmičke zrake u zenitu bila je 3.5 Hz. Energijski prag teleskopa CT1 za kozmičke γ-zrake u zenitu iznosio je oko 700 GeV. Tako se energijsko područje dostupno teleskopu protezalo od 700 GeV do približno 20 TeV.

RXTE (Rossi X-ray Timing Explorer) je NASA-in satelit za opažanje X-zračenja namijenjen istraživanju promjenljivih izvora. Lansiran je u prosincu 1995. godine i do danas radi iznimno uspješno. Satelit nosi tri instrumenta:

• PCA (Proportional Counter Array) niz je od pet proporcionalnih plinskih brojača ukupne detekcijske površine od 6500 cm^2. PCA je osjetljiv u energijskom području od 2–60 keV. Energijsko razlučivanje mu je 18% (pri 6 keV), a vremensko 1 μs.

• ASM (All Sky Monitor) sastoji se od tri širokokutne kamere, s proporcionalnim brojačima, ukupne površine 90 cm^2. ASM motri oko 80% neba u svakom orbitalnom periodu (za kružnu orbitu na visini od 580 km, odgovarajući orbitalni period je 96 minuta) u energijskom području 2–12 keV.

• HEXTE (High Energy X-ray Timing Experiment) se sastoji od dva grozda od po četiri scintilatora NaI/CsI i pokriva energijsko područje od 15 do 250 keV. Svaki grozd ima detekcijsku površinu 800 cm^2 i energijsko razlučivanje 15% (pri 60 keV).

U tezi smo koristili samo podatke prikupljene detektorom ASM.

Slika 3.6 prikazuje optički teleskop *Kungliga Vetenskaps Akademien* (KVA) smješten na opservatoriju *Roque de los Muchachos* (ORM) na kanarskom otoku La Palma na nadmorskoj visini od 2200 m. Od jeseni 2003. godine, teleskopom se upravlja automatski iz opservatorija Tuorla u Finskoj. KVA je Cassegrainov teleskop aperture 60 cm i ekvatorske montaže. Teleskop je posvećen dugotrajnim fotometrijskim opažanjima blazara u bliskoj suradnji s projektom MAGIC. KVA je opremljen CCD kamerom tipa Santa Barbara ST-1001E i standardnim filtrom Johnson-Cousins R.

3.2 Opažanja blazara Mkn 421

Emisijski se mehanizam blazara najbolje može razumjeti iz kombiniranih opažanja unutar cijelog elektromagnetskog spektra [483]. Istovremena opažanja pri kojima nekoliko teleskopa prati isti objekt na različitim valnim duljinama zovu se viševalne kampanje. Takve se kampanje za Mkn 421 provode godinama. Jedna od prvih bila je organizirana još

1995. godine [483]. Najvažniji rezultat viševalnih kampanja je jasna potvrda korelacija između toka X-zračenja i toka γ-zraka u području TeV. U ovoj smo tezi analizirali opažanja teleskopom CT1 blazara Mkn 421 iz 2001. godine (kad je izvor bio u aktivnoj fazi) te iz 2003. godine (kad je izvor bio u tihoj fazi). Podatke iz 2001. godine analizirala je i objavila kolaboracija HEGRA [31], osim jednog dijela podataka koji je izostavljen zbog slabije atmosferske transparentnosti. Ti su podatci prvi put analizirani u ovom radu i korigirani za promjenljivu atmosfersku transparentnost (VAT). Podatci iz 2003. godine naša su vlastita opažanja provedena u periodu od 25. veljače do 6. ožujka 2003. godine. Dio su viševalne kampanje u kojoj su sudjelovali HEGRA-in Čerenkovljev teleskop CT1, optički teleskop KVA te satelit RXTE za detekciju kozmičkog X-zračenja. Premda je izvor bio u tihoj fazi, uočene su korelacije X/γ te po prvi put uopće korelacije optičkih podataka s X- i $\gamma-$podatcima. Ovi se podatci intenzivno analiziraju i uskoro će biti objavljeni.

4. Pljuskovi čestica u atmosferi

4.1 Atmosfera

Atmosfera je sastavni dio svakog Čerenkovljevog *imaging*-teleskopa pa odaziv teleskopa stoga ovisi o nepredvidljivim atmosferskim promjenama [310]. S obzirom da za Čerenkovljeve teleskope ne postoji test-snop, kalibracija počiva u potpunosti na simulacijama *Monte Carlo* (MC). Simulacije MC obično se satoje iz dva dijela:

• simulacije pljuskova čestica u atmosferi izazvanih upadom kozmičke zrake (nabijene čestice), kozmičke γ-zrake ili kozmičkog neutrina; te

• simulacije detektora.

Prvi je dio simulacija zajednički svim eksperimentima iz γ-astronomije, neutrinske astronomije te iz područja istraživanja kozmičkih zraka. Drugi je pak dio specifičan za svaki pojedini eksperiment. U ovoj smo tezi uveli još i simulacije *promjenljive atmosferske transparentnosti* (VAT) – posebni dio simulacija MC koje se odnose na loše vremenske uvjete. Kako bi razvili simulacije VAT, morali smo detaljno proučiti fiziku atmosfere te naročito oblake.

Atmosfera je tanki plinoviti omotač koji okružuje planet Zemlju. Sastoji se od dušika (N_2, $\sim$78%), kisika (O_2, $\sim$21%), argona (Ar, $< 1\%$) te drugih plinova u tragovima: ugljikovog dioksida (CO_2, $\sim$0.03%), vodene pare (H_2O, 0–4%) i ozona (O_3, 0–0.0012%). Premda vodena para i ozon čine tek manji dio atmosfere, imaju važnu ulogu u atmosferskoj tranparentnosti. Uobičajeno, atmosfera se dijeli na slojeve (u okomitom smjeru) prema promjeni temperature s visinom. Slika 4.1 poazuje uobičajenu podjelu. Najniži je dio *troposfera* koja sadrži 75% ukupne mase zraka i proteže se do visine od oko 20 km. Temperatura troposfere opada linearno s visinom ($\mathrm{d}T/\mathrm{d}h \approx -6.5$ K/km) sve do tropopauze ($\mathrm{d}T/\mathrm{d}h \approx 0$). Idući je sloj *stratosfera* koja sadrži oko 24% ukupne mase zraka i proteže se od 20 do 50 km nadmorske visine. Stratosfera sadrži ozonski omotač čija je koncentracija u ovisnosti o visini prikazana na slici 4.19. Temperatura stratosfere raste s visinom. Sloj atmosfere na visini od 50 do 90 km zove se *mezosfera*, a iza nje se proteže *termosfera* do visine od čak 600 km. Termosfera je područje vrlo rijetkog zraka i velikih temperaturnih fluktuacija. Konačno, *egzosfera*, iznad 600 km, sadrži tek poneku molekulu. To je područje u kojem su smješteni umjetni sateliti. Za vrh atmosfere (TOA) uzima se, u praksi, 1000 km. Većina pljuskova četica u atmosferi, potaknutih upadom kozmičkih zraka, započinje i proteže se u najnižem sloju - troposferi. Poneki pljusak započinje i u

stratosferi, no većina Čerenkovljeve svjetlosti nastaje u troposferi. Također, (praktički) svi oblaci leže u troposferi.

Atmosfera je prevelika i presložena da bismo je mogli u potpunosti opisati. Umjesto toga, koriste se približni modeli. Najčešće korišteni model atmosfere je *U.S. Standard Atmosphere 1976*. Standardna je atmosfera hipotetska okomita raspodjela temperature, tlaka i gustoće koja grubo odgovara godišnjim prosječnim vrijednostima. Slike 4.1, 4.2 and 4.3 prikazuju okomite raspodjele temperature, tlaka i gustoće za standardnu atmosferu. *U.S. Standard Atmosphere 1976* je idealizirani prikaz prosječnih godišnjih vrijednosti na sjevernoj zemljopisnoj širini od 45°. Koristili smo ovaj model u simulacijskom paketu CORSIKA za simulacije pljuskova čestica u atmosferi kao i programu Reflector za Rayleighjevo raspršenje. U principu, najbolje bi bilo koristiti dnevne lokalne atmosferske profile koji se mogu odrediti npr. korištenjem radiosondi na malim meteorološkim balonima.

4.2 Oblaci

Grubo govoreći, *oblaci su voda*. Oni nisu vodena para. Vodena je para jednako prozirna kao i suhi zrak. Ova je razlika ključna u kontekstu promjenljive atmosferske transparentnosti (VAT). Oblaci su vidljive nakupine malih kapljica tekuće vode ili kristalića leda. Nastaju kad se vodena para u zraku kondenzira u kapljice tekuće vode ili sublimira u kristaliće leda. Svaka je pojedina kapljica dovoljno lagana da lebdi u zraku.

U savršeno čistom zraku, približno 130 molekula H_2 trebalo bi se sudariti u istom trenutku kako bi nastala najmanja vodena kapljica. Vjerojatnost za takav događaj praktički je nula. Međutim, oblaci se ipak formiraju. Razlog je tome prljav zrak. Postoje male čestice u zraku zvane *aerosoli*. Mnoge od njih su higroskopne i djeluju kao kondenzacijska središta (CCN) pri formiranju sitnih kapljica vode. Drugim riječima, CCN su gradivni elementi oblaka [110]. Tri su glavne vrste kondenzacijskih središta oblaka:
(1) čestice soli iz oceana (veličine od 0.01 μm do 10 μm);
(2) sulfati koji nastaju izgaranjem ruda (veličine od par 0.1 μm);
(3) sitne čestice tla koje nosi vjetar (veličine manje od 10 μm).
Veličina vodenih kapljica u oblacima kreće se od 2 μm (u visokim rijetkim oblacima) pa do 200 μm (u debelim kišnim oblacima). Prosječni je promjer od 5 to 20 μm. Za usporedbu, kapljice kiše imaju promjer od 0.5 mm do 7 mm. Koncentracije kapljica vode u oblacima kreću se od 10 cm^{-3} to 1000 cm^{-3}. Tipična koncentracija je 200 cm^{-3} [110].

Oblaci se imenuju prema visini na kojoj se nalaze te prema izgledu. Prvi dio imena obično se odnosi na visinu, a drugi na izgled. Oblaci na velikim visinama imaju prefiks *ciro*. Cirusi su ledeni, paperjasti oblaci čupavog izgleda. Oblaci na srednjim visinama imaju prefiks *alto* dok niski oblaci nemaju prefiks. Dva su tipična izgleda oblaka: *kumulusi* and *stratusi*. Kumulusi su pojedinačni oblaci koji liče na cvjetače dok su stratusi slojeviti oblaci koji prekrivaju veći dio neba. Tablica 4.1 and slika 4.5 prikazuju uobičajenu klasifikaciju oblaka.

Opservatorij *Roque de los Muchachos* (ORM) na kanarskom otoku La Palma iznimno je dobro mjesto za astronomska opažanja [354]. Niski oblaci ostaju gotovo uvijek ispod planinskih vrhunaca (slika 4.6). S obzirom da su visoki oblaci, cirusi, tanki i raspršeni te da su uglavnom iznad visina na kojima nastaje većina Čerenkovljeve svjetlosti, nismo ih uključili u simulacije Monte Carlo. Tako su preostali samo oblaci na srednjim visinama od kojih su, po našem mišljenju, samo altostratusi vrijedni simulacija. Za ORM (s nadmorskom visinom 2200 m) niži altostratusi (od 2000 do 3000 m) mogu se tretirati kao magla, a za maglovitog vremena opažanja se ionako ne provode. Stoga smo za simulacije

uzimali u obzir samo altostratuse za koje je baza oblaka na visinama od 3000 do 7000 m. Za opservatorij na La Palmi koristili smo sljedeće parametre oblaka: srednja veličina vodenih kapljica 4.5 μm i koncentracija vodenih kapljica 450 cm^{-3}.

4.3 CORSIKA

COsmic Ray SImulations for KAscade (CORSIKA) je program za detaljne *simulacije Monte Carlo* razvoja pljuskova čestica čestica u atmosferi izazvanih upadom visokoenergijske kozmičke zrake [254]. Primarne čestice mogu biti protoni, lake jezgre do željeza, kozmičke γ-zrake te mnoge druge čestice. Sve se čestice u pljusku prate do raspada ili reakcije s drugim česticama. CORSIKA uzima u obzir sve postojeće znanje o jakim i elektromagnetskim međudjelovanjima. *Hadronska međudjelovanja na visokim energijama* opisuju se jednim od šest ponuđenih modela [251]: VENUS, QGSJET, DPMJET, SIBYLL, HDPM ili neXus. *Hadronska međudjelovanja na niskim energijama* opisuju se jednim od tri modela [251]: GHEISHA, FLUKA ili UrQMD. Za *elektromagnetska međudjelovanja* moguća su dva pristupa [253]: EGS4 ili NKG. U ovom smo radu koristili modele VENUS, GHEISHA and EGS4 u okviru kompilacije *MAGIC Monte Carlo software* (Mmcs). Mmcs je priredila i opisala Dorota Sobczyńska [441].

4.4 Čerenkovljeva svjetlost u atmosferi

Čerenkovljeva svjetlost je zračenje koje emitira dielektrični medij kad kroz njega prolazi nabijena čestica brzinom većom od brzine svjetlosti u mediju. Nabijena čestica u mediju uzrokuje preraspodjelu naboja odnosno polarizira medij. Pri malim brzinama čestice takva je polarizacija potpuno simetrična pa nema rezultantnog polja na velikim udaljenostima, odnosno nema zračenja. Giba li se nabijena čestica brzo (brže od svjetlosti u mediju) tada polarizacija više nije potpuno simetrična [282]. Rezultantno polje na velikim udaljenostima tada više nije nula, odnosno molekule medija uzrokuju emisiju Čerenkovljeve svjetlosti. Učinak, analogan udarnom valu u akustici, može se zorno prikazati Huygensovom konstrukcijm (slika 4.7). Čerenkovljev je uvjet dan izrazom (4.4). Tablica 4.2 prikazuje vrijednosti energije praga za tipične nabijene čestice u atmosferi. Kad je uvjet (4.4) zadovoljen, Čerenkovljeva se svjetlost emitira pod kutom ϑ u odnosu na smjer nabijene čestice. Iz geometrije na slici 4.7 slijedi $\cos\vartheta = \frac{1}{n\beta}$ Ovaj je izraz poznat kao *Čerenkovljeva relacija* i pokazuje nekoliko važnih činjenica [282]:

• Postoji granična brzina $v_{\min} = \frac{c}{n}$ ispod koje nema emisije Čerenkovljevog zračenja;
• Za ultrarelativističke čestice ($\beta \approx 1$) postoji najveći kut $\vartheta_{\max} = \cos^{-1}(\frac{1}{n})$;
• Zračenje nastaje uglavnom u vidljivom i ultraljubičastom području gdje je indeks loma $n > 1$. Emisija u X-području (gdje je $n < 1$) nije moguća.

Primjena Čerenkovljevog zračenja u eksperimentima fizike visokih energija počela je od 1951. godine kad je J.V. Jelley prvi put detektirao, s velikom učinkovitošću, pojedinačne brze nabijene čestice koristeći destiliranu vodu i fotomultiplikator [282]. Godine 1953. Jelley i Galbraith opazili su kratkotrajne, slabe bljeskove Čerenkovljeve svjetlosti na noćnom nebu. Zbog malog indeksa loma zraka ($n \approx 1.0003$ na nultoj nadmorskoj visini i $n \approx 1.0002$ na visini od 2200 m) Čerenkovljev je kut mali – oko 1^o (pa do 1.3^o na nivou mora). Stoga je Čerenkovljevljeva svjetlost jako usmjerena i pripadajući svjetlosni bazen na tlu ima polumjer od oko 130 m (slika 4.8).

Atenuacija Čerenkovljeve svjetlosti u atmosferi javlja se zbog apsorpcije i raspršenja. U valnom području od interesa (290 do 600 nm), važna je jedino apsorpcija na ozonu u ultraljubičastom području (do 360 nm). Raspršenje je proces u kojem sitne čestice raspršene u atmosferi raspršuju dio upadnog zračenja. Za Čerenkovljevu svjetlost u atmosferi važna

su dva procesa raspršenja: Rayleighjevo raspršenje na molekulama u atmosferi (dušiku i kisiku) te Mieovo raspršenje na aerosolima. Oba su procesa detaljnije opisana u odlomku 4.7.1. Vrste čestica koje uzrokuju raspršenje svjetlosti u atmosferi nabrojene su u tablici 4.3. U oblacima, dominantnu ulogu ima raspršenje.

4.5 Simulacije pljuskova čestica u atmosferi

Simulacije Monte Carlo pljuskova čestica u atmosferi zahtijevaju mnogo procesorskog vremena stoga ih je prikladno izvoditi u većim računalnim centrima [252]. Koristili smo računalni grozd Isabella u Sveučilišnom računskom centaru (SRCE) u Zagrebu. Računalni grazd Isabella nastao je 2002. godine s ciljem da hrvatskim znanstvenicima omogući rad na europskom projektu DataGrid što ga vodi CERN. Danas je Isabella dostupna svim zainteresiranim znanstvenicima u Hrvatskoj. Grozd se trenutno sastoji od 88 računala s 224 procesora, 288 GB radne memorije te više od 8 TB diskovnog prostora.

Slike 4.10, 4.11, 4.12, and 4.13 prikazuju pljuskove čestica u atmosferi koje je potaknula primarna $\gamma-$zraka ili proton. Odabrali smo 500 GeV za energiju primarne $\gamma-$zrake (što je malo ispod energijskog praga teleskopa CT1) te 1 TeV (što je malo iznad praga CT1). Hadronski potaknuti pljuskovi zahtijevaju otprilike tri puta veću početnu energiju kako bi proizveli istu količinu Čerenkovljeve svjetlosti kao i pljuskovi potaknuti primarnom $\gamma-$zrakom. Za sve četiri navedene slike odabrana je visina od 25 km kao prosječna visina na kojoj se događa prvo međudjelovanje. U projekcijama $x-z$ i $x-y$, x i y označuju koordinate na tlu, a z okomitu koordinatu. Simulirano je područje $\pm$ 5 km oko osi pljuska te od 0 do 25 km po visini.

4.6 Simulacija detektora

Kako bi se precizno mogli izračunati tok i energijski spektar kozmičkih izvora $\gamma-$zračenja, potrebno je razviti detaljni model teleskopa. Takav model omogućuje računanje učinkovitosti detekcije [266]. Stoga se simulacije eksperimenata u području visokoenergijske astronomije $\gamma-$zračenja sastoje od dva dijela: simulacija pljuskova u atmosferi te simulacije detektora (reflektora i kamere teleskopa) kao što je prikazano na slici 4.14. Prvi dio simulacija isti je za sve Čerenkovljeve teleskope (čak i puno širu klasu eksperimenata). Većina eksperimenata u području fizike astročestica koriste za simulaciju pljuskova programski paket CORSIKA. Drugi dio simulacija opisuje specifične karakteristike pojedinog detektora. U ovom smo radu koristili ponešto modificirane MAGIC-ove programe: *Reflector* i *Camera*.

Program Reflector (verzija 0.6) čita izlaz iz programa CORSIKA te daje ulazne podatke za program Camera – podatke o svim Čerenkovljevim fotonima u pljusku koji dolaze u ravninu teleskopa. Geometrija teleskopa MAGIC opisana je u datoteci *magic.def*. Na isti smo način definirali geometriju teleskopa CT1 u datoteci *CT1.def*.

Simulacija kamere zadnji je korak u simulacijskom lancu. Koristili smo program Camera (verzija 0.7) koji daje izlazne podatke u istom formatu u kojem su i pravi podatci stvarnog opažanja. Program Camera ne simulira samo kameru teleskopa (MAGIC ili CT1) nego i svu pripadajuću elektroniku. Simulacija noćnog neba također se može uključiti u ovom koraku. Za predočavanje rezultata dobivenih programom Camera koristili smo MAGIC-ove programske pakete MARS i STAR. Slike 4.15 i 4.16 pokazuju primjere slika u kameri teleskopa CT1. Slike smo nacrtali uz pomoć programa MARS, koristeći podatke iz vlastitih simulacija Monte Carlo.

4.7 Promjenljiva transparentnost za Čerenkovljevu svjetlost

Slika 4.17 opisuje geometriju korištenu u simulacijama Čerenkovljeve svjetlosti u atmosferi. U danom trenutku, h je nadmorska visina Čerenkovljevog fotona, L je udaljenost od fotona do teleskopa, φ je zenitni kut, h_1 nadmorska visina opservatorija (za CT1 $h_1 = 2200$ m), h_2 je prava visina na kojoj je foton emitiran, a R je polumjer Zemlje. Dva su procesa uzeta u obzir pri prolasku fotona kroz atmosferu od mjesta emisije do mjesta detekcije: Rayleighjevo raspršenje i Mievo raspršenje.

Rayleighjevo raspršenje je raspršenje svjetlosti na česticama koje su manje od valne duljine svjetlosti. U atmosferi su takve čestice molekule zraka koje su tipične veličine 0.2 nm. Valna duljina Čerenkovljeve svjetlosti koja se može opaziti u kameri teleskopa CT1 je od 290 nm do 600 nm. Transmisijski koeficijent za Rayleighjevo raspršenje T_{R} računali smo numerički koristeći program Reflector [360].

Mievo raspršenje je raspršenje svjetlosti na sfernim, dielektričnim česticama bilo koje veličine. U atmosferi, to su sitne čestice prašine (aerosoli) ili male vodene kapljice (oblaci). Njihova je veličina usporediva s valnom duljinom Čerenkovljeve svjetlosti. Raspšenje i apsorpcija elektromagnetskih valova na sfernim kapljicama vode može se egzaktno riješiti Mievom teorijom. U vidljivom području, Mievo raspršenje gotovo je neovisno o valnoj duljini. Za ozonsku apsorpciju koristili smo Eltermanov model i program Reflector [360]. Transmisijske koeficijent za Mievo raspršenje T_{M} i ozonsku apsorpciju T_{o} računali smo numerički, modificiranim programom Reflector.

Ukupni transmisijski koeficijent je $T_{\mathrm{total}} = T_{\mathrm{R}} \cdot T_{\mathrm{M}} \cdot T_{\mathrm{o}}$ i njegovo je značenje vjerojatnost da Čerenkovljev foton (onaj koji uopće može doći do zrcala teleskopa) **ne** bude prigušen (raspršen ili apsorbiran) u atmosferi.

5. Analiza podataka

5A Metode analize

5.1 Analiza slika pljuskova

Manje od 0.1% ukupnog kozmičkog zračenja koje upada u zemljinu atmosferu su γ-zrake. Većina kozmičkog zračenja su hadronske čestice, uglavnom protoni, koji su zapravo smetnja za Čerenkovljeve teleskope. Stoga je razdvajanje γ-događaja od hadronskih događaja jedan od glavnih izazova zemaljske astronomije γ-zračenja.

Učinkovito razdvajanje γ/hadron prvi je uveo A.M. Hillas 1985. godine. Ono se temelji na tehnici "imaging": slike pljuskova nastale u kameri teleskopa parametriziraju se i rezovi (obično optimizirani u simulacijama Monte Carlo) omogućuju učinkovito razdvajanje γ-zraka od hadrona u energijskom području od 500 GeV do 10 TeV.

U današnje vrijeme razvijene su i druge metode razvajanja γ-zraka od hadrona, ali tehnika "imaging" je još uvijek najefikasnija i najrobusnija.
Tipično mjerenje teleskopom CT1 sastojalo se od:
• očitanja pedestala (trajanja oko 30 sekundi),
• kalibracije (trajanja oko 30 sekundi),
• opažanja (trajanja oko 20 minuta).
Sirovi podatci S_i su podatci iz opažanja. Podatci pedestala P_i su podatci zabilježeni u odsutnosti signala. Služe da bi se odredio nulti nivo svakog kanala kao i širina fluktuacija. Kalibracijski podatci L_i su podatci dobiveni iz 100 pulseva LED jednake amplitude. Izraženi su u jedinicama broja ADC.

Konačno, kalibrirani podatci s_i su podatci spremni za daljnju analizu – računanje parametara slika. Oni su dobiveni oduzimanjem pedestala od sirovih podataka te pretvaranjem broja ADC u u broj fotoelektrona.

Ovaj prvi korak analize CT1 zove se preprocesiranje i može se provesti programom *preproc* koji je dio softvera CTS. Prije računanja parametara slika podatci se moraju filtrirati kako bi se:
• odbacio šum pozadine noćnog neba; te
• ispravio položaj teleskopa.
Parametri slika ili Hillasovi parameri su skup parametara koji opisuju sliku pljuska u kameri Čerenkovljeva teleskopa. Neki od parametara su WIDTH, LENGTH, DIST, MISS, ALPHA, SIZE i CONC.

Najvažniji parametar za točkaste izvore je ALPHA. Definiran je kao kut između longitudinalne osi slike i spojnice središta slike i središta kamere [427]. Ako je teleskop usmjeren prema izvoru, os slike pljuska potaknutog $\gamma-$zrakom prolazi kroz središte kamere. Tada raspodjela parametra ALPHA ima najveću vrijednost blizu nule. S druge strane, hadronski pljuskovi dolaze iz svih smjerova pa je raspodjela parametra ALPHA jednolika za sve kutove. Koristili smo najjednostvniju metodu razdvajanja γ/hadron temeljenu na statičkom rezu parametara slika [427]. Vrijednosti reza dobivene su iz simulacija Monte Carlo.

5.2 Softver za analizu slika pljuskova

Čerenkov telescope software (CTS) sastoji se od softvera za CT1 (pisanog u programskom jeziku C) i MARS-a (pisanog u C++). Koristili smo MARS samo za predočavanje slika u kameri teleskopa CT1.

Softver za CT1, skup programa namijenjen analizi podataka prikupljenih teleskopom CT1, uzima sirove podatke i daje npr. krivulje sjaja i energijske spektre. Programski kod razvijali su mnogi autori bivše kolaboracije HEGRA. U ovom smo radu koristili sljedeće dijelove programskog paketa:
• **preproc** – čita sirove podatke, binarne datoteke koje sadrže: signale u jedinicama ADC za svaki pojedini piksel, vremena i položaj objekta na nebu.
• **imager** – preuzima izlazne podatke iz programa *preproc* i stvara "ntuple".
• **xeos** – grafičko korisničko sučelje za analizu sirovih podataka koristili smo za pozivanje programa *preproc* i *imager*.
• **jacuzzi** – izvodi i crta krivulje sjaja (tok u ovisnosti o vremenu).
Program *preproc* naisao je Dirk Petry, a kasnije ga je usavršio Martin Kestel. Programe *imager*, *xeos* i *jacuzzi* napisali su Thomas Schweizer i Daniel Kranich.

5.3 Popravci za nesavšenu atmosfersku transparentnost

U mnogim izvještajima o opažanjima s IACT ističe se važnost *promjenljive atmosferske transparentnosti* (VAT). Na primjer:
– "Treba voditi računa o promjenljivim atmosferskim uvjetima, koji mogu izazvati vremenski ovisne promjene u opažanjima" [24].
– "najkritičnije su kratkotrajne promjene atmosferske transmisije" [24].
– "Loši vremenski uvjeti i mjesečina mogu onemogućiti kontinuirana opažanja" [8].
– "Glavni izvor sistemastskih pogrešaka može biti nedovoljno poznavanje atmosferske transmisije" [471].
– "Atmosferska svojstva iznimno su važna za pouzdanu analizu" [289].
Odaziv Čerenkovljevog teleskopa osjetljiv je na promjenljive atmosferske uvjete. Stoga

se vremenske prilike neprestano prate i podatci prikupljeni za lošeg vremena se obično odbacuju. Kriterij za prihvaćanje/odbacivanje podataka obično se temelji na:
• ekstinkcijskim vrijednostima s optičkih teleskopa;
• učestalosti trigera za kozmičke zrake.
Odabir podataka prikupljenih teleskopom CT1 (s obzirom na vremenske uvjete) obično se sastojala od nekoliko koraka [300]:
• u bilješkama su tražene napomene o lošem vremenu i pripadajući podatci su odbačeni;
• korištena su mjerenja atmosferske ekstinkcije meridijan-teleskopa Carlsberg uz zahtjev da je r' manji od 0.25;
• prosječna učestalost trigera, popravljena za zenitni kut, trebala je biti blizu nominalne vrijednosti.
Najkorisniji pokazatelj atmosferskih uvjeta, od gore spomenutih, je prosječna učestalost trigera. Nju je moguće iskoristiti za korekcije toka $\gamma-$zraka.

2001. godine, LeBohec and Holder iz kolaboracije VERITAS, razvili su jednostavnu, ali učinkovitu metodu za korekcije krivulja sjaja [310]. Metoda je posebno važna za proučavanje visokoenergijskih brzopromjenljivih γ-izvora kao što su blazari. Modificirali smo njihovu originalnu metodu kako bi ju prilagodili podatcima teleskopa CT1.

Svaki opaženi Čerenkovljev događaj može se karakterizirati luminoznošću Q [310]. Za podatke prikupljene teleskopom CT1, koristili smo parametar SIZE – zbroj svih fotoelektrona u svim pikselima koji daju doprinos slici u kameri. SIZE je definiran jednadžbom (5.45).

S obzirom da je učestalost opažanja kozmičkih zraka stalna (do na fluktuacije), razlike u raspodjelama parametra SIZE (dobivene pri istom zenitnom kutu) odražavaju samo varijacije uzrokovane promjenljivom atmosferskom transparentnošću. Pretpostavili smo ovdje stabilne postavke eksperimenta, posebice visoki napon fotomultiplikatora kamere.

S druge strane, ukoliko je atmosferska transparentnost nepromijenjena tada raspodjela parametra SIZE odražava ovisnost o zenitnom kutu. Kako zenitni kut raste, atmosferska debljina približno raste s $\frac{1}{\cos\vartheta}$. Tako, prosječna učestalost trigera opada s $\cos\vartheta$ kao što se vidi na slici 5.7.

Napravili smo histogram parametra SIZE za opažanja jedne odabrane noći s dobrim vremenskim uvjetima (prema oba kriterija, atmosferskoj ekstinkciji i učestalosti trigera). Taj smo histogram kasnije koristili kao referencu za kalibraciju ostalih noći čiji su vremenski uvjeti bili lošiji. Za sve druge noći napravili smo histograme $F_{\mathrm{meas}}\times$ SIZE. Tada smo prilagođavali faktor propusnosti F_{meas} sve dok se raspodjela nije najbolje slagala s referentnom.

LeBohec i Holder predložili su primjenu korekcija direktno na opaženi tok $\gamma-$zračenja [310]. Korigirani tok $\gamma-$zračenja opisan je formulom (5.67). Očekivani faktor propusnosti $F_{\mathrm{exp}}(\vartheta)$ nismo računali po približnom analitičkom modelu kao u članku [310], nego prilagodbom podataka referentne noći na krivulju $A\cos\vartheta$. Ovisnost faktora propusnosti o zenitnom kutu F prikazana je na slici 5.8.

5B Rezultati i rasprava

5.4 Viševalno opažanje Markariana 421 (2003.)

Viševalna proučavanja promjenljive emisije iz aktivnih galaktičkih jezgri iznimno su važna za razumijevanje prirode čestica i mehanizma ubrzavanja u mlazovima [310].

Ovdje izvještavamo o viševalnom opažanju blazara Mkn 421 iz veljače i ožujka 2003.

Tablica 5.2 pokazuje vremena opažanja i pripadajuće uvjete.

Analizirali smo potpuni skup podataka iz spomenutog opažanja. Ova su mjerenja (ukupno 49.7 sati) napravljena pod dobrim vremenskim uvjetima i još nisu objavljena. Dobivene krivulje sjaja pokazuju promjenljivost toka premda je aktivnost izvora bila mala. Studija korelacija ovih podataka predstavljena je u odlomku 6.2.

5.5 Odabrani rezultati simulacija promjenljive transparentnosti

Simulirali smo 10.000 događaja Monte Carlo, pljuskova izazvanih primarnom $\gamma-$zrakom, koristeći programe Mmcs [441], Reflector [360] i Camera [131]. U programskom kodu Reflector modificirali smo Eltermanove podatke o aerosolima (tablica 4.7) kako bi opisali oblake. U principu, oblaci su različiti od aerosoli, ali postoji snažna veza među njima. Izmaglica, magla i neki oblaci, mogu se tretirati kao aerosoli [316] [456].

Svi događaji generirani su za teleskop CT1. U obzir su uzeti: geometrija reflektora i kamere, nadmorska visina teleskopa te lokalna vrijednost geomagnetskog polja. Događaji su generirani u energijskom rasponu od 750 GeV do 10 TeV s indeksom energijskog spektra -2.6. Za parametar upada uzeto je 200 metara, a za zenitni kut 0^o (okomiti pljuskovi). Logika trigera korištena u simulacijama bila je ista kao i za analizu podataka:
– granični napon ekvivalentan 13 fotoelektrona;
– dva susjedna piksela iznad granice, unutar 6 ns.

Pri proučavanju učestalosti trigera odabrali smo oblake tipa altostratus debele 1000 metara. Relativna učestalost trigera dana je s obzirom na vedro nebo. Slika 5.17 pokazuje ovisnost učestalosti trigera o visini osnovice oblaka za stalnu gustoću vodenih kapljica od 200 cm^{-3}. Svaka točka predstavlja 10 000 događaja. Ovisnosti o visini osnovice oblaka gotovo nema.

Slika 5.18 prikazuje ovisnost o gustoći kapljica oblaka za altostratus debeo 1000 metara čija je visina osnovice 4 km. Učestalost trigera snažno ovisi o gustoći vodenih kapljica. Gustoća kapljica najvažnija je karakteristika oblaka s obzirom na VAT u kontekstu IACT.

Ove simulacije Monte Carlo napravljene su da se pokaže pouzdanost dobivenih rezultata korekcija VAT.

5.6 Rezultati korekcija podataka Markariana 421 (2001.)

U 2001. godini Mkn 421 bio je iznimno aktivan. Izvor je opažan mnogim zemaljskim teleskopima (od radiovalova do visokoenergijskih $\gamma-$zraka) i svemirskim teleskopima(npr. u X-području).

Opažanja teleskopom CT1 blazara Mkn 421 u 2001. godini objavljena su [31], osim 20 sati podataka isključenih zbog lošeg vremena. Dio tih podataka (ukupno 14 sati) pokazao se prikladnim za testiranje naše korekcijske metode. Vremena opažanja i pripadajući uvjeti pobrojani su u tablici 5.9. Prosječna učestalost trigera u zenitu bila je 3.48 Hz.

6. Analiza fizike

6A Metode analize

6.1 Nova metoda analize korelacija

Linearni korelacijski faktor definiran je izrazom (6.2). Edelson i Krolik [195] primijenili su (6.2) na krivulje sjaja uvodeći mogući vremenski pomak između dvaju skupova podataka

(6.3). U slučaju kad nema vremenskog pomaka ($\Delta t = 0$), izraz (6.3) svodi se na definiciju (6.2). Jednadžba (6.3) nazvana je diskretna korelacijska funkcija (DCF). Prema [195], signifikantnost je dana izrazom (6.4)

Za neku opaženu vrijednost korelacijskog faktora r_o, vjerojatnost $p_n(|r| \geq |r_o|)$ znači da će n mjerenja dviju neovisnih varijabli x i y dati korelacijski faktor r manji ili jednak r_o. Vjerojatnost $p_n(|r| \geq |r_o|)$ može se izračunati iz integrala (6.6). Važno je uočiti da $p_n(|r| \geq |r_o|)$ jako ovisi o n.

Ako je r korelacijski faktor koji može poprimiti bilo koju vrijednost između -1 i 1, možemo napisati $f(x)\mathrm{d}x$ kao vjerojatnost da r bude između x i $x + \mathrm{d}x$. Funkcija $f(x)$ je funkcija gustoće vjerojatnosti (PDF) [235]. Ako je varijabla x diskretna, onda je f_i diskretna funkcija gustoće vjerojatnosti.

Za usporedbu dviju empiričkih raspodjela koristili smo metodu temeljenu na konvoluciji. Ista se tehnika koristi u statistici za računanje raspodjele zbroja dviju slučajnih varijabli [388]. Fourierova konvolucija dana je izrazom (6.10), a odgovarajuća kumulativna funkcija izrazom (6.11).

Jednostrana vjerojatnost $H(0)$ za nul-hipotezu da ne postoji razlika između dviju funkcija gustoće vjerojatnosti f and g opisana je izrazom (6.12). Dvostrana vjerojatnost je $p = 2H(0)$ koja je 100% za potpuni preklop funkcija, a 0 kad uopće nema preklopa. Ukratko, konvolucijom se računa vjerojatnost za svaki mogući ishod uzimajući u obzir sve moguće kombinacije dviju neovisnih raspodjela [387].

Prilagodili smo ovu metodu kako bih analizirao diskretne empiričke raspodjele korelacijskih faktora. Slika 6.5 prikazuje primjer dviju raspodjela korelacijskih faktora. Funkcija $f(x)$ je funkcija gustoće vjerojatnosti raspodjele korelacijskih faktora, $g(x)$ funkcija gustoće vjerojatnosti za takozvanu "auto-korelaciju". Obje raspodjele su tek primjeri za opis metode. Njihovo porijeklo i značenje objašnjeno je kasnije u tekstu. Raspodjele su prikazane kao histogrami s n binova (u primjeru je $n = 100$). F_i i G_j su brojevi događaja po binu koji odgovaraju raspodjelama f i g. Ukupni broj događaja je N (u primjeru $N = 100.000$).

Diskretne raspodjele korelacijskih faktora definirane su izrazima (6.27) i (6.28). Jednodimenzionalna diskretna konvolucija, koja odgovara izrazu (6.14), opisana je formulom (6.32) te prikazana na slici 6.7.

Konačno, dvostrana vjerojatnost $p = 2H(0)$, korigirana za vrijednost polovice zbroja glavne dijagonale, opisana je izrazom (6.35). U slučaju dviju nepreklapajućih raspodjela, formula (6.35) daje $p \equiv 0$. Slika 6.8 pokazuje takav primjer. Za dvije identične raspodjele, formula (6.35) daje $p \equiv 1$. Takav je primjer prikazan na slici 6.9.

7. Sažeti pregled

Ova disertacija izlaže istraživanje promjenljivog visokoenergijskog zračenja iz tri obližnja blazara; Mkn 421, Mkn 501 i Mkn 180. Blazari su podklasa aktivnih galaktičkih jezgara koje su snažni radioizvori i čija je prostorna orijentacija takva da je jedan od dva relativistička mlaza usmjeren prema nama. Opaženo visokoenergijsko zračenje iz blazara najverojatnije je stvoreno u relativističkim mlazovima, u blizini crne rupe.

Dvije različite klase modela predložene su kako bi se objasnila fizika mlazova, no trenutno se nijedan od njih ne može pouzdano odbaciti.

Prema takozvanom hadronskom modelu, visokoenergijske gama-zrake nastaju u ras-

padima relativističkih neutralnih piona. Dobro je poznato da pri visokoenergijskim sudarima hadrona istovremeno nastaju i neutralni i nabijeni pioni. S obzirom da se nabijeni pioni dalje raspadaju na mione i neutrine, jedini je pouzdani pokazatelj hadronskog scenarija istovremena detekcija visokoenergijskih neutrina i gama-zraka. Jedan od glavnih ciljeva nedavno pokrenutog neutrinskog eksperimenta IceCube na Antartiku precizno je opažanje kozmičkih neutrina iz blazara, po mogućnosti u koincidenciji s gama-zrakama opaženim na sjevernoj polutci. Cilj budućeg opservatorija CROATEA upravo je takav – neprekidno promatranje emisije gama-zraka bliskih galaksija tipa Markarian.

Prema leptonskom modelu, dominantan izvor gama-zraka relativistički su elektroni koji se raspršuju na niskoenergijskim fotonima unutar mlaza (inverzno Coptonovo raspršenje), učinovito im prenoseći svoju energiju. Niskoenergijski fotoni (vidljivi, ultraljubičasti, X-zračenje) stvoreni su istom populacijom elektrona, kao sinkrotronsko zračenje. S obzirom da sinkrotronsko zračenje (SR) daje fotone za inverzno Coptonovo raspršenje (IC) te da ista populacija elektrona može biti odgovorna za oba procesa, opaženi tok zračenja SR i IC trebao bi biti snažno koreliran.

Ova je disertacija usmjerena na precizno proučavanje korelacija X-zračenja i gama-zraka kao test mehanizma emisije. Naš je doprinos dvojak. Prvo, razvili smo novu metodu za produljenje vremena kontinuiranog opažanja gama-zraka. Istraživanje korelacija brzo promjenljivih tokova X-zračenja i gama-zraka temelji se na istovremenim i kontinuiranim opažanjima. Jedan od razloga prekida u opažanjima kod Čerenkovljevih teleskopa su periodi nesavršenih vremenskih uvjeta, npr. periodi ograničene atmosferske transparentnosti. Do sada su opažanja provedena u oblačnim periodima uobičajeno odbacivana. Pokazali smo da se podatci prikupljeni za oblačnog vremena mogu iskoristiti, uz primjenu prikladnih popravaka. Naša nova korekcijska metoda indirektno uzima u obzir atmosfersku transparentnost kroz mjerenje hadronske pozadine te iz nje računa popravke toka gama-zraka. Metoda je inspirirana jednostavnom idejom takozvanog faktora propusnosti, koju je originalno razvila kolaboracija Whipple. Korekcijska metoda testirana je na podatcima Mkn 421, prikupljenim teleskopom CT1 kolaboracije HEGRA pri lošim vremneskim uvjetima 2001. godine. Popravljeni podatci dobro se uklapaju u komplementarni skup podataka prikupljenih u istom periodu, ali tijekom dobrog vremena. Naša korekcijska metoda mogla bi značajno povećati radni ciklus praktički svih teleskopa za opažanje kozmičkih gama-zraka. No, ona je posebno važna za teleskope smještene na manjim visinama poput teleskopa CANGAROO i CROATEA. Ova se metoda može smatrati direktnim doprinosom opservatoriju CROATEA.

Ubrzo nakon što smo se prihvatili analize korelacija toka X-zračenja i gama-zraka, spoznali smo da općenito prihvaćena metoda - standardni račun linearnih korelacijskih faktora - ne može biti ispravna ako se primijeni na podatke s pogreškama. Valja uočiti da je ovo najopćenitija tvrdnja. Međutim, u gama-astronomiji ova je pogreška posebno razorna i stalno iznova vodi na pogrešne zaključke o jakosti korelacija, podcjenjujući korelacije. Razlog je vrlo jednostavan – očekivana vrijednost korelacijskog faktora u slučaju savršeno koreliranih podataka s konačnim pogreškama uvijek je manja od jedinice; što su pogreške veće korelacijski faktor je manji. Razvili smo novu metodu za analizu korelacija, koja ispravno uzima u obzir konačne pogreške i uspoređuje mjerenja korelacija za različita očekivanja. Primjena ove metode na sve raspoloživе podatke vodi do općenitog zaključka da je tok gama-zraka puno jače koreliran s tokom X-zračenja nego što se ranije mislilo, što ide u prilog leptonskom modelu.

Primijenili smo ovu metodu na sve raspoložive podatke za Mkn 421, Mkn 501 i Mkn 180. Također, proveli smo potpunu analizu podataka viševalnog opažanja Mkn

421 (mjerene teleskopom CT1 u gama-području, RXTE satelitom u X-području te KVA teleskopom u optičkom području). U veljači i ožujku 2003. godine, sudjelovali smo u prikupljanju podataka na La Palmi, u okviru posebno organizirane "viševalne kampanje." Unatoč slaboj aktivnosti izvora tijekom kampanje, utvrdili smo promjenljivost toka visokoenergijskih gama-zraka te pronašli pozitivne korelacije s tokom X-zračenja. Ostali analizirani podatci uključuju nedavna mjerenja aktivnih galaksija Mkn 421 (2005. godine), Mkn 501 (2005. godine) i Mkn 180 (2006. godine) provedenih teleskopom MAGIC. U nekim je slučajevima signifikantnost vrlo mala i neuvjerljiva, uglavnom zbog velikih relativnih pogrešaka te zbog malog broja točaka. Snažni bljeskovi bez iznimke pokazuju jake korelacije. Većina mjerenja pokazala je pozitivne korelacije između X-zračenja i gama-zraka, ponovo u prilog leptonskom modelu.

Koristeći našu tehniku analize korelacija, opazili smo također druge dvije zanimljive pojave. Prvo, pronašli smo pozitivne korelacije optičkog toka i toka X-zračenja, uz pretpostavku jednodnevnog kašnjenja u optičkoj krivulji sjaja. Ta je pojava proizašla iz analize podataka Mkn 421 iz veljače/ožujka 2003. te predstavlja prvo opažanje pozitivne korelacije između optičkog i X-zračenja. Drugo, neovisno smo potvrdili izuzetno zanimljivo nedavno opažanje – energijski ovisno četverominutno kašnjenje u snažnom bljesku gama-zračenja, koje je kolaboracija MAGIC pronašla u podatcima blazara Mkn 501. Oba fenomena mogla bi baciti novo svjetlo na mehanizam emisije u mlazovima blazara. S druge strane, drugi je rezultat već privukao veliku pažnju, s obzirom da bi mogao poslužiti za testiranje jedno od najtemeljnijih predviđanja kvantne gravitacije – ovisnost brzine svjetlosti o energiji fotona.

Appendix A
List of used acronyms

A&A	—	**A**stronomy **&** **A**strophysics
ACD	—	**A**nti-**C**oincidence **D**etector
ACIT	—	**A**tmospheric **Č**erenkov **I**maging **T**echnique
ADC	—	**A**nalog to **D**igital **C**onverter
ADS	—	**A**strophysics **D**ata **S**ystem
AGILE	—	**A**stro-rivelatore **G**amma a **I**mmagini **LE**ggero (*Extremely Light Imager for Gamma Astronomy*)
AGN	—	**A**ctive **G**alactic **N**ucleus
ALTAI	—	**A**tmospheric **L**ight **T**elescope **A**rray **I**mage
AMADEUS	—	**A**utonomus **M**odule for **A**coustic **D**etection **U**nder the **S**ea
AMANDA	—	**A**ntartic **M**uon **A**nd **N**eutrino **D**etector **A**rray
AMS	—	**A**lpha **M**agnetic **S**pectrometer
ANTARES	—	**A**stronomy with a **N**eutrino **T**elescope and **A**byss environmental **RES**earch
ANITA	—	**AN**tarctic **I**mpulsive **T**ransient **A**ntenna
APD	—	**A**valanche **P**hoto**D**iode
APh	—	**A**stroparticle **Ph**ysics
ApJ	—	**A**stro**p**hysical **J**ournal
ApPEC	—	**A**stro**p**article **P**hysics **E**uropean **C**oordination
ARGO-YBJ	—	**A**strophysics **R**esearch at **G**round-based **O**bservatory at **Y**ang**B**a**J**ing
ASHRA	—	**A**ll-sky **S**urvey **H**igh **R**esolution **A**ir shower detector
asl	—	**a**bove **s**ea **l**evel
ASM	—	**A**ll **S**ky **M**onitor
au	—	**a**rbitrary **u**nit
au	—	**a**stronomical **u**nit
BAT	—	**B**urst **A**lert **T**elescope
BATSE	—	**B**urst **a**nd **T**ransient **S**ource **E**xperiment
BBHS	—	**B**inary **B**lack **H**ole **S**ystem
BH	—	**B**lack **H**ole
BHFP	—	**B**lack **H**ole **F**inder **P**robe
blazar	—	**BL** Lac object and qu**asar**
BL Lac	—	Variable object named **BL** in the constellation of **Lac**erta (originally wrongly classified as a peculiar variable star)
CALIOP	—	**C**loud-**A**erosol **LI**dar with **O**rthogonal **P**olarization
CALIPSO	—	**C**loud-**A**erosol **L**idar and **I**nfrared **P**athfinder **S**atellite **O**bservation
CANGAROO	—	**C**ollaboration of **A**ustralia and **N**ippon for a **GA**mma **R**ay **O**bservatory in the **O**utback
CASTER	—	**C**oded **A**perture **S**urvey **T**elescope for **E**nergetic **R**adiation
CAT	—	**C**herenkov **A**rray at **T**hémis
CCD	—	**C**harge-**C**oupled **D**evice
CCN	—	**C**loud **C**ondensation **N**ucleus
CDM	—	**C**old **D**ark **M**atter
CELESTE	—	**CE**renkov **L**ow **E**nergy **S**ampling and **T**iming **E**xperiment
CERN	—	**C**onseil **E**uropéen pour la **R**echerche **N**ucléaire (*European Organization for Nuclear Research*)
CF	—	**C**onversion **F**actor
CGR	—	**C**osmic **G**amma **R**ay
CGRO	—	**C**ompton **G**amma **R**ay **O**bservatory
CIB	—	**C**osmic **I**nfrared **B**ackground
CMB	—	**C**osmic **M**icrowave **B**ackground
CMT	—	**C**arlsberg **M**eridian **T**elescope
COBE	—	**C**osmic **M**icrowave **B**ackground **E**xplorer
COMPTEL	—	**COMP**ton **TEL**escope
CORSIKA	—	**CO**smic **R**ay **SI**mulation for **KA**SCADE

COS-B — **CO**smic ray **S**atellite - **B**
CP — **C**harge conjugation **P**arity
CR — **C**osmic **R**ay
CROATEA — **C**osmic **R**ay **O**bservatory **A**t **T**he **E**astern **A**driatic
CT — **Č**erenkov **T**elescope
CTA — **Č**erenkov **T**elescope **A**rray
CTS — **Č**erenkov **T**elescope **S**oftware
DAQ — **D**ata **A**c**Q**uisition
DCF — **D**iscrete **C**orrelation **F**unction
DE — **D**ark **E**nergy
DEBRA — **D**iffuse **E**xtragalactic **B**ackground **RA**diation
DEC — **DEC**lination
DIAL — **DI**fferential **A**bsorption **L**idar
DM — **D**ark **M**atter
DPMJET — **D**ual **P**arton **M**odel with **JET**s
EAS — **E**xtensive **A**ir **S**hower
EBL — **E**xtragalactic **B**ackground **L**ight
ECAL — **E**lectromagnetic **CAL**orimeter
ECO-1000 — **E**uropean **Č**erenkov **O**bservatory 1000
EGB — **E**xtragalactic **G**amma-ray **B**ackground
EGCR — **E**xtra**G**alactic **C**osmic **R**ay
EGRET — **E**nergetic **G**amma **R**ay **E**xperiment **T**elescope
EGS4 — **E**lectron **G**amma **S**hower system version **4**
EHE — **E**xtremely **H**igh **E**nergy
EIC — **E**xternal **I**nverse **C**ompton
EM — **E**lectro**M**agnetic
ESA — **E**uropean **S**pace **A**gency
EUSO — **E**xtreme **U**niverse **S**pace **O**bservatory
EUVE — **E**xtreme **U**ltra**v**iolet **E**xplorer
EXIST — **E**nergetic **X**-ray **I**maging **S**urvey **T**elescope
FADC — **F**lash **A**nalog to **D**igital **C**onverter
FLT — **F**irst **L**evel **T**riger
FLUKA — **FLU**ktuierende **KA**skade
(*Fluctuating cascade*)
FoV — **F**ield **o**f **V**iew
FR — **F**anaroff-**R**iley
FSRQ — **F**lat **S**pectrum **R**adio **Q**uasar
FWHM — **F**ull-**W**idth at **H**alf-**M**aximum
GAW — **G**amma **A**ir **W**atch
GBM — **G**LAST **B**urst **M**onitor
GC — **G**alactic **C**enter
GCR — **G**alactic **C**osmic **R**ay
GLAST — **G**amma-ray **L**arge **A**rea **S**pace **T**elescope
GNCT — **G**lobal **N**etwork of **Č**erenkov **T**elescopes
GR — **G**eneral **R**elativity
GRB — **G**amma-**R**ay **B**urst
GRBR — **G**amma-**R**ay **B**urst **R**emnant
GRH — **G**amma-**R**ay **H**orizon
GZK — **G**reisen-**Z**atsepin-**K**uzmin
HAGAR — **H**igh **A**ltitude **GA**mma-**R**ay observatory at Hanle
HATS — **H**igh **A**ltitude **T**elescope **S**ystem
HAWC — **H**igh **A**ltitude **W**ater **Č**erenkov
HBL — **H**igh-frequency peaked **BL** Lac
HE — **H**igh **E**nergy
HEAO — **H**igh **E**nergy **A**strophysical **O**bservatory
HEGRA — **H**igh **E**nergy **G**amma **R**ay **A**stronomy
HESS — **H**igh **E**nergy **S**tereoscopic **S**ystem
HEXIT — **H**igh **E**nergy **X**-ray **I**maging **T**elescope

HEXTE — **H**igh **E**nergy **X**-ray **T**iming **E**xperiment
HPD — **H**ybrid **P**hoto**D**etector
HST — **H**ubble **S**pace **T**elescope
HV — **H**igh **V**oltage
IACT — **I**maging **A**tmospheric **Č**erenkov **T**elescope
IC — **I**nverse **C**ompton
ICRC — **I**nternational **C**osmic **R**ay **C**onference
IGMF — **I**nter **G**alactic **M**agnetic **F**ield
IMBH — **I**ntermediate-**M**ass **B**lack **H**ole
INTEGRAL — **INTE**rnational **G**amma-**R**ay **A**strophysics **L**aboratory
IR — **I**nfra**R**ed
IT — **I**maging **T**echnique
ISCO — **I**nnermost **S**tabile **C**ircular **O**rbit
ISM — **I**nter**S**tellar **M**edium
ISRF — **I**nter**S**tellar **R**adiation **F**ield
ISS — **I**nternational **S**pace **S**tation
JD — **J**ulian **D**ay
KAMIOKANDE — **KAMIOKA** **N**eutrino **D**etector **E**xperiment
KASCADE — **KA**rlsruhe **S**hower **C**ore and **A**rray **DE**tector
KVA — **K**ungliga **V**etenskaps**A**kademien
(*Royal Academy of Sciences*)
LAT — **L**arge **A**rea **T**elescope
LBL — **L**ow-frequency peaked **BL** Lac
LE — **L**ow **E**nergy
LED — **L**ight **E**mission **D**iode
LIDAR — **LI**ght **D**etection **A**nd **R**anging
LIGO — **L**aser **I**nterferometer **G**ravitational-wave **O**bservatory
LISA — **L**aser **I**nterferometer **S**pace **A**ntenna
LONS — **L**ight **O**f the **N**ight **S**ky
LOWTRAN — **LOW** resolution **TRAN**smittance code
LTT — **L**ow **T**hreshold **T**elescope
LVD — **L**arge **V**olume **D**etector
LWC — **L**iquid **W**ater **C**ontent
MACE — **M**ajor **A**tmospheric **C**erenkov **E**xperiment
MACHO — **MA**ssive **C**ompact **H**alo **O**bject
MAGIC — **M**ajor **A**tmospheric **G**amma-ray **I**maging **Č**erenkov detector
MARS — **MAGIC** **A**nalysis and **R**econstruction **S**oftware
MBR — **M**icrowave **B**ackground **R**adiation
MC — **M**onte **C**arlo
ME — **M**edium **E**nergy
MILAGRO — **M**ultiple **I**nstitution **L**os **A**lamos **G**amma **R**ay **O**bservatory
MJD — **M**odified **J**ulian **D**ay
Mmcs — **MAGIC** **m**onte **c**arlo **s**oftware
MODTRAN — **MOD**erate resolution **TRAN**smittance code
MWL — **M**ulti-**W**ave**L**ength
NASA — **N**ational **A**eronautics and **S**pace **A**dministration
NEMO — **NE**utrino **M**editerranean **O**bservatory
NESTOR — **N**eutrino **E**xtended **S**ubmarine **T**elescope with **O**ceanographic **R**esearch
NKG — **N**ishimura **K**amata **G**reisen
NS — **N**eutron **S**tar
NN — **N**ext **N**eighbor
NSB — **N**ight **S**ky **B**ackground
OCO — **O**rbiting **C**arbon **O**bservatory
ORM — **O**bservatorio del **R**oque de los **M**uchachos
(*Roque de los Muchachos Observatory*)
OSETI — **O**ptical **SETI**
OSSE — **O**riented **S**cintillation **S**pectrometer **E**xperiment
OVV — **O**ptically **V**iolently **V**ariable

PACT — **P**achmarhi **A**rray of **Č**erenkov **T**elescopes
PARASOL — **P**olarization and **A**nisotropy of **R**eflectances for **A**tmospheric **S**cience coupled with **O**bservations from a **L**idar
parsec — **par**allax of one arc **sec**ond
PBH — **P**rimordial **B**lack **H**ole
pc — **p**ar**s**ec
PCA — **P**roportional **C**ounter **A**rray
PD — **P**hoto**D**iode
PDA — **P**article **D**etector **A**rray
PDF — **P**robability **D**ensity **F**unction
PE — **P**hoto**E**lectron
PID — **P**article **Id**entification
PMT — **P**hoto**M**ultiplier **T**ube
PSF — **P**oint **S**pread **F**unction
PSR — **P**ul**S**a**R**
pulsar — **pulsa**ting **r**adio source
QCD — **Q**uantum **C**hromo**D**ynamics
QE — **Q**uantum **E**fficiency
QGSJET — **Q**uark **G**luon **S**tring model with **JET**s
QPO — **Q**uasi-**P**eriodic **O**scillation
QSO — **Q**uasi-**S**tellar **O**bject
quasar — **quas**i-stel**lar**
RA — **R**ight **A**scension
RADAR — **RA**dio **D**etection **A**nd **R**anging
RBL — **R**adio-selected **BL** Lac
RF — **R**andom **F**orest
RICH — **R**ing **I**maging **Ch**erenkov
RL — **R**adiation **L**ength
RMS — **R**oot **M**ean **S**quare
ROSAT — **Rö**ntgen**sat**ellit
RPC — **R**esistive **P**late **C**hamber
RXTE — **R**ossi **X**-ray **T**iming **E**xplorer
SAS — **S**mall **A**stronomy **S**atellite
SE — **S**haft **E**ncoder
SED — **S**pectral **E**nergy **D**istribution
SETI — **S**earch for **E**xtra**T**errestrial **I**nteligence
SGARFACE — **S**hort **GA**mma **R**ay **F**ront **A**ir **Č**erenkov **E**xperiment
SGR — **S**oft **G**amma-ray **R**epeater
SiMP — **Si**licon **P**hoto**M**ultiplier
SLT — **S**econd **L**evel **T**riger
SM — **S**tandard **M**odel
SMBH — **S**uper-**M**assive **B**lack **H**ole
SN — **S**uper**N**ova
SNLS — **S**uper**N**ova **L**egacy **S**urvey
SNR — **S**uper**N**ova **R**emnant
SSC — **S**ynchrotron **S**elf-**C**ompton
SSC — **S**canning **S**hadow **C**amera
SSRQ — **S**tep **S**pectrum **R**adio **Q**uasar
STACEE — **S**olar **T**ower **A**tmospheric **C**herenkov **E**ffect **E**xperiment
STAR — **ST**andard **A**nalysis and **R**econstruction
STP — **S**tandard **T**emperature and **P**ressure
SUSY — **SU**per **SY**mmetry
TA — **T**elescope **A**rray
TACTIC — **T**eV **A**tmospheric **C**erenkov **T**elescope with **I**maging **C**amera
TD — **T**opological **D**efect
TF — **T**hroughput **F**actor
TOA — **T**op **O**f **A**tmosphere
TOMS — **T**otal **O**zone **M**apping **S**pectrometer

TR — **T**rigger **R**ate
UHE — **U**ltra **H**igh **E**nergy
UHECR — **U**ltra **H**igh **E**nergy **C**osmic **R**ay
UIT — **U**ltraviolet **I**maging **T**elescope
ULX — **U**ltra-**L**uminous **X**-ray source
UrQMD — **U**ltra**r**elativistic **Q**uantum **M**olecular **D**ynamics
UV — **U**ltra**V**iolet
UVOT — **U**ltra**V**iolet **O**ptical **T**elescope
VAT — **V**ariable **A**tmospheric **T**ransmission
VENUS — **V**ery **E**nergetic **NU**clear **S**cattering
VERITAS — **V**ery **E**nergetic **R**adiation **I**maging **T**elescope **A**rray **S**ystem
VHE — **V**ery **H**igh **E**nergy
VIHKOS — **V**irtuelles **I**nstitut für **H**ochenergiestrahlungen aus dem **KOS**mos (*Virtual Institute for High Energy Cosmic Rays*)
VLA — **V**ery **L**arge **A**rray
VLBI — **V**ery **L**arge **B**aseline **I**nterferometry
XBL — **X**-ray-selected **BL** Lac
XMM — **X**-ray **M**ulti-**M**irror
XRB — **X**-**R**ay **B**inary
XRF — **X**-**R**ay **F**lash
XRT — **X**-**R**ay **T**elescope
WD — **W**hite **D**warfs
WEBT — **W**hole **E**arth **B**lazar **T**elescope
WIMP — **W**eakly **I**nteracting **M**assive **P**article
WMAP — **W**ilkinson **M**icrowave **A**nisotropy **P**robe
ZA — **Z**enith **A**ngle

Appendix B

List of frequently used web sites

Ground-based VHE gamma-ray astronomy:

{1} The MAGIC Telescope Project
http://magic.mppmu.mpg.de/

{2} The H.E.S.S. Project
http://www.mpi-hd.mpg.de/HESS/

{3} VERITAS Homepage
http://veritas.sao.arizona.edu/

{4} CANGAROO's Page
http://icrhp9.icrr.u-tokyo.ac.jp/

Space-borne gamma-ray and X-ray detectors:

{5} GLAST: The Gamma Ray Large Area Space Telescope
http://www-glast.stanford.edu/

{6} RXTE: The Rossi X-Ray Timing Explorer Project
http://xte.mit.edu/

{7} The Chandra X-ray Observatory Center
http://chandra.harvard.edu/

Space-borne cloud detectors:

{8} CALIPSO: Cloud Aerosol Lidar and Infrared Pathfinder Satellite Observations
http://smsc.cnes.fr/CALIPSO/

{9} CloudSat
http://cloudsat.atmos.colostate.edu/

Journals:

{10} The Astrophysical Journal (**ApJ**)
http://www.journals.uchicago.edu/ApJ/

{11} Astronomy and Astrophysics (**A&A**)
http://aa.springer.de/

{12} Astroparticle Physics (**APh**)
http://www.sciencedirect.com/science/journal/09276505

{13} Nature
http://www.nature.com/nature/

{14} New Astronomy
http://www.sciencedirect.com/science/journal/13841076

Preprints:

{15} Astrophysics at e-Print arXiv
http://arxiv.org/archive/astro-ph

{16} The NASA Astrophysics Data System
http://adswww.harvard.edu/

Software:

{17} CORSIKA
http://www-ik.fzk.de/corsika/

{18} ROOT
http://root.cern.ch/

Appendix C

Selected C++ codes and ROOT scripts

Here I described in technical details how I had calculated and plotted the distributions of correlation coefficients and corresponding probabilities $p_{\rm AB}$ and $p_{\rm AC}$. E.g. I plotted the **Figure 6.15** using my ROOT script `plotMULTI.c`.

The script `plotMULTI.c` reads four input files (`output.dat`, `NOcorr.dat`, `auto.dat`, and `N26.dat`) and writes two output files (`histoAUTO.dat` and `histoNO.dat`). Both output files are histograms (containing 100 bins) that are needed for the probability calculation (`probability.c++`). All input files are huge sets ($N = 100000$) of correlation coefficients. E.g. the file `output.dat` is generated by C++ code `MC.c++`. It is the main distribution (full black curve in the Figure 6.15).

Here are some of C++ codes [313] and ROOT scripts [144] mentioned above:

plotMULTI.c

```
{
    void main()
    {
    float scale = 1./2000.;
    const int n = 100;  // number of bins
    const int m = 100000;  // number of events
    const int k = 201;
    int i;
    float r1[m], r2[m], r3[m], x[k], f[k];
    float temp1, temp2, temp3;
    fstream data1("output.dat", ios::in);
    for(i = 0; i < m; i++)
    {
       data1 >> r1[i];
       r1[i] = r1[i];
    }
    fstream data2("NOcorr.dat", ios::in);
    for(i = 0; i < m; i++)
    {
       data2 >> r2[i];
       r2[i] = r2[i];
    }
    fstream data3("auto.dat", ios::in);
    for(i = 0; i < m; i++)
    {
       data3 >> r3[i];
       r3[i] = r3[i];
    }
    fstream data4("N26.dat", ios::in);
    for(i = 0; i < k; i++)
```

```
    {
       data4 >> x[i];
       data4 >> f[i];
       f[i] = f[i]*scale;
    }
    TH1F *CF1 = new TH1F("","", n,-1,1);
    for(i = 0; i < m; i++)
    {
       CF1 -> Fill(r1[i]);
    }
    CF1 -> SetTitle("Correlation #gamma-rays/X-rays (2001) Mkn 421");
    CF1 -> GetXaxis() -> SetTitle("#font[12]{r}");
    CF1 -> GetYaxis() -> SetTitle("#font[12]{f}(#font[12]{r})");
    CF1 -> Scale(scale);
    CF1 -> SetMaximum(5.0);
    CF1 -> Draw();
    TH1F *CF2 = new TH1F("","",n,-1,1);
    for(i = 0; i < m; i++)
    {
       CF2 -> Fill(r2[i]);
    }
    CF2 ->Scale(scale);
    CF2 -> Draw("same");
    TH1F *CF3 = new TH1F("","",n,-1,1);
    for(i = 0; i < m; i++)
    {
       CF3 -> Fill(r3[i]);
    }
    CF3 ->Scale(scale);
    CF3 -> Draw("same");
    TGraph *curve = new TGraph(k,x,f);
    curve -> Draw("c");
    legend = new TLegend(0.5,0.75,0.89,0.89);
    legend -> AddEntry(CF1,"#font[12]{f}_{A}","l");
    legend -> AddEntry(CF3,"#font[12]{f}_{B}","l");
    legend -> AddEntry(CF2,"#font[12]{f}_{C}","l");
    legend -> AddEntry(curve,"#font[12]{f}_{D}","l");
    legend -> Draw();
    fstream out("histoNO.dat", ios::out);
    for(i = 1; i < n+1; i++)
    {
       temp1 = (CF1->GetBinContent(i))*2000.0;
       temp2 = (CF2->GetBinContent(i))*2000.0;
       out<<i<<"   "<<temp1<<"   "<<temp2<<endl;
    }
fstream out("histoAUTO.dat", ios::out);
for(i = 1; i < n+1; i++)
    {
```

```
        temp1 = (CF1->GetBinContent(i))*2000.0;
        temp3 = (CF3->GetBinContent(i))*2000.0;
        out<<i<<"   "<<temp3<<"   "<<temp1<<endl;
     }
     }
}
```

MC.c++

```
#include <iostream>
#include <fstream>
#include <cstdlib>
#include <ctime>
using namespace std;
double gauss (double, double, double);
double montecarlo (double, double);
int main()
{
   const int n = 26;   // number of data points
   int i, j;
   double r;
   double MJDx[n], x[n], dx[n], MCx[n];
   double MJDy[n], y[n], dy[n], MCy[n];
   double SUMx, SUMy, AVEx, AVEy, VARx, VARy, COV;
   fstream CT1data("CT1data2001", ios::in);   // input of CT1 data
   for(j = 0; j < n; j++)
   {
      CT1data >> MJDx[j];
      CT1data >> x[j];
      CT1data >> dx[j];
   }
   fstream RXTEdata("RXTEdata2001", ios::in);   // input of RXTE data
   for(j = 0; j < n; j++)
   {
      RXTEdata >> MJDy[j];
      RXTEdata >> y[j];
      RXTEdata >> dy[j];
   }
   ofstream out("output.dat");   // output file (correlation coefficients)
   srand((unsigned)time(0));   // SEED for Monte Carlo
   for (i = 0; i < 100000; i++)
   {  // beginning of the main loop
      for(j = 0; j < n; j++) // moving of data points
      {
         MCx[j] = montecarlo (x[j], dx[j]);
         MCy[j] = montecarlo (y[j], dy[j]);
      }
      SUMx = 0;
      SUMy = 0;
```

```
      VARx = 0;
      VARy = 0;
      COV = 0;
      for(j = 0; j < n; j++)
      {
         SUMx = SUMx + MCx[j];
         SUMy = SUMy + MCy[j];
      }
      AVEx = SUMx / n;
      AVEy = SUMy / n;
      for(j = 0; j < n; j++)
      {
         VARx = VARx + (MCx[j] - AVEx) * (MCx[j] - AVEx);
         VARy = VARy + (MCy[j] - AVEy) * (MCy[j] - AVEy);
         COV  = COV  + (MCx[j] - AVEx) * (MCy[j] - AVEy);
      }
      r = COV / (sqrt(VARx) * sqrt(VARy));
      out << r << endl;
      }   // the end of the main loop
      return 0;
}
double gauss (double z, double m, double s)   // Gauss PDF
{
   double e, f, cte, half;
   cte = (double)(0.39894228);
   half = (double)(-0.5);
   e = (z - m) / s;
   f = (cte / s) * exp(half * e * e);
   return f;
}
double montecarlo (double flux, double dflux)   // Monte Carlo
{
   double g, cte, divisor;
   double random1, random2, x, u;
   cte = (double)(0.39894228);
   divisor = (double)(RAND_MAX) + (double)(1);
   do  // the acceptance-rejection method
   {
      random1 = (double)rand() / divisor;
      x = flux - (double)(5)*dflux + (double)(10)*dflux * random1;
      random2 = (double)rand() / divisor;
      u = cte * random2 / dflux;
      g = gauss(x,flux,dflux);
   }
   while ( !((x > (double)(0)) && (u <= g)) );
   return x;
}
```

probability.c++

```
#include <iostream>
#include <fstream>
#include <cstdlib>
#include <ctime>
using namespace std;
int main()
{
   const int n = 100;      // number of bins
   const int N = 100000;   // number of events
   int j,k;
   int bin[n], F[n], G[n];
   double f[n], g[n];
   double sum1, sum2, p;
   fstream histo("histoAUTO.dat", ios::in);
   for(j = 1; j < n+1; j++)
   {
      histo >> bin[j];
      histo >> F[j];
      histo >> G[j];
   }
   for(j = 1; j < n+1; j++)
   {
      f[j] = (double)(F[j]) / (double)(N);
      g[j] = (double)(G[j]) / (double)(N);
   }
   sum1 = (double)(0);
   sum2 = (double)(0);
   for(k = 1; k < n+1; k++)
   {
      for(j = 1; j < k+1; j++)
      {
         sum1 += f[j] * g[n-k+j];
      }
   }
   for(j = 1; j < n+1; j++)
   {
      sum2 += f[j] * g[j];
   }
   p = (double)(2) * sum1 - sum2;
   cout << p << endl;
   return 0;
}
```

Biographical information

I was born in Koprivnica, Croatia on June 22, 1970. In my born-town, I finished elementary and high school.

In 1997 I graduated from the Faculty of Science in Zagreb with the thesis title "*Doprinos razvoju teleskopa MAGIC za detekciju gama zračenja iz kompaktnih kozmičkih objekata*" ("Contribution to the MAGIC telescope development for gamma-ray detection from compact cosmic objects") (3).

During the study, I was a scholarship fellow of Ruđer Bošković Institute and after graduation I spent some time working at the Institute in the field of medium energy theoretical physics (2).

After study, I spent a few months at CERN where I was working on hybrid photodetector design under the supervision of Dr. Daniel Ferenc (1).

Since 1998 I was employed at the Faculty of Electrical Engineering and Computing in Zagreb as a teaching assistant and I was working in the field of experimental hypernuclear physics. In 1998 I spent two months at the University of Houston constructing multiwire chamber detectors for hypernuclear experiments. In 2001 I had one month IAEA fellowship in the field of applied nuclear physics at the Western Kentucky University.

At the beginning of 2002 I obtained a Master's degree at the Faculty of Science in Zagreb with the thesis title "*Primjena neutralnog mezonskog spektrometra (NMS-a) u istraživanju (K^-, π^0) hipernuklearne reakcije*" ("Utilization of the Neutral Meson Spectrometer (NMS) in the study of (K^-, π^0) hypernuclear reaction"). In 2002 I was working in the field of theoretical hypernuclear physics at the Faculty of Electrical Engineering and Computing in Zagreb.

At the end of 2002 I joined Professor Ferenc's group in the CROATEA project, I was participating in decommission of two HEGRA's Čerenkov telescopes for CROATEA at Roque de los Muchachos Observatory at La Palma and I started to work on my PhD thesis. In 2003 I was participating in HEGRA's multiwavelength campaign at La Palma.

Since 2003 I have been employed at Ruđer Bošković Institute as an assistant and I have also worked at the Faculty of Electrical Engineering and Computing as an adjunct teaching assistant. I have been working on MC simulations for CROATEA, data analysis of HEGRA's data as well as setting up the CROATEA observatory.

I live in Koprivnica with my wife Nataša, son Martin, and daughter Lucija.

List of publications:

(1) J.A. Barrio et al. (the MAGIC Collaboration) and D. Hrupec[1], *The MAGIC Telescope Design study for the construction of a* 17 m *Čerenkov telescope for Gamma-Astronomy above* 10 GeV, Technical Report MPI-PhE/98-5, Max-Planck-Institut fur Physik (Werner-Heisenberg-Institut) March 1998

(2) J. Albert et al. (the MAGIC Collaboration) and D. Hrupec[5], *Variable VHE gamma-ray emission from Markarian 501*, The Astrophysical Journal, **669** (2007) 862–883

(3) D. Ferenc, D. Hrupec[2] and E. Lorenz, *Solution to the ion feedback problem in Hybrid Photon Detectors and Photo Multiplier Tubes*, Nuclear Instruments and Methods in Physics Research A **427** (1999) 518–523

(4) S. Ceci, D. Hrupec[3] and A. Švarc, *The importance of the nucleon-nucleon correlations for the $\eta\alpha$ S-wave scattering length, and the $\pi^0\eta$ mixing angle in the low-energy $\eta\alpha$ scattering length model*, Journal of Physics G: Nuclear and Particle Physics **25** (1999) L35–L41

(5) T. Petković and D. Hrupec[4], *A Precise method for the detection of the two photons from the π^0 decay in hypernuclear spectroscopy*, Proceedings of the 17$^{\text{th}}$ International IUPAP Conference on Few-Body Problems in Physics (FB 17), Durham, North Carolina, 5–10 June 2003

(6) D. Ferenc and D. Hrupec, *A new approach to multi-wavelength correlation studies in blazars*, In preparation

(7) M. Pasanen, D. Hrupec, D. Kranich, A. Sillanpää, D. Ferenc, I. Puljak, Ž. Antunović *Optical, X-ray and γ-ray correlated variability and time lags observed during multi-wavelength campaign on the blazar Mkn 421 during February and March 2003*, In preparation

[1] http://magic.mppmu.mpg.de/publications/proposals/
[2] http://xxx.lanl.gov/abs/physics/9811028
[3] http://xxx.lanl.gov/abs/nucl–th/0104038
[4] http://xxx.lanl.gov/abs/nucl-ex/0312010
[5] http://xxx.lanl.gov/abs/astro-ph/0702008